Universidad Autónoma de Madrid

Departamento de Física Aplicada

Centro de Micro-Análisis de Materiales

Structural and compositional characterization of wide bandgap semiconductor heterostructures by ion beam analysis

Ph.D. thesis

Andrés Redondo Cubero

Madrid, 15th May 2010

Directors:

Dr. Raúl Gago Fernández

Prof. Dr. Elías Muñoz Merino

What another would have done as well as you, do not do it.

What another would have said as well as you, do not say it;

what another would have written as well as you, do not write it.

Be faithful to that which exists nowhere but in yourself

and thus make yourself indispensable.

(André Gide)

Contents

Acknowledgments

If I have seen more than the others is because I was settled on shoulders of giants. (Isaac Newton)

A big enterprise is rarely the work of one single person, and this thesis is not an exception. During my last five years I had the opportunity to enjoy Physics, not only from the textbooks, but from the day by day experiment, and I am indebt to a lot of people for making this dream real. I have had the possibility of living very exciting moments, as the first day of this thesis on the 26th of September of 2005. I can still remember very clearly that experiment at CMAM… how I could forget a nuclear reaction analysis with 3 MeV protons in the first day! Then everything was new and mysterious, but at the same time fascinating. I can say now, more than one hundred beam-days ago, that Physics is still amazing and worthy. I was so lucky to enjoy Science with the company of many good and wise people that I want to express here my tribute to all of them.

Of course, I thank my supervisors Raúl Gago and Elías Muñoz. They put their faith on me from the very first moment, when I knew nothing about ion beam analysis and wide bandgap semiconductors, and they taught me how to make Science, with capital letters. They were a constant source of inspiration and they supported me always, in everything. Raúl, you showed me the way of perseverance, honesty and enthusiasm. You shared with me day and night experiments, opinions, trips, and you provided me with your priceless wisdom. There are not words enough to tell you how fortunate I feel for having you there all this time. Elías, your experience and advices were the light needed to illuminate the road towards here and you offered me this big chance. You made me to give all of my best, and your restraint and compromise with this thesis were fundamental pillars to go ahead. This thesis would have never been possible without both of you, and I hope it will cover at least a part of all those things you did for me.

I have to acknowledge, evidently, to all the family of CMAM, for contributing to make this work easier. CMAM has been my home all this time and I would always remember the nice moments I passed, and the friends I leave. I want to thank very especially Ángel Muñoz-Martín, for his generosity and his everlasting willingness for helping me. I learnt from him so many things that it would not be fair to write only a few here, but he was, without any doubt, one of those giants holding me all this time, and a part of this thesis also belongs to him.

I would like to mention the aid of my tutor Aurelio Climent too, who opened me the doors of CMAM to develop my work and accepted me as a part of the accelerator staff without reservations. Naturally, I am very fond of my roommates at CMAM, Nuria Gordillo and Carolina Gutiérrez. We shared good and bad moments, but it was great to have you nearby to pass them! And I cannot forget the friendship and support of Mª Dolores Ynsa and Raquel González-Arrabal, for showing me the courage to go ahead and for being there whenever I needed it. Finally, a special remark for the administrative, the scientific and the technical team of CMAM, for working so hard and helping me every day.

My second home during these years was ISOM, and a lot of people from there have contributed to make this thesis, not only better, but even possible. First, I acknowledge the funding from the KORRIGAN European project and all the people working in it with me: Fernando González-Posada and Fátima Romero. We started together in this long quest, and much of the work we did is shown in this manuscript. I do not want to forget Alejandro Braña, who was a model of efficiency and dedication. Obviously, I have to thank Sergio Fernández-Garrido and Juan Pereiro, who prepared several series of samples included in this thesis. I learnt from them all I know about the growth of III-nitrides by MBE, and I enjoyed very much our discussions. I also thank Javier Grandal, Ana Bengoechea, and María Utrera for helping me during this time. At the end of my thesis, I started to work on ZnO with Adrián Hierro, and I want to express him my gratitude too, for considering me within the project and introducing me in this new and unknown field. It was a real pleasure to work with all of you.

Several collaborators have contributed to this thesis in a significant way, and I would like to mention them. In particular, I thank Marie-Antoinette Poisson (III-V Labs., France), Vittorianna Tasco and Adriana Passaseo (Lecce University, Italy), within the

KORRIGAN project. Regarding ZnO, I thank specially Atsushi Nakamura and Jiro Temmyo (Shizuoka University, Japan), who were always ready to hear my ideas and to prepare more samples.

During these years, I made two scientific stays at ITN (Lisbon), which became a crucial point in my thesis. I can honestly say that I felt at home there, and I need to thank a lot of people for taking care of me and including me in their family. I will be forever indebt to Katharina Lorenz, who adopted me from the first day with a smile. Her kindness, patience and friendship will stay forever in my heart, as well as the great moments we lived with my surprising samples, the Monte Carlo simulations and, of course, the talks during the chocolate break... I can hardly explain how many things she did for this thesis and for me, except saying thanks once more, thanks a lot! It was really pleasant to make Science with you, Katharina.

Also at ITN, I want to acknowledge Eduardo Alves. He received me with open arms, and he was always ready for helping with the experiments and the discussions: *obrigadisimo*, Eduardo. I thank Nuno Franco, the master of XRD, for his lessons and support in my experiments; and Sergio Magalhães for sharing his experience with me. To the rest of the people: Micaela, Luís, Ana, Teresa, Rui, Vania, José, Nuno… all my gratitude for so nice moments.

I also made a short stay at FZD (Dresden) to carry out some of the experiments of this thesis. I want to thank Dieter Grambole and Ullrich Kreissig for helping me with the NRA and the ERD-BIC. Mykola Vinnichenko deserves a special mention too, because of his intense efforts on growing ZnO samples at FZD. He was always ready for sharing with me his opinion and data, and he represents perfectly what a scientist should be. Thanks, Mykola.

I take advantage of this opportunity to thank all my friends, who have being always there, not only in the development of this thesis, but also in other important moments of my life. To my forever partners Patri, Mary, and David, and their family. To the Physics and Mathematics team: Esther, Carmen, Olga and Sylvi. To David Miguel, who started teaching me about the beauty of Science long time ago, when I was just a kid.

Thanks, finally, to my family, for dedicating so much time and efforts in my education. This is only a small reward after so long time. And thanks to you, Estrella, for patiently listening to me, for keeping me strong, but most of all, for sharing your life with me.

Andrés Redondo Cubero

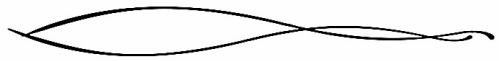

Madrid, 15th May 2010

Abstract

This thesis addresses the application of ion beam analysis (IBA) to the study of several wide bangdap semiconductor heterostructures. The studies carried out along this thesis were motivated by the need of improving the epitaxial growth of the active and base layers composing high electron mobility transistors (HEMTs) and high-power optoelectronic devices. At the same time, this thesis explores the advantages and limits of ion beam techniques for the structural and compositional characterization of such heterostructures, as an alternative and complement to X-ray diffraction methods. Next, the main aspects considered within this work are specified.

Concerning the growth of base layers on sapphire, the effect of the nucleation layers and the temperature was investigated for GaN and ZnO, respectively. The results obtained in this research were used to determine the optimum conditions for the growth of GaN and ZnO layers, especially regarding the crystal quality and the adequate incorporation of the different elements to the wurtzite lattice.

As an important point for the development of HEMTs, the presence of Al gradients affecting the AlGaN/GaN interface was studied by different IBA techniques. Such compositional Al profiles were examined together with the induced strain relaxation. The application of IBA in very thin AlGaN layers is also tackled for two different base layers. In relation with this study, high-resolution depth profiles of hydrogen were developed in samples prepared by different growth methods. The relevant role of the in-diffusion mechanisms for the introduction of hydrogen in the two-dimensional electron gas of HEMTs is explored.

This memory also deals with the difficult growth of high-quality ternary InGaN layers associated to the low miscibility of In inside the GaN matrix. This phenomenon is investigated for a series of samples covering the whole compositional range and grown with different substrate temperatures. The deterioration of the crystal quality of InGaN

layers for intermediate contents of In is verified and evaluated as a function of the progressive relaxation of the lattice parameters. The critical effect of the temperature in this sense is emphasized. The obtained results helped to establish a growth diagram of InGaN on the basis of the effective composition.

The bandgap engineering in MgZnO films is investigated in terms of the Mg content to determine the dependence of the electrical properties on the stoichiometry. These layers are also used for N doping by means of ion implantation. The optimization of the thermal annealing processes after the implantation to recover the crystal quality and the dopant activation is carried out and checked with additional photoluminiscence studies.

Finally, the studies showed in this thesis about lattice-matched AlInN and AlGaInN heterostructures revealed the synergy of the III/V ratio and the substrate temperature on the growth of epitaxial layers, affecting the crystal quality and the composition. The strain state of the films was analyzed by ion channeling and X-ray diffraction, evidencing the presence of anomalous channeling behaviors. Monte Carlo simulations explained these phenomena, linked to the steering effects of the projectiles at the interface. These simulations were also used to establish the role of the tetragonal distortion, thickness, and beam energy on this effect. The breakdown of the anomalous channeling is demonstrated theoretically and experimentally in specific lattice-matched heterostructures, allowing the accurate determination of the strain state.

1

Introduction and motivation

This chapter presents the general motivation of this thesis, based on the past and present state-of-the-art related to the crystal growth of wide bandgap semiconductors (WBS). The interest of the studies developed on these materials is discussed. The main properties and applications of WBS will be introduced, stressing the open-issues of these materials and their relation with the need of accurate characterization techniques. Finally, the structure and objectives of the thesis are exposed.

It is still an unending source of surprise for me to see how a few scribbles on a blackboard or on a sheet of paper could change the course of human affairs. (Stanislaw Ulam)

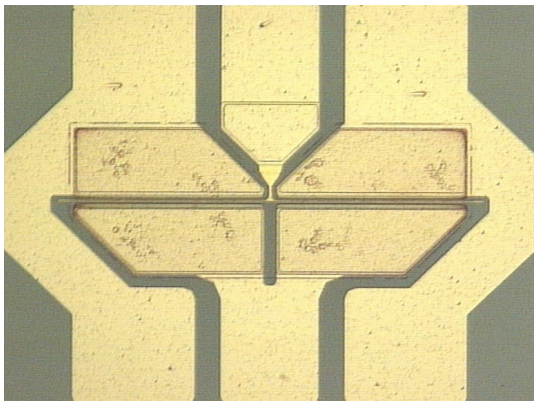

High electron mobility transistor based on GaN.
(Courtesy of F. Romero)

1.1. Historic perspective and motivation

Within the last decades, and especially after 1990, wide bandgap semiconductors (WBS) have become a point of great interest in Science and Technology [1]. Rather possibly, the fast dawning they have experienced is motivated by the limitations of the well-established semiconductor technology, mostly based on Si and GaAs [2]. In particular, the degradation of the devices at high operating temperatures and the restricted range and power of light emitting devices were two important weakness recognized long time ago [3]. This situation responds, essentially, to the intrinsic properties of such materials (gap, carrier concentration, breakdown field, saturation drift velocity, mobility…), which could not be further improved [2, 4]. Therefore, the quest of new alternatives for the development of high-temperature and high-power microelectronic and optoelectronic systems was strongly considered at the end of the 20th century [1].

Simultaneously to the need of novel materials, the constant demand of faster and more extended telecommunications (3G cellular networks as GSM or WiMAX, wireless systems, satellite communications, radars) stimulated the expansion of the semiconductor industry towards high-power electronics, mainly amplifiers working in the microwave range (0.3-300 GHz) [5]. Thus, civil and military applications of such devices turned out to be one of the driving forces for the development of high electron mobility transistors (HEMTs) based on WBS [6].

Apart from this, the generation of cheap, bright and long-lasting white light sources and full-color displays focused the attention on WBS too [7]. By 1990, the light emitting diodes (LEDs) based on GaAs and GaP were able to cover the red and yellow regions, but not the green and blue ones [1, 7]. Therefore, the production of white light by the combination of colors was not feasible. Nevertheless, the incredible reduction of power consumption of LEDs (80-90%) over other incandescent lamps or compact fluorescents would mean an important industrial and ecological breakthrough [2], which could not be ignored for long time.

Besides, close to year 2000, the constraint of optical storage devices for computers (mainly DVDs) was also an increasing problem linked to the wavelength of laser diodes

(LDs). In consequence, the absence of LDs in the blue region became another barrier for the progress in new formats of higher density data storage.

Taking into account this scenario, several private and public projects were destined to move forward the research of WBS, which is still far from maturity. Actually, the WBS market keeps on growing, reaching record values in 2008: about $900M for the power amplifier section [8] and $5100M for high-brightness LED area [9].

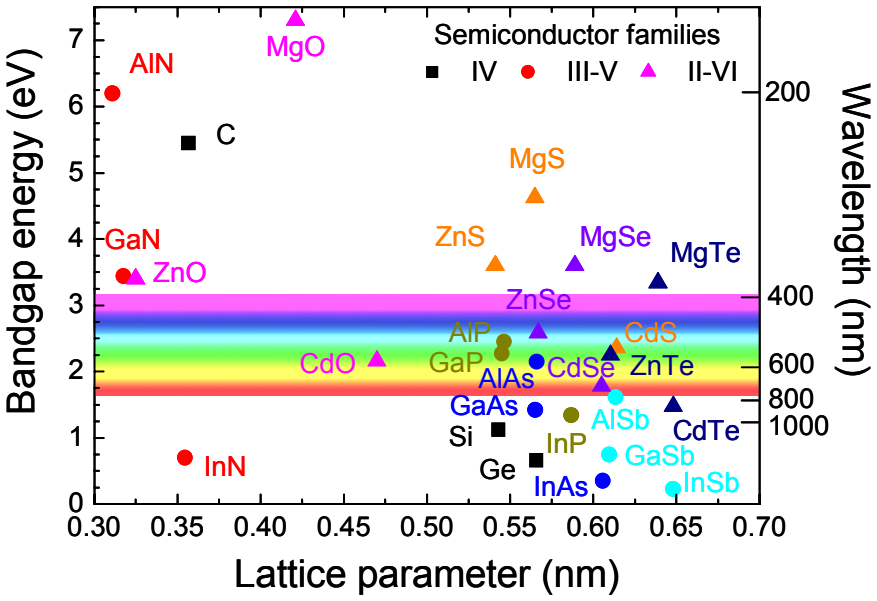

Figure 1.1 Chart of the main semiconductor families. Data from [1].

Technically, a WBS is a material with a bandgap energy higher than 2 eV [1], which corresponds to emission/absorption wavelengths shorter than 620 nm, i.e., the green/blue regions of the visible spectrum, up to UV light. Figure 1.1 shows that this characteristic is shared by different semiconductor families belonging to IV (diamond, SiC), III-V (GaN, GaP) or II-VI (ZnO, ZnSe) groups [10]. However, the desired requirements for high-power applications depends on the combination of several physical parameters of each semiconductor, which can be measured by means of a combined figure of merit (CFOM) [2], defined as:

$$CFOM = \lambda\varepsilon\mu_e v_s E_b^2 / (\lambda\varepsilon\mu_e v_s E_b^2)_{\mathrm{Si}},$$

where λ is the thermal conductivity, ε is the dielectric constant, μ_e is the electron mobility, v_s is the saturation drift velocity, and E_b is the breakdown field.

Figure 1.2 summarizes the CFOM of some relevant semiconductors. It becomes clear from Figure 1.2 that the group of III-nitrides (III-N) constitutes one of the most valuable WBS. On the one hand, the CFOM of GaN is 493, the highest after diamond; and on the other hand, the combination of the different binaries (AlN, GaN, InN) allows electronic bandgap engineering in a wide range: from 0.7 eV to 6.2 eV. Furthermore, these properties are in good correspondence with the high thermal and mechanical stability, the large piezoelectric fields, and the different heterostructure (HS) technology that GaN-based compounds can support [2, 11]. Because of these features, III-N HSs have been subjected to intense research during the last 20 years.

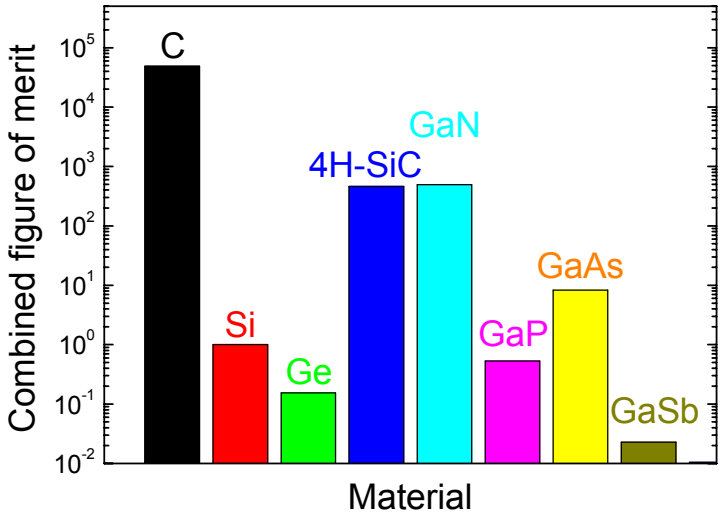

Figure 1.2 Combined figure of merit for different semiconductors. Note the logarithmic scale.

Of course, the road towards the implementation of III-N devices has not been easy, mainly due to the structural characteristics of GaN. In contrast to Si or GaAs, the stable phase of GaN is the hexagonal wurtzite structure (also for AlN and InN), what has been a very significant drawback for the growth and compatibility [11]. Despite GaN was first synthesized in 1932 by Johnson *et al.* [12], it was not produced in single crystalline form until 1959 [13]. The difficult growth of bulk GaN crystals triggered the use of different substrates for heteroepitaxy, being sapphire the most extended one [14]. The first reference to GaN single crystals on sapphire was published by Maruska and Tietjen in 1969 [15]. However, the large mismatch between sapphire and GaN (~13%) affects the crystal quality and, hence, the device properties. As a matter of fact, the optimization of the growth systems can be still considered the Aquile's heel of GaN-based electronics, mainly related with both defects and impurities.

Only in 1986, Amano *et al.* reported high-quality GaN crystals using a low temperature AlN buffer layer [16]. Five years later, Nakamura *et al.* proposed a GaN buffer layer [17] instead of the AlN one, but in 1995 the dislocation density of GaN-based HSs was still as high as $2 \cdot 10^{10}$ cm^{-2} [18]. Although this value has been improved, today the dislocation density of commercial templates is in the range of 10^8-10^9 cm^{-2} (*Lumilog*), which is far away from the qualities obtained for Si or GaAs (about 500 cm^{-2} for prime grade wafers).

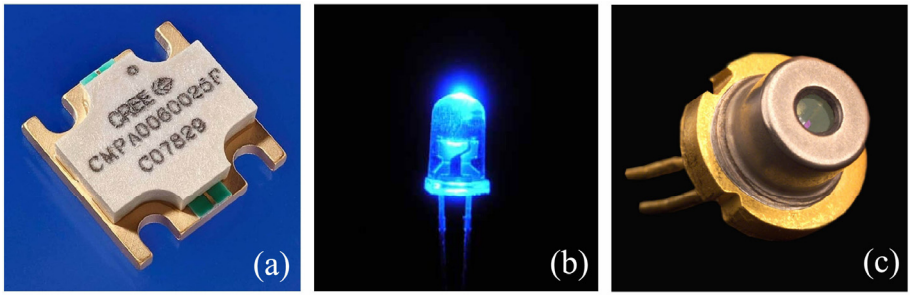

Figure 1.3 Current electronic devices based on GaN: (a) HEMT, (b) blue LED, (c) blue LD.

If crystal quality was a weak point of GaN at the beginning of 1990, p-type doping was another issue to be solved. Although the first GaN-based blue LED was reported by Pankove *et al.* in 1972 [19], the understanding of the p-type doping was not really complete until 1991, thanks to the discoveries of Akasaki *et al.* [20], Amano *et al.* [21] and Nakamura *et al.* [22]. In particular, Nakamura *et al.* demonstrated the reproducible activation of p-type GaN:Mg after a thermal annealing in N_2 or vaccum at 750ºC [22]. Interestingly, it was found that H impurities were playing an essential role in the compensation of the acceptor level from the dopant.

All these breakthroughs made possible the development of GaN-based devices at the end of the 20th century: AlGaN/GaN HEMTs [23] in 1991, high-brightness InGaN/GaN blue LEDs [24] in 1994, and InGaN-MQW blue LDs in 1996 [25]. Consequently, the efforts devoted to GaN were broadly rewarded, in such a way that the III-N group has become the keystone of present blue and UV photonic devices, as well as high-power, high-frequency and high-temperature technology. Indeed, HEMTs, LEDs and LDs based on GaN are now a commercial reality (see Figure 1.3), being distributed by several international companies. These new devices have brought an enormous variety of applications, from the *Blu ray disc* (launched by *Sony* and *Philips* in 2006), to the high-luminosity displays and lights in automobiles (*Audi* started to use white LEDs as

daylights), traffic lights (implanted already in many cities, in USA this could save 2.5 millions kW/h), street panels, etc.

Nowadays, it can be stated that III-N technology has evolved from promising to competitive. Nevertheless, since GaN and related compounds are relatively novel materials, there are still remaining difficulties which require further optimization to reach the best predicted capabilities in terms of efficiency and reliability [3]. In particular, several drawbacks linked to structural properties have not been completely solved [14, 26]. Recognized deficiencies found in III-N are: the lack of large high-quality GaN bulk substrates [26], the high dislocation density and residual stress in GaN templates on sapphire [14], the controlled n-type and p-type doping range [14], the high trap density and non-abrupt AlGaN/GaN interfaces in HEMTs [27], the phase separation for intermediate compositions in InGaN/GaN HSs [28, 29], the complex epitaxial growth of lattice-matched HSs [28-31], the high resistance of contacts in p-type materials [27], the elevated migration of metal contacts [27] and, last but not least, the difficult compatibility with Si technology.

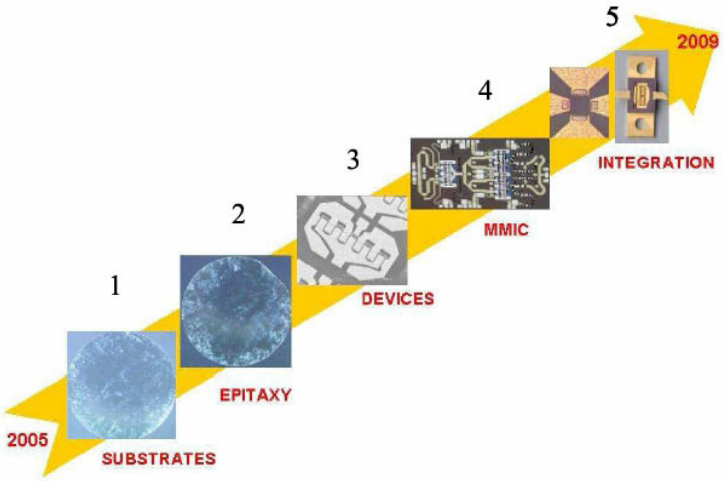

Figure 1.4 Roadmap of KORRIGAN project: from growth optimization to integration of devices [32].

This thesis was born to understand and overcome some of these issues, trying to shed light on the structural properties of these materials, as a part of the European project KORRIGAN (Key Organization for Research on Integrated Circuits in GaN Technology) [32, 33]. This project started in 2005 with the aim of developing GaN-based compounds for high-power devices in Europe, establishing at the same time a supply chain [32]. Figure 1.4 shows the roadmap of the KORRIGAN project consisting of five steps; the first two devoted to the optimization of the growth technology, which

is the goal of this thesis. Together with KORRIGAN, other national and international endeavors have extended the use of III-N to photodiodes or photodetectors, covering almost all the possible $Al_xGa_{1-x-y}In_yN$/GaN HSs. As a result, this thesis has adopted the broad interest on these general HSs, incorporating them to the present study.

During this work, and following the evident success of GaN, other WBS have appeared with relative intensity and frequency. In particular, due to the structural and electrical similarities (Figure 1.1), ZnO is currently being considered for reproducing, or enhancing, the results obtained with III-N [34-36]. Therefore, both GaN and ZnO are considered inside this manuscript; although they will not have the same specific weight due to the early stage of ZnO-based devices. Indeed, several of the difficulties already beaten in III-N persist in ZnO (p-type doping as the most important one, with an open and unresolved debate).

Of course, apart from III-N and ZnO, there are some other WBS with interesting properties for electronics and optoelectronics, such as SiC or ZnSe (Figure 1.1) [1]. However, due to the limited scope and time scale of this work, these materials will not be taken into account. Thus, in the following, only III-N and ZnO-based compounds will be consider in relation to WBS.

1.2. Structural properties of wurtzite-type WBS

As it was mentioned before, the physics of III-N (and ZnO) is dominated by their crystal structure, which is indeed the central point investigated in this thesis. The stable phase at room temperature of these materials is the wurtzite structure ($P6_3mc$, C^4_{6v}) [11, 14]. The wurtzite lattice exhibits hexagonal symmetry, with the unit cell defined by two lattice parameters (a, c). The theoretical ratio c/a is 1.633, and only structures with c/a ratios lower or equal to this value are stable [37]. Figure 1.5 shows the major crystallographic directions in a wurtzite lattice and its stereographic projection.

The stereographic projection is a bidimensional map of the crystal, with the fundamental characteristic of preserving all the angles between the planes (and axes) [38-41]. It is worth to notice that all III-N (AlN, GaN, InN) and ZnO share the same stable state (wurtzite), but this is not true for MgO and CdO, which have a cubic

(rocksalt) stable structure. Therefore, the stereographic projection shown in Figure 1.5a does not apply for them.

Because of the hexagonal system of the wurtzite lattice, twelve principal planes are distinguished in the projection, crossing the <0001> axis each φ=30º. These planes correspond to two families: the $\{0\bar{1}10\}$ and the $\{2\bar{1}\bar{1}0\}$. Of course, the growth direction selected for WBS is usually the <0001> axis, because it has the highest symmetry, but in some cases it is possible to find layers with other non-polar orientations (actually becoming more and more popular).

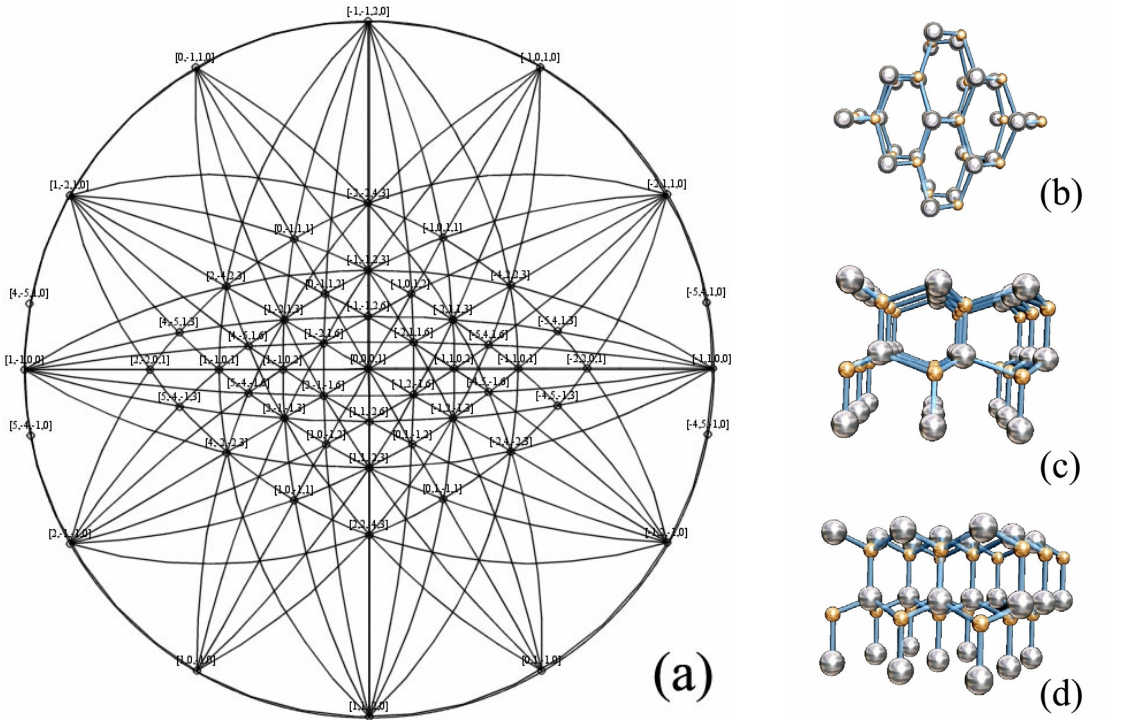

Figure 1.5 Stereographic projection of a wurtzite crystal (a) and perspective view of the main symmetry directions: (b) $[0001]$, (c) $[11\bar{2}0]$, and (d) $[10\bar{1}0]$.

In the wurtzite structure each atom is joined to its four first neighbors by hybrid sp^3 bonds [11]. This bond is strongly covalent, what explains the high melting point and the great mechanic stability of III-N. Table 1.1 summarizes other relevant physical properties of III-N, such as the lattice and the elastic constants. These parameters characterize the binary compounds, but can play also a significant role when extrapolating to ternary or quaternary films, so they have to be carefully considered. In particular, the common rule accepted for the mixed layers is Vegard's law [42], which estimates the modification of the lattice parameters by means of a linear dependence with the composition. Thus, in the most general case:

$$\begin{aligned} a_{Al_xGa_{1-x-y}In_yN} &= x \cdot a_{AlN} + (1-x-y) \cdot a_{GaN} + y \cdot a_{InN} \\ c_{Al_xGa_{1-x-y}In_yN} &= x \cdot c_{AlN} + (1-x-y) \cdot c_{GaN} + y \cdot c_{InN} \end{aligned} \tag{1.1}$$

The wrong application of the Vegard's law can induce an inaccurate analysis of the composition, the density or the strain state, so the error in the original lattice parameters is not negligible at all. To avoid this kind of situations in the current work, data from the review of Moram and Vickers [37] were assumed. This reference gives a complete list of relaxed lattice parameters of III-N. Considering these data, the mean value and the standard deviation of *a* and *c* were calculated, adopting them for the following analysis.

The variations in the lattice parameters of III-N are very common because of the absence of high-quality GaN bulk substrates and the large mismatch of the HSs. ZnO exists as bulk crystal but requires a high vapor pressure, so it is also frequently grown on sapphire, and the comments on the lattice distortion can be extended to it. The properties of the HSs are quite sensitive to the elastic strain, which can induce phase separation and relaxation of the lattice parameters. Thus, its characterization has become a key point [43, 44], even more considering the high piezoelectric constants of III-N [45], which are properties exploited very frequently in HEMTs [46] (although detrimental in photonic devices). Indeed, the polarization of WBS plays an important role in the design of the devices and, due to its link with the strain state [45], the control of the lattice deformation is critical when tuning the electrical properties of the HSs.

In general, the deformation of the crystal can be described by means of the classic Hooke's law [11]. Taking advantage of the hexagonal symmetry of the lattice, the equation between the stress forces (σ_{ij}) and the strain (ε_{ij}) can be expressed as:

$$\begin{pmatrix} \sigma_{xx} \\ \sigma_{yy} \\ \sigma_{zz} \\ \sigma_{xy} \\ \sigma_{yz} \\ \sigma_{zx} \end{pmatrix} = \begin{pmatrix} C_{11} & C_{12} & C_{13} & 0 & 0 & 0 \\ C_{12} & C_{22} & C_{13} & 0 & 0 & 0 \\ C_{13} & C_{13} & C_{33} & 0 & 0 & 0 \\ 0 & 0 & 0 & C_{44} & 0 & 0 \\ 0 & 0 & 0 & 0 & C_{55} & 0 \\ 0 & 0 & 0 & 0 & 0 & C_{66} \end{pmatrix} \begin{pmatrix} \varepsilon_{xx} \\ \varepsilon_{yy} \\ \varepsilon_{zz} \\ \varepsilon_{xy} \\ \varepsilon_{yz} \\ \varepsilon_{zx} \end{pmatrix} . \tag{1.2}$$

The coefficients C_{ij} are the elastic constants of the crystal. When the crystal is strained in the (0001) plane, the layer can expand or constrict in the [0001] direction, so the only non-vanishing terms of (1.2) are:

$$\varepsilon_{xx} = \varepsilon_{yy} = \frac{a - a_0}{a_0}$$
$$\varepsilon_{zz} = -2\frac{C_{13}}{C_{33}}\varepsilon_{xx} = \frac{c - c_0}{c_0} \quad , \tag{1.3}$$

where a_0 and c_0 are the relaxed values of the layer, obtained theoretically via Vegard's law for ternary or quaternary alloys. The relation (1.3) is often known as Poisson's equation of elasticity [37]. The in-plane strain given by ε_{xx} is called parallel strain, and the ε_{zz} is called perpendicular strain. The strain can be compressive or tensile, but of course (1.3) relates both kinds of states, being a parallel compression connected with a perpendicular elongation. Therefore, the tetragonal distortion of the lattice can be defined as $\varepsilon_T = \varepsilon_{xx} - \varepsilon_{zz}$, obtaining $\varepsilon_T<0$ for compressive states and $\varepsilon_T>0$ for tensile states.

Table 1.1 Selected properties of III-N at room temperature.

Parameter	*AlN*	*GaN*	*InN*	*Reference*
Melting point (ºC)	3487	2791	1873	[47]
Binding energy (eV)	2.28	2.20	1.98	[48]
Density (g/cm^3)	3.23	6.15	6.81	[47]
Lattice parameter a_0 (nm)	0.31112(2)	0.31889(1)	0.35377(1)	[37]
Lattice parameter c_0 (nm)	0.49796(2)	0.51855(1)	0.57038(2)	[37]
Elastic constant C_{13} (GPa)	99	103	121	[49]
Elastic constant C_{33} (GPa)	389	405	182	[49]
Band gap (eV)	6.14	3.43	0.64	[47]

Table 1.1 includes the constants C_{13} and C_{33} of III-N. There are still slight discrepancies depending on the selected reference, but here the values given in the review [49] were accepted. As the lattice parameters, the elastic constants interfere in the application of Vegard's law to strained layers, so it is important to fix them with the lowest possible error.

In addition to the strain, and sometimes related with it, the structure of WBS is limited in a great way by the extended defects [11, 50]. In particular, the heteroepitaxy processes normally produce the appearance of threading dislocations parallel to the

<0001> direction and originated at the interface with the substrate [51]. These dislocations emerge as relaxing mechanisms when the lattice mismatch is high, and they have normally a mixed character (both edge and screw dislocations take place) [51]. Together with the dislocations, the growth mode of the HS by means of coalescent islands can derive in additional defects, known as grain boundaries. Thus, the microcrystals can suffer tilt and torsion around the growth direction, increasing the mosaicity of the layers [11]. The study of these defects is essential because they affect the optical and electrical properties of the devices, and they will be partially investigated along this thesis.

1.3. Structural and compositional characterization of WBS

The underlying principle of bandgap engineering in WBS is the controlled combination of the different binaries to fabricate compounds with different composition. The relative proportion of one or another compound modifies the bandgap (Figure 1.6) and, therefore, it can be used to produce active layers for the device. In theory, the different phases can coexist within the WBS compound preserving the crystal quality. Of course, in practice, the compositional variations are always associated to structural changes of the lattice, generating diverse defects during the growth. Thus, there are physical limits for the miscibility of the constituting elements, which restrict the actual compositional range of high-quality epitaxial ternary and quaternary films (Figure 1.6).

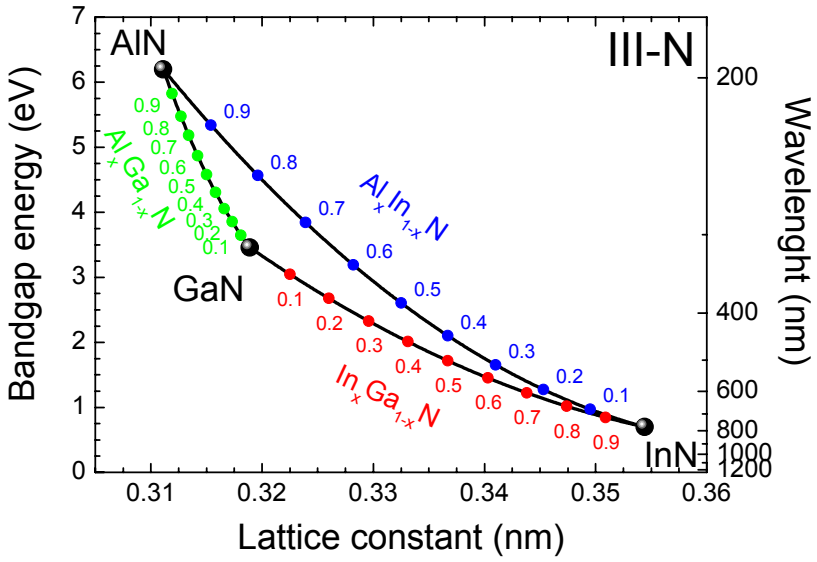

Figure 1.6 Bandgap engineering in III-N. Composition modifies both structural and electrical properties.

The intrinsic differences of the binary WBS involved in the HSs (see Table 1.1) establish a fundamental boundary for the enhancement of the devices and, e.g., the important role of the In clustering on the bandgap bowing parameter has been verified very recently by *ab initio* simulations [52]. As a consequence, the characterization of the HSs has become a key issue providing an essential feedback about the growth processes. Hence, the need of accurate techniques giving physical information about composition, crystallinity, strain, defects, impurities, phase separation, etc. is very high.

In general, characterization techniques of thin films can be divided as a function of the probing particle (photons, electrons, ions…) [52, 53]. The absorption inside the sample depends on the type and energy of each incident particle and, thus, the range and resolution of the techniques can vary significantly. At the same energy, the mass of the projectile determines in a great way the penetration range, being photons more penetrating than electrons, and electrons more than ions. Taking into account the nanometric dimensions of the WBS HSs, the desired techniques for characterization should cover, at least, several hundreds of nm. Figure 1.7 summarizes the penetration depths of different probes for a wide energy range (from 1 to 10000 keV). The most representative techniques for the structural and compositional determination of WBS, such as X-ray diffraction (XRD), transmission electron microscopy (TEM), Rutherford backscattering spectrometry (RBS), or secondary ion mass spectrometry (SIMS), remain within these energies.

Of course, not only the range, but also the sensitivity of the technique is important. The interaction between the particles and the target is manifested in different physical phenomena, which reveals information about the properties of the material. The intrinsic cross sections of the processes involved in the particle-solid interaction, together with the resolution of the experimental instruments, establish the detection limits of each technique. Consequently, the election of one or another characterization method depends on many factors. Table 1.2 summarizes the most used techniques in terms of the quantitative analysis of the structure and the composition, showing at the same time the depth resolution and the sensitivity. It can be seen that, among the large variety of methods, three techniques excel because of their high potential [54]: XRD, TEM and RBS.

Concerning WBS HSs, XRD is, as in many crystalline materials, the most extended method for routine measurements [55]. XRD provides very accurate quantitative information about the structure of the layers (lattice parameters, defects, strain, texture…), so it is a fundamental approach to determine the crystal quality after the growth. Actually, XRD is an indispensable part of the quality control in semiconductor industry. However, the low absorption of X-rays (of ~8 keV, Figure 1.7) makes the spatial resolution of XRD too high (~1 μm) to carry out depth-resolved studies in thin films, except for grazing incidence angles [56]. In addition, the indirect calculation of the composition (depending on the validity of Vegard's law) for ternary and quaternary systems is very limited [56]. Thus, the demand of complementary techniques to XRD is clear, especially considering the unstable processes of some WBS compounds (e.g., phase separation of InGaN and AlInN during the growth) [43, 57].

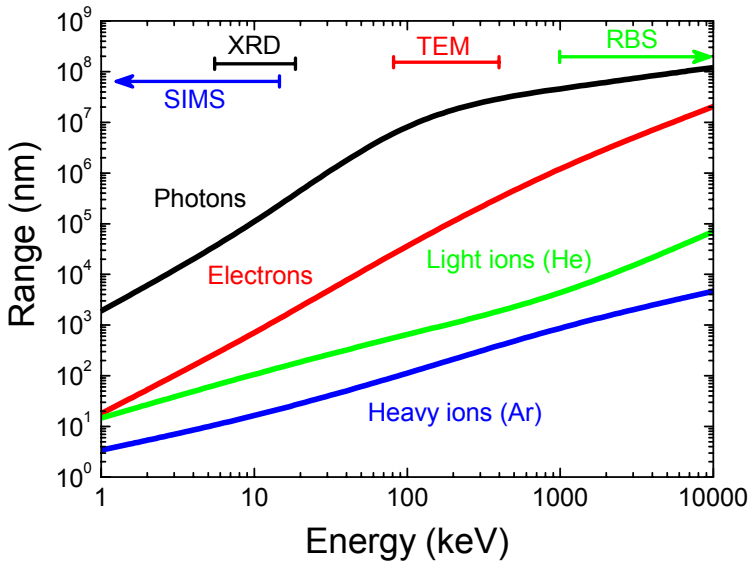

Figure 1.7 Penetration range in Si of different probing particles used for thin film analysis. For photons, the half-layer value was considered [58]. Electron and ion ranges were simulated with CASINO [59] and SRIM [60] programs, respectively. The typical range for XRD, TEM, RBS and SIMS is also shown (top).

Since the interaction of charged particles with the matter is of short range (Figure 1.7), they are a firm alternative to photon-based methods, providing depth-resolved analysis. Actually, XRD is frequently compared with TEM [56], which is a well-established technique for imaging very thin films (up to monolayer resolution) [52]. The structural information obtained from TEM is very valuable for the understanding of the growth mechanisms of the layers, because it can display the lattice defects with high sensitivity

(often combined with electron diffraction analysis). Moreover, this technique is especially interesting for the study of interfaces; a very critical point in WBS due to the heteroepitaxy processes [52]. Nevertheless, TEM can quantify the composition of the layers just in very small regions (few nm) due to the efficient electronic absorption in the target for conventional energies (80-400 keV, Figure 1.7). This circumstance makes the sample preparation very delicate and time-consuming, with the main drawback of the destruction of the specimen. Consequently, TEM is rarely used as a routine measurement of WBS.

Table 1.2 Comparison of different characterization techniques giving information about structure (S), composition (C), thickness (T) and density (D). Data from [52, 54].

Technique	*Probe*	*S*	*C*	*T*	*D*	*Resolution (nm)*	*Sensitivity (at. %)*
XRD	Photon	●	○	●	●	1*	0.1
XPS^{+}	Photon	-	○	-	-	0.2	0.1
SE	Photon	○	-	●	●	1	-
TEM	Electron	●	-	●	-	0.2	-
EDXS	Electron	-	○	●	-	-	0.1
EELS	Electron	○	○	-	●	-	0.1
AES^{+}	Electron	-	○	-	-	3	0.1
RBS^{++}	Light ion	●	●	○	-	5-10	0.1
NRA^{++}	Light ion	●	●	○	-	5-100	0.01
ERD	Heavy ion	-	●	○	-	20	0.1
SIMS	Heavy ion	-	○	-	-	10	<0.001

$^{+}$ In connection with ion sputtering. $^{++}$ In connection with ion channeling. *GI-XRD.
Legend: quantitative (●), semi-quantitative (○) and difficult/impossible (-).

Because many of the structural variations in WBS are induced by or linked to compositional gradients [57], a complete characterization of the HSs requires the absolute measurements of the composition with depth-resolution, which cannot be carried out properly with XRD and TEM due to the above discussed limitations. This fact points out the need of additional methods for a deep understanding of the growth processes affecting the crystal quality (and device performance) of WBS. In this regard, ion beam analysis (IBA) techniques have demonstrated to be particularly suitable,

allowing the compositional study of thin films (in the nm range) in an absolute way [61-63]. This group of techniques (Figure 1.8) comprises RBS, but also elastic recoil detection (ERD), nuclear reaction analysis (NRA), and particle induced X-ray emission (PIXE). The great potential of IBA lies on the diversity of ion-solid interactions that can take place in the target sample [64], making possible the determination of elemental profiles with high selectivity and sensitivity. Thus, for example, RBS and ERD respond to elastic scattering of ions, which allow the characterization of the samples in a very wide range of masses. Complementary, NRA and PIXE depend on more specific inelastic processes (with the production of γ-rays or X-rays), used for the detection of light and heavy atoms, respectively.

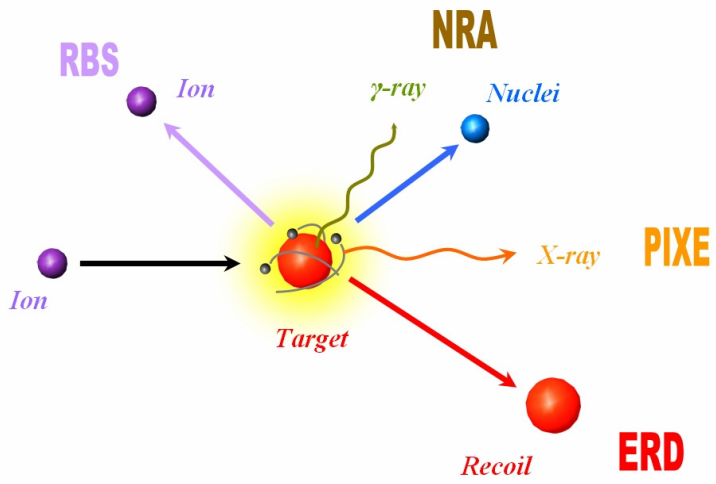

Figure 1.8 Basic ion beam analysis techniques depending on the ion-solid interaction.

Nonetheless, RBS is still the most popular IBA technique [65] because of its versatility and power. Actually, RBS is a fast, non-destructive and quantitative method for the compositional depth-profiling of materials, and it can be performed in special geometries (with the beam aligned to the crystal) for probing the structural properties of single crystals by means of a channeling phenomenon (RBS/C) [63]. Since the structural characterization of RBS/C allows the identification of phase separation and strain relaxation with depth-resolution, it can provide very valuable information about the growth mechanisms of WBS. Consequently, RBS (and IBA in general) is placed in an excellent position to compete and complete conventional XRD or TEM analyses.

Due to the depth range of conventional HSs, IBA methods require a MeV probing beam produced in a particle accelerator, which is a disadvantage when compared to XRD or

TEM compact systems. In spite of this, nowadays there are more than 100 accelerators all over the world [66], and IBA has become more and more available. Besides, the tunable beam energy increases the flexibility of the IBA because different resolutions and different regions of the sample can be selected.

As a result of the benefits of IBA, these techniques are currently quite extended in the characterization of WBS HSs, and the studies reported in the last years have probed their capability and efficacy [31, 43, 57, 67]. Hence, this thesis will continue this approach in order to give the most exact and complete description of the physical phenomena contributing to the enhancement of WBS HSs. In particular, RBS will be used as the main tool for the compositional characterization of the layers, often combined with ERD and NRA for specific studies. The basic structural properties of the HSs will be determined by means of RBS/C, and compared with XRD measurements, because of the different sensitivities of both techniques and the complementary information they give. Therefore, this investigation will serve to understand some fundamental questions about the growth of the HSs but, also, to establish the actual limits of IBA techniques. Remarkably, the accuracy of the RBS/C quantification of the strain state in thin HSs will be evaluated in detail, motivated by the importance of this parameter in WBS.

1.4. Objectives of the thesis

This thesis is heading for the enhancement and increase of our knowledge on the physical phenomena which restrict the capabilities of WBS HSs, especially concerning the design of electronic devices. As it was mentioned before, this goal is set within the KORRIGAN project, to enhance and develop high-power devices based on WBS. However, a general electronic device can be incredibly complex, containing several parts and requiring different processes for each step: growth, lithography, metallic contacts, thermal annealing, passivation, etc. Figure 1.9 shows an example of the diversity of components and steps for the fabrication of a HEMT. Since each process affects in a different way the device, it is important to control every stage as much as possible.

Nevertheless, in order to fix concrete objectives, this research is focused on the characterization of the active and base layers of the devices (a and b in Figure 1.9), i.e.,

the HS composed by the WBS compound (AlGaN, InGaN, MgZnO, etc.) and the GaN or ZnO layer grown on sapphire. Certainly, the growth of WBS HSs determines the initial quality of the material and it is still the bottleneck for many of the current applications (see section 1.1). Some of the other processes, as the diffusion of the ohmic contacts or the deposition of passivant layers [68] have been studied too during this thesis, but are not considered within this memory. Next, the specific objectives of this thesis are described.

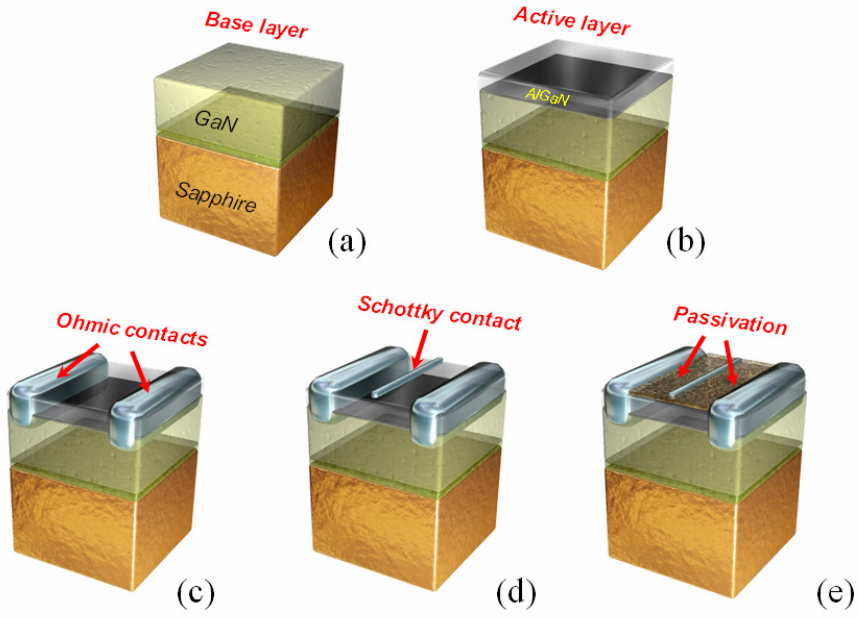

Figure 1.9 Main steps for the construction of an AlGaN/GaN HEMT: (a) GaN template, (b) growth of the HS, (c) deposition and diffusion of source and drain ohmic contacts, (d) deposition of base Schottky contact, and (e) passivation. In (c)-(e) steps, the processing involves lithography and etching too.

- **Optimization of the crystal quality of base layers: GaN and ZnO**

The first part of a WBS HS is always a base layer, so its optimization is essential for the construction of a high-quality device. Thus, one of the objectives of this thesis is to determine the best conditions for the growth of both GaN and ZnO base layers on sapphire (0001). As discussed in section 1.1, the properties of the previous nucleation layer (NL) is decisive for the final quality of the GaN crystal, so it will be investigated in detail using two different deposition methods. Its impact on the crystallinity and on the diffusion of impurities will be determined too. Of course, the substrate temperature is also an essential parameter affecting the heteroepitaxy, but since the conditions for GaN are well-known [16, 17], this point will be only analyzed on ZnO base layers.

- **Optimization and characterization of AlGaN and InGaN HSs**

AlGaN and InGaN layers are the main compounds for the development of the current electronic and optoelectronic devices based on GaN. However, the properties of these layers are very dependent on the composition, thickness, strain, impurities and crystal quality. Therefore, the optimization and characterization of these HSs is an important goal of this thesis. In particular, since the key point of HEMTs is the 2D electron gas (2DEG) [27] formed at the AlGaN/GaN interface, the role of the compositional Al gradients in such boundary will be studied by different methods. Besides, the presence of important impurities with potential effects on the 2DEG will be explored too.

On the contrary to AlGaN, which composition and thickness are tightly fixed by the requirements of the HEMTs [69], the limitations on the InGaN layers are mostly dependent on the miscibility of the binaries. Therefore, the main objective regarding InGaN will be the optimization of the growth conditions for the whole compositional range. Different parameters, as the temperature and the III/V rate will be modified to analyze their influence on the composition, crystal quality, and strain.

- **Characterization and doping of MgZnO layers**

The limits of the bandgap engineering and doping of ZnO compounds are not well established right now, so there are many open questions which need further analysis. The inclusion of Mg in the wurtzite lattice of ZnO allows the modification of the bandgap within certain limits, but the p-type doping is still not well understood. Therefore, as a part of the objectives of this thesis, the relation between composition and bandgap for MgZnO HSs will be investigated, and then, a systematic study of the doping of MgZnO will be carried out. Considering the achievements of p-type layers with elements of the III group, the evaluation of the effect of the N implantation (and thermal annealing) will be analyzed for different stoichiometries of MgZnO layers.

- **Optimization of lattice-matched HSs: AlInN and AlGaInN**

Lattice-matched (LM) systems have emerged as the most attractive alternatives to reduce the deficiencies of AlGaN and InGaN HSs. In particular, $Al_{1-x}In_xN$ layers with x~17% can fit the in-plane lattice parameter of GaN grown on the <0001> direction. Thus, these layers are perfect candidates for the development of quantum wells,

distributed Bragg reflectors and even HEMTs [70]. The situation can be improved if a quaternary AlGaInN system is used, because it allows the independent control of the lattice parameters and the bandgap. The inclusion of a low amount of In in AlGaN has been, besides, proposed as one important method to enhance the radiative recombination probability [71]. However, the difficult growth control and the intrinsic differences between the binaries (see Table 1.1) make these LM HSs very challenging. Therefore, along this thesis, the optimum growth conditions for both AlInN and AlGaInN systems will be explored, paying special attention to the achievement of LM HSs. Moreover, XRD measurements of these LM films have shown fundamental restrictions when giving accurate results about composition and strain state, so taking advantage of IBA the difficult characterization of such systems will be examined.

1.5. Structure of this thesis

This manuscript is divided into seven chapters. The first one is this introduction, where the initial motivations and the objectives of the thesis were described. Next, chapter 2 will be dedicated to the description of the main experimental methods, comprising both growth and characterization techniques used for the development and the study of the WBS HSs. These HSs will cover especially the AlGaN, InGaN, AlInN, AlGaInN systems, but also some others based on ZnO (MgZnO and MgZnO:N). In chapter 3, the basic principles of ion channeling will be exposed, as well as the Monte Carlo methods for modeling such phenomena. This chapter will allow the understanding of the structural information obtained in the experiments.

The following chapters (4, 5 and 6) are devoted to the results obtained along this research work. As mentioned before, one of the basic difficulties of WBS is the growth of high-quality base layers by heteroepitaxy, so chapter 4 is focused on this issue. In particular, the evaluation of fundamental physical parameters affecting the growth of GaN and ZnO base layers on sapphire will be shown there. Then, chapter 5 will include the analysis of HSs out of lattice-matched conditions (AlGaN, InGaN, and MgZnO). These systems are the building blocks of current WBS devices but, as it will be shown, their growth is not always fully controlled. Chapter 6 will evaluate the most complex and novel HSs, essentially related with lattice-matched compounds: AlInN and AlGaInN. These ternary and quaternary layers have been pointed out as one of the most promising options to reduce the structural defects of the classic approaches (AlGaN and

InGaN). Of course, they are a new technological test, even for the characterization techniques.

Finally, chapter 7 will summarize the main results and conclusions obtained along this thesis, proposing at the same time future works on this topic.

1.6. References

[1] K. Takahashi, A. Yoshikawa and A. Sandhu, *Wide bandgap semiconductors* (Springer, Berlin, 2007).

[2] S. J. Pearton, F. Ren, A.P. Zhang and K.P. Lee, Mat. Sci. Eng. R-Rep. **30**, 55 (2000).

[3] V. V. Buniatyan, and V.M. Aroutiounian, J. Phys. D: Appl. Phys. **40**, 6355 (2007).

[4] S. M. Sze, K.K. Ng, *Physics of semiconductor devices* (John Wiley and Sons, New Jersey, 2007).

[5] O. Ambacher, J. Phys. D: Appl. Phys. **31**, 2653 (1998).

[6] U. K. Mishra, P. Parikh and Y.F. Wu, IEEE Proceedings **90**, 1022 (2002).

[7] E. F. Schubert, *Light-emitting diodes* (Cambridge University Press, Cambridge, 2006).

[8] *GaN RF '08*, (Research and markets, 2008). http://www.researchandmarkets.com/reports/616371/

[9] *High-Brightness LED Market Review and Forecast 2009*, (Strategies Unlimited, 2009). http://su.pennnet.com/report_display.cfm?rep_id=199

[10] S. Adachi, *Properties of group-IV, III-V and II-VI semiconductors* (John Wiley & Sons, 2005).

[11] H. Morkoç, *Nitride semiconductors and devices* (Springer, Berlin, 1999).

[12] W. C. Johnson, J.B. Parsons and M.C. Crew, J. Phys. Chem. **234**, 2651 (1932).

[13] H. Grimmeiss, and H. Koelmans, Z. Naturfg. **14a**, 264 (1959).

[14] L. Liu, and J.H. Edgar, Mater. Sci. Eng. R **37**, 61 (2002).

[15] H. P. Maruska, and J.J. Tietjen, Appl .Phys. Lett. **15**, 367 (1969).

[16] H. Amano, N. Sawaki, I. Akasaki and Y. Toyoda, Appl .Phys. Lett. **48**, 353 (1986).

[17] S. Nakamura, Jpn. J. Appl. Phys. **30**, L1705 (1991).

[18] S. D. Lester, F.A. Ponce, M.G. Crawford and D.A. Steigenvald, Appl .Phys. Lett. **66**, 1249 (1995).

[19] J. I. Pankove, E.A. Miller and J.E. Berkeyheiser, J. Luminescence **5**, 84 (1972).

[20] I. Akasaki, T. Kozowa, K. Hiramatsu, N. Sawak, K. Ikeda and Y. Ishii, J. Luminescence **40-41**, 121 (1988).

[21] H. Amano, M. Kito, K. Hiramatsu, I. Akasaki, Jpn. J. Appl. Phys. **28**, L2112 (1989).

[22] S. Nakamura, T. Mukai, M. Senoh and N. Iwasa, Jpn. J. Appl. Phys. **31(2B)**, L139 (1991).

[23] M. Asif Khan, J. M. Van Hove, J. N. Kuznia and D. T. Olson, Appl .Phys. Lett. **58**, 2408 (1991).

[24] S. Nakamura, T. Mukai and M. Senoh, Appl .Phys. Lett. **64**, 1687 (1994).

[25] S. Nakamura, M. Senoh, S. Nagahama, N. Iwasa, T. Yamada, T. Matsushita, H. Kiyoku and Y. Sugimoto, Jpn. J. Appl. Phys. **35**, L74 (1996).

[26] A. Denis, G. Goglioa and G. Demazeau, Mat. Sci. Eng. R **50**, 167 (2006).

[27] R. F. Davis, S. Einfeldt, E.A. Preble, A.M. Roskowski, Z.J. Reitmeier and P.Q. Miraglia, Acta Mater. **51**, 5961 (2003).

[28] M. Ferhat, and F. Bechstedt, Phys. Rev. B **65**, 075213 (2002).

[29] T. Matsuoka, N. Yoshimoto, T. Sasaki and A. Katsui, J. Electron. Mater. **21**, 157 (1992).

[30] C. Hums, J. Bläsing, A. Dadgar, A. Diez, T. Hempel, J. Christen, A. Krost, K. Lorenz and E. Alves, Appl .Phys. Lett. **90**, 022105 (2007).

[31] E. Monroy, N. Gogneau, F. Enjalbert, F. Fossard, D. Jalabert, E. Bellet-Amalric, L. S. Dang and B. Daudin, J. Appl. Phys. **94**, 3121 (2003).

[32] G. Gauthier, and F. Reptin, *KORRIGAN: Development of GaN HEMT Technology in Europe*, (CS MANTECH 2006). http://www.csmantech.org/Digests/2006/

[33] G. Gauthier, *KORRIGAN: Key Organisation for Research on Integrated Circuits in GaN Technology*, FP6 Proposal (Thales Research and Technology, 2003).

[34] Ü. Özgür, Ya. I. Alivov, C. Liu, A. Teke, M. A. Reshchikov, S. Doğan, V. Avrutin, S.-J. Cho, and H. Morkoç, J. Appl. Phys. **98**, 041301 (2005).

[35] S. J. Pearton, D.P. Norton, K. Ip, Y.W. Heo, T. Steiner, Prog. in Mat. Sci. **50**, 293 (2005).

[36] H. Morkoç, and Ü. Özgür, *Zinc oxide: fundamentals, materials and device technology* (Wiley-VCH, Weinheim, 2009).

[37] M. A. Moram, and M. E. Vickers, Rep. Prog. Phys. **72**, 036502 (2009).

[38] J. J. Rousseau, *Basic crystallography* (John Wiley & Sons, Surrey, 1999).

[39] F. C. Phillips, *An introduction to crystallography* (Oliver & Boyd, Edinburgh, 1971).

[40] J. S. Smaill, *Metallurgical stereographic projections* (Adam Hilger Ltd., London, 1972).

[41] C. Klein, *Manual of mineral science* (Wiley-VCH, New Jersey, 2001).

[42] L. Vegard, Z. Phys. **5**, 17 (1921).

[43] K. Lorenz, N. Franco, E. Alves, S. Pereira, I.M. Watson, R.W. Martin, K.P. O'Donnell, J. Cryst. Growth **310**, 4058 (2008).

[44] V. Darakchieva, M. Beckers,M.-Y. Xie, L. Hultman, B. Monemar, J.-F. Carlin, E. Feltin, M. Gonschorek and N. Grandjean, J. Appl. Phys. **103**, 103513 (2008).

[45] F. Bernardini, V. Fiorentini and D. Vanderbilt, Phys. Rev. B **56** R10024 (1997).

[46] O. Ambacher, J. Smart, J. R. Shealy, N. G. Weimann, K. Chu, M. Murphy, W. J. Schaff, L. F. Eastman, R. Dimitrov, L. Wittmer, M. Stutzmann, W. Rieger and J. Hilsenbeck, J. Appl. Phys. **85**, 3222 (1999).

[47] J. Wu, J. Appl. Phys. **106**, 011101 (2009).

[48] J. H. Edgar, *Group-III nitrides* (INSPEC, London, 1994).

[49] A. F. Wright, J. Appl. Phys. **82**, 2833 (1997).

[50] S. Nakamura, Science **281**, 956 (1998).

[51] X. H. Wu, L. M. Brown, D. Kapolnek, S. Keller, S. P. Denbars and J. S. Speck, J. Appl. Phys. **80**, 3228 (1996).

[52] H. Bubert, H. Jenett, *Surface and thin film analysis* (Wiley-VCH, Weinheim, 2002).

[53] J. C. Vickerman, I.S. Gilmore, *Surface analysis: the principal techniques* (John Wiley and Sons, Chichester, 2009).

[54] D. Brune, R. Hellborg, H.J. Whitlow, O. Hunderi, *Surface characterization* (Wiley-VCH, Weinheim, 1997).

[55] U. Pietsch, V. Holy, T. Baumbach, *High-resolution X-ray scattering* (Springer, New York, 2004).

[56] D. K. Bowen, B.K. Tanner, *High resolution X-ray diffractometry and topography* (Taylor & Francis, London, 1998).

[57] S. Pereira, M.R. Correia, E. Pereira, K.P. O'Donnell, E. Alves, A.D. Sequeira and N. Franco, Appl. Phys. Lett. **79**, 1432 (2001).

[58] J. H. Hubbell, and S.M. Seltzer, *Tables of X-ray mass attenuation coefficients and mass energy-absorption coefficients from 1 keV to 20 MeV for elements Z=1 to 92 and 48 additional substances of dosimetric interest*, (National Institute of Standards and Technology, 2004). http://www.nist.gov/physlab/data/xraycoef/index.cfm

[59] D. Drouin, A.R. Couture, R. Gauvin, P. Hovington, P. Horny, H. Demers, *Monte Carlo simulation of electron trajectory in solids*, http://www.gel.usherbrooke.ca/casino/index.html (2007).

[60] J. F. Ziegler, M.D. Ziegler and J.P. Biersack, *SRIM*, http://www.srim.org (2008).

[61] J. R. Tesmer, M. Nastasi, *Handbook of modern ion beam material analysis* (MRS, Pittsburg, 1995).

[62] R. C. Bird, J.S. Williams, *Ion beams for materials analysis* (Academic Press, London, 1989).

[63] L. C. Feldman, J. W. Mayer and S. T. Picraux, *Materials analysis by ion channelling* (Academic Press, New York 1982).

[64] M. Nastasi, J.W. Mayer, J.K. Hirvonen, *Ion-solid interactions: fundamentals and applications* (Cambridge University Press, Cambridge, 1996).

[65] W.-K. Chu, J.W. Mayer and M.-A. Nicolet, *Backscattering spectrometry* (Academic Press, New York, 1978).

[66] *Ion beam, spallation neutron and synchrotron light sources in the world*, (International Atomic Energy Agency, 2010). http://www-naweb.iaea.org/napc/physics/accelerators/database/datasets/accelerators/all_acc/all_acc.html

[67] J. C. Zhang, M.F. Wu, J.F. Wang, J.P. Liu, Y.T. Wang, J. Chen, R.Q. Jin and H. Yang, J. Cryst. Growth **270**, 289 (2004).

[68] A. Redondo-Cubero, R. Gago, M. F. Romero, A. Jiménez, F. González-Posada, A.F. Braña and E. Muñoz, Phys. Status Solidi c **5**, 518 (2007).

[69] A. Jiménez, *Crecimiento y fabricación de transistores HEMT de AlGaN/GaN por epitaxia de haces moleculares*, (Universidad Politécnica de Madrid, Madrid, 2003).

[70] R. Butté, J-F. Carlin, E. Feltin, M. Gonschorek, S. Nicolay, G. Christmann, D. Simeonov, A. Castiglia, J. Dorsaz, H. J. Buehlmann, S. Christopoulos, G .Baldassarri Höger von Högersthal, A. J. D. Grundy, M. Mosca, C. Pinquier, M. A. Py, F. Demangeot, J. Frandon, P. G. Lagoudakis, J. J. Baumberg and N. Grandjean, J. Phys. D: Appl. Phys. **40**, 6328 (2007).

[71] S. F. Chichibu, A. Uedono, T. Onuma, B. A. Haskell, A. Chakraborty, T. Koyama, P. T. Fini, S. Keller, S. P. Denbaars, J. S. Speck, U. K. Mishra, S. Nakamura, S. Yamaguchi, S. Kamiyama, H. Amano, I. Akasaki, J. Han, and T. Sota, Nat. Mater. **5**, 810 (2006).

2

Experimental methods

The main experimental methods used in this work for the growth and characterization of wide bandgap semiconductor heterostructures are briefly described here. Ion beam analysis techniques are introduced as the most relevant tool in this thesis, paying special attention to RBS and the compositional characterization of thin films. The experimental methods for structural studies, comprising ion channeling and XRD, are thoroughly discussed too.

No amount of experimentation can ever prove me right; a single experiment can prove me wrong. (Albert Einstein)

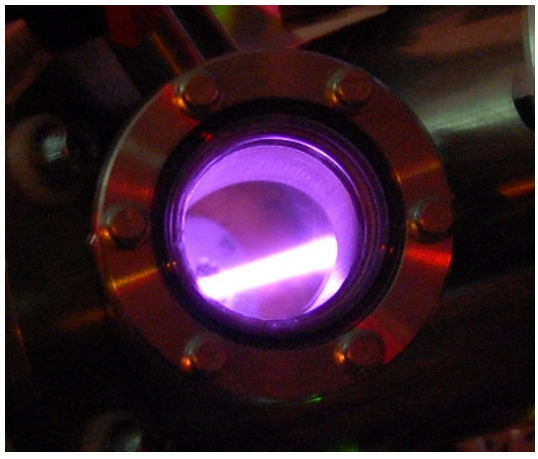

High energy He beam at CMAM.
(Courtesy of Dr. A. Muñoz-Martín)

2.1. Introduction

Considering the complex growth of crystalline WBS heterostructures (HSs) [1] discussed in the previous chapter, the experimental techniques for epitaxy and characterization play a fundamental role in the final development of the (opto)electronic devices. Hence, there is a rising interest in the analysis of the composition, thickness, crystal quality, strain, defects, impurities, etc. and its relation with the growth conditions. The exact knowledge of these parameters serves to enhance and optimize the WBS systems, so they provide an important feedback for increasing the quality of the materials.

Along this chapter the classical techniques for the growth of WBS HSs will be described, comprising the chemical vapor deposition (CVD) and the molecular beam epitaxy (MBE). Several of the samples showed in this thesis were grown by these methods, which have been successfully applied in GaN and ZnO-based devices [1]. Other techniques, as pulsed magnetron sputtering (PMS), still represent a residual part compared with CVD and MBE, but they have attracted more attention in the last years, especially due to the possible growth of epitaxial ZnO [2]. Therefore, the PMS system applied to these layers will also be discussed.

Of course, a precise characterization of the material is as important as a good growth method. In chapter 1, different advantages and drawbacks of thin film analysis techniques were mentioned. As it was clearly pointed out, although X-ray diffraction (XRD) is a very powerful method for the study of the structural properties of WBS [3, 4], its limitations in the absolute determination of the composition (assuming the validity of Vegard's law [5] and Poisson's equation of elasticity) are significant. Moreover, the high penetration of X-rays precludes in-depth analysis by XRD measurements at large-angle geometries. Consequently, the averaging values obtained in XRD makes the interpretation of the data difficult in certain conditions, i.e., when compositional gradients or progressive relaxation of the lattice parameters are present. This kind of phenomenon, however, plays a fundamental role in the appearance of phase separation [6], so it must be evaluated in detail in WBS.

Since the main goal of this thesis is to give the most accurate description of the compositional and structural mechanisms affecting the quality of the WBS HSs, apart

from the XRD experiments, an extensive ion beam analysis (IBA) of WBS samples was carried out [7, 8]. The IBA techniques complement perfectly the information obtained by XRD, because they allow a direct determination of the composition with depth-resolution and in a non-destructive way (in contrast, for example, with TEM). Moreover, the combination of IBA methods with ion channeling [9] provides structural details about the strain state, the defect density, the lattice-site location, etc. Consequently, IBA can assist and overcome most of the restrictions of XRD when characterizing WBS.

Next, the principles and experimental systems of IBA and XRD, which compose the backbone of this work, are described. Of course, additionally to the structural and compositional analysis, other techniques have been often required to correlate the results with physical properties such as the morphology, the electrical characteristics, the chemical bonding… These experiments comprise AFM, SEM, TEM, PL, Hg-CV, Raman spectroscopy, etc. and they were carried out thanks to several collaborations. When used, the details of the auxiliary techniques will be briefly explained or referenced inside the following chapters.

2.2. Growth techniques

Several growth techniques are available for the production of WBS [1, 10], depending on the purpose of the HS. These techniques determine in a great way the properties of the final device, especially in GaN-based systems due to the lack of ideal substrates [11]. The most extended growth method for WBS is the metal-organic chemical vapor deposition (MO-CVD), allowing the deposition of large areas in a fast way [12, 13]. However, the great structural differences between the binaries composing the WBS and the residual presence of impurities may require more controlled conditions for specific analysis. In such situations, MBE systems are used, because they ensure a clean environment, a low growth rate, and an accurate control of the different parameters and dopants [12].

In the last years, the deposition through PMS has gained attention too. This technique, as CVD, provides high growth rates and the deposition can be carried out on large wafers, but it is useless for the growth of GaN-based HSs because of the low melting point of Ga. Its capability in the epitaxial growth of ZnO, nevertheless, has been

demonstrated [2], opening a new path for the development of HSs. Here, these three techniques, employed for the growth of different samples in this thesis, are briefly described.

2.2.1. Chemical vapor deposition (CVD)

CVD is based on the decomposition of several precursors in gaseous phase to form a solid product on a substrate. Since the precursor gases for the CVD growth are neutral, the activation of the species is required (by electrical discharges, temperature, radiation…), normally producing a plasma which allows the chemical reaction and the intermixing. The whole process involves three steps: the gas entrance, the heterogeneous reaction and the elimination of the subproducts.

The growth of WBS by CVD was developed circa 1970 [1], but the optimization was delayed for several years [14]. The metal incorporation is generated by the pyrolysis of metal-organic precursors (trimethyl-Ga, diethyl-Zn, etc.) [15], so the technique is known as MO-CVD. Normally, the III/V or II/VI ratios in MO-CVD are very low (~0.001) to avoid the decomposition of the deposited material. This drawback is more relevant for GaN-based compounds due to the high binding energy of N_2 (9.5 eV), which makes ammonia (NH_3) the preferred precursor gas.

Apart from the gas pressure, another important parameter for the growth of WBS is the substrate temperature. In MO-CVD, the growth temperature of the layers can be as high as 1100 ºC [1, 13] to ensure a good epitaxial growth. Both temperature and fluxes can be used to control the lateral growth of the layers. The composition of the films is generally determined in first order by the flux ratio of the elements, while the crystal quality is mainly dependent on the temperature. However, the correct growth of the epitaxial films, usually achieved on sapphire substrates, is also conditioned by the nucleation layers [14], making more complex the optimization of these parameters.

The partial pressures involved in CVD growth do not keep UHV conditions and, therefore, the presence of residual impurities such as H and C coming from the precursors have to be considered with attention. Actually, the historical difficulties for p-type doping of GaN with Mg were due to the H compensation [16].

The studied MO-CVD III-N samples in this thesis were grown in an *Aixtron* 200 RF reactor (Figure 2.1a) at III-V Lab. of Thales (France) [6] and at Lecce University (Italy) [17]. This system is a horizontal tube reactor with a laminar flow inside a stainless steel housing. The gas entrance is separated by a plate to keep metal-organic and NH_3 gases in independent regions, avoiding chemical pre-reactions that result in unwanted products and low growth efficiency. Consequently, the reaction takes place at the surface of the substrate, which is a crucial point for the growth. The substrate is rotated on a graphite plate and heated by a RF-coil.

Variations of these systems have been also used for MO-CVD of ZnO-based layers. In particular, in this thesis the plasma enhanced MO-CVD system at Shizuoka University (Japan) was used for the growth of ZnO and MgZnO layers [18]. The mayor difference with respect to the growth of III-N is that O radicals are generated directly from O_2 gas, because the dissociation of this molecule is easier than for N_2. Apart from this, the general set-up is very similar to those described before. More details about MO-CVD can be found in references [13, 19].

2.2.2. Molecular beam epitaxy (MBE)

MBE arose as a technique for the growth of thin films with high purity, successfully demonstrated in the decade of 1970 for III-V semiconductors [20]. The method consists on the evaporation of one or more elements confined in cells, in such a way that each individual molecular flux can be controlled and directed towards a substrate, where the film is deposited. This process takes place in a chamber under UHV conditions ($<10^{-9}$ mbar) and with a cooled shroud (by liquid N_2), which warrant a low or negligible incorporation of impurities from the residual gases.

The individual molecular beams are produced in separate Knudsen effusion cells, where the temperature can be modified and stabilized with high accuracy using proportional-integral-derivative (PID) parameters. The material to evaporate is placed in a melting pot made of pyrolytic boron nitride, which is heated by a filament. Every cell has a mechanic shutter to stop the molecular beam flux when needed. Of course, the use of Knudsen cells requires solid targets, so N or O must be incorporated in gas phase by a different procedure. There are different variations of MBE which allow the introduction of gases, such as GS-MBE (with gas source), MO-MBE (with metal-organics) or PA-MBE (plasma assisted) [19]. The latter is suitable for enhancing the previous activation

of the gases, even in the case of pure N_2 (difficult to dissociate because of the high binding energy). Therefore, PA-MBE can avoid the use NH_3 ensuring a H-clean environment, which is one of its main advantages regarding the III-N growth.

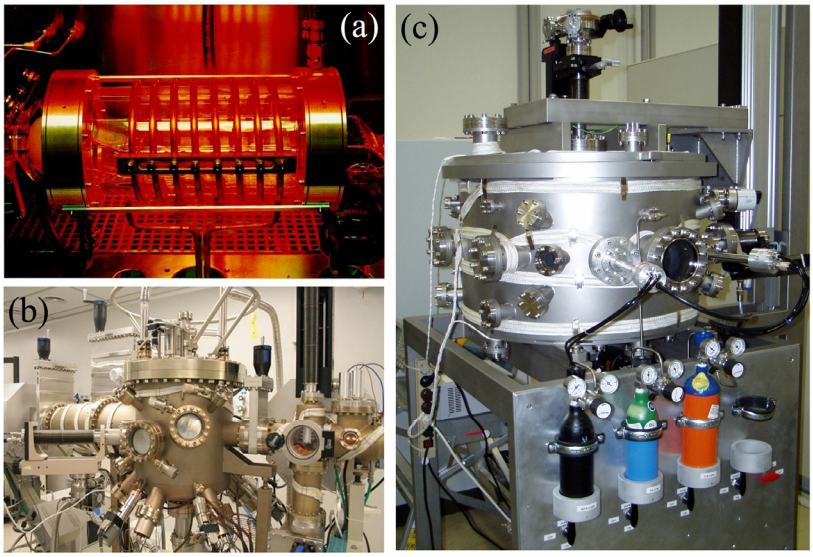

Figure 2.1 Experimental systems used for the growth of WBS HSs: (a) Aixtron 200RF for CVD, (b) Riber 21S for MBE and (c) PMS.

The elemental individual metal fluxes are controlled by the temperature of the cells. The composition of the film is mainly regulated by the relative flux value. However, it is important to note that, independently on the flux, deviations from the nominal value may be produced due to the different sticking coefficient of each element and the reemission of deposited material. Therefore, in several cases, the stoichiometry of the compound does not correspond to the calculated one from the fluxes and, therefore, a good calibration is essential.

The substrate is located on a sample holder, which is rotated for a better homogeneity of the lateral coverage. The temperature can be modified too but, normally, it can reach lower values than in CVD due to design limitations. On the contrary, to enhance the incorporation of the atoms in low energy positions the growth rates are ~1 μm/h (few monolayers per second). The crystal quality is very dependent on the temperature, but also on the topography derived by the growth regime, which can follow different 2D and 3D modes (Volmer-Weber, Frank-van der Merwe or Stranski-Krastanov) [19].

In this thesis, all the PA-MBE samples were grown in a *Riber Compact* 21S system at ISOM (Figure 2.1b). This system is designed for the growth of 2 inches wafers, and

contains two consecutive chambers for transference (load lock from ambient to UHV conditions) and for growth, respectively. The main chamber has a base pressure of 10^{-11} mbar. Four Knudsen cells are available, three for group III elements (Al, Ga, In) and another one for the dopants (Mg or Si). The N plasma is generated by applying a RF power to ultra-pure (99.999999 %) N_2 molecular gas, and the working pressure is ~10^{-5} mbar. The manipulator on which the substrate is placed rotates typically at 60-120 rpm and it can be heated up to 900 ºC.

Apart from the growth items, there are several in-situ characterization techniques that allow a good real-time control of the MBE growth: a reflection high energy electron diffraction system (RHEED) with a CCD camera, an optic pyrometer and a quadrupole mass spectrometer (QMS). In particular, RHEED patterns are sensitive to the roughness of the layers, so they are very useful to identify the growth mode. Further details about this system can be found in reference [21].

2.2.3. Pulsed magnetron sputtering (PMS)

One of the most extended physical vapor deposition techniques for thin film growth is PMS. This method is based on the directional ejection of atoms from an ion irradiated target towards a substrate. In this sense, it is similar to MBE, but here the atoms are not emitted by evaporation. In contrast, in PMS the target is bombarded by an additional plasma (usually Ar), which is confined close to the target thanks to a magnetic field. Therefore, there is no limitation on the melting point of the target (as in MBE), but solid materials are required. However, the low melting point of Ga (29.8 ºC) makes PMS useless for the growth of GaN-based materials. Fortunately, this drawback does not exist for Zn, so this approach does work in ZnO compounds [2].

The growth of ZnO by PMS is normally carried out inside a chamber with high-vacuum conditions (~10^{-6} mbar). For the target, a high purity (99.99 %) Zn disk is fixed inside the magnetron. The gas system allows the introduction of different species (Ar, O_2, N_2), After a discharge, the plasma is activated and confined close to the target, acting as a cathode. Therefore, the target is bombarded with ions of certain energy (normally hundreds of eV), regulated by a power supply. To achieve an oxide film, the plasma is composed of a mixture of Ar and O_2. The reaction of the plasma with the surface of the target (reactive sputtering) makes possible the combination of Zn and O in different

charge states. Varying the partial pressure of the gas mixture, the stoichiometry can be modified and, varying the power, the growth rate can be tuned. Before the deposition, the target is cleaned by a pre-sputtering to avoid poisoning, and the growth is not started until a stable condition is reached. Then, the shutter is opened for starting the growth process. The substrate is placed on a sample holder which, as in MBE, can be normally rotated and heated for a better control of the lateral homogeneity and the crystal quality.

In this thesis, the PMS used was a home-made system at FZD (Figure 2.1c) [2, 22]. The chamber contains two unbalanced magnetrons (*MightyMAK*) for 2 inches targets operating in parallel at medium-frequency (2.5 kHz with a duty cycle of 50 %). The average operation power of the magnetrons is about 115 W. Before each deposition, the chamber can be baked up to 100 °C, obtaining a base pressure of ~10^{-7} mbar. The Ar and O_2 gases are available in separated bottles, being the mixture limited by a gas flow controller (*MKS*). The sample holder is installed 6 cm distant from the magnetrons. The substrate can be heated up to 500ºC. Additional details of the PMS system can be found in references [2, 22].

2.3. Compositional characterization techniques

Nowadays, there are several characterization techniques providing compositional analysis of materials. However, as discussed in chapter 1, not all of them offer the same accuracy, resolution, sensitivity, selectivity, quickness, etc. Therefore, the election of one or another method may represent the difference between a conclusive and an unreliable analysis. In this sense, IBA [7, 8] arises as an alternative to XRD, being one of the most versatile methods for the absolute compositional characterization of materials, either in bulk or in thin films. The large variety of systems and physical processes taking part in IBA, make possible a wide set of experiments in many fields, including the semiconductor science. In particular, IBA can help to understand and optimize the mechanisms influencing the growth of HSs, which is a principal issue in the WBS technology. Next, the main IBA techniques used in this thesis for the compositional characterization of WBS are described.

2.3.1. Rutherford backscattering spectrometry (RBS)

(a) Basic concepts of ion-solid interaction

RBS is a well-established [23, 24] powerful technique for the compositional characterization of materials [25]. Essentially, the idea behind RBS is similar to that developed by Geiger and Marsden in 1909 [23]: a beam of energetic particles is launched toward a target (sample) and the scattered projectiles are detected at a certain angle. When the beam reaches the sample, a small portion of the incoming ions suffer close encounters with the target nuclei and, due to the Coulombic interaction, are backscattered. Such elastic processes can be treated within the classical mechanics framework since the involved velocities are not high (2 MeV He beam has a velocity of 0.033*c*). As an additional simplification, only binary collisions between the projectile and the atom can be considered, so the problem can be solved exactly assuming a two-body model [25]. Imposing conservation laws for the energy and the momentum, the velocity and scattering angle of the projectiles can be obtained as a function of the initial parameters of the incoming ion [25].

Three main aspects have to be considered during RBS experiments: the mass resolution, the sensitivity limits for the compositional analysis and the depth resolution. The accuracy of an RBS analysis depends essentially on these factors.

In first place, RBS can provide mass-resolved information of the elements belonging to the specimen. This fact is a consequence of the mass-dependence of the energy loss during the collision with the atom. Actually, due to the elastic behavior of the collision, the ratio between the final and the initial energies of the ion, known as the kinematic factor (*K*), will be lower than 1. If M_1 and M_2 are the masses of the projectile and the target atom and θ is the scattering angle, then it can be proved that [25]:

$$K_{RBS} = \left(\frac{(M_1/M_2)\cos\theta + \sqrt{1-(M_1/M_2)^2 \operatorname{sen}^2\theta}}{1+(M_1/M_2)} \right)^2 . \qquad (2.1)$$

Assuming that the collision takes place only at the surface, the mass of the element can be measured only by the reduction of the energy of the projectile ($\Delta E = E - KE$). Thus, the mass resolution is a function of *K* (actually proportional to $(\partial K/\partial M_2)^{-1}$) [25]. If the

difference in the kinematic factor is high, the resolution is high too; whereas similar values of K lead to a difficult separation of the elements.

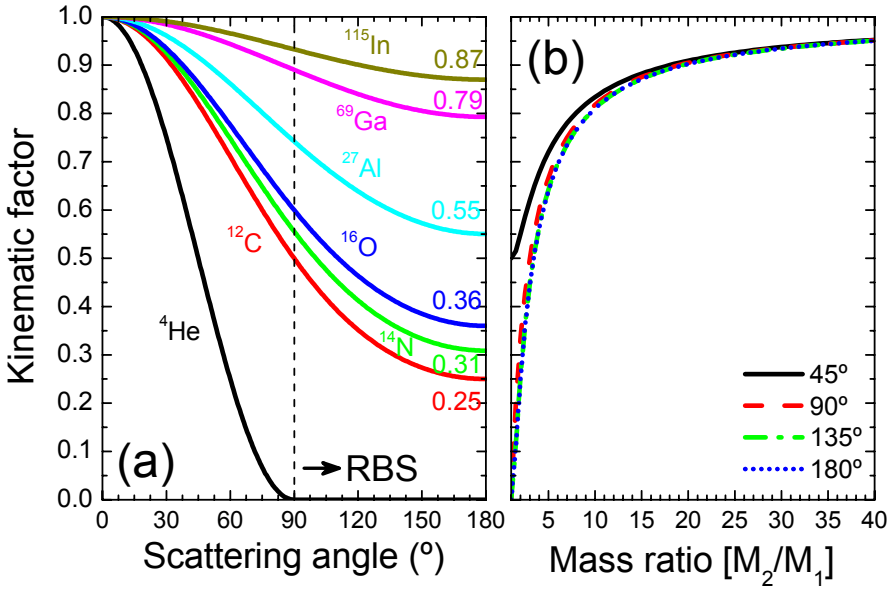

Figure 2.2 Kinematic factor for He ions as a function of the scattering angle (a) and the mass ratio (b).

Figure 2.2a shows the angular dependence of K for different atoms. The largest separation between elements takes place at 180º, indicating that this position corresponds to the best mass resolution. Actually, this is the reason to place the detectors in backscattering geometry in the experimental chambers. Moreover, K is almost constant in a wide range close to 180º, which allows an increase in the solid angle of the detector without changing significantly the depth resolution. This fact is clearly shown in Figure 2.2b, where the variation of K with the scattering angle is almost indistinguishable for every particle-atom couple, especially between 135º-180º. Figure 2.2b also shows that heavy atoms will scatter the impinging ions with higher energies than light atoms, which means that they will appear at higher energies in the spectrum too. However, even more remarkable, heavy elements are worse resolved in mass than light elements in RBS. This is evidenced by the asymptotic behavior obtained for large mass ratios. Thus, for example, a difference of ΔM_2=4 between C and O corresponds to ΔK=0.11, whereas a large difference of ΔM_2=46 for heavy elements such as ^{115}In or ^{69}Ga has only ΔK=0.08. The measurement of heavy elements with a small difference ΔK might require special conditions in the experiment to separate the signals in the spectrum (e.g., when the energy resolution is lower than the detector resolution).

Once the identification of the individual elements of the target is known, the second aspect to consider in RBS is how to quantify their concentration. Of course, the number of detected backscattered particles (yield) will be proportional to the number of target atoms per unit area (concentration), but also to other factors such as the number of incident particles or dose (Q) and the solid angle of the detector (Ω). All of these factors can be known experimentally. Nevertheless, there is another important variable to consider when calculating the concentration: the scattering probability. Atoms with different masses have different scattering probabilities because the Coulombic potential depends on the atomic number and, therefore, the repulsing force will be higher for heavy elements than for light ones.

The physical quantity representing the scattering probability is the differential cross section ($d\sigma/d\Omega$) [24], and it is the essential parameter to consider for the calculation of the concentration. The physical meaning of the cross section is the effective area of each nucleus presented to the beam of incident particles. The calculation $d\sigma/d\Omega$ was first derived by Rutherford for the Coulombic potential [24] and, in the laboratory frame of reference, it can be expressed as [25]:

$$\frac{d\sigma}{d\Omega} = \left(\frac{Z_1 Z_2 e^2}{16\pi\varepsilon_0 E} \right)^2 \frac{4}{\sin^4\theta} \frac{\sqrt{1-\left[(M_1/M_2)\sin\theta\right]^2} + \cos\theta}{\sqrt{1-\left[(M_1/M_2)\sin\theta\right]^2}}, \qquad (2.2)$$

where E is the energy of the ion and Z_1 and Z_2 are the atomic numbers of the ion and the target atom, respectively.

From the quadratic dependence with Z_2, it can be deduced that heavy atoms are more efficient scatterers than light atoms, i.e., RBS is much more sensitive to them. This is also true for the impinging ions: the yield obtained with a He (Z_1=2) beam is four times as large as the obtained with a proton beam (Z_1=1). Indeed, this is one of the reasons to prefer He instead of H as probing particles in RBS. However, the use of heavier ions than He results in the deterioration of the energy resolution of the detectors, so they are not suitable for RBS, except for very specific configurations.

Following (2.2), the cross section has its lowest value for angles close to 180º, which means that backscattering events at such angles are very rare. Unfortunately, those angles provide normally the best conditions to enhance the mass separation, although

the constant value of the kinematic factor at ~180º makes possible the use of large detectors (high Ω) without the loss of mass resolution. Additionally, the statistics of the experiment can be increased using high doses too.

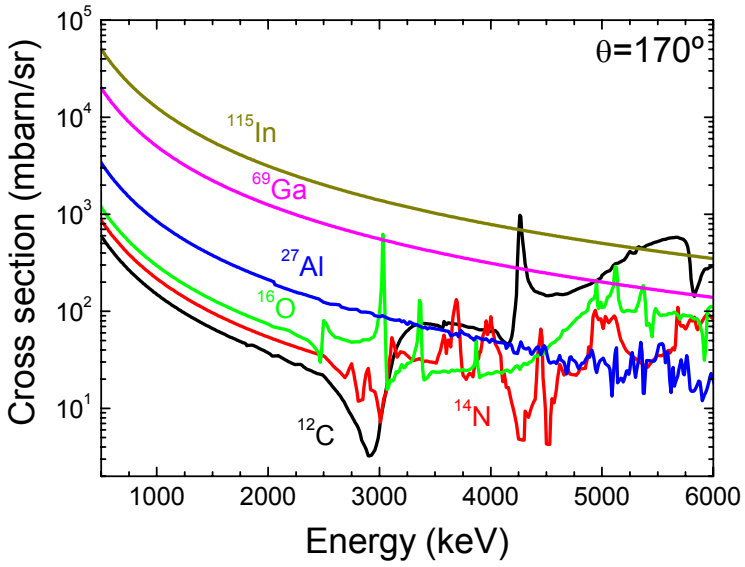

Figure 2.3 Cross sections for selected elements at 170º with a He beam.

But probably the most relevant consequence of (2.2) is the energy dependence of the scattering probability. The cross section is proportional to E^{-2}, what means that backscattering yield will increase very rapidly with decreasing projectile energy before the collision event. This point explains the conventional 1-2 MeV energies used in RBS experiments and the typical rising yield in the low energy region of the spectra (see, for example, Figure 2.5).

Figure 2.3 shows the cross sections of different elements as a function of the energy for He scattering at an angle of 170º. Note that, below 2 MeV, the cross section follows the behavior predicted by (2.2) independently of the target atom. This is also true for high energies if just heavy elements as In or Ga are considered. For light elements, however, severe deviations to the Rutherford scattering cross section exist. These deviations appear because, at high energies, the ion-atom distance of closest approach is reduced to the dimensions of nuclear sizes [25]. In such circumstances, not only the Coulombic electronic force, but also nuclear forces influence the scattering process. Therefore, nuclear resonances can affect the RBS spectrum when measuring at high energies. Some of these resonances are shown in Figure 2.3 for C, O, N and Al.

Although the non-Rutherford cross sections have to be tabulated [26], they should not be considered always as an inconvenient. On the contrary, the nuclear resonances become a great help for the enhanced detection of light elements, which are more difficult to detect in RBS experiments. As shown in Figure 2.3 the resonances take place for specific energies (and usually for specific scattering angles too). For example, the cross section of C at 4.065 MeV is 128 times greater than Rutherford's one, what makes the detection of a C atom even easier than the detection of an In atom. Furthermore, the resonance character (narrow peak in σ) can be used to profile the corresponding light element.

Once the cross section is known, the quantification of the composition can be developed as a function of Ω, Q and the experimental backscattering yield (Y). In the simplest case of RBS on a thin film under normal incidence, the areal density (number of atoms per unit area) can be calculated as $N_A = Y/Q\sigma\Omega$, where σ is the average cross section (coinciding with the $d\sigma/d\Omega$ for small Ω). However, this formula is only a surface approximation, where a constant energy of the particles is assumed. When the beam enters into the target, the ions slow down and lose energy. To take this effect into account a new variable must be considered: the stopping force.

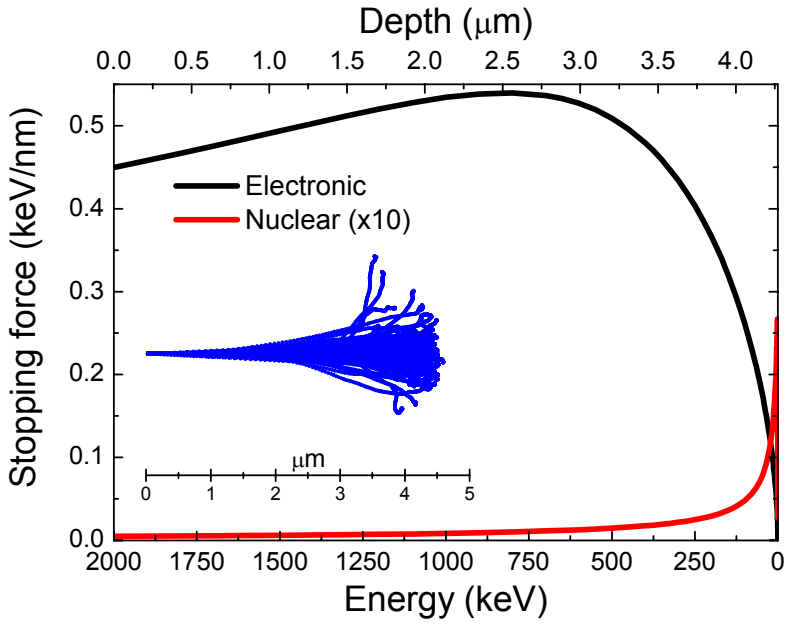

Figure 2.4 Stopping force for 2 MeV He ions into GaN. Inset shows MC simulations of 100 tracks.

As the particles travel into the sample, the interaction with the surrounding atoms makes decrease their energy. This energy loss per unit length is called stopping force ($S=dE/dx$). The two principal processes contributing to the energy loss are the interaction of the ion with the bound or free electrons (electronic stopping) and with the nuclei of the target atoms (nuclear stopping), being the total S described by the sum of both factors. The definition of the stopping force is not completely convenient for RBS calculations, because it depends on the thickness of the target and not on the atomic areal density. A more practical magnitude is the stopping cross section ($\varepsilon=S/N$), i.e., the energy loss normalized by the atomic density of the material.

Although the stopping force can be experimentally measured (e.g. by transmission experiments), the most extended approach is its determination via the Monte Carlo (MC) program SRIM [27, 28]. Figure 2.4 shows the results of the simulation of SRIM for a 2 MeV He beam entering in GaN. Both electronic and nuclear stopping forces are illustrated, confirming the predominant role of the electronic processes for high energies. The stopping force increases up to 1 MeV and then decreases again. However, along most of the trajectory, the stopping force is approximately constant (0.5 keV/nm). The total range of the ions is also shown (see inset). When the target is composed by mixed species, the stopping cross section is assumed to verify the linear additivity, i.e., the energy loss in the mixed layer is the sum of the losses in the constituent elements, weighted proportionately to their abundance in the compound. This principle is known as Bragg's rule [25].

The stopping force is the physical link between energy and depth and, therefore, it is the mechanism providing depth resolution to RBS. Thus, the total energy loss by an ion can be divided in three steps. First the ion travels from the surface towards the target atom, feeling the stopping force of the surrounding electrons of the material. Then, the ion interacts with the atom in a two-body collision, losing energy proportionally to the kinematic factor. Finally, the backscattered ion leaves the sample losing more energy, again, due to the stopping force. Consequently, if the same ion-atom collision is considered but occurring at the surface and in-depth, the backscattered ion will be found at very different energies for each case, because in the first situation it does not lose energy inside the target, whereas in the second case it does. This is the key feature of RBS allowing depth concentration profiling. Assuming the surface energy

approximation (constant stopping force), the quantification of energy loss ΔE at a depth d responds to the equation [25]:

$$\Delta E = Sd\left[\frac{K}{cos\theta_1} + \frac{1}{cos\theta_2}\right],$$

where θ_1 and θ_2 are the incident and exit angles (with respect to the surface normal).

Apart from the stopping force, the statistical behavior of the close encounters also provokes the energy loss. In particular, this fact makes identical energetic particles not to have exactly the same energy after passing through a thickness of a homogeneous medium. Therefore, the energy loss is also subjected to fluctuations, a phenomenon known as energy straggling. As it is clear from Figure 2.4, the principal factor contributing to the straggling is the interaction of the beam with the electrons. As the beam penetrates deeper into the sample, the straggling becomes more important, so it establishes a limit for the depth resolution of RBS.

Figure 2.5 shows the general sketch of an RBS experiment and the interpretation of the spectrum for the simple case of a bilayer (with two elements $M_1 > M_2$), taking into account the kinematic factor, the cross section and the stopping force. Note that heavier atoms (M_1) appear at higher energies and exhibit higher yields. The concentration of the elements is proportional to the yield. Since M_2 belongs to two layers, the spectrum shows two regions. The first one (higher energies) corresponds to the shallower layer with a concentration of 50% and, hence, the signal is approximately the half of the second one (substrate, 100%). The thickness of the layer is measured through the energy loss ΔE.

Due to the large number of parameters that must be considered for a complete analysis of an RBS spectrum, there are many commercial programs to develop the simulation and fitting of the experimental data [29], such as SimNRA [30], NDF [31], RBX [32], etc. In this thesis, the RBX code was used for the analysis of RBS spectra. This software is based on the interactive spectrum synthesis, i.e., the fitting is done by assuming a certain layer structure and comparing the result of the simulation with the experimental data in an iterative process. RBX takes into account the kinematic factor, the scattering cross section, the stopping cross section (from SRIM) and the straggling, but also adds several other theoretical and experimental corrections. In particular, one of the main

advantages of RBX is that it is the only software incorporating analytical simulations of channeling, which is an important phenomenon for structural analysis, discussed later on.

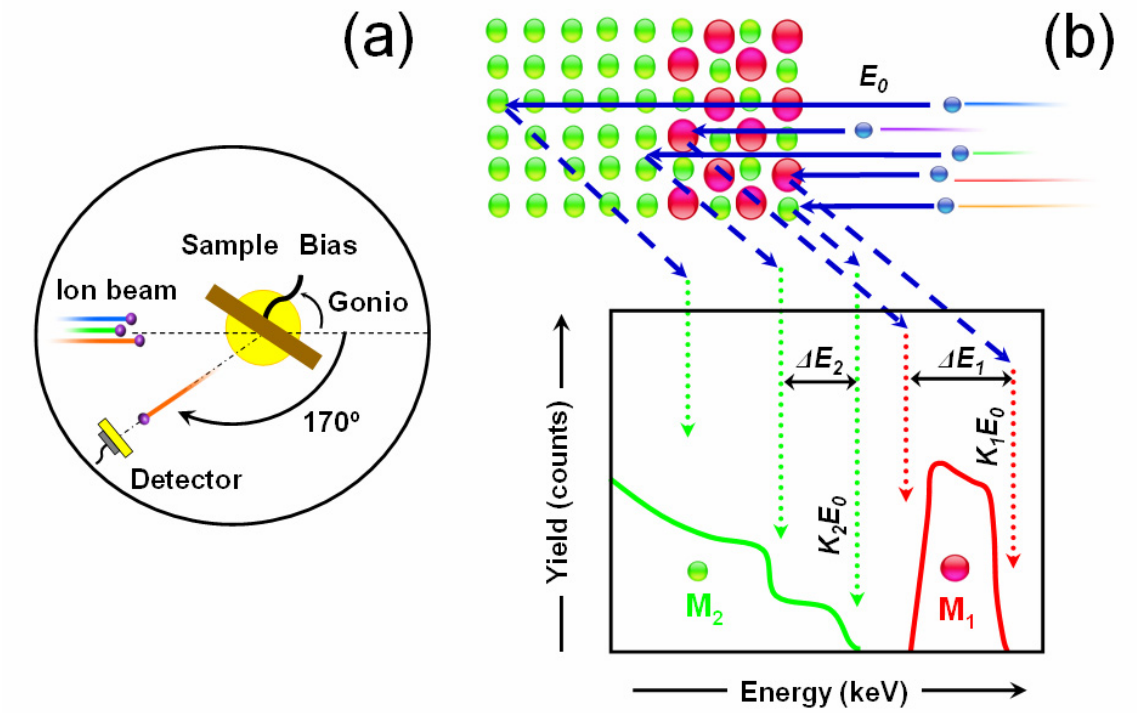

Figure 2.5 (a) Sketch of a RBS experimental system. (b) Representation of an RBS spectrum for the simple case of two layers (M_1>M_2).

Apart from the experimental configuration (energy, geometry, detectors…), the main inputs for RBX simulations are: the thickness of the layers (in at/cm^2), the elements present in the specimen and their composition. The output is the simulated spectrum and the depth profile. RBX incorporates a χ^2 test to check the accuracy of the fitting and, actually, the estimation of the error in the fitting process is an important point to consider when extracting the results. In this thesis, a regular procedure to obtain the uncertainty in the composition and thickness was used, which is discussed next.

The error in the composition is obtained as the addition of the error from the simulation and the statistical error. First, the error in the simulation is calculated as the minimum increment that allows a clear distinction between the fitting and the experimental spectrum. The statistical error is obtained assuming that backscattering events follow a Poisson's distribution [33], i.e., the error for a yield Y is $Y^{1/2}$. It is important to note that the error in the simulation is difficult to estimate if several elements are present in the

same layer. In particular, since the cross section is higher for heavier atoms, the error in these elements is lower than in the lighter ones. However, the composition of the whole layer must be unity, so the error in one atom propagates to the others. For example, it is usually possible to distinguish a difference of 5 % in Ga but not in N, although, when considering the total error for the whole layer, both errors are dependent. For ternary and quaternary layers, the determination of the uncertainty is more difficult. In such circumstances, the additional hypothesis of a stoichiometric nitride (50 % of N) is used to facilitate the analysis.

For the estimation of the error in the thickness, two sources are considered. Firstly, the calculation of the error in the simulation is done. This value is obtained as the minimum increment that allows the discrimination of the simulation from the experimental data. Secondly, it is necessary to transform the units from at/cm^2 to nm, which involves the knowledge of the atomic density of the material. The accuracy in the density is normally difficult to find, so a zero error is assumed for that. However, there is an additional problem when working with compounds: the total density is unknown and it must be estimated by Vegard's law [5], as a linear combination of the binary densities. Therefore, the error in the composition is affecting the error in the density and in the final thickness. Then, the propagation of errors determines the final uncertainty in the thickness.

(b) Experimental system for RBS

Three elements are required for a RBS experiment: beam, sample and detector; but since high energy beams have to be used in order to reach deep regions of the targets, a large facility comprising an accelerator system is needed. Most part of the measurements shown in this thesis were carried out in the Standard (STD) beam line at CMAM (Madrid), but some specific experiments were developed at ITN (Lisbon) during two scientific stays. In the following, the main elements of the experimental set-up at CMAM are described.

The generation of the beam starts with the ignition of a He plasma in a Duoplasmatron ion source (*HVEE*). Then, the ions are driven into the accelerator using electromagnetic lenses and one injector magnet. The accelerator system is a two-step 5 MV Tandetron accelerator (*HVEE*) [34, 35]. This accelerator uses a Crockoft-Walton system to control the terminal voltage, applied through 115 corona rings. A N_2 stripper gas in the middle

of the accelerating tube allows the charge exchange of the ions and, consequently, the achievement of high energies. The beam at the exit of the accelerator is focused and carried into the line by means of a set of three quadrupoles and a bending magnet. Figure 2.6 shows a panoramic view of the accelerator and beam lines at CMAM. Additional details of the whole system can be found in reference [36].

Figure 2.6 Panoramic view of the accelerator and beam lines at CMAM.

In the STD beam line, two sets of slits are used for the collimation of the beam after its exit of the bending magnet. The combination of the slits allows a collimated beam spot of 1 mm^2 on the surface of the sample, with a divergence of ~0.1º. The beam line and the experimental chamber are under high-vacuum conditions (~10^{-6} mbar) to avoid the beam losses and the contamination of the samples with the residual gas. Figure 2.7 shows a picture of the STD chamber, with several elements to control the experimental conditions. Three detectors are installed in the chamber: two Si barrier particle detectors (*Ortec* BU-012-050-500) for RBS and one reverse-electrode Ge detector (*Canberra* GR3520) for gamma-ray detection. One of the Si detectors is fixed at 170º (Ω=4.75 msr) and the other is movable (Ω=7.09 msr) and has a carrousel of foils for making additional measurements. Both detectors have a nominal resolution of 12 keV. In order to control the total dose, the sample is positively biased to suppress the effect of secondary electrons. The STD chamber incorporates a cable to apply +180 V bias for this purpose.

The center of the STD chamber at CMAM is occupied by a 3-axes goniometer (*Panmure Instruments*), where the sample holder is mounted. The accuracy of the movement in the 3 axes is ±0.01º, although the range is different for each degree of freedom. For phi (φ) and theta (θ), the range is 360º, while for the tilt (χ) it is only ±30º. The whole goniometer is mounted on a translation table which allows the change in the vertical direction and then, the possibility of measuring in different points. All the

movements are driven by stepping motors, being the intersection of all three axes within a 0.05 mm diameter sphere. The sample holder is placed in the center of the goniometer, so the zero position of both elements (holder and goniometer) is shared.

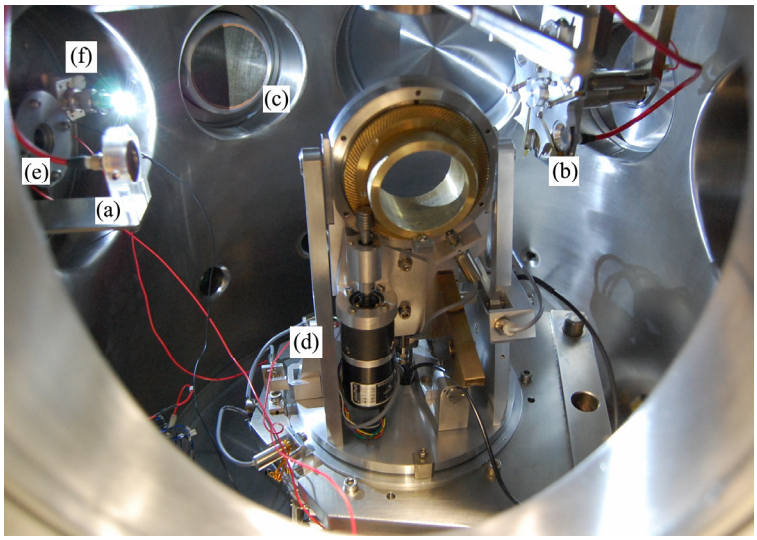

Figure 2.7 Picture of the experimental chamber in the STD beam line (CMAM). Several elements are visible: (a) RBS fixed detector, (b) RBS movable detector with the foils carousel, (c) gamma detector (d) 3-axes goniometer, (e) beam entrance and (f) light.

One frequent problem in RBS analysis is the acquisition of an accurate random spectrum, i.e., a spectrum which does not privilege any certain direction of the specimen (equivalent to an amorphous layer). In samples with good crystal quality, the deviation of the measured yield from the one given by the simulation can be high. This difference arises from the fortuity alignment of the beam with a crystallographic direction, which produces the channeling of the ions thought the lattice (RBS/C, see section 2.4.1) and reduces the backscattering events. Therefore, an accurate random spectrum without directional effects is needed to avoid misleading estimations of the composition. Since most semiconductor HSs are, in fact, single crystalline, this point has to be taken into account when performing the experiments.

One conventional way of acquiring a random spectrum is evading the crystallographic position moving the sample some degrees (~7º) in θ and χ. However, depending on the sample structure, some channeling may be still present. Another approach is the rotation of the sample during the measurements to average all directions. This is a better solution but the rotation of φ can only be performed for one single specimen (in the center of the sample holder).

In order to take advantage of the other two axes of the goniometer, a faster method to acquire the random spectrum was used in this work. This procedure is based on a batch of ~200 spectra of low dose (~25 nC) recorded during the combined movement of θ and χ angles (within a short range of ~2º). Both θ and χ are moved describing a circumference (or ellipse) around the center of the axis. This movement can be easily parameterized with only one variable (the angular step t, related with the number of acquisition points), following the equation: $(\theta,\chi)=(\theta_0 cost, \chi_0 sint)$.

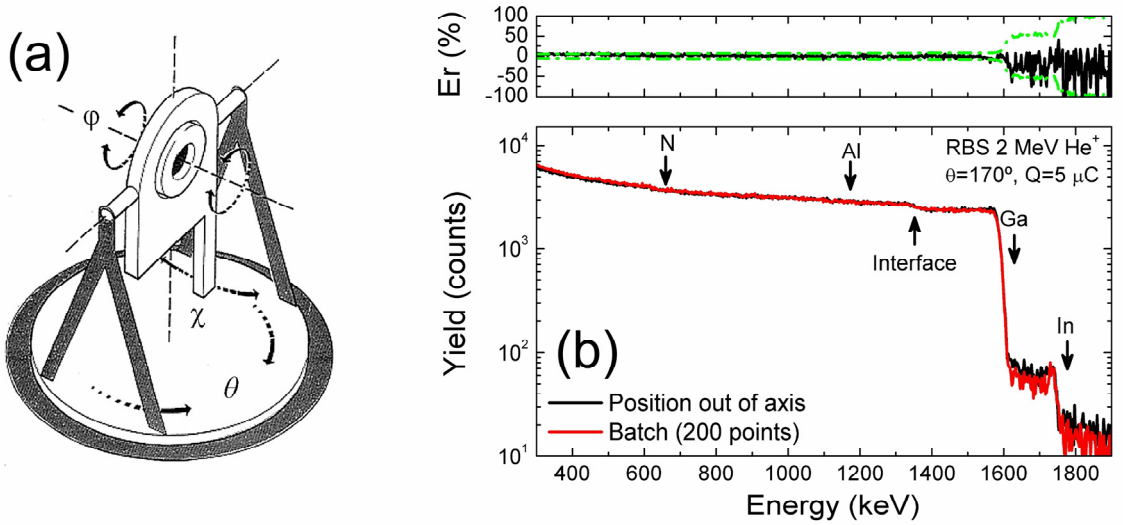

Figure 2.8 (a) Goniometer movements for angular scans. (b) Comparison of random spectra obtained by two methods in an AlGaInN/GaN HS: finding a position out of the axis (black line) and with the addition of 200 spectra acquired in a batch (red line). Relative error is also shown on top and compared with the statistical one (green).

Consequently, using the batch, a random spectrum of the sample can be generated by the sum of all the individual spectra. As it will be shown in section 2.4.1, this kind of scan has a very important additional advantage when used to perform channeling experiments.

To make possible the circular scan in θ-χ, a Visual Basic program called *AngScan* was developed. This program was inspired in previous versions of Dr. Ángel Muñoz-Martín and the source code is shown in the Appendix II. The program creates automatically the θ-χ batch, but it also allows single angular scans in φ, θ and χ with a selected step and dose for each point (see Figure 2.8a). Figure 2.8b shows the comparison of two random spectra of an AlGaInN/GaN heterostructure. The first one was obtained finding a position out of the axis and the second one by the batch method. The relative error

between them is inside the statistical uncertainty, showing that both measurements cannot be distinguished.

2.3.2. Elastic recoil detection (ERD)

RBS has significant limitations when measuring trace elements in a heavy matrix, because the overlapping signals and the lower cross section for the light elements make their detection difficult. However, such light elements can play an important role as impurities, so its eventual presence in the semiconductor HSs is crucial. The elastic recoil detection (ERD) was developed to solve these problems, as a complement to RBS analysis. Actually, in RBS the impinging ion is lighter than the detected elements, but it is also possible to use ions heavier than the elements in the target. In this latter situation, the atoms inside the sample can be recoiled and detected, which is the essence of ERD technique.

Conventional ERD measurements use a symmetric geometry with a grazing incident and exit angle, detecting the recoils in a Si barrier detector. However, in this configuration there is a big amount of forward scattered projectiles that hit the detector. The filtering of this large signal is needed to obtain the desirable yield from the recoils, and to avoid the saturation and damage of the detector. Consequently, a foil is placed in front of the detector, being the material and thickness dependent on the particular experimental conditions. The inclusion of the foil increases the energy straggling and reduces the depth resolution of ERD significantly. For this reason several alternative methods have been developed, as the time-of-flight or the energy loss/energy ($\Delta E/E$) systems [7].

Apart from conventional ERD measurements in the STD beam line at CMAM, more accurate experiments were carried out using ERD with a Bragg ionization chamber (BIC) at FZD, which is shown in Figure 2.9. The geometry is fixed by a grazing incidence angle of 10º and a scattering angle for BIC of 30º. A Si detector (covered with an Al-range foil) is placed at a scattering angle of 38º for H detection. The BIC is filled with pure isobutane at a pressure of 100 mbar, with all particles entering through the 670 nm thick polypropylene window. The particles are stopped progressively by the gas and the emitted electrons from the ionization drift along the parallel electric field created by a Frisch-grid inside the BIC. Thus, electrons produce pulses in the anode with a typical time structure.

The maximum of the electron pulses (Bragg peak height) is obtained before the stopping of the particle, being the length of the path proportional to the atomic number of the detected particle and the integral to its energy. Thus, the typical ERD-BIC spectrum splits the yield as a function of these two parameters: the energy channel (integral) and the mass channel (Bragg peak). Therefore, the scattered ions and recoils can be separated according to their atomic number without any overlap. This is the main advantage of the ERD-BIC configuration. The beam in the ERD-BIC experiments was 40 MeV Cl^{8+}, being the total number of incident ions determined by a beam chopper placed in front of the target. More details of this system can be found in reference [37].

2.3.3. Nuclear reaction analysis (NRA)

The sensitivity and resolution of RBS and ERD to specific light elements can be greatly enhanced by nuclear reaction analysis (NRA). These methods take advantage of the ion-ion, ion-gamma, and ion-neutron reactions during the beam-target interaction. Due to the large variety of isotopes, excited energies and angular distributions, NRA involves complex treatments and measurements [8]. The most usual case of the nuclear reaction is the resonant scattering mentioned before, where the detected particle after the reaction is the primary projectile. However, ion-gamma reactions are also frequent in IBA.

During this thesis, several NRA were used, such as the $^{27}Al(p,p'\gamma)^{27}Al$ or the $^{24}Mg(p,p'\gamma)^{24}Mg$, but here only the $^{1}H(^{15}N,\alpha\gamma)^{12}C$ reaction will be discussed, which was applied for analyzing the H content with high depth-resolution [38, 39]. In this NRA, 4.43 MeV γ-rays are produced resonantly for a projectile energy of 6.385 MeV. This is one of the most sensitive techniques for the quantification of the H content, having a detection limit of 0.02 at. %. The H content is determined by the total number of characteristic γ-rays [40], after the subtraction of the normalized natural background. The determination of the exact zero-depth is made using the H signal from the surface of a reference Si single crystal. Then, depth profiling can be developed by sweeping the energy of the impinging ^{15}N ions around the resonance value. Since the energy width of the resonance is ~8 keV, the depth resolution of this method can be as low as few nanometers for regions close to the surface.

The ^{15}N NRA experiments were carried out at FZD, and the experimental set-up is described in detail in reference [40]. Figure 2.9 shows the experimental chamber from

its back side. The beam enters in the chamber passing through a set of collimator slits and then collides with the sample. To enhance the depth resolution, a tilted geometry can be used (30º in the set-up used in this thesis). The emitted radiation is detected with a 100 mm diameter bismuth germinate (BGO) detector, placed about 20 mm behind the sample (see Figure 2.9).

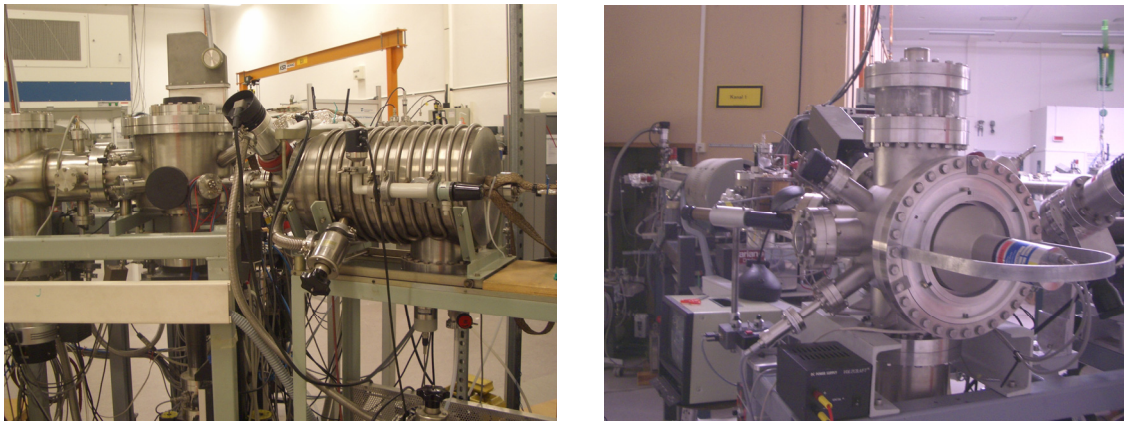

Figure 2.9 Experimental chambers for ERD-BIC (left) and NRA (right) measurements at FZD.

2.4. Structural characterization techniques

Compositional changes in WBS are frequently associated to structural variations, so a complete understanding of the phenomena affecting the growth of HSs requires the determination and quantification of the crystalline modifications in the material. The crystal quality, the strain state, or the phase separation are some of the points of interest which deserve a special attention when treating with WBS. Now, the two principal techniques of this thesis concerning the structural characterization are explained.

2.4.1. Ion channeling (RBS/C)

When measuring crystalline materials, RBS can be carried out with the beam aligned along a major crystallographic direction (RBS/C). This particular geometry allows the appearance of a physical phenomenon called channeling [41], i.e., ions entering inside the crystal are steered by the atomic rows (Figure 2.10) and, consequently, there is a reduction of the measured backscattering events. This is the main feature of channeling, characterized by a pronounced dip of the RBS yield when making an angular scan. Taking advantage of this effect, a depth-resolved structural analysis can be carried out [9]. Here, only the experimental methods used for the development of channeling measurements in wurtzite crystals are described. The theoretical modeling of ion

channeling phenomena is complex and often requires Monte Carlo simulations, so it will be explained in more detail in the next chapter due to its relevance for this thesis.

(a) Set-up and special considerations for RBS/C

There are several special considerations that have to be taken into account when performing RBS/C experiments [7]. Firstly, due to the directional principle of channeling, a good collimated beam is required. Secondly, an accurate measurement of the dose is needed since the comparison between aligned and random spectra depends on it. The slits and the bias in the STD beam line allow a good control of both parameters, as it was already discussed.

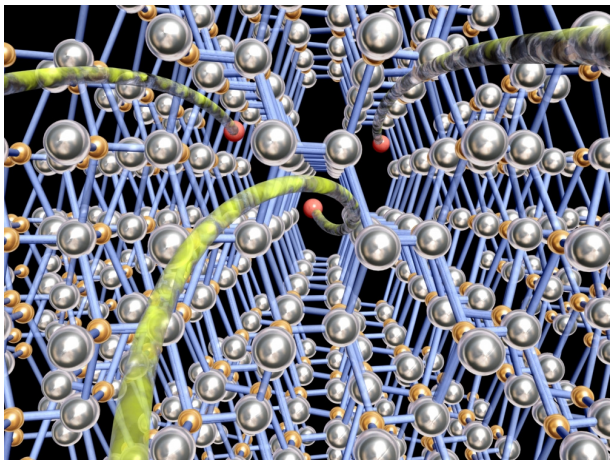

Figure 2.10 Illustration of the channeling phenomenon in a wurtzite lattice.

In addition, to avoid double-alignment geometries (both incident and exit beams aligned with crystallographic directions) in RBS/C, a large generous solid angle is needed. Moreover, the blocking of the exit beam when aligned with an axis is very intense at 180º, so the geometry should be far from this scattering angle to neglect this effect. Since the fixed detector of the system at CMAM is placed at 170º with a solid angle of 4.75 msr, it fulfills the required conditions. Nevertheless, the use of the movable detector placed at a different scattering angle is also very practical to detect blocking situations, so it was always employed in the channeling experiments shown in this work.

However, the most crucial part of the system for RBS/C is the goniometer, since it is the tool for the alignment of the crystals, and the accuracy of the angular scans is limited by the good control of the position provided by the stepping motors. The center or the goniometer coincides with the center of the sample holder so, when a complete

alignment of the crystal is required, the target must be set also in the center of the sample holder. Otherwise, the translation movement makes impossible the alignment of φ, which is very useful for the localization of the crystallographic planes.

Table 2.1 Main crystallographic axes of the wurtzite crystals.

Plane $\{0\,\bar{1}\,10\}$		Plane $\{2\,\bar{1}\,\bar{1}\,0\}$	
Axis	θ (º)	Axis	θ (º)
$<0001>$	0.00	$<0001>$	0.00
$<\bar{2}119>$	11.60	$<\bar{1}014>$	14.92
$<\bar{2}116>$	17.11	$<\bar{1}013>$	19.56
$<\bar{4}229>$	22.31	$<\bar{1}012>$	28.06
$<\bar{2}113>$	31.61	$<\bar{3}035>$	32.61
$<-10\,5\,5\,12>$	37.58	$<\bar{2}023>$	35.40
$<\bar{2}112>$	42.72	$<\bar{3}034>$	38.65
$<-10\,5\,5\,9>$	45.73	$<\bar{1}011>$	46.83
$<\bar{4}223>$	50.91	$<\bar{4}043>$	54.88
$<-10\,5\,5\,6>$	56.98	$<\bar{3}032>$	57.98
$<\bar{2}111>$	61.56	$<\bar{2}021>$	64.87
$<\bar{8}443>$	67.90	$<\bar{5}052>$	69.43

As mentioned before, the acquisition of a precise random spectrum is as important as the acquisition of the aligned one. Actually, it can be understood that finding a good random spectrum is more difficult than finding a good aligned one: there is only one way of getting the aligned spectrum but there are infinite ways to collect a random spectrum. Therefore, for channeling experiments the θ-χ batch described in section 2.3.1 was used to find a reliable random spectrum. Simultaneously to the acquisition of the spectra in the θ-χ mixed scan, the different crystallographic planes of the crystal are crossed, so the position of the axis can be also determined by the intersection of all of these planes. Therefore, the program *AngScan* can be used to find the aligned position searched for channeling. Since the program allows single scans in the three axes, the obtained position can be corrected to enhance the accuracy.

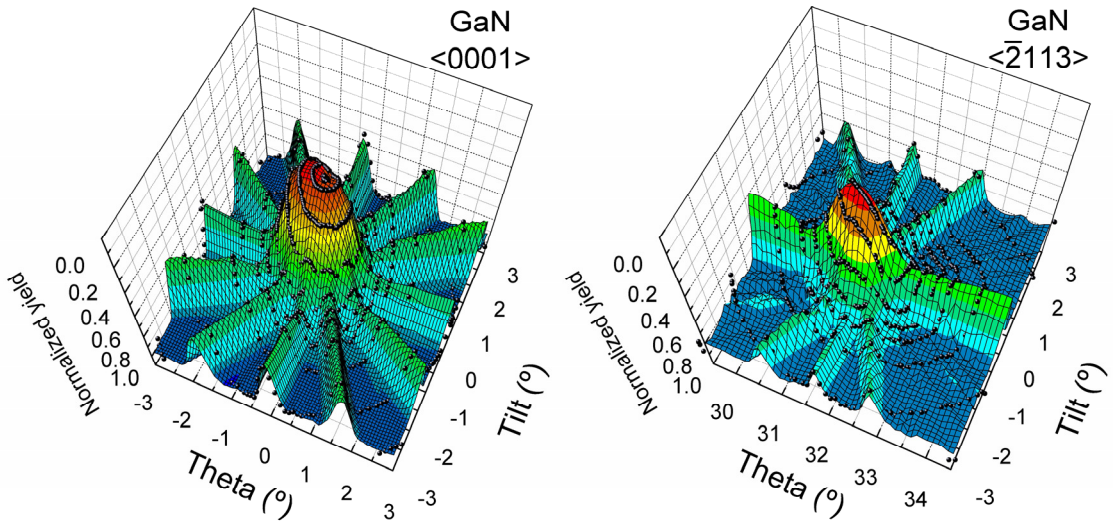

Figure 2.11 Angular scans around <0001> and $<\bar{2}113>$ axes in a GaN crystal. The central dip corresponds to the axis. Six crossing planes are visible in the first case and four in the second one. The scale is inverted for a better view. Spheres are the experimental data.

The calculation of the dips requires the integration of the yield in some energy windows of the spectra. To make this, a new program called *Dipito* was developed (see Appendix III). It allows the definition of three energy windows for both detectors (fixed and movable). The program reads the spectra and integrates them in the selected windows. The subsequent Gaussian fitting of the dips determines the (θ,χ) pairs in the circumference, and the intersection of such pairs gives the center of the axis. Of course, *Dipito* can also be used for the calculation of single scans in φ, θ and χ.

As a demonstration of the application of the batch scan, Figure 2.11 shows the result of the integration with *Dipito* program in two different axes of a wurtzite crystal [42]. The solid spheres are the experimental points acquired with *AngScan*. A total of 200 points was used in every θ-χ batch. For the <0001> axis, twelve dips are recognized (6 crossing planes), while the $<\bar{2}113>$ axis shows eight dips (4 crossing planes). The intersection of all the dips coincides with the position of the axis, where the most pronounced dip is found.

(b) Alignment of wurtzite crystals by RBS/C

The essential tool for the alignment of a crystal is the stereographic projection [7], because it provides a complete representation of the crystal planes and axes [43-46]. The stereographic projection of a wurtzite crystal was introduced in chapter 1, but its crystallographic axes are summarized here (Table 2.1). These data were obtained from

Carine software [47], which allows the identification of all the crystal directions. As commented in chapter 1, the hexagonal symmetry is revealed by the twelve principal planes that cross the <0001> axis each φ=30º.

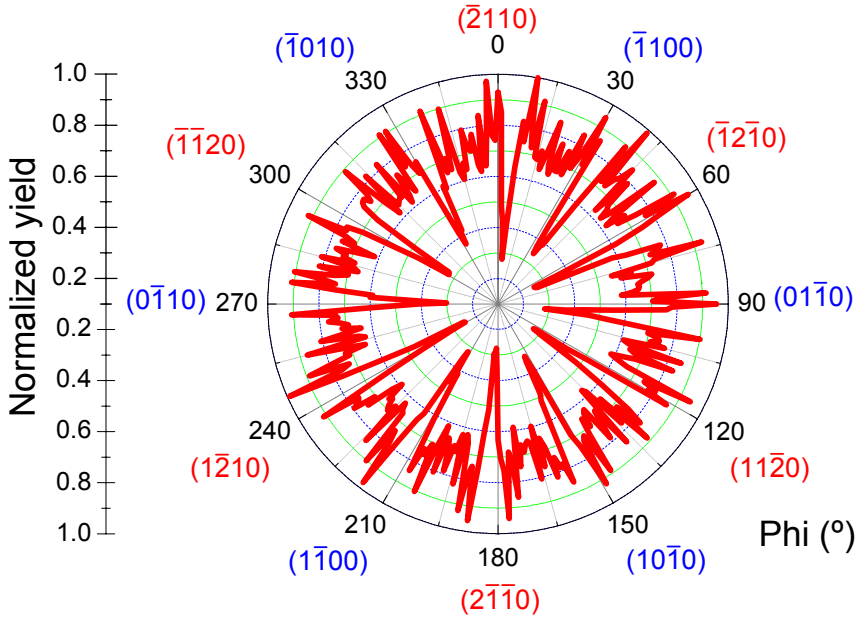

Figure 2.12 Experimental φ-scan in a wurtzite crystal showing the different intensity of the planes.

One of the important features of the wurtzite structure is that $\{0\bar{1}10\}$ and $\{2\bar{1}\bar{1}0\}$ planes are not equivalent. In ion channeling experiments this fact is characterized by a different minimum yield in the φ-scans of both planes [48]. The dips along the $\{0\bar{1}10\}$ plane are less intense than in the $\{2\bar{1}\bar{1}0\}$. This feature is the key for a fast alignment in wurtzite crystals when measuring along oblique axes. Figure 2.12 shows a φ-scan for a wurtzite GaN crystal. The minimum of the dips oscillates each 30º, demonstrating the different behavior of the $\{0\bar{1}10\}$ and $\{2\bar{1}\bar{1}0\}$ families. The principal planes were identified using this relative intensity, and verifying the position of specific axes inside them by means of θ-scans.

As a guide for the selection of the axes in RBS/C of wurtzite crystals, the experimental θ-scans inside both $\{0\bar{1}10\}$ and $\{2\bar{1}\bar{1}0\}$ planes are shown in Figure 2.13 (compare these results with Table 2.1). The accurate location of the oblique axis is essential for the determination of the strain state of the films, as it will be explained in the next section.

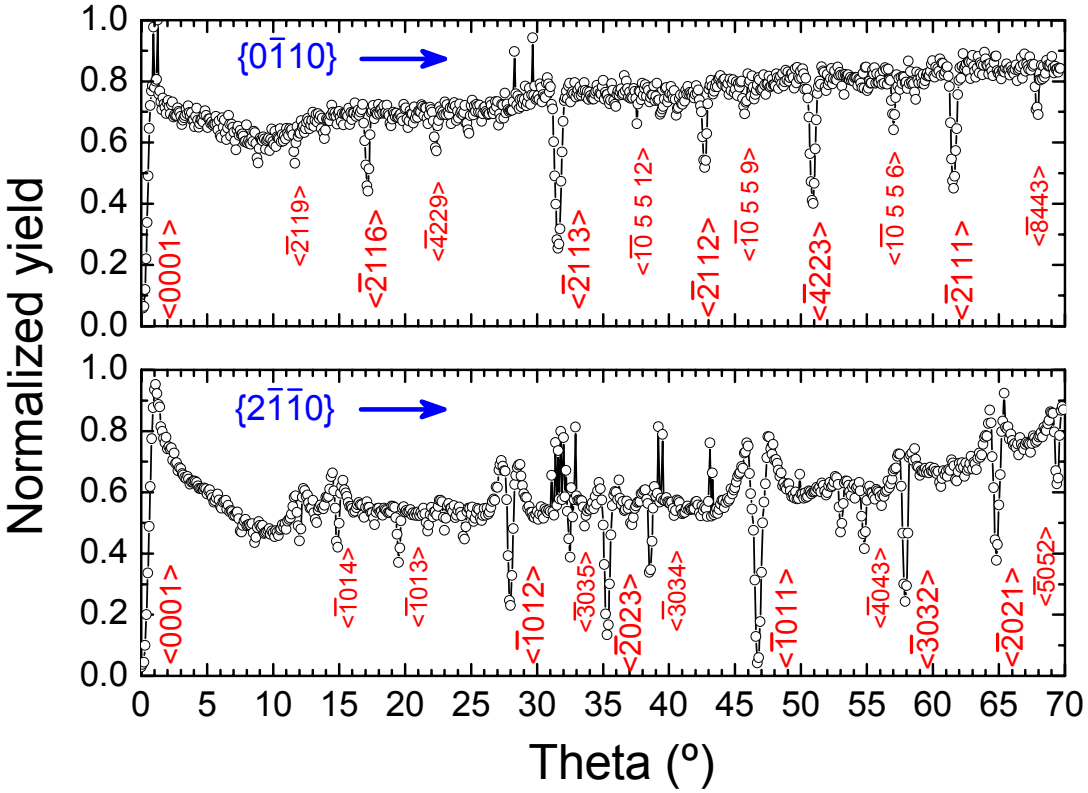

Figure 2.13 Angular scans following the two principal planes of the wurtzite crystal. The measurements were done with 2 MeV He^+ beam (170º scattering angle) and the data are normalized to the maximum.

(c) Determination of crystal quality and strain by RBS/C

From the experimental point of view, the crystal quality of a material can be measured by RBS/C using the ratio between the aligned and the random yields, called minimum yield (χ_{min}, see chapter 3 for a more exact description of its meaning). The determination of χ_{min} requires only two spectra, one in a random configuration and one aligned. In wurtzite crystals the normal growth direction is the <0001> so crystal quality is checked for that axis. However, the calculation of χ_{min} can be carried out in any axis, since it is a relative measurement.

Previously, the acquisition of a random spectrum was demonstrated by combining both θ-χ axes of the goniometer. After this procedure, the (θ,χ) coordinates for the aligned spectrum are obtained from the initial circular scan. This coordinates can be corrected to increase the accuracy by additional single scans in θ, χ and φ, but once centered in the channel, the variations in the aligned spectrum are normally minor. The χ_{min} is finally determined by the integration of the aligned and random yields for a concrete energy window. The selection of this window depends on the signals present in the spectra and

the statistics required. If possible, a region related to the near surface (but after the surface peak) should be selected, since this warrants a low influence of the dechanneling (see section 3.2.4). For the integration, ~20 channels are enough if the element has a high cross-section.

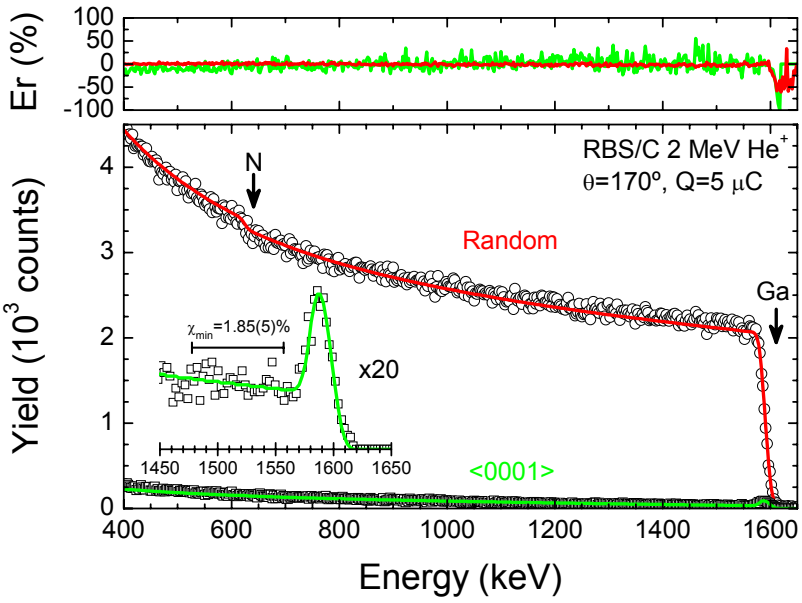

Figure 2.14 Experimental calculation of the minimum yield in a GaN template and relative error between the fitting and the data (top).

Figure 2.14 shows the experimental random and <0001> aligned spectra of a GaN template. The energy window selected for the calculation is also shown, giving a χ_{min}=1.85(5) % for Ga. The error in the χ_{min} is only dependent on the statistics of the window and the error in the charge. Since backscattering events follow a Poisson distribution, the error is proportional to the square root of the yield. Thus, the final error for χ_{min} can be deduced from the propagation of the uncertainties.

The fitting of the spectra was made using RBX [32]. This software allows the analytical fitting of the aligned spectra, including the surface peak intensity, the minimum yield and the dechanneled fraction (section 3.2.4). For the GaN template, a constant dechanneled fraction of 0.32 % was obtained, which can be used as a reference for other GaN-based layers. As it is shown in Figure 2.14 (top), the relative error between the experimental and the simulated spectra is very low.

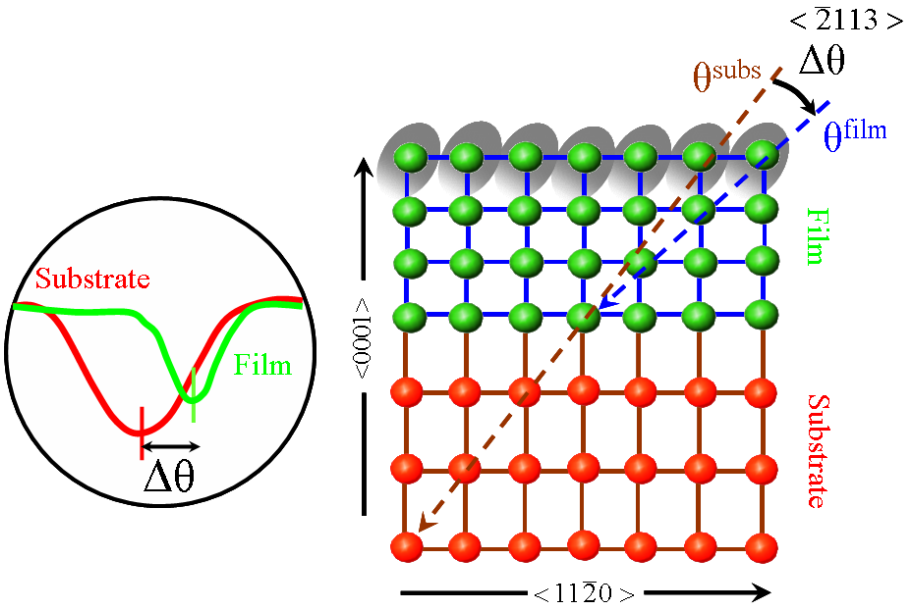

Figure 2.15 Determination of the strain state in a wurtzite HS through the measurement of the kink angle.

The determination of the strain state by RBS/C requires a more complex method than for χ_{min}. The basic idea for the measurement of the strain state is that any average distortion of the lattice parameters is reflected in a change of the incidence angle for channeling. For example, in a wurtzite crystal, the angle between the <0001> and the $<\bar{2}113>$ axis along the $\{0\bar{1}10\}$ plane verifies $\tan\theta = a/c$. Thus, if the position θ is known for an oblique axis (such as $<\bar{2}113>$), this value can be compared with the nominal one for a completely relaxed layer, finding the tetragonal strain (see chapter 1). However, the absolute position of an oblique axis requires a high-accuracy in the goniometer, which has to be moved several times for the alignment of the crystal. Therefore, this kind of approach can introduce additional errors, especially for samples with low strain states.

To overcome the limitations of the goniometer, an alternative method based on a relative angular measurement can be used [6, 7, 49]. Figure 2.15 describes the procedure in the particular case of a wurtzite-type HS, where such strain determination is of interest. The essence of the technique is the comparison of the positions of the incident angles for the film and the substrate (or what can be considered as substrate). Now, the magnitude measured in the experiment is the shift between the channeling dips from both layers and, consequently, the substrate provides an additional reference which avoids the need of absolute measurements. This angular shift is known as kink angle, and it is defined as:

$$\Delta\theta = \theta^{film} - \theta^{subs}. \tag{2.3}$$

To find the kink angle, just a θ-scan along an oblique axis of the crystal is needed, which has to be recorded within the plane. Then, using two energy windows (one for the layer and one for the substrate), $\Delta\theta$ can be calculated. As shown in Figure 2.13, there are several oblique axes for the strain analysis, but not all of them are suitable. On the one hand, the sensitivity is enhanced when the χ_{min} is low. On the other hand, the better depth-resolution is obtained at large θ values. A compromise between both parameters for wurtzite crystals is found in the $<\bar{2}113>$ axis at θ=31.6º along the $\{0\bar{1}10\}$ plane and in the $<\bar{1}011>$ axis at θ=46.8º along the $\{2\bar{1}\bar{1}0\}$ plane. In this thesis, the $<\bar{2}113>$ axis was selected as a standard procedure for strain measurements. The relation between the incident angle and the lattice parameter for the $<\bar{2}113>$ axis is:

$$\tan\theta^{<\bar{2}113>} = a/c. \tag{2.4}$$

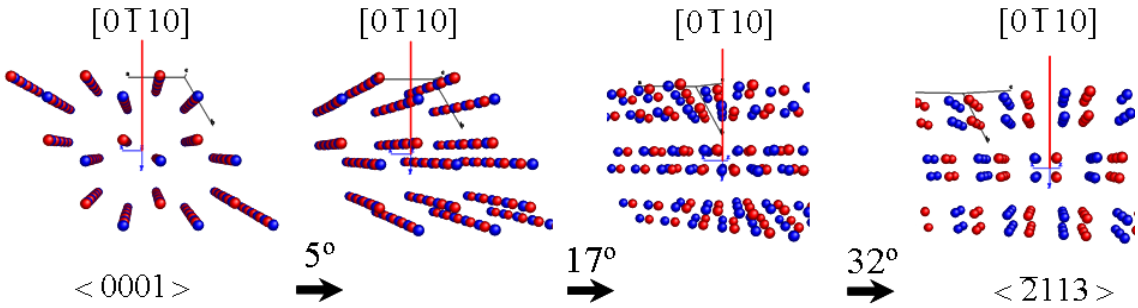

Figure 2.16 Angular θ-scan inside the $\{0\bar{1}10\}$ plane connecting the <0001> and the $<\bar{2}113>$ axes.

The alignment for the determination of the kink angle in the $<\bar{2}113>$ axis is carried out in the following way. Firstly, the (θ,χ) positions of the <0001> axis are found. After this step, the tilt coordinate remains fixed. Now, the $\{0\bar{1}10\}$ plane should be found to travel inside it towards the $<\bar{2}113>$ axis (see Figure 2.16). Then, a φ-scan out of the <0001> axis (θ~5º) is acquired to detect the planes of the crystal. Using its different minimum yield, the $\{0\bar{1}10\}$ plane is selected. A little error in the alignment of the <0001> axis can induce a shift in the φ value obtained at 5º when moving to larger θ. Therefore, sometimes a new φ-scan at θ~30º is advisable. When the φ coordinate of the plane is fixed, the last θ-scan across the $<\bar{2}113>$ axis is acquired. Normally, a step of not less than 0.1º is used, covering a total range of 4º. The statistics required depend on

the element with the lower signal in the spectrum. A reasonable value for the dose is the one that warrants a minimum integrated yield of 1000 counts (3.2 % error).

It is important to notice that $\Delta\theta$ is *not* a direct measurement of the strain since it compares relative changes between two different layers. The strain state, however, is the distortion of the actual layer related to the theoretical relaxed value of the *same* layer. Therefore, it is necessary to compare $\Delta\theta$ with the theoretical shift of a relaxed film on the same substrate ($\Delta\theta_0$). This is shown in Figure 2.17. Usually, the assumption of a relaxed substrate is valid within the limits of RBS/C, and the nominal values from the literature can be accepted. If this is not applicable, the lattice parameters of the substrate must be obtained from another technique such as XRD to eliminate the contribution of the substrate in the comparison. Then, the value of $\Delta\theta_0$ is found using (2.3), (2.4) and Vegard's law [5]. After these intermediate calculations, the angular shift of the film can be expressed as:

$$\Delta\theta - \Delta\theta_0 = (\theta - \theta_0)_{film} - (\theta - \theta_0)_{subs} = \Delta\theta_{film}. \tag{2.5}$$

Once $\Delta\theta_{film}$ is known, the tetragonal strain can be determined by the derivation of (2.4):

$$sec^2\theta \cdot \Delta\theta_{film} = \frac{a}{c}\left(\frac{\Delta a}{a} - \frac{\Delta c}{c}\right) = tan\theta \cdot \varepsilon_T. \tag{2.6}$$

The substitution of (2.5) in (2.6) gives the equation:

$$\varepsilon_T = \frac{\Delta\theta_{film}}{\sin\theta^{<\bar{2}113>}\cos\theta^{<\bar{2}113>}}. \tag{2.7}$$

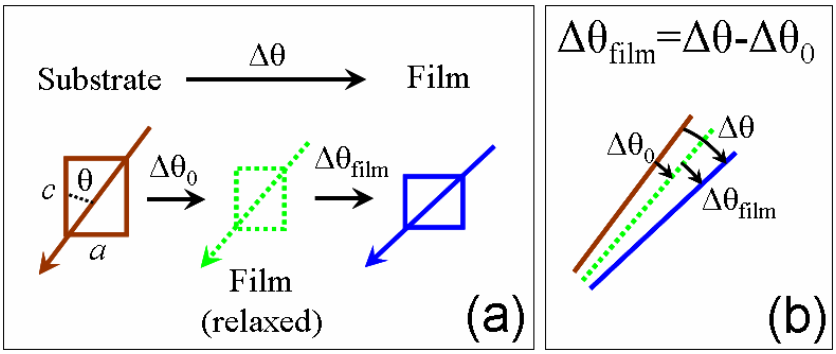

Figure 2.17 (a) Angular shifts to consider for strain determination. (b) Relation between experimental kink angle and calculated angular shift for the film.

The application of (2.7) for the determination of the strain provides an accurate method to analyze wurtzite HSs, and it will be profusely used in the following chapters for the calculation of the strain state of different HSs. An example of the use of RBS/C for the calculation of ε_T is shown in Figure 2.18 for an AlInN/GaN HS. Firstly, random and aligned spectra (Figure 2.18a) are acquired to fix the energy windows and the dose required for additional angular scans (note that these windows may be slightly different for different axes). In this case, one window (w_2) for the film and one for the substrate (w_3) were used. Note that w_1 was not selected because of the channeling effect is not present there (polycrystalline or amorphous layer). Thanks to the depth resolution of RBS/C this kind of phase separation can be detected and analyzed independently [6].

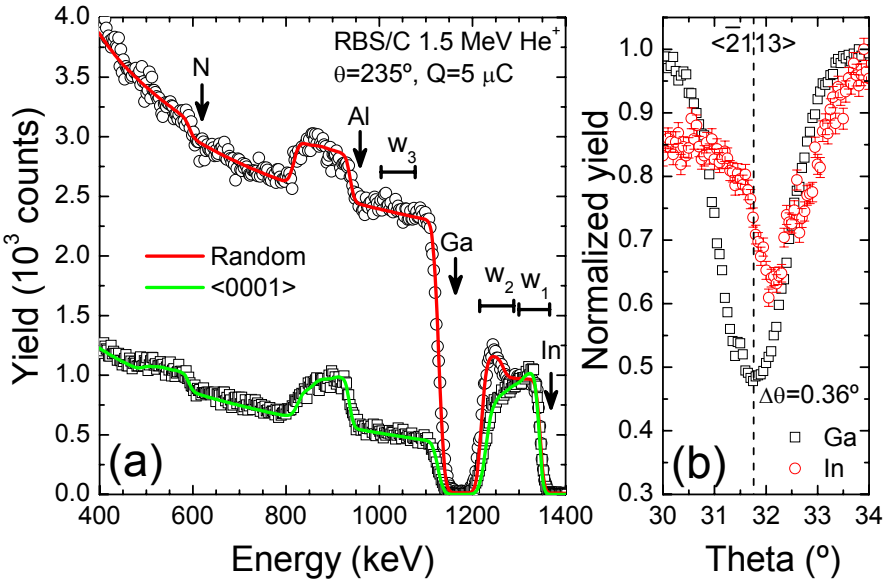

Figure 2.18 (a) Random and <0001> aligned spectra of an AlInN/GaN HS. (b) Angular scan along the $<\bar{2}113>$ axis for In (w_2) and Ga (w_3) showing a kink angle of 0.36º.

After the alignment of the <0001> axis, the angular scan in the $<\bar{2}113>$ axis is recorded (Figure 2.18b), measuring a $\Delta\theta$=0.36(2)º. By means of Vegard's law, the lattice parameters of the relaxed $Al_{1-x}In_xN$ layer were calculated, assuming the RBS composition (x=18%) and the references from Table 1.1. Therefore, using (2.6), a $\Delta\theta_0$=0.366º was found. Following (2.5) and (2.7), the final value of the tetragonal distortion is ε_T=0.7%, which can be considered as an almost relaxed film. Very often, an accurate analysis of the strain requires MC simulations to take into account all the physical parameters affecting the steering of the ions inside the channel. The modeling

of such phenomena involves several considerations that will be further considered in the next chapter.

2.4.2. X-ray diffraction (XRD)

The discovery of XRD took place few years after the Geiger-Marsden experiment [50], but it was faster developed than RBS and ion channeling. As a result XRD is nowadays, without any doubt, the most extended technique for structural characterization of semiconductors [4, 51]. Its power, versatility and accuracy find hardly any competitor for the analysis of crystalline samples, and WBS are not an exception [52]. Therefore, the information given by XRD is a perfect complement to RBS/C analysis. In particular, the higher accuracy and the direct determination of the lattice parameters in XRD measurements is a very useful characteristic that enhance and complete the strain analysis by RBS/C.

The basic idea behind XRD is the probing of a crystal with radiation having a wavelength close to the lattice spacing. The electron cloud of the atoms interacts with the X-rays producing a scattering phenomenon. Figure 2.19 shows a sketch of the X-ray diffraction process for two incident beams with the same wavevector. When the path difference AB between the X-rays is a multiple of the wavelength, the interaction of the diffracted X-rays gives a constructive interference which can be detected as a peak. The geometric relation for such interference is known as Bragg's law [50] and can be expressed by:

$$n\lambda = 2d_{hkl}\sin\theta, \tag{2.8}$$

where d_{hkl} is the distance between planes (*hkl*), λ is the wavelength of the X-rays and θ is the angle between the beam and the plane. Very frequently, Bragg's law is also derived in terms of the reciprocal lattice of the crystal, which is a useful representation of the crystal [43].

In such case, the diffraction can be understood by means of the momentum transfer between the incident ($\vec{k}_0$) and diffracted ($\vec{k}$) wavevectors, both having a magnitude $1/\lambda$. Thus, if the scattering vector is defined as $\vec{Q} = \vec{k} - \vec{k}_0$, Bragg's law appears as a natural consequence of the equation:

$$\left|\vec{Q}\right| = \left|\vec{d}^{*}\right| \quad \Rightarrow \quad 2ksin\theta = 1/d_{nkl},$$

where $\vec{d}^{*}$ is the reciprocal lattice vector of the plane (*hkl*). For hexagonal systems the distance between planes (i.e., the length of the reciprocal lattice vector) is a function of both *a* and *c* lattice parameters, following the relation:

$$\frac{1}{d_{hkl}^2} = \frac{4}{3}\frac{h^2 + k^2 + hk}{a^2} + \frac{l^2}{c^2}. \tag{2.9}$$

Since the studied planes are not necessarily parallel to the surface of the sample, the measured angle is 2θ, which is independent on the orientation of the sample. The tilt angle of the sample is called ω, which coincides with θ only for planes parallel to the surface. Therefore, to distinguish these cases, two main geometries are defined in XRD: symmetric ($2\omega=2\theta$) and asymmetric ($2\omega\neq2\theta$).

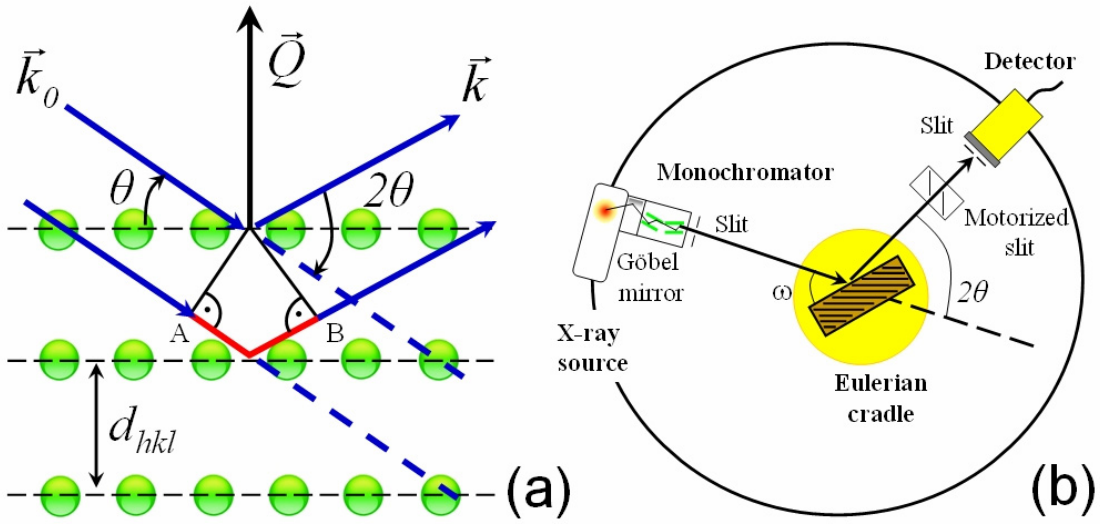

Figure 2.19 (a) Geometric interpretation of Bragg's law (b) HR-XRD system.

(a) Set-up and special considerations for XRD

The resolution of the XRD method in the determination of d_{hkl} depends on the monochromaticity of the beam ($\Delta\lambda$) and the angular divergence (δ) [52]. Then, for high resolution (HR-XRD) measurements, these parameters must be controlled with additional optical elements such as mirrors, monochromators, and slits. Figure 2.19b shows the experimental set-up for HR-XRD measurements.

For the characterization of the samples in this thesis, a D8 Discover (*Bruker-AXS*) diffractometer was used during the stays at ITN. The generation of the X-rays is done inside a ceramic tube where an accelerated focused electron beam bombards a Cu target. The ionization and relaxation processes of the electrons in the target produce a characteristic radiation at a wavelength λ of 0.15405974(15) nm ($K_{\alpha 1}$) [52]. After the generation of the X-rays, a Göebel mirror is placed to collect the photons emerging from the line focus of the tube within an acceptance angle, forming an intense parallel beam with very low divergence [3]. Then, an asymmetric 2-bounce Ge (220) monochromator is used to reduce the uncertainty in the wavelength. The beam is finally collimated with a slit (0.2 mm) before traveling toward the sample.

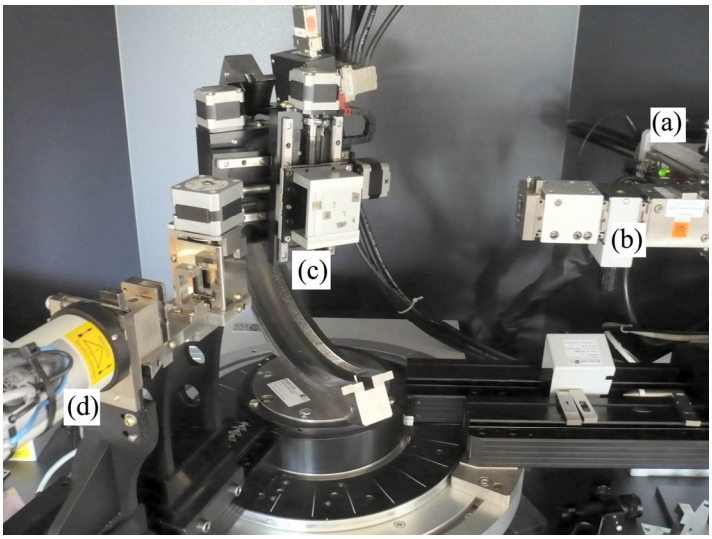

Figure 2.20 D8 Discover system used for HR-XRD studies in a ω/2θ geometry: (a) X-ray tube, (b) optical elements and absorber, (c) sample holder and Eulerian cradle and (d) detector with motorized slits.

The sample is mounted on a 6-axes Eulerian cradle, making possible translation (x,y,z) and rotation (ω,χ,φ) independent movements. The movement of the detector introduces another additional axis (2θ). The (χ,φ) angles are normally used for the alignment of the crystal, but they are not taking part in the XRD measurement. The ω angle covers the whole 360º range while 2θ can be varied from -4º to 170º. The $\omega/2\theta$ reproducibility is ±0.0001º. Note that (ω,χ,φ) angles in the XRD system are in correspondence with the (θ,χ,φ) angles in the RBS/C set-up.

To reduce the divergence in the detector, the diffracted beam is passing through two sets of slits, one motorized anti-scattering slit (0.5 mm) and one fixed slit (0.1 mm). A

scintillation NaI(Tl) detector receives the diffracted X-rays from the sample. Figure 2.20 shows a picture of the HR-XRD system at ITN.

It is important to note that, by changing the angles ω and 2θ (Figure 2.19), the incident (k_0) and diffracted (k) wavevectors can be modified to reach different points in the reciprocal space (Q). Actually, the in-plane (Q_x) and out-of-plane (Q_z) reciprocal lattice points can be calculated considering the formulae [52]:

$$Q_x = \frac{2\pi}{\lambda}\left[\cos\omega - \cos(2\theta - \omega)\right]$$
$$Q_z = \frac{2\pi}{\lambda}\left[\sin\omega + \sin(2\theta - \omega)\right]$$

Therefore, controlling the $\omega/2\theta$ relation, different planes of the sample can be probed. For this purpose, several angular scans are available: the ω-scan, the $\omega/2\theta$ (or the $2\theta/\omega$), and the 2θ-scan. In the ω-scan, the detector remains stationary and the sample is rotated in the ω axis, so the length Q is constant, but its direction changes. In the $\omega/2\theta$ scan, both sample and detector are rotated simultaneously keeping the ratio 1:2. Therefore, the length Q changes but the direction remains the same. Note that both ω and $\omega/2\theta$ scans can be properly called "rocking curves" (RC) since they involve rocking the sample along the ω-axis (this often causes confusion). Finally, in the 2θ-scan, only the detector is moved, and Q changes its direction and length describing an arc in the reciprocal space.

More sophisticated scans can be performed thanks to the software options. In particular, for reciprocal space maps (RSMs) a Q-scan can be developed. This scan moves ω and 2θ in non-integer ratios, changing Q along a given direction in the reciprocal space. This is one of the best ways to determine accurately the lattice parameters of the films [52], and several examples will be shown in the next chapters.

(b) Alignment of wurtzite crystals by XRD

As in RBS/C, the main tool for the alignment of the crystals is the stereographic projection. Different planes are accessible for HR-XRD experiments in wurtzite crystals as shown in Figure 2.21. The most used symmetric planes are the (0002) and the (0004), which are often analyzed when measuring the crystal quality. On the contrary, for strain

determination asymmetric reflections are required, being $(10\bar{1}4)$ and $(10\bar{1}5)$ the most extended ones.

Prior to the alignment, a calibration of the zero position of the detector (2θ=0º) is necessary, which is done facing the detector to the source and making a 2θ-scan. Then, the sample position is fixed with the aid of the translation movements of the goniometer. The positions x and y can be determined with the help of a telescope, while the surface of the sample is aligned by means of a z-scan in the 2θ=0º configuration (with ω=90º). After this, only the three angles of the sample cradle (ω,φ,χ) and the 2θ angle of the detector are moved.

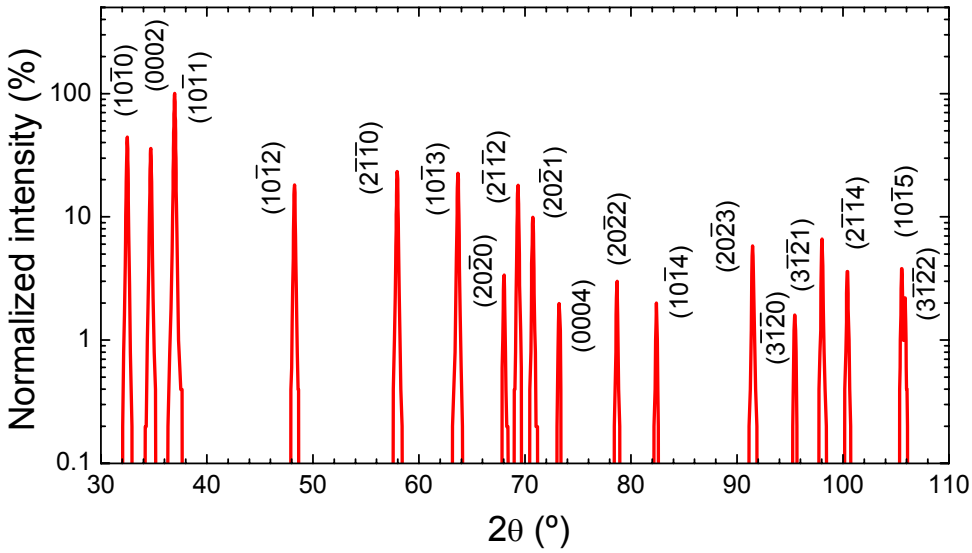

Figure 2.21 Calculated 2θ angles and intensities for main planes in a GaN crystal.

To start the alignment, the $\omega/2\theta$ condition must satisfy Bragg's law. This condition is $2\omega=2\theta$ for symmetric planes, but not for asymmetric ones because there is an additional offset in the ω-axis, corresponding to the angle between the plane and the surface. This offset can be calculated from the stereographic projection assuming the growth direction. For example, in the $(10\bar{1}4)$ reflection the offset is 25.12º, which is the angle between this plane and the (0004). These angles can be deduced for any set of planes in the computer program *Carine* [47], but the exact $\omega/2\theta$ relation in the experiment will demand corrections by angular scans in every particular sample.

Once the $\omega/2\theta$ relation is fixed the optimization of the other axes (φ,χ) can be carried out. Normally, several iterative scans are necessary to find the exact position,

combining φ-scans (or χ-scans) with ω-RCs. The alignment of φ has to be performed using asymmetric reflections, since (000*l*) planes do not depend on this orientation. On the contrary, the tilt angle χ is better optimized in symmetric planes. Consequently, at least two different geometries are required for an exact alignment of the crystal.

(c) Determination of crystal quality and strain by XRD

HR-XRD experiments can be used to determine the crystal quality and the strain state of crystalline films. Actually, the diffraction is very sensitive to any change of the lattice parameters, much more than RBS/C. However, for conventional measurements on thin films the detector collects the X-rays from the whole layer, almost independently of the depth where the scattering process takes place. Therefore, the technique does not provide depth-resolution of the physical parameters such as the crystal quality and the strain state, which has to be considered for the analysis to avoid misunderstandings [6].

The usual way of determining the crystal quality by HR-XRD is to measure the integral breadth (β=peak area/peak height) in the diffraction peak for one specific plane [53]. For Gaussian peaks, β is exactly the full-width at half maximum (FWHM) of the peak. Nevertheless, the comparison of the FWHM depends on the shape of the peak, and for Lorentzian peaks $\beta=0.62\cdot$FWHM. Intermediate combinations can also take place, giving mixed contributions, as in the Voigt function. The crystallite size, the misorientation (mosaic tilt or twist) and the microstrain are the main parameters affecting the FWHM [53].

In wurtzite crystals the planes explored for the crystal quality are normally the (0002) or the (0004), since they correspond to the growth orientation and provide a good statistics. Therefore, the procedure to estimate the crystal quality is a ω-scan around the selected (000*l*) plane. The FWHM of the diffracted peak is extracted from the fitting with Gaussian, Lorentzian or Voigt functions, depending on the shape of the peak. Figure 2.22 shows the Lorentzian fitting in two RCs for the (0004) plane. Depending on the sign of the 2θ angle, there are two possible configurations of ω ($\omega_+\sim36.67^\circ$ and $\omega_-\sim143.33^\circ$) that allow the diffraction in the (0004) plane. Both of them should be equivalent if the other angles (φ,χ) are optimized. Note that the tilt angle (χ) does affect the intensity of (000*l*) reflections so it must be considered before the ω-RC.

As in RBS/C, the measure of the strain state by HR-XRD is more complex than the one for the crystal quality, because the lattice parameters have to be determined absolutely and with high accuracy. One of the precise procedures (few parts per million) to obtain absolute measurements of the lattice parameters is the Bond method [54, 55]. This method involves ω-RC in two symmetric and two asymmetric reflections, at both positive and negative 2θ angles, eliminating the zero error in the detector. From the symmetric RCs, normally acquired in the (0004) plane, the c parameter is estimated using the crystal setting (ω_+ and ω_-) and the Bragg's law. From the asymmetric RCs, normally acquired in the $(10\bar{1}4)$ plane, the a parameter is determined in the same way, but using (2.9) and the previous c value.

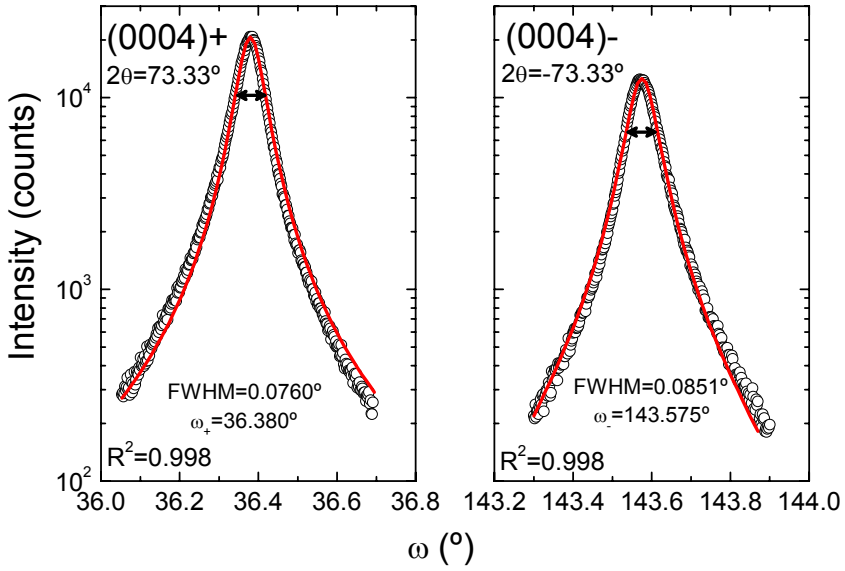

Figure 2.22 Rocking curves for a GaN layer in the (0004)+ and the (0004)- geometries. The FWHM is very similar in both cases because of the symmetric configuration and it can be used as an estimator of the crystal quality. The lines correspond to the Lorentzian fittings.

The Bond method is a good and fast approach for lattice parameters determination, but it depends on ω-RCs with an open detector (no slits in the front of the detector). Therefore, the peaks from the layer and the substrate are broad and may overlap. To avoid this drawback, RSMs are normally used [3]. In this latter case, the Bond method is only carried out on the substrate peak (GaN). The calculation of the absolute lattice parameters of the substrate establishes a fixed reciprocal lattice point, which can be considered as a reference in the RSMs. Thus, the acquired RSM around a *(hkl)* reflection will allow to detect the peak from the layer in the correct units (Q_x,Q_z). The

final determination of the lattice parameters of the layer for such specific *(hkl)* plane can be obtained as [52]:

$$a = \frac{2\pi}{Q_x}\sqrt{\frac{h^2 + k^2 + kl}{3/4}}$$
$$c = \frac{2\pi}{Q_z} l$$

Only asymmetric reflections are sensitive to the *a* parameter, so these planes must be used for the determination of the strain state. In particular, for wurtzite type crystals the most common plane is the $(10\bar{1}5)$. Figure 2.23 shows an example of the $(10\bar{1}5)$ RSM in an AlInN/GaN heterostructure [6]. Both *ω-2θ* units and Q_x-Q_z units are shown.

The strain state of the film, when measuring by HR-XRD, is directly calculated from the definition because the lattice parameters are determined absolutely. However, the final strain in the mixed layers depends on the correct application of Vegard's law. Consequently, the accurate measurement of the composition of the film is as important as the determination of the lattice parameters.

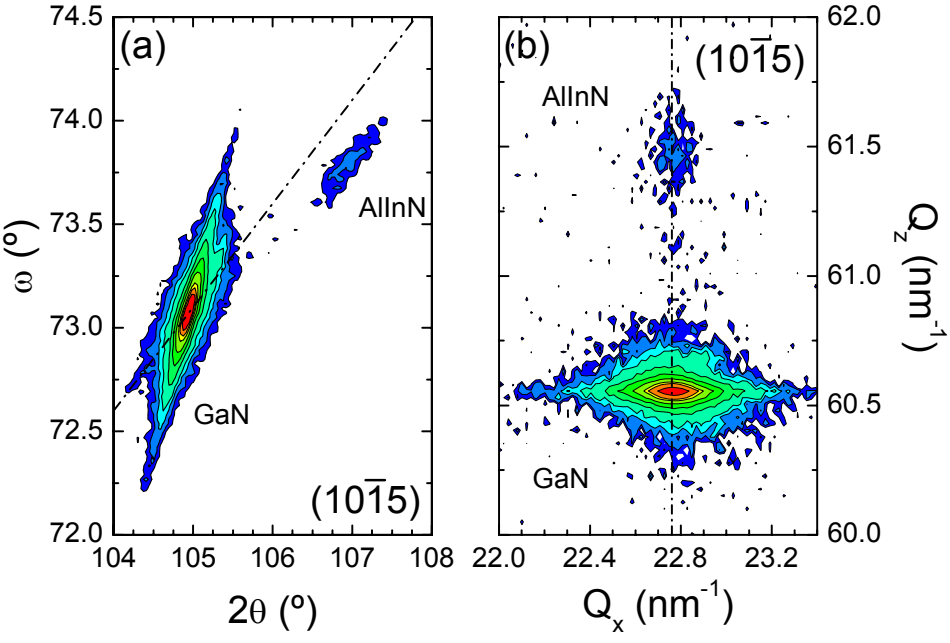

Figure 2.23 RSM along the $(10\bar{1}5)$ plane for an AlInN/GaN HS in (a) *ω-2θ* units and (b) Q_x-Q_z units.

For ternary HSs such as $Al_xGa_{1-x}N$, $In_xGa_{1-x}N$ or $Al_{1-x}In_xN$, the composition can be indirectly calculated from HR-XRD too. This is achieved separating the contribution

from the strain and from the composition (x) via Poisson's equation (note that this is not true for quaternaries because there are two stoichiometric coefficients):

$$\left[c - c_0(x)\right] + 2\frac{C_{13}}{C_{33}}\frac{c_0(x)}{a_0(x)}\left[a - a_0(x)\right] = 0 \qquad (2.10)$$

Since the a and c parameters are extracted from RSMs, and C_{13} and C_{33} are constants, the only variable in equation (2.10) is x. Then, the solution of the cubic equation (2.10) can be obtained by numerical methods such as regula falsi or Newton's method, imposing the restriction $0<x<1$. This procedure involves several parameters such as the relaxed lattice parameters of the binaries, and thus the error in the final value can be high. Moreover, the existence of compositional or strain gradients as well as the appearance of phase separation can affect considerably the accuracy of the method [6]. Therefore, this approach should be confronted with RBS or other techniques giving strain-independent compositional results. This point will be discussed in detail in following chapters of this thesis.

2.5. References

[1] H. Morkoç, *Nitride semiconductors and devices* (Springer, Berlin, 1999).

[2] M. Vinnichenko, N. Shevchenko, A. Rogozin, R. Grötzschel, A. Mücklich, A. Kolitsch, and W. Möller, J. Appl. Phys. **102**, 113505 (2007).

[3] U. Pietsch, V. Holy, T. Baumbach, *High-resolution X-ray scattering* (Springer, New York, 2004).

[4] M. Birkholz, *Thin Film Analysis by X-Ray Scattering* (Wiley-VCH, Weinheim, 2006).

[5] L. Vegard, Z. Phys. **5**, 17 (1921).

[6] A. Redondo-Cubero, K. Lorenz, R. Gago, N. Franco, M.-A. di Forte Poisson, E. Alves and E. Muñoz, J. Phys. D: Appl. Phys. **43**, 055406 (2010).

[7] J. R. Tesmer, M. Nastasi, *Handbook of modern ion beam material analysis* (MRS, Pittsburg, 1995).

[8] R. C. Bird, J.S. Williams, *Ion beams for materials analysis* (Academic Press, London, 1989).

[9] L. C. Feldman, J. W. Mayer and S. T. Picraux, *Materials analysis by ion channelling* (Academic Press, New York 1982).

[10] M. Grundmann, *The physics of semiconductors* (Springer, Berlin, 2006).

[11] L. Liu, and J.H. Edgar, Mater. Sci. Eng. R **37**, 61 (2002).

[12] D. A. Neumayer, and John G. Ekerdt, Chem. Mater. **8**, 9 (1996).

[13] P. Gibart, Rep. Prog. Phys. **67**, 667 (2004).

[14] H. Amano, N. Sawaki, I. Akasaki and Y. Toyoda, Appl. Phys. Lett. **48**, 353 (1986).

[15] R. D. Dupuis, Science **226**, 623 (1984).

[16] S. Nakamura, T. Mukai, M. Senoh and N. Iwasa, Jpn. J. Appl. Phys. **31(2B)**, L139 (1991).

[17] V. Tasco, A. Campa, I. Tarantini and A. Passaseo, F. González-Posada, A. Redondo-Cubero, K. Lorenz, N. Franco and E. Muñoz, J. Appl. Phys. (2009).

[18] K. Yamamoto, K. Enomoto, A. Nakamura, T. Aoki and J. Temmyo, J. Cryst. Growth **298**, 468 (2007).

[19] J. M. Albella, *Láminas delgadas y recubrimientos: preparación, propiedades y aplicaciones* (C.S.I.C., Madrid, 2003).

[20] A. Y. Cho, Thin Solid Films **100**, 291 (1983).

[21] S. Fernández-Garrido, *Crecimiento de nitruros del grupo III por epitaxia de haces moleculares para la fabricación de diodos electroluminiscentes en el rango visible-ultravioleta*, (Universidad Politécnica de Madrid, Madrid, 2009).

[22] A. I. Rogozin, M. Vinnichenko, A. Kolitsch and W. Möller, J. Vac. Sci. Technol. A **22**, 349 (2004).

[23] H. Geiger, and E. Marsden, Proc. Roy. Soc. London **A 82**, 495 (1909).

[24] E. Rutherford, Phil. Mag. **21**, 669 (1911).

[25] W.-K. Chu, J.W. Mayer and M.-A. Nicolet, *Backscattering spectrometry* (Academic Press, New York, 1978).

[26] A. F. Gurbich, *Ion Beam Analysis Nuclear Data Library*, http://www-nds.iaea.org/ibandl/ (2003).

[27] J. F. Ziegler, J.P. Biersack and U. Littmark *The stopping and range of ions in solids* (Pergamon Press, New York, 1985).

[28] J. F. Ziegler, M.D. Ziegler and J.P. Biersack, *SRIM*, http://www.srim.org (2008).

[29] N. Barradas, K. Arstila, G. Battistig, M. Bianconi, N. Dytlewski, C. Jeynes, E. Kótai, G. Lulli, M. Mayer, E. Rauhala, E. Szilágyi and M. Thompson, Nucl. Instr. and Meth. B **262**, 281 (2007).

[30] M. Mayer, AIP Conf. Proc. **475**, 541 (1999).

[31] N. P. Barradas, C. Jeynes, and R.P. Webb, Appl. Phys. Lett. **71**, 291 (1997).

[32] E. Kótai, Nucl. Instrum. Meth. B **85**, 588 (1994).

[33] E. Rutherford, H. Geiger and H. Bateman, Phil. Mag. **20**, 698 (1910).

[34] A. Gottdang, D.J.W. Mous, R.G. Haitsma, Nucl. Instr. Meth. B **190**, 177 (2002).

[35] A. Climent-Font, F. Pászti, G. García, M.T. Fernández-Jiménez, F. Agulló, Nucl. Instr. Meth. B **219-220**, 400 (2004).

[36] C. Pascual, *Experimental determination of stopping forces for ions in matter*, (Universidad Autónoma de Madrid, Madrid, 2004).

[37] U. Kreissig, R. Gago, M.Vinnichenko, P. Fernández-Hidalgo, R.J. Martín-Palma and J.M. Martínez-Duart, Nucl. Instr. and Meth. B **219-220**, 908 (2004).

[38] J. F. Ziegler, C.P. Wu, P. Williams, C.W. White, B. Terreault, B.M.U. Scherzer, R.L. Schulte, E.J. Schneid, C.W. Magee, E. Ligeon, J.L. 'Ecuyer, W.A. Lanford, F.J. Kuehne, E.A. Kamykowski, W.O. Hofer, A. Guivarc'h, C.H. Filleux, V.R. Deline, C.A. Evans Jr., B.L. Cohen, G.J. Clark, W.K. Chu, C. Brassard, R.S. Blewer, R. Behrisch, B.R. Appleton and D.D. Allred, Nucl. Instr. Meth. **149**, 19 (1978).

[39] W. A. Landford, Nucl. Instr. Meth. **149**, 1 (1978).

[40] W. Rudolph, D. Grambole, R. Grotzschel, C. Heiser, F. Herrmann, P. Knothe and C. Neelmeijer 1988 Nucl. Instr. Meth. B **33** 503 (1988).

[41] J. Lindhard, Mat. Phys. Medd. K. Dan. Vidensk. Selsk. **34**, 1 (1965).

[42] A. Redondo-Cubero, K. Lorenz, N. Franco, S. Fernández-Garrido, R. Gago, P.J.M. Smulders, E. Muñoz, E. Calleja and E. Alves, J. Phys. D: Appl. Phys. **42**, 065420 (2009).

[43] J. J. Rousseau, *Basic crystallography* (John Wiley & Sons, Surrey, 1999).

[44] F. C. Phillips, *An introduction to crystallography* (Oliver & Boyd, Edinburgh, 1971).

[45] J. S. Smaill, *Metallurgical stereographic projections* (Adam Hilger Ltd., London, 1972).

[46] C. Klein, *Manual of mineral science* (Wiley-VCH, New Jersey, 2001).

[47] C. Boudias, and D. Monceau, *Carine Crystallography*, http://pagespro-orange.fr/carine.crystallography (1998).

[48] B. Holländer, S. Mantl, M. Mayer, C. Kirchner, A. Pelzman, M. Kamp, S. Christiansen, M. Albrecht and H.P. Strunk, Nucl. Instr. Meth. **136–138**, 1248 (1998).

[49] W. C. Turkenburg, W. Soszka, F.W. Saris, H.H. Kersten and B.G. Colenbrander, Nucl. Instr. Meth. **132**, 587 (1976).

[50] W. L. Bragg, Proc. Cambridge Phil. Soc. **17**, 43 (1913).

[51] D. J. Dunstan, J. Mater. Sci.-Mater. Electron. **8**, 337 (1997).

[52] M. A. Moram, and M. E. Vickers, Rep. Prog. Phys. **72**, 036502 (2009).

[53] M. E. Vickers, M.J. Kappers, R. Datta, C. McAleese, T.M. Smeeton, F.D.G. Rayment and C.J. Humphreys, J. Phys. D: Appl. Phys. **38**, A99 (2005).

[54] W. L. Bond, Acta Crystallogr. **13**, 814 (1960).

[55] N. Herres, L. Kirste, H. Obloh, K. Köhler, J. Wagner and P. Koidl, Mat. Sci. Eng. B **B91-92**, 425 (2002).

3

Characterization by ion channeling: models and simulations

The classical theory of ion channeling is described in this chapter due to the relevant implication of RBS/C in the structural characterization of WBS. The main parameters for modeling ion channeling are defined, and the analysis via Monte Carlo simulations is considered in detail, introducing the FLUX program as a tool for fitting the angular scans.

Do not despise to anybody; an atom makes shade. (Pythagoras)

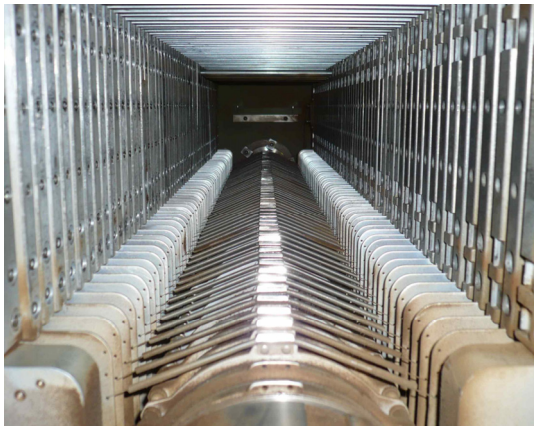

Core of the Van de Graff accelerator at ITN.

3.1. Introduction

Previous chapters have pointed out the relevance of the structural modification in the growth of ternary and quaternary WBS HSs. As discussed before, the characterization of the crystal quality, the strain state, and the defects in such layers is usually carried out by means of XRD (see section 2.4). However, depth-resolved studies are essential to detect phase separation or strain gradients during the growth, which have focused the attention on other alternatives, and specifically, on ion channeling. Actually, the current fields covered by channeling are very large, including the epitaxial growth, the implantation damage, the location of dopants and impurities, the surface reconstruction, etc. [1]. This thesis continues this line using RBS/C for a complete study of the WBS HSs. In chapter 2, the experimental methods and set-ups for RBS/C were illustrated, including the calculation of the minimum yield or the strain state. Nevertheless, an exact analysis by RBS/C frequently requires a theoretical approach, since these parameters can be affected by several physical variables as the beam energy and divergence, the incident angle, the Debye temperature of the material, etc. Therefore, a whole description of the channeling phenomena needs a precise modeling, involving sometimes Monte Carlo (MC) simulations too. This chapter will introduce this theoretical basis for the understanding of the main features of RBS/C.

The general foundations of channeling were established by J. Lindhard in 1965 [2]. The Lindhard's theory explains the steering of charged particles inside the matter by means of a classical collision model [3, 4], and defines the most important parameters such as the critical angle (see section 3.2.2) or the minimum yield (section 3.2.3). Interestingly, the first proposal indicating the directional effect of the propagation of radiation (charged particles or X-rays) took place ~50 years before the Lindhard's theory, since J. Stark introduced this idea in 1912 [5]. However, the simultaneous discovery of XRD delayed the development of ion channeling until 1963, when two independent works demonstrated, from experimental [6] and theoretical [7] approaches, the effect of the crystalline structure on the penetration ranges of charged particles.

After 1965, certain experimental discrepancies have evidenced the limitations of the Lindhard's theory, demanding the use of MC programs [4]. As a result, several MC codes were developed in the decade of 1970 for an accurate treatment of the underlying mechanisms of channeling [8-10]. Although in conventional ion channeling

measurements the MC methods could be considered unnecessary or excessive, this is clearly false for some concrete applications as it will be shown in chapter 6. Therefore, MC programs have become a fundamental tool to extract all the physical information in the angular scans, and particularly for the strain and the lattice site determination.

Considering the essential role of ion channeling in quite a few analyses exposed in this thesis, next the modeling of channeling phenomena is explained, focusing on the essential parameters needed for the analysis. Then, the simulations via MC code FLUX [9] will be discussed.

3.2. Basic concepts and theoretical model of channeling

Channeling is a directional effect that takes place when a charged particle beam is aligned with a major symmetry direction of a crystal [2]. Two different classes of channeling can be defined: axial (the direction is parallel to an axis) and planar (the direction is parallel to a plane). However, as it was shown in chapter 2, for the crystal characterization by RBS/C the first case is the most extended method; so in the following only axial channeling will be considered.

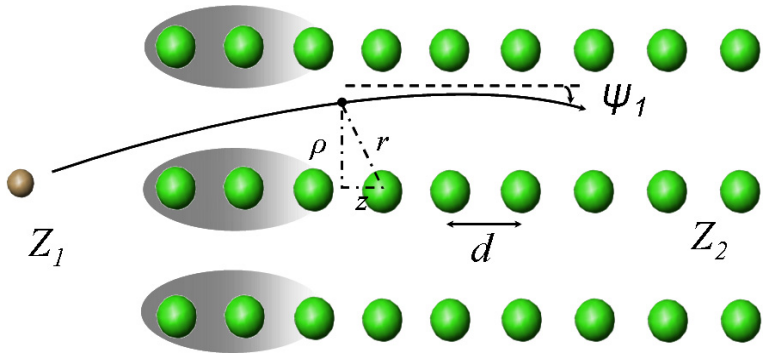

Figure 3.1 String model of channeling.

The channeling effects can have different manifestations in the experimental spectra depending on the impact parameter of the ions but, regarding the concrete case of RBS, the result of channeling is an intense reduction of the scattering events (backscattered yield). This reduction is a consequence of the correlated series of small-angle screened Coulomb collisions between the ions and the lattice atoms [11]. Therefore, the close encounter probability decreases and ions can travel large distances inside the material. In this way, channeling-based techniques have a high sensitivity to any lattice

perturbation such as extended defects (interstitials, dislocations, stacking faults, etc), strain, impurities, phase separation or implantation damage.

3.2.1. Continuum collision model

The basic theory of channeling explains the effect in terms of a correlated series of elastic two-body collisions. Nevertheless, Lindhard proved the validity of a classical continuum collision model [2] when: (a) the scattering angles are small, (b) the successive collisions are strongly correlated, (c) the collisions are elastic encounters between two bodies and (d) the crystal can be approximated by perfect strings of atoms with a uniform spacing. Under these conditions, the ion can be considered to move in an average transverse potential energy given by [2]:

$$U_T(\rho) = \frac{1}{d}\int_{-\infty}^{\infty} V\left[\sqrt{\rho^2 + z^2}\right] dz \,. \tag{3.1}$$

Here, ρ is the distance of the ion from the string of atoms, z is the distance traveled along the string and d is the spacing between atoms along the string direction (see Figure 3.1). Note that d may coincide with a specific interplanar distance d_{hkl} as in XRD, but this is not true in general.

For intermediate impact parameters, the two-body potential of (3.1) is generally well-described by the Thomas-Fermi model [12]:

$$V(r) = \frac{Z_1 Z_2 e^2}{4\pi\varepsilon_0 r} f(x), \tag{3.2}$$

where Z_1 and Z_2 are the atomic numbers of the incident ion and the atom in the string, e is the electronic charge, r is the nuclear separation distance, a is the screening distance $f(x)$ is the screening function, and $x=r/a$ is the reduced radius. For continuum calculations the screening function has different analytical approximations. Lindhard [2] and Molière [13] developed two of the most used models for the potential (3.2). In particular, for Lindhard's theory, the model is described by:

$$a_L = \frac{0.8854 \cdot a_0}{\left(Z_1^{2/3} + Z_2^{2/3}\right)^{1/2}}$$

$$f_L(x) = 1 - \frac{x}{\left(3 + x^2\right)^{1/2}}.$$

Nevertheless, the choice of the analytical approximation of the potential is a compromise between the accuracy and the simplicity required. In order to use a universal function, Ziegler-Biersack-Littmark (ZBL) proposed a repulsive potential, constructed by fitting the screening function to theoretically obtained potentials calculated for a large variety (521 combinations) of ion-target pairs [14]. Nowadays, this general treatment is replacing the most classical approaches. The ZBL screening parameter and function are [14, 15]:

$$a_{ZBL} = \frac{0.8854 \cdot a_0}{Z_1^{0.23} + Z_2^{0.23}}$$

$$f_{ZBL}(x) = 0.1818e^{-3.2x} + 0.5099e^{-0.9423x} + 0.2802e^{-0.4028x} + 0.02817e^{-0.2016x}$$

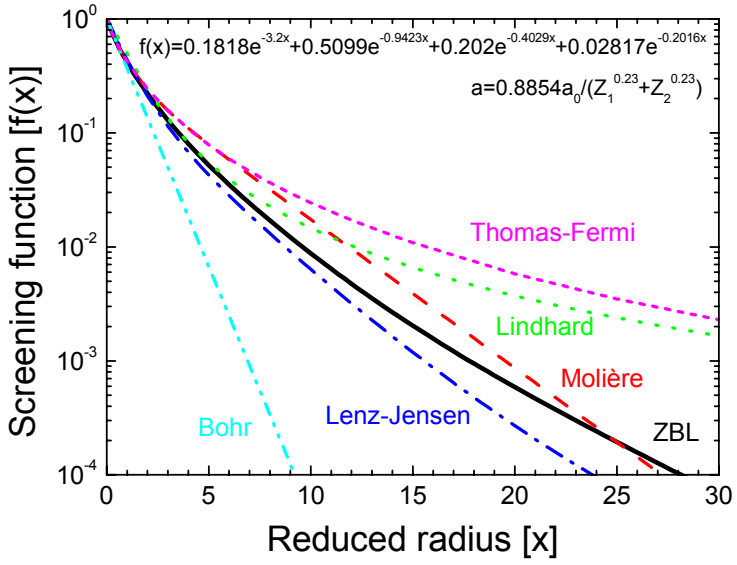

Figure 3.2 The universal ZBL screening function compared with the different approximations to the Thomas-Fermi potential.

The comparison of the ZBL reduced screening function with the other approximations to the Thomas-Fermi solution is shown in Figure 3.2. It can be seen that Lindhard's approximation is closer to the Thomas-Fermi solution for large distances since both of them are slightly shielded. Molière's potential, on the contrary, is closer to the ZBL.

The integration of (3.1) using the Thomas-Fermi potential (3.2) gives the string potential controlling the motion of ions into the crystal. Of course, the calculation of the string potential depends on the selected approximation of the screening function. Assuming Lindhard's model, the string potential energy takes the simple form [2]:

$$U_T(\rho) = \frac{Z_1 Z_2 e^2}{4\pi\varepsilon_0 d} ln\left[1 + \left(\frac{3a}{\rho}\right)^2\right]. \tag{3.3}$$

Molière's approximation gives a more complex transverse energy but the current calculations, and also MC programs, usually consider the ZBL potential. However, the validity of the continuum string potential requires that many collisions are involved in the scattering of the ion as it approaches to the string of atoms. Therefore, under high-energy conditions, the continuum potential is limited to certain incident angles lower than a characteristic angle. For the situations where this is not fulfilled, MC simulations can give a more accurate description of the experimental phenomena.

3.2.2. Critical angle for channeling

Channeling is linked to the relative alignment of the ion beam and the crystal, so the fundamental feature that characterizes it is the angular dependence. This dependence can be easily understood by means of the shadow cone. The first atoms at the surface of the crystal are exposed to the direct beam, and hence they act as shields for the atoms behind them. However, the shielding effect is less efficient as the incident angle increases. This is shown in Figure 3.3. For an incident angle ψ=0º, the shadow cone of the first atom of the row covers all the atoms behind it. However, for ψ=0.25º only three atoms are shadowed by the first one, and the situation is even worse for ψ=0.5º. Therefore, it is clear that there must be a critical angle acting as a threshold for the steering of ions within the channel.

This critical angle can be defined in terms of the Lindhard's theory as the limit for the application of the continuum model. The physical condition for the use of the string model demands that the scattering in the vicinity of the string is due to many atoms. This means that there is a critical approach distance (ρ_{min}) within which non-continuum scattering is possible. This closest approach is reached when the transversal kinetic energy of the ion equals the transversal potential energy of the string:

$$U_T(\rho_{min}) = E\sin^2\psi_c \cong E\psi_c^2 . \qquad (3.4)$$

This restriction (3.4) defines the critical angle for channeling and, if the Lindhard's potential (3.3) is assumed, it gives:

$$\psi_c = \frac{\psi_1}{\sqrt{2}}\left\{ ln\left[\left(\frac{3a}{\rho_{min}}\right)^2 + 1\right]\right\}^{1/2} .$$

The value of ψ_1 was first defined by Lindhard [2] using additional approximations (of the collision time scales and velocities), and it contains all the relevant physical information. This Lindhard's critical angle is given by:

$$\psi_1 = \sqrt{\frac{2Z_1Z_2e^2}{4\pi\varepsilon_0 Ed}} . \qquad (3.5)$$

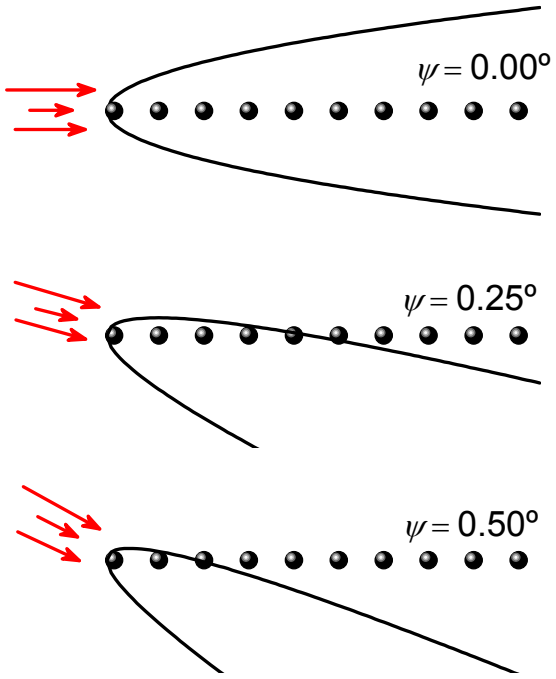

Figure 3.3 Calculated shadow cones for different incident angles in a wurtzite lattice.

It is important to notice that ψ_1 depends mainly on the kinetic energy of the particle and on the charge per unit length of the string (Z_2e^2/d), but it is independent on the atomic screening radius. In the following, ψ_1 will be used instead of ψ_c for the discussion, since this later is difficult to estimate accurately. Actually, a realistic limit for ρ_{min} is given by the root mean square of the thermal vibrational amplitude normal to the axis

($u_2=2^{1/2}\cdot u_1$). The one-dimensional vibrational amplitude (u_1) is calculated from the Debye approximation [16]:

$$u_1 = 12.1\sqrt{\left(\frac{\varphi(t)}{t}+\frac{1}{4}\right)/M_2\theta_D}\ , \tag{3.6}$$

where $\varphi(t)$ is the Debye function, M_2 the atomic mass of the crystal atoms, θ_D is the Debye temperature and $t= \theta_D/T$, being T the substrate temperature. Since the Debye temperature of GaN is still uncertain [17], the value of ψ_c cannot be fixed exactly.

Technically, ψ_1 is only a parameter determining the applicability of the Lindhard's continuum model, but the physical meaning of the critical angle is clear: it is the maximum incidence angle for which an ion will be specularly reflected from the string potential. MC simulations also confirm this point showing that ions entering with $\psi<\psi_1$ are well-steered by the continuum potential, while ions with $\psi>\psi_1$ suffer large impact collisions which finally turn into the dechanneling of the ions.

Despite ψ_1 is not directly accessible experimentally, it is a well-established quantity related with the half-angle of the angular scans (the width of the dip when the normalized yield is 50 %, $\psi_{1/2}$). In general, it has been proved that experimental values of $\psi_{1/2}$ are systematically lower than predicted ψ_1 [3]. MC simulations developed by Barrett suggest the inclusion of a constant factor $C_\psi(u_1)$, close but lower than unity [11]. This constant factor depends on the vibrational amplitude of the crystal (u_1), substituting the Lindhard's potential by Molière's one, which is more screened (see Figure 3.2). Therefore, although experimental $\psi_{1/2}$ varies in the predicted way with the ion energy, the atomic spacing, and the atomic numbers, several corrections are needed to find the exact value.

Figure 3.4 shows two angular scans for a GaN crystal with a 2 MeV He^+ beam. The experimental values of $\psi_{1/2}$ are 0.67(2)º in the <0001> axis and 0.51(2)º in the $<\bar{2}113>$. On the contrary, theoretical calculations of ψ_1 (for Ga, Z_2=31) give 0.75º and 0.69º, respectively. Thus, the overestimation of ψ_1 was confirmed in this case too. As a normal procedure, for binary compounds such as GaN, an average target element number (Z_2) is selected in the calculations. However, even assuming that, the theoretical ψ_1 has to be corrected because it is necessary to take into account the effect of the lattice

vibrational amplitude. From the calculations carried out in this thesis, a $C_\psi(u_1)=\psi_{1/2}/\psi_1$ between 0.89 and 0.74 was deduced.

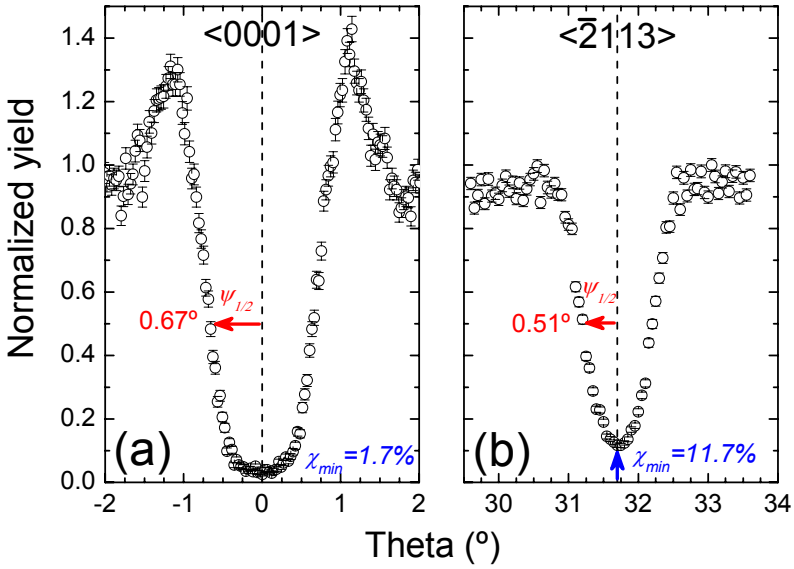

Figure 3.4 Experimental angular scans for a wurtzite GaN: (a) across the <0001> axis and (b) across the $<\bar{2}113>$. The ion beam was 2 MeV He^+.

In principle, $\psi_{1/2}$ could be a good physical parameter for the estimation of d. Nevertheless, the limited accuracy of the goniometers (±0.01°), the difficult control of the temperature and, specially, the uncertainty in the vibrational amplitude, make this enterprise very difficult. Consequently, to extract useful information from $\psi_{1/2}$, the MC approach has to be used here, which allows fitting the vibrational amplitude with the experimental data. The details of such simulations will be discussed later on.

3.2.3. *Minimum yield*

The second fundamental parameter for quantification of channeling is the minimum yield (χ_{min}). This variable was defined already in chapter 2 (section 2.4.1) in terms of the experimental yields under aligned and random geometries. However, from a theoretical point of view and according to the Lindhard's continuum model, χ_{min} is exactly describing the fraction of the channel area which is forbidden by the vibrating strings of atoms. Figure 3.5 shows a graphical representation of this concept. The total available area is given by $1/Nd$, where N is the atomic density ($8.745\cdot10^{22}$ at/cm^3 for GaN) and d is the interatomic spacing defined in section 3.2.1). On the contrary, the distance

covered by the atoms in the string is given by the vibrational amplitude u_2. Thus, the minimum yield is:

$$\chi_{min}^{<uvw>} = \pi N d u_2^2 . \qquad (3.7)$$

The striking feature of (3.7) is that χ_{min} is independent of beam parameters, and it is determined solely by the properties of the crystal. Besides, the minimum yield has to be defined for a particular <*uvw*> axis, since the accessible areas are different depending on the direction. Normally, for perfect crystals only 1-5% of the particles entering in the crystal are not channeled. Since the accessible area is very sensitive to the defects in the crystal, χ_{min} is the main physical parameter for the estimation of the crystal quality (see chapter 2).

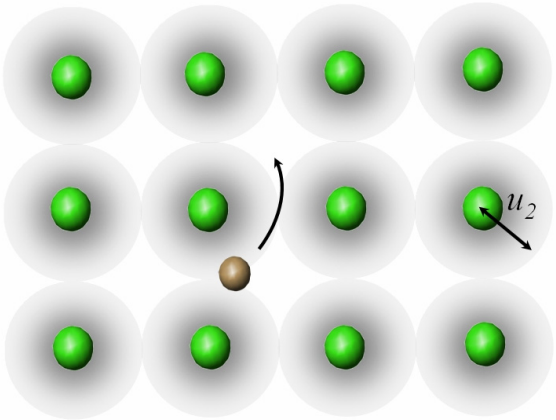

Figure 3.5 Accessible areas for ion channeling depending on the vibrational amplitude of the atoms.

MC simulations carried out by Barrett show that the values obtained from (3.7) have to be corrected by a factor of ~3. Furthermore, Barrett related χ_{min} with ψ_1, so the independence of χ_{min} on the beam energy cannot be assumed for accurate calculations (note that ψ_1 does depend on the energy). However, in most of the cases, these considerations are unnecessary because relative comparisons of χ_{min} are normally carried out. Actually, χ_{min} is directly calculated from the experiment as the ratio between the aligned and random backscattering yields (section 2.4.1). Since this calculation can be carried out for different elements and at different energy windows, RBS/C provides very useful information about the crystal quality with depth resolution. Figure 3.4 shows the values obtained in this work for GaN crystals aligned in the <0001> and

$< \bar{2}113 >$ axes. Of course, the axes with less symmetry have a higher χ_{min}, because of the more reduced accessible area for the ions (and because of twists and dislocations).

3.2.4. Dechanneling

An imperfect crystal contains defects. These defects, together with the combination of multiple scattering by electrons and thermally displaced atoms, lead to an increase with depth of χ_{min} (and a decrease in $\psi_{1/2}$ too). This increase is due to the gradual modification of the transverse energy (E_T), which can be estimated as:

$$\frac{dE_T}{dz} = E\frac{d\psi^2}{dz} + \psi^2\frac{dE}{dz}.$$

The second term can be neglected since the variations of the kinetic energy with depth are small. The first term represents the change due to the multiple scattering and it is the responsible of dechanneling. The effect of nuclear collisions on dechanneling is more significant in the near surface, while the multiple electronic scattering becomes important deeper in the target [4].

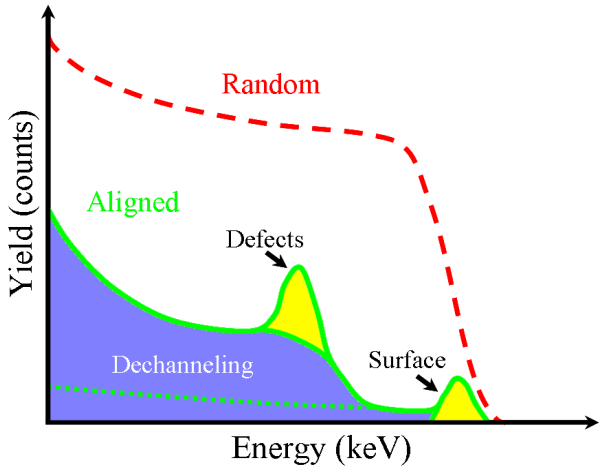

Figure 3.6 Main features in an aligned RBS spectrum of a crystal with defects.

For experimental considerations, dechanneling can be defined as the rate at which the normalized yield is changing with depth ($d\chi/dz$) [3]. The magnitude of dechanneling processes depends on the nature and concentration of defects. The intrinsic sources of dechanneling (electron scattering and thermal vibrations) are normally playing a minor role. However, the presence of point or extended defects can be strongly marked in the aligned spectrum, provoking an intense peak of dechanneling when they are located inside a narrow depth region. All these features are summarized in Figure 3.6.

Dechanneling is an essential parameter to quantify the density of defects and the crystal disorder of a material. For interstitial atoms, stacking faults and grain or twin boundaries, dechanneling is proportional to the defect concentration, $n_d(z)$ [16]. However, the estimation of the dechanneled fraction requires the deconvolution of direct scattering events from random scattering in the crystal. The most used phenomenological model states that the dechanneled fraction of ions (χ_D) is the sum of the random scattered component (χ_R) and the contribution from the direct scattering by defects (χ_S):

$$\chi_D(z) = \chi_R(z) + \chi_S(z) = \chi_R(z) + [1 - \chi_R(z)]\frac{f \cdot n_d(z)}{N}, \tag{3.8}$$

where $n_d(z)$ is the concentration of defects, f is the direct scattering probability and N is the atomic density. Note that (3.8) can be inverted to find the defect concentration as a function of χ_D and χ_R. Unfortunately, despite χ_D is experimentally known, χ_R is not a direct measurable quantity. However, the probability rate for random dechanneling per unit depth is proportional to the defect density via a cross section σ_d (theoretically estimated) [3]. Thus, χ_R is given by [3]:

$$\chi_R(z) = 1 - [1 - \chi_V(z)]exp\left(-\int_0^z \sigma_d n_d(z')dz'\right), \tag{3.9}$$

where χ_V is the random fraction for a defect-free (virgin) crystal. The expression (3.9) can be approximated to a linear expression for small defect concentrations, and therefore, it can be calculated from the RBS spectra, channel by channel. As mentioned in chapter 2, some of the programs simulating channeling analytically, as RBX [18], can provide the dechanneled fraction by fitting the aligned spectrum. Practical examples of this method will be found in the next chapters of this thesis.

3.2.5. *Spatial flux distribution of channeled particles*

The channeling phenomenon is time dependent. Ions entering inside the crystal are initially uniformly distributed but, as they are steered by the string potential, the ion trajectories oscillate between the channel walls, suffering a focusing effect towards the center of the channel. These oscillations are less regular for axial channeling than for planar channeling, since in the first situation ions can move easily to the neighboring channels. The steering process starts even in the first nm's of the crystal. Therefore, the

oscillations are reasonably mitigated some nm's below the surface, and then become depth-independent. For that reason, at room temperature it is difficult to appreciate such oscillations in the yield of the RBS/C spectra. An estimation of the transverse wavelength of the ion oscillations is given by Lindhard's relation [2]:

$$\lambda_{\perp}^{-1} = \frac{\pi^2}{4} Nda\psi_1^2/\psi \,. \tag{3.10}$$

For channeling of 2 MeV He^+ ions in GaN this wavelength ($\lambda_\perp$) is ~50 nm and, as it will be shown in the next chapters, this parameter has a relative importance for the strain determination.

In analytical calculations, the oscillation processes are omitted and it is further assumed that statistical equilibrium of ion positions is reached. Under this hypothesis, established by Lindhard, ions entering with an initial angle ψ and at a distance ρ_{in} from the atomic string, are uniformly distributed within an accessible area. Since the transverse component of the energy is conserved (energy losses are neglected), this accessible area is specified by the equation:

$$E\psi^2 + U_T(\rho_{in}) = U_T(\rho_A),$$

where $\pi\rho_A^2$ is the forbidden area close to the string. In such conditions, the ion flux is enhanced near the center of the channel [3, 11]. This peaked flux distribution is the most prominent feature of channeling, namely, that the close encounter probability is almost zero close to the atomic rows. Analytical expressions for the flux distribution can be obtained using the Lindhard's potential and the cylindrical symmetry of the lattice [3], finding:

$$F(r,\psi) = \begin{cases} e^{2\psi^2/\psi_1^2} ln\dfrac{1}{1-(r/r_0)^2}, & \psi \le \psi_1\sqrt{ln\dfrac{r_0}{r}} \\ e^{2\psi^2/\psi_1^2} ln\dfrac{1}{1-e^{-2\psi^2/\psi_1^2}}, & \psi > \psi_1\sqrt{ln\dfrac{r_0}{r}} \end{cases}. \tag{3.11}$$

It is important to remark the inverse relation between the flux distribution (F) and the normalized backscattering yield (χ). If the number of particles inside the channel is high, the yield of the atoms belonging to the lattice is low and vice versa. Thus, the flux

distribution is normalized assuming a random orientation, in such a way that F=1 corresponds to the number of ions that would be found inside the channel under non-aligned conditions.

Figure 3.7 shows the theoretical flux distribution given by (3.11) inside a crystal channel for different incident angles. For the perfect alignment (ψ=0) the most part of the ions are focused (F>1) on the center of the channel. This behavior is not preserved for angles close to ψ_1, where F~1 for every distance to the string. The flux distribution inside the channel is the main physical quantity indicating the motion of the ions into the lattice, so MC programs also calculates it directly. In the next sections, the use of MC simulations to determine the effective flux in wurtzite crystals will be shown.

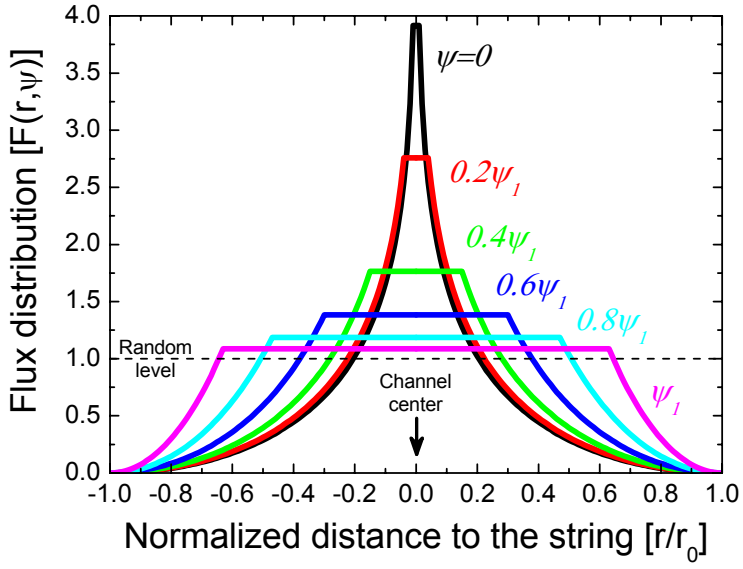

Figure 3.7 Theoretical spatial flux distribution inside a lattice channel. For low incident angles the flux is enhanced at the center of the channel, being few times higher than the random level.

3.3. Monte Carlo simulations of channeling

Lindhard's theory of channeling is a useful guide to explain the main physical mechanisms for the steering of ions in crystals, but there are several approximations restricting the applicability of the model. Some of the recognized deficiencies of the continuum description of channeling are the wrong dependence of the probability distribution on the distance traveled by the ions and on the azimuthal angle of the

transverse momentum [9]. Actually, the inadequacy of the statistical equilibrium hypothesis was recognized quite early [19].

The improvement of the analytical model is obtained frequently by means of MC programs [8, 10, 19], which can include several effects affecting the channeling phenomenon. Furthermore, in some cases, MC simulations are the only way to extract reliable information from the experimental data. Since MC codes incorporate the lattice structure, they are particularly effective in the determination of lattice sites of atoms, which require a complicated triangulation procedure (three different directions must be measured) [11]. Next, the principal features of the MC program FLUX [9] are explained, which were used in several studies of wurtzite HSs in this thesis.

3.3.1. FLUX program

In general, there are two approaches for MC simulations: the binary collision model and the continuum approximation. In the first one, the ion suffers a series of collisions and it is influenced only by the nearest atom. In the second, the ion feels a uniform charge distribution which determines the movement across the atomic rows. Both methods are equivalent for small angular deflections, but both are incomplete. FLUX program was developed by P.J.M. Smulders and D.O. Boerma [9] to overcome these limitations and provide a more accurate description of channeling.

The main feature of FLUX is that it combines the binary collision and the continuum approximation in the same code. Thus, FLUX treats the effect of the nearby atoms in the binary collision approximation and the effect of the surrounding strings in the continuum model. In addition, FLUX considers many other effects, such as the impact-parameter dependent interaction with electrons, the angular spread of the incoming beam and the thermal vibrations and their correlations. This last point is important, because the continuum approximation introduces the thermal vibrations through a convolution and, therefore, an ion with the same initial conditions will follow the same trajectory. This is physically unrealistic since the time of passage of an ion is much shorter than the vibrational period of atoms [9].

FLUX program follows the trajectories of the ions on their path along a channel, recording their (x,y,z) coordinates and velocities. Thus, the flux distribution can be obtained as a function of the transverse coordinates (x,y) and integrated over a depth z

[9]. The atomic lattice is incorporated to the program using the *XY* plane perpendicular to the direction *z*. This plane is divided into identical rectangular cells, which can be translated or reflected to generate the whole crystal. All the calculations are confined to one of these unit cells. Then, the effect of the atoms close to the unit cell is divided in two. On the one hand, the force of the surrounding atoms far from the unit cell is calculated by the continuum approximation. On the other hand, the nearby atoms are treated in the binary collision mode.

In the inner loop of the program, the trajectory is supposed to be a straight line between equidistant planes perpendicular to the string. At each plane, the particle position and velocity are updated considering: (a) the binary collisions with the central atoms, (b) the deflection due to the surrounding strings and (c) the energy loss and angular scattering due to the interaction with electrons. For each collision, the close encounter probability, the weighted average energy loss and the average energy straggling are recalculated.

The ion-atom binary collisions are treated by means of the Thomas-Fermi screened potential described in (3.2). Three types of screening functions can be used, comprising the Lindhard's potential, the Molière's potential and the universal ZBL potential. As discussed in the previous sections, the ZBL function is a good compromise for the development of calculations, so it is the most used.

The continuum force of the strings is given by the potential of the individual atoms, which is smeared out in the direction parallel to the string. Therefore, it is calculated via equation (3.1). Debye's model is assumed for thermal vibrations, so atoms have a Gaussian distribution of positions around their equilibrium position, with a mean distance u_1 given by (3.6). The convolution of the Gaussian distribution and the continuum potential (3.1) gives the thermally modified potential, which allows the calculation of the string force. Contributions of surrounding strings are added vectorially.

Probably the most complex calculation within FLUX code is the energy loss due to the collisions with the nuclei and the electrons. In particular, the interaction with the nuclei is treated in the binary collision model, but the modeling of the energy loss with the electrons is more complicated. Fortunately, FLUX program incorporates satellite codes facilitating this work, dividing the contribution in two terms: for inner shell electrons

and for outer shell electrons. The exact details of the analytical calculation can be found in reference [9].

After the calculation of all the interactions of the particles, the program gives the normalized yield as the main output parameter. This yield is obtained at each depth using the close encounter probabilities averaged over all the trajectories [8, 9] and normalized to the random probability. This parameter is directly dependent on the area per atom viewed by the beam of ions, which is determined during each step of the simulation. Thus, angular scans are derived from the close encounter probability for different angles. This probability, of course, is also affected by the election of the vibrational amplitudes, so it is important to fix realistic values of u_1, as discussed later on.

3.3.2. Physical parameters for FLUX simulations

The first point to establish in the MC simulations is the lattice structure. FLUX reduces the calculations to one unit cell, considering the neighbors in a different way depending on the distance. Figure 3.8 shows the unit cells of a wurtzite crystal for two different axes. In the <0001> direction, the unit cell (in blue) is very simple, containing just one Ga and one N atom (numbers 1 and 2). The first neighbors (3 and 4) are used for the binary collisions, while the second ones (5-8) are treated in the continuum approximation. Thus, a total number of 8 atoms are considered for the calculations. The $< \bar{2}113 >$ axis requires more atoms (28). The unit cell contains 4 atoms (1 to 4), the first neighbors are 12 (5-16) and the surrounding atoms are 12 (17-28). For the simulations, the incident beam is randomly distributed over the unit cell so channeling effects are not assumed *a priori*.

Once the lattice for the simulations is established, FLUX requires a set of physical parameters. In the case of a general HS, these variables are: beam energy and divergence, layer structure (elements, composition and thickness), lattice parameters and vibrational amplitude of the atoms (or Debye temperature), weighted stopping power for valence and core electrons (these values are provided by other programs called DEDX and DETTMANN), distribution of atoms (uniform, Gaussian…), cross section (Rutherford or not), rotation and translation matrix between the layers, number of ions (dose) for the simulation, and the set of incident angles.

Note that most of the parameters, as the layer structure, are directly known from RBS experiments. The most difficult quantity to know in the case of GaN or ZnO is the vibrational amplitude, since the Debye temperature is under debate [17]. In addition, the Debye temperature is defined for a compound, but the FLUX program can incorporate the vibration of each individual atom, which requires further approximations. Consequently, this parameter is usually fitted with the angular scans. Actually, the exact fitting of the crystal quality is made through the vibrational amplitude, since both magnitudes χ_{min} and u_1, are intimately connected via equation (3.7). Following the work of Lorenz *et al.* [20], in this thesis the assumed vibration amplitudes u_2 are 0.008 nm (Al), 0.011 nm (Ga), 0.013 nm (In) and 0.009 nm (N). Values for Al and Ga were extracted from the current literature [21, 22], while the other ones were determined from the best fit with the data.

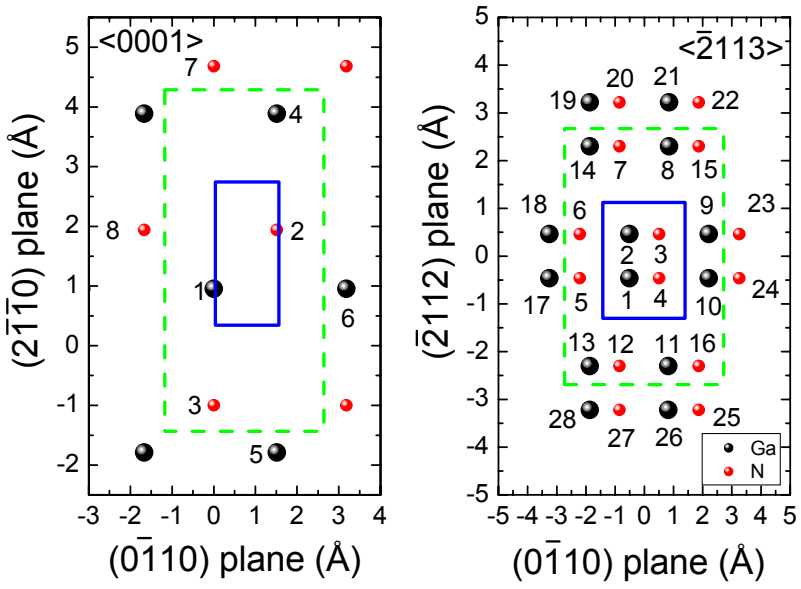

Figure 3.8 Projections of the wurtzite lattice along the <0001> and the < $\bar{2}$113 > axes. Unit cells for FLUX simulations of channeling are marked in blue. The atoms inside the green dashed border are considered in the binary collision approximation, whereas the atoms outside are used in the continuum mode.

For the analysis of the strain state in HSs, a rotation matrix is needed. This matrix relates the angular difference between the substrate and the film, so it introduces the kink angle (see section 2.4.1) in a natural way. The MC simulations of angular scans in HSs close to lattice-matched conditions are very useful to determine the strain state

accurately because, as it will be shown in the next chapters, the input kink angle and the experimental one do not always coincide.

The total number of ions required for good statistics depends on the computational available time. In general, 10000 ions warrant a good simulation. However, in some cases, this number can be reduced to produce faster simulations. In particular, this is a good procedure for fitting the input parameters with the data before the final simulation. The angular step of the scans can be as low as wished, but again, a compromise between the accuracy and the computational time must be obtained. Since the experimental angular scans have a normal step of 0.1º, this is a reasonable value.

3.3.3. Results from FLUX

FLUX program calculates the ion trajectories directly and produces different output files for the analysis. Among the physical results given by the program, the most important parameter is the normalized yield, because it can be correlated with the experimental backscattering yield measured in the RBS/C experiments. The normalized yield depends on the spatial flux distribution (section 3.2.5) and, consequently, the predictions of the program are based on the statistical variations of the particle flux for different depths. Note that the depth and time scales are related by means of the ion velocity but, since the depth is in direct correspondence with the energy windows defined in the RBS/C spectra (see section 2.4.1), the flux distribution is integrated over it and not over time.

Figure 3.9 shows the MC calculated ion distribution (integrated over 2 μm and normalized to the maximum number of ions) in a wurtzite GaN crystal. Ga and N sites are marked, and both <0001> and $< \bar{2}113 >$ are shown (compare with Figure 3.8). As it is clear from the color scale, the ion distribution at the center of the channel is enhanced, which is the expected behavior because of the channeling effect. This feature is accompanied by a reduction of the close encounter probability and, then, associated to low χ values. On the contrary, the string positions are free of ions (white regions), representing the shadow cones created by the atoms. This lattice sites are effective scattering centers where the normalized yield rises.

The confinement of the ions in the lattice channels is accompanied by the typical oscillatory behavior discussed in the previous sections. The MC methods can also

reproduce this in-depth characteristic, as shown in Figure 3.10, where the ion density is determined as a function of the depth in a GaN crystal oriented along the <0001> axis. The highlighted single trajectories prove that ions travel from one side of the lattice to the other in the quasi-harmonic motion predicted by Lindhard's model. Thus, the explanation of the most significant processes of channeling can be developed by means of the spatial and angular coordinates of the particles [23] given by FLUX.

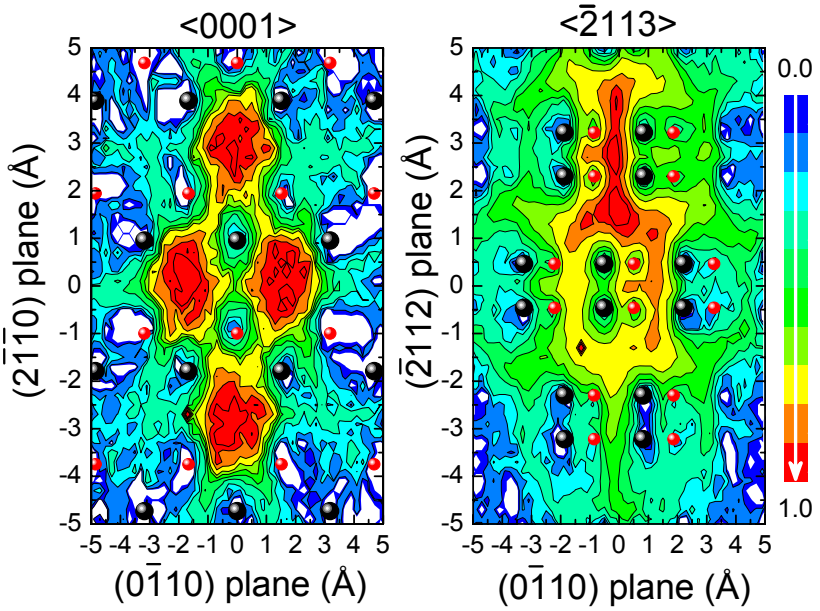

Figure 3.9 MC simulations of 2 MeV He^+ tracks for a wurtzite crystal along the <0001> and the $< \bar{2}113 >$ axes. The ion distribution is normalized to the maximum value and integrated over the 2 μm layer. Black spheres are Ga-sites while red ones are N-sites.

Since channeling is a depth-dependent phenomenon, MC predictions can help to understand several of the observables, such as the minimum yield, the half-angle or the dechanneling, in every particular situation. Indeed, some of the features of the angular scans, such as shoulders, asymmetries or double minima can contain very valuable physical information about the lattice-sites, defects or strain state. Considering the complex alignment of the crystals, these situations can be easily mistaken by experimental failures and, in this sense, MC programs are essential to understand and predict such anomalous situations. Actually, these anomalous scans have been reported in several semiconductor materials [20, 24-27], depending on the thickness or the strain state of the HSs.

Of course, the ion distribution cannot be measured in RBS/C experiments in a direct way, so the comparison with MC simulations requires the calculation of the normalized yield. As discussed in section 3.3.1, this parameter is obtained theoretically by the integration over the total number of trajectories of the close encounter probability, which can be compared with the experimental one in the angular scans. Therefore, varying the incidence angle of the beam in the MC analysis, the whole angular scan can be reproduced and compared with the experimental one.

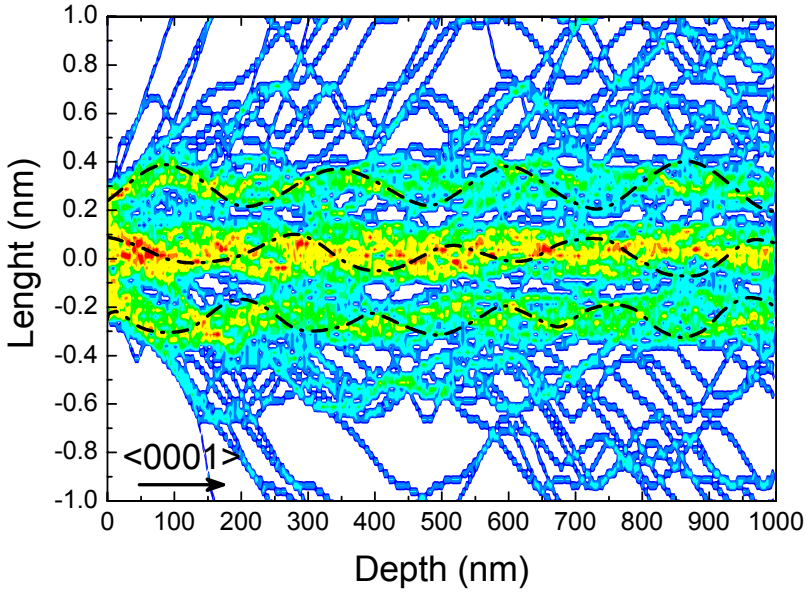

Figure 3.10 MC simulations of 100 He^+ tracks (at 2 MeV) for a wurtzite crystal along the <0001> axis. Three particular trajectories are highlighted (dashed lines), demonstrating the oscillatory behavior of ions.

As a demonstration of the accuracy of this procedure in the description of the experimental data in RBS/C, Figure 3.11 shows the FLUX simulations of angular scans along the <0001> and $<\bar{2}113>$ axes in GaN, together with the experimental results [28]. The agreement between both experiment and simulation is excellent, even for the more complicated features, as the shoulders at ±1º in the <0001> scan. The reason for those shoulders is that ions entering at angles slightly larger than $\psi_{1/2}$ have a higher probability of colliding than the average, i.e., the effective area covered by the atoms is larger than in a random configuration. For several compounds the characteristic shoulder of the dip in an oblique direction is asymmetric, because the first atoms generating the shadow cone alternate with the tilt angle [29]. Nevertheless, the presence of the shoulders is not always easy to detect if the quality of the crystal is low or the

dechanneling high. In fact, MC simulation of the $< \bar{2}113 >$ axis in Figure 3.11b shows the shoulders, but they cannot be distinguished in the experimental data.

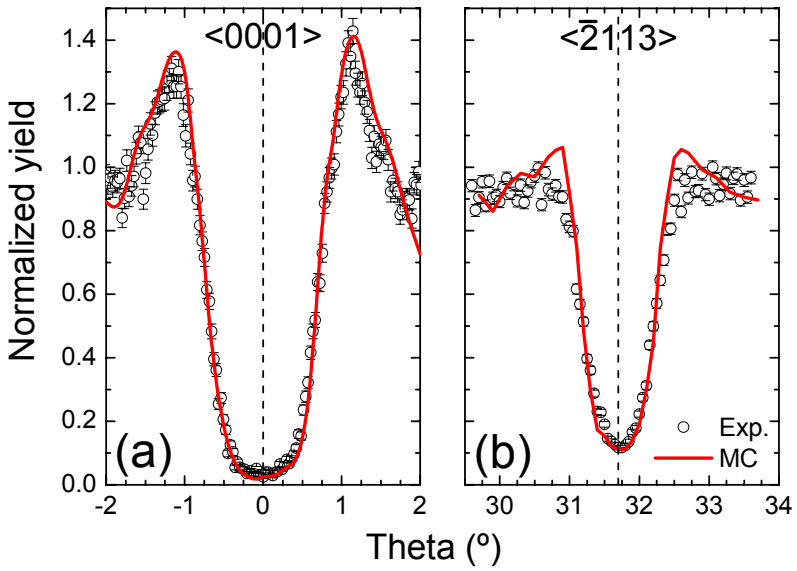

Figure 3.11 MC simulations and experimental data of <0001> and $< \bar{2}113 >$ angular scans in GaN.

Due to the effect of the shoulders (usually more pronounced when the scan is performed within the plane), the normalization of the dip is normally done some degrees out of the minimum to have a good reference of the random level. However, it is important to note that, when the scan is carried out inside a crystallographic plane (as in the strain measurements), the spectra are collected under planar channeling, and values associated to unity cannot be really considered as a random level.

In the next chapters, more particular examples of the combination of RBS/C and MC simulations will be shown in relation to the determination of the strain state in lattice-matched HSs. In all the cases, the angular scans were derived as in Figure 3.11, using the FLUX code to quantify the scattering probability at a certain depth.

3.4. References

[1] M. L. Swanson, Rep. Prog. Phys. **45**, 47 (1982).

[2] J. Lindhard, Mat. Phys. Medd. K. Dan. Vidensk. Selsk. **34**, 1 (1965).

[3] L. C. Feldman, J. W. Mayer and S. T. Picraux, *Materials analysis by ion channelling* (Academic Press, New York 1982).

[4] D. S. Gemmell, Rev. Mod. Phys. **46**, 129 (1974).

[5] J. Stark, Phys. Z. **13**, 973 (1912).

[6] G. R. Piercy, F. Brown, J.A. Davies and M. McCargo, Phys. Rev. Lett. **10**, 399 (1963).

[7] M. T. Robinson, and U.S. Oen, Phys. Rev. **132**, 2385 (1963).

[8] J. H. Barrett, Phys. Rev. B **3**, 1527 (1971).

[9] P. J. M. Smulders, and D.O. Boerma, Nucl. Instr. Meth. B **29**, 471 (1987).

[10] J. H. Barrett, Nucl. Instrum. Meth. B **44**, 367 (1990).

[11] J. R. Tesmer, M. Nastasi, *Handbook of modern ion beam material analysis* (MRS, Pittsburg, 1995).

[12] B. H. Bransden, and C.J. Joachain, *Physics of atoms and molecules* (Longman, London, 1983).

[13] G. Molière, Z. Naturforsch. A **2**, 133 (1947).

[14] J. F. Ziegler, J.P. Biersack and U. Littmark *The stopping and range of ions in solids* (Pergamon Press, New York, 1985).

[15] M. Nastasi, J.W. Mayer, J.K. Hirvonen, *Ion-solid interactions: fundamentals and applications* (Cambridge University Press, Cambridge, 1996).

[16] R. C. Bird, J.S. Williams, *Ion beams for materials analysis* (Academic Press, London, 1989).

[17] C. Roder, S. Einfeldt, S. Figge, and D. Hommel, Phys. Rev. B **72**, 085218 (2005).

[18] E. Kótai, Nucl. Instrum. Meth. B **85**, 588 (1994).

[19] J. H. Barrett, Phys. Rev. Lett. **31**, 1542 (1973).

[20] K. Lorenz, N. Franco, E. Alves, I.M. Watson, R.W. Martin and K.P. O'Donnell, Phys. Rev. Lett. **97**, 85501 (2006).

[21] E. Gabe, Y. Le Page and S.L. Mair, Phys. Rev. B **24**, 5634 (1981).

[22] A. Yoshiasa, K. Koto, H. Maeda and T. Ishii, Japan J. Appl. Phys. **36**, 781 (1997).

[23] M. B. H. Breese, D.G. de Kerckhove, P.J.M. Smulders and D.N. Jamieson, Nucl. Instr. Meth. B **159**, 248 (1999).

[24] A. Redondo-Cubero, K. Lorenz, R. Gago, N. Franco, S. Fernández-Garrido, P. J. M. Smulders, E. Muñoz, E. Calleja, I. M. Watson and E. Alves, Appl .Phys. Lett. **95**, 051921 (2009).

[25] C. Wu, S. Yin, J. Zhang, G. Xiao, J. Liu and P. Zhu, J. Appl. Phys. **68**, 2100 (1990).

[26] G. M. Cohen, D. Ritter, V. Richter and R. Kalish, Appl. Phys. Lett. **74**, 43 (1999).

[27] T. Matsushita, W. Sakai, K. Nakajima, M. Suzuki, K.Kimura, A. Agarwal, H.-J. Gossmann, M. Ameen and H. Harimac, Nucl. Instr. Meth. B **249**, 432 (2006).

[28] V. Tasco, A. Campa, I. Tarantini and A. Passaseo, F. González-Posada, A. Redondo-Cubero, K. Lorenz, N. Franco and E. Muñoz, J. Appl. Phys. (2009).

[29] T. Haga, H. Suzuki, M.H. Rashid, Y. Abe and A. Tanaka, Appl .Phys. Lett. **52**, 200 (1988).

4

Analysis of GaN and ZnO base layers

The first element of a WBS HS is always a base layer, so its properties are relevant to reduce the imperfections in the upper films. Here, two different effects affecting the epitaxial growth and crystal quality of base layers are analyzed. First, the importance of the nucleation layers, used to alleviate the lattice mismatch of GaN with sapphire, is investigated. In second place, the influence of the growth temperature in the production of high-quality ZnO films is determined.

In science "fact" can only mean "confirmed to such a degree that it would be perverse to withhold provisional consent". I suppose that apples might start to rise tomorrow, but the possibility does not merit equal time in physics classrooms. (Stephen Jay Gould)

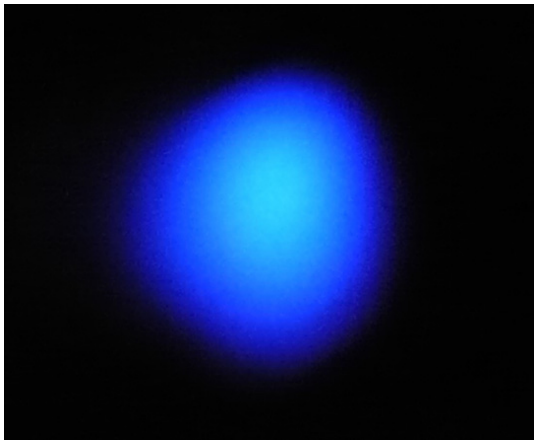

Ionoluminiscence of ZnO obtained during a RBS experiment of this thesis.

4.1. Introduction

Base layers are the main pillars for building a semiconductor HSs, so their quality is a critical factor for the subsequent crystal growth of the upper layers and the performance of the device. This is even more critical in the case of GaN and ZnO based devices, since they are normally grown on sapphire wafers, with a great lattice-mismatch of ~13% (see chapter 1). Indeed, the defects originated in the base layers can be transmitted to the surface, being sometimes more important than the intrinsic defects of the top layers [1]. Consequently, the development of high-quality WBS HSs depends, to a large extend, on the optimization of the base layers.

As discussed in chapter 1, one of the points restricting the capacities of MO-CVD GaN is the need of adapting the lattice parameters of GaN and sapphire [2]. This transition is enhanced by means of an intermediate buffer or nucleation layer (NL), which allows the rearrangement of the lattice avoiding defects as twisting, tilting and prismatic growth of GaN [3]. This fact was early recognized by Amano *et al.*, who demonstrated the benefits of a thin AlN NL [4, 5]. However, other groups introduced the use of a low temperature GaN NL [6] instead of an AlN one, and some recent works have even suggested the use of double or multi-buffer layers to grow high-quality GaN-based compounds [7]. The initial stages in the growth of the base layer are decisive for the development of 2D (layer-by-layer), 3D (island growth) or mixed modes, which determine in a great way the final quality of the base layer. Nowadays, commercial GaN templates still exhibit high dislocation densities (~10^9 cm^{-2}), so further improvements are needed. Due to the technological relevance of this issue, both AlN and GaN NLs will be investigated in detail during this chapter, analyzing their effects on the growth mode and the crystallinity of the GaN layers of the HS.

In the case of the growth of ZnO on sapphire, some NLs can be used (MgO, NiO, etc.) prior to the deposition of the layer, but quite frequently it is grown without any buffer layer [8], just using a surface pretreatment of the substrate. This latter situation is normally associated with a 3D growth of the layer [8], which affects the morphology and the crystal quality of the layers. As a result of this, the main parameter determining the epitaxial growth of ZnO base layers is the substrate temperature. This variable can control the mobility of the adatoms and it is crucial for the incorporation of the elements

into the crystal lattice. Regarding this point, the growth of ZnO epilayers at low temperatures (T<600 ºC) has been recently demonstrated by PMS (see chapter 2) [9]. This method normally provides worse crystal quality than conventional MBE or CVD systems, but its low cost and high growth rates make this approach very promising for future applications. In consequence, along this chapter the influence of the substrate temperature will be evaluated for ZnO layers grown by PMS.

4.2. Effect of the nucleation layers in the growth of GaN

Despite some groups have demonstrated the feasibility of bulk GaN crystals [10], the use of self-standing GaN substrates is still rare. The most frequent GaN growth is carried out by MO-CVD on other substrates such as sapphire. As mentioned, due to the large mismatch of these materials with GaN, the dislocation density and the in-plane stress is high, representing a limit for the performance of GaN-based devices [11].

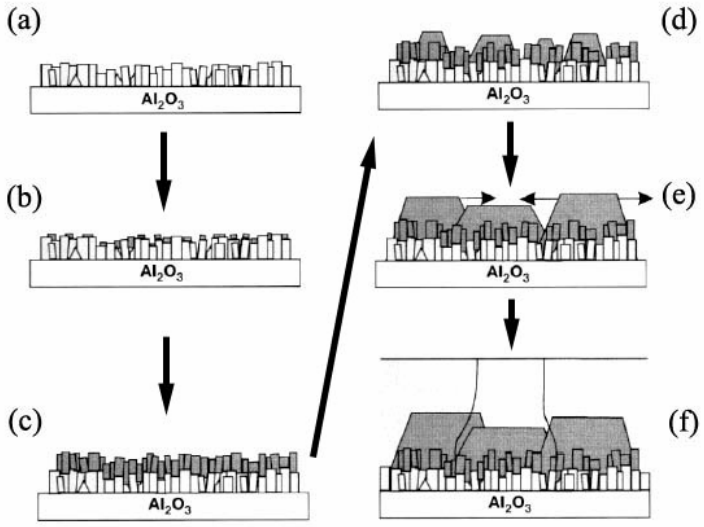

Figure 4.1 Model for the growth of GaN on a NL. Six steps are distinguished: (a) buffer layer deposition, (b) GaN nucleation, (c) geometric selection, (d) island growth, (e) lateral growth and (f) uniform growth. Adapted from [5].

The growth of GaN layers has different steps (Figure 4.1) and, depending on the growth conditions of the NL (rate, III/V ratio, pressure, temperature), the surface morphology and the structural quality of the GaN final layer can be modified [12]. Therefore, it is very important to understand the origin of the different results obtained when using AlN or GaN NL. Furthermore, considering the large variety of buffer layers currently used in

different HSs, it is important to establish a common procedure to assure high-quality layers.

In order to clarify the debate between the AlN and the GaN NL, a set of six samples was prepared and analyzed by IBA [13]. All epitaxial films were grown by MO-CVD on (0001) sapphire substrates (see section 2.2.1 for details). A 100 nm-thick AlN NL was directly grown on the substrate at 1150°C, followed by 300 nm of GaN grown at the same temperature. Direct comparison of these samples was done with GaN epilayers of the same thickness, but grown on conventional 50 nm-thick GaN NL deposited at low temperature (560 °C) and then annealed at 1100 °C for ten minutes before GaN epilayer deposition (300 nm). In the following, the discussion will be focused only in two samples, selected as prototypes of each series of samples, although all of them were analyzed.

The morphological evolution of the layers, studied by atomic force microscopy (AFM), shows a different behavior of the NLs (Figure 4.2). The surface morphology of the AlN NL (Figure 4.2a) reveals a high density of uniform and small grains with a diameter of about 50 nm and a height of 20 nm. Conversely, larger grains with wide size dispersion (diameter of the order of 1 μm and height of the order of 100 nm) characterize the GaN NL after annealing (Figure 4.2b). These particular surface features correspond to the first stages (a-c in Figure 4.1) of the growth, which take place in a different way for each NL.

Apart from these initial differences, AFM also confirms that, after the deposition of ~10 nm, the AlN NL induces a fast coalescence of the overgrown GaN islands (Figure 4.1d). As the growth proceeds up to 50 nm, the complete reconstruction of GaN layer occurs, leading to a continuous film with an atomic step morphology and smooth surface (Figure 4.1e). Only some voids can be observed on such surface, and the very low density of these features (10^7 cm^{-2}) can be considered as a fingerprint of the high rate of the lateral GaN growth on AlN NL (Figure 4.1f). For the thickness of 300 nm the 2D morphology is further improved for the AlN NL sample, where randomly oriented atomic steps can be observed, suggesting a step flow growth mode, with a roughness of only 0.3 nm (Figure 4.2c).

In opposition, a completely different morphology results from 300 nm GaN on GaN NL (Figure 4.2d). In this case, the increased coverage of GaN induces only an increase of the island lateral size up to some microns with a height of 80 nm. The complete island coalescence observed on the AlN NL is not promoted in this case, unless a deposition as thick as 600 nm is performed. The correlation between these changes and the structural quality of the base layers was analyzed in detail, and it is explained in the next section.

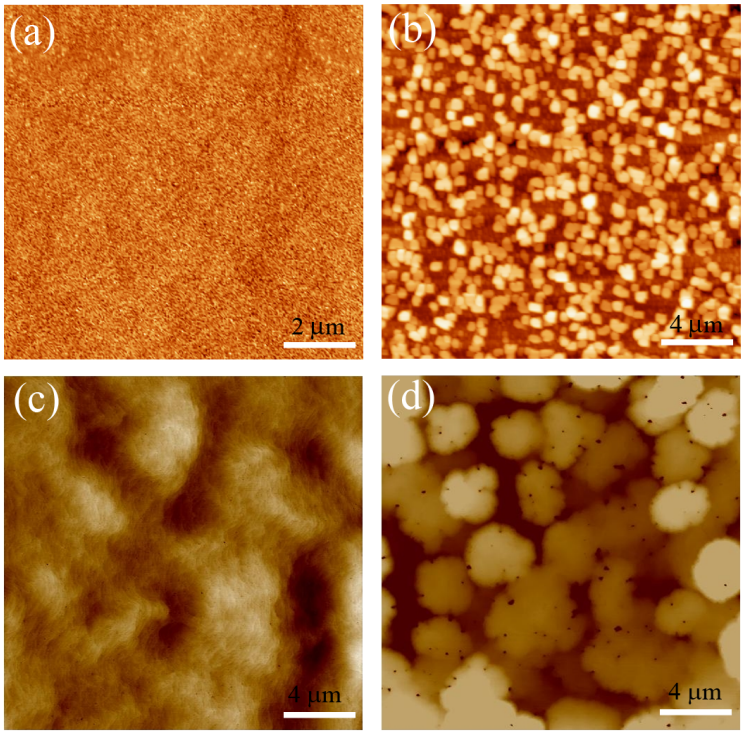

Figure 4.2 AFM images of as grown (a) AlN NL (z scale 25 nm) and (b) GaN NL (z scale 450 nm). The surface of the final GaN layer is also shown with (c) AlN NL (z scale 10 nm) and (d) GaN NL (z scale 55 nm). A different morphology and roughness is observed. Courtesy of F. González-Posada and V. Tasco [13].

4.2.1. Structural characterization of base layers with different NLs

The structural evolution of the base layers was assessed by a comparative HR-XRD and RBS/C study (see section 2.4 for experimental details). Reciprocal space maps (RSMs) in both symmetric (0004) and asymmetric $(10\bar{1}5)$ reflections were investigated (Figure 4.3). The first remarkable feature of the (0004) RSMs is the broad peak of the GaN layer when a GaN NL is used. Indeed, the sample grown on AlN NL can be fitted by means of a Lorentzian function, but the sample with a GaN NL only fits accurately to a Gaussian function. In addition, the FWHM is 8 times higher for the GaN NL than for the samples with an AlN NL. Generally, the elongation along the Q_x-axis in symmetric

reflections is attributed to crystallographic blocks with smaller lateral sizes and higher out-of-plane misorientation (tilt) [14]. Therefore, the Lorentzian shape of the (0004) reflection in Figure 4.3a could mean a narrower distribution of the block orientations in the mosaic structure of GaN samples grown on AlN NL. However, since RSMs are acquired around the GaN reflection, the large differences between both samples might be due to the contribution of the disordered GaN NL, which is not present in the sample grown on the AlN NL. Therefore, this point will be further analyzed by RBS/C experiments and discussed later on.

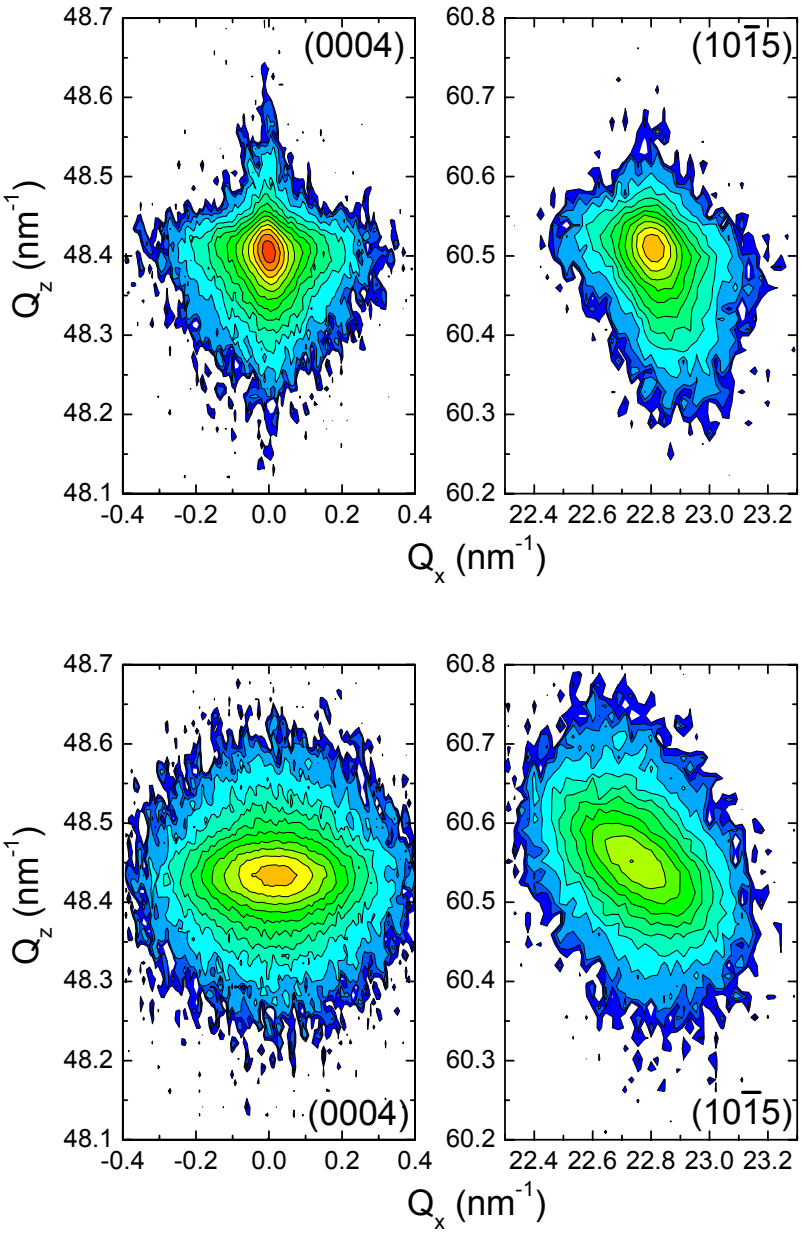

Figure 4.3 RSMs along the (0004) and the (10$\bar{1}$5) reflections of GaN layers grown on (a-b) AlN nucleation layer and (c-d) GaN nucleation layer.

Concerning the $(10\bar{1}5)$ reflection, a clear tilt is visible in both samples, but it is more pronounced in the GaN NL. In asymmetric reflections, the mosaic tilt and lateral coherence induce both an elongation and a rotation of the RSM in the Q_x-axis [15]. The different intensity distribution along Q_z-axis can be ascribed to the strain influence. For the sample with a GaN NL, the higher symmetry of the intensity contours around the $(10\bar{1}5)$ reciprocal lattice point indicates the absence of large scale strain gradients along the growth direction (i.e. a nearly constant strain state) and a rather statistical distribution of mosaic blocks. Conversely, for the sample with AlN NL, the GaN layer follows a strained pseudomorphic growth as a consequence of a partially relaxed NL. This point was further confirmed by XRD simulations of $\omega/2\theta$ curves, where the AlN NL was found to have a relaxation coefficient lower than 1, indicating the presence of strain.

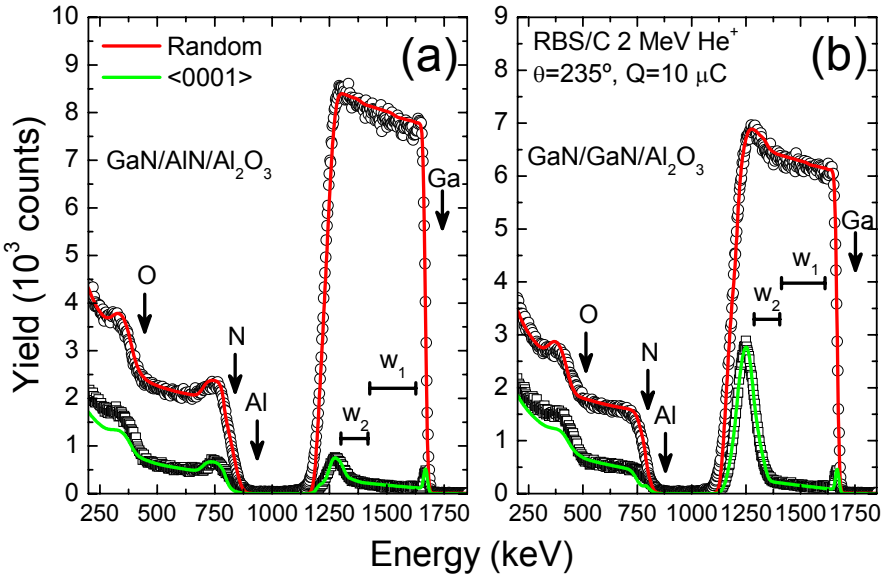

Figure 4.4 Random and <0001> aligned RBS spectra of GaN layers grown on (a) AlN nucleation layer and (b) GaN nucleation layer.

RBS/C measurements were performed on the samples at 2 MeV to complement the HR-XRD analysis. Figure 4.4 shows the random and <0001> aligned spectra of samples grown with AlN (a) and GaN (b) NL. The RBX simulation is also shown. The increase of the Al signal for energies between 670 and 800 keV is clearly visible in the spectrum (a), corresponding to the 100 nm AlN NL. Both samples were simulated with a stoichiometric nitride, except for a slight Ga-rich region at the interface of sample (b).

Two regions of interest were established, corresponding to energy windows w_1 (1351-1640 keV) and w_2 (1100-1350 keV). These windows can be related to the surface (~50 nm) and buried GaN (~250 nm), respectively. The selection of the interval for w_2 was made in order to prevent overlapping of Ga signals from NL and GaN film in the analysis. This situation could only take place for GaN NL, but selecting w_2 ~100 nm far away from the interface with sapphire, the possible influence of defects from the NL can be neglected. Therefore, with RBS/C the restrictions of HR-XRD analysis can be overcome, and one can select an exact depth range for the analysis of the crystal quality.

The minimum yield of the samples was determined for the Ga signal close to the surface (w_1). The results show χ_{min}=1.72(4)% for the sample with the AlN NL and χ_{min}=2.13(5)% for the GaN NL. These values are comparable to commercial GaN templates [16], but they evidence only slight differences between the two samples in w_1. Consequently, the minimum yields in w_1 do not explain the results obtained in HR-XRD (i.e., the large change in the FWHM).

Further analysis of w_1 and w_2 energy windows was developed using the angular scans (Figure 4.5). The <0001> dips confirm the similar behavior in w_1 for both NLs. However, a substantial difference was found between both samples when χ_{min} is determined in w_2. In such case, the results show χ_{min}=6.81(6) % for the sample with AlN NL, and χ_{min} =21.8(1) % for the sample with GaN NL. As w_2 was placed 100 nm far away from the interface with sapphire, the difference in χ_{min} (by a factor ~3) can be directly ascribed to higher defect density in sample (b). The RBX simulation also shows a considerable increase of dechanneling in the w_2 region, which is 10 times higher than for w_1. This could be interpreted as a consequence of the confinement of defects in the first 50 nm of GaN. Actually, AFM measurements suggested a columnar growth via not completely coalesced islands for samples with GaN NL, and the observed deviation can be understood because of the higher mosaicity, also in agreement with HR-XRD data. Indeed, the steering of ions through crystal axes is very sensitive to the critical angle (see chapter 3). Then, the different tilt angles of GaN columns will contribute to an increase of dechanneling compared with the continuous 2D film obtained on AlN NL.

As in the <0001> axis, the $< \bar{2}113 >$ dips show no differences in w_1, confirming the similar quality of the samples in the near surface region. On the contrary, a clear asymmetry is visible in the dip of w_2 for both samples. This asymmetry can be

considered as a sign of strain or misorientation in the first stages of the GaN growth. Monte Carlo simulations with FLUX show, indeed, that a GaN interface with a kink angle of ~0.3º would produce asymmetric features in the $< \bar{2}113 >$ dip. Nevertheless, AFM images suggest mixed effects, not only due to strain, but also caused by the grain size and the mosaic tilt in the first stages of the GaN growth. The higher sensitivity of HR-XRD to these phenomena may explain the difference in the $(10\bar{1}5)$ RSMs of both samples, which is not resolved in the dips of w_2.

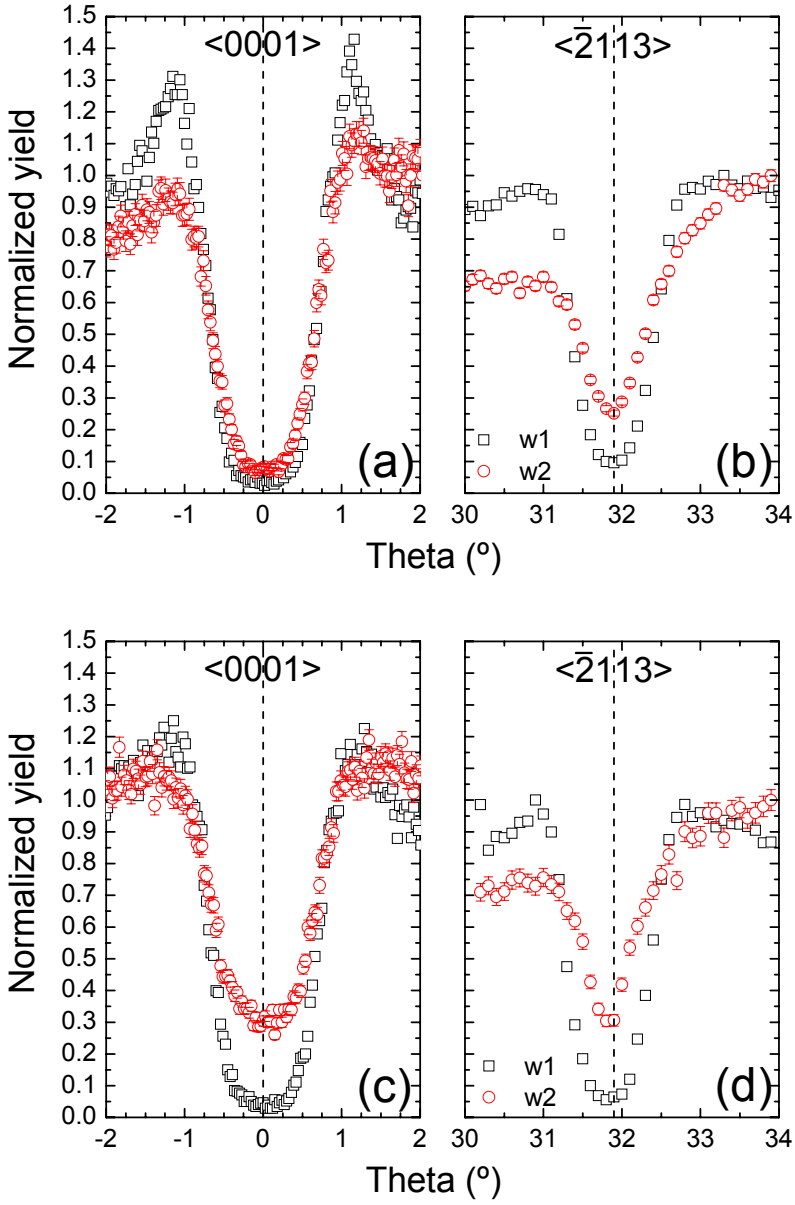

Figure 4.5 Angular scans along the <0001> and $< \bar{2}113 >$ axes for GaN layers grown on (a-b) AlN nucleation layer and (c-d) GaN nucleation layer. Two energy windows are analyzed, one at the surface and one at the interface.

Therefore, the described differences could be interpreted as different surface dynamics experienced by the growing species on the two different NLs. On AlN, because of the high density of small nuclei (with diameter of 50 nm), the impinging adatoms have enough mobility to promote a fast lateral growth (2D). Moreover, in this case their diffusion length is much longer (in the μm range) [17] than the island sizes. This fact is reinforced by the high strain field generated at the AlN/GaN interface and the high binding energy of AlN, which further enhance Ga adatom mobility, leading to a faster lateral coalescence [18]. Thus, the accommodation of the GaN layer is faster, being the number of the defects at the interface lower (as RBS/C and HR-XRD show). For the GaN NL, the defect density is higher at the interface (see the peak in the RBS/C spectrum), associated with a growth based on mosaic blocks. However, this growth mode at later stages of the deposition seems to reduce the crystal quality at the surface only slightly, as compared to AlN NLs.

4.2.2. Effect of the incorporation of light impurities (C and O)

As a final test, the possible influence of the NL on the presence of impurities was evaluated. This point is relevant because oxygen out-diffusion from sapphire might occur at the high growth temperatures used, allowing the incorporation in the GaN layer. This depends on the diffusion barrier effect of the NL, which could show different behaviors in AlN and GaN NLs. RBS experiments for the depth-resolved detection of O were performed to verify this. The incorporation of impurities could also be responsible for the structural changes discussed before, so it is important to confirm or discard this hypothesis. Additionally, the presence of C was also investigated, since this is a common impurity in MO-CVD systems due to the use of organic precursor gases for the growth.

To develop these studies, two GaN samples were selected: one on AlN NL and one on GaN NL. Of course, since both C and O are light elements with a (expected) low concentration, their detection is difficult by conventional RBS measurements with He^+ ions at 2 MeV. A common way to overcome this limitation is the use of specific beam energies where these elements have a non-Rutherford cross section at certain angles (see chapter 2 about resonances in RBS). Taking advantage of these phenomena, the presence of small amounts of O and C can be detected with higher sensitivity by RBS.

In the experiments, the 3035 keV resonance (at a scattering angle of 170º) for O [19] and the 4265 keV resonance (at 170º) for C [20] were chosen. In the first case, the cross-section is 24 times higher than Rutherford's, whereas for C the situation is even better: 128 times higher than given by Rutherford's formula (see Figure 2.3). Since the resonances only take place in a very narrow energy window, the depth-resolved compositional analysis can be carried out by changing the probing energy in certain steps. Thus, the resonance peak shifts as the energy increases, and its intensity gives information about any compositional profile.

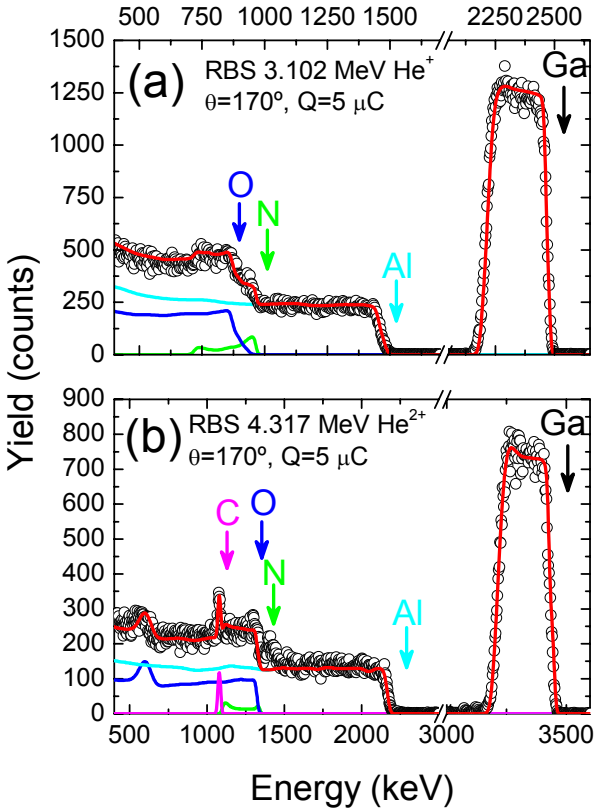

Figure 4.6 RBS spectra of GaN with a GaN NL for two different energies.

The election of the energy steps was made considering the thickness of the sample and the energy loss. From previous RBS/C experiments, the thickness of the samples (~300 nm) is known. Then, a total number of 6 points for the analysis (each of 60 nm) was assumed. The energy loss was calculated using the SRIM code [21] for an incoming He beam of 3.035 MeV and 4.266 MeV on GaN. The obtained energy loss is 0.3732 keV/nm (for O) and 0.3142 keV/nm (for C). Therefore, to measure the 6 points selected, the beam energy has to be changed in steps of 22.4 keV (O) and 18.8 keV (C). It is

important to note that the FWHM of the resonances are ~13 keV (O) and ~33 keV (C), so they cover about 35 nm and 105 nm, respectively.

As an example of the obtained spectra, Figure 4.6 shows two RBS spectra of the same GaN sample (with a GaN NL) at different energies. The first spectrum (a) was acquired at 3102 keV, what corresponds to a depth of 180 nm for the maximum of the resonance. Ga, Al, N and O signals are clearly visible in the spectrum, but no peak related with O at ~180 nm is visible, indicating that the concentration is under the detection limit. Therefore, the experimental data were well-fitted with a GaN/Al_2O_3 structure. The second spectrum (b) was acquired at 4317 keV, also corresponding to 180 nm depth. In this case a clear peak corresponding to C appears in the spectrum. However, the simulation demonstrates that this peak is related to the surface contamination and not to the presence of C at ~180 nm. Then, as in the previous case, the C concentration at the selected depth is under the detection limit.

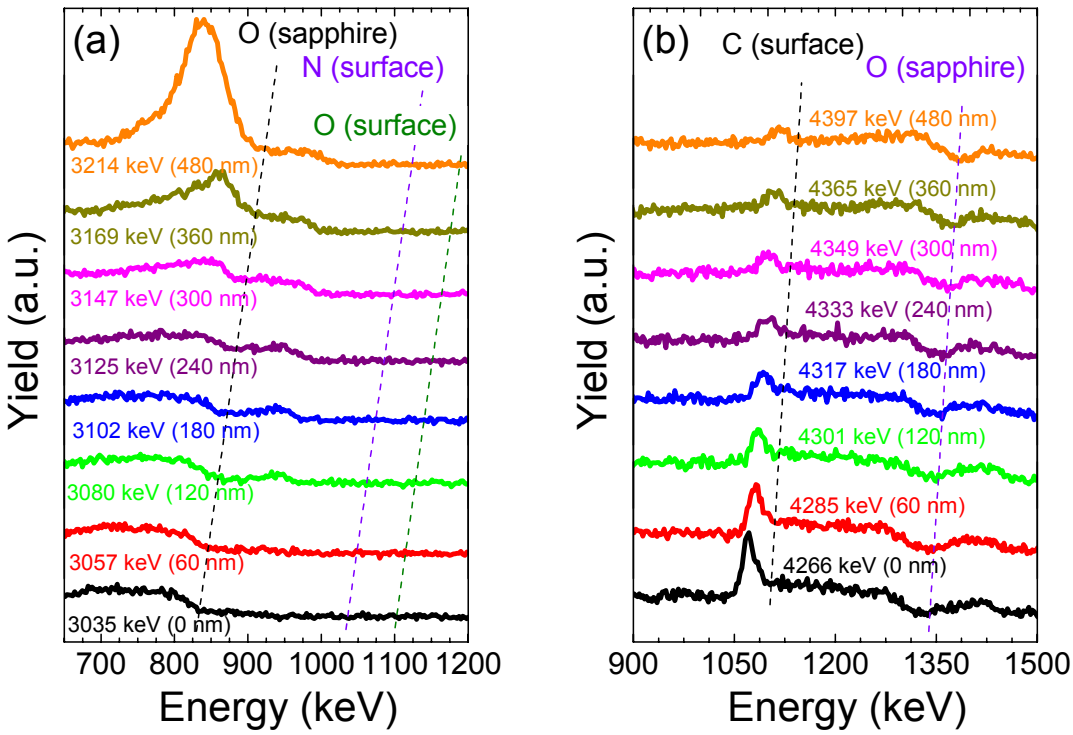

Figure 4.7 RBS spectra at different energies for the depth-resolved analysis of O (a) and C (b) in a GaN base layer with an AlN NL.

The absence of in-depth contamination due to C or O was further checked using different energies. Figure 4.7 shows the regions of interest of the RBS spectra in the

sample with the AlN NL. The starting energy was 3035 keV for O detection (Figure 4.7a), corresponding to the surface of the sample. No O signal was detected at such energy and even at higher energies, up to 3147 keV. At this value, the interface with the sapphire begins to be visible in the spectrum (at ~850 keV), and the resonance becomes more and more intense. However, the lack of any peak at energies below 3147 keV demonstrates the low or negligible presence of O in the film. Similar results were found with the sample containing a GaN NL (not shown here). Further studies of the simulations confirm that the detection limit in these conditions is 1 % or even lower, so it can be stated that O concentration is below this value.

Regarding C experiments (Figure 4.7b), the starting energy was 4266 keV. In this case, a clear peak was detected in the spectrum, revealing the presence of C at the surface (~1070 keV) of the sample. This kind of contamination is frequent due to the organic cleaning and the ambient exposure of the samples. However, the peak does not shift towards lower energies as the impinging energy (terminal voltage) increases. On the contrary, the surface peak just decreases because the resonance becomes less intense at the surface. Therefore, the lack of a clear signal in the spectra at low energies proves that C is not being incorporated deep into the GaN layer, at least above the detection limit of the technique. This fact was also verified in the sample with a GaN NL. The simulations establish a detection limit lower than 0.5 % for C, since the sensitivity of the C resonance is higher than the one for O. As a result of these data, the presence of impurities as O and C in the GaN base layer can be ruled out, confirming that diffusion mechanisms seem to play no role in the structural changes found by HR-XRD and RBS/C.

4.3. Effect of the substrate temperature in the growth of ZnO

As in the case of GaN, the growth of ZnO bulk crystals is complex because of the high vapor pressure required [22]. Therefore, the heteroepitaxy on sapphire is quite frequently the conventional way of growing ZnO. One of the advantages of ZnO over GaN is the possible growth by pulsed magnetron sputtering (PMS) due to the availability of proper targets. This kind of growth system has not been generally considered in the scientific community for the epitaxial growth, but the achievement of ZnO epilayers by this method has been recently demonstrated [9]. The influence of the

energetic particles in PMS processes represents a significant advantage over other methods as MBE or CVD because it allows non-equilibrium growth conditions. As a result, the crystal ordering can be induced at lower temperatures than in MBE or CVD (>700 ºC) [9]. However, as in the case of GaN, the large lattice mismatch between sapphire and ZnO makes the growth difficult. Therefore, to avoid multiple-domain layers and to mitigate the presence of dislocations, pretreatments of the substrate surface are often used, in combination with moderate substrate temperatures (<700 ºC) during the growth. Here, the temperature dependence of the PMS epitaxial growth of ZnO is evaluated to understand the mechanisms affecting the crystal quality and texture of the layers.

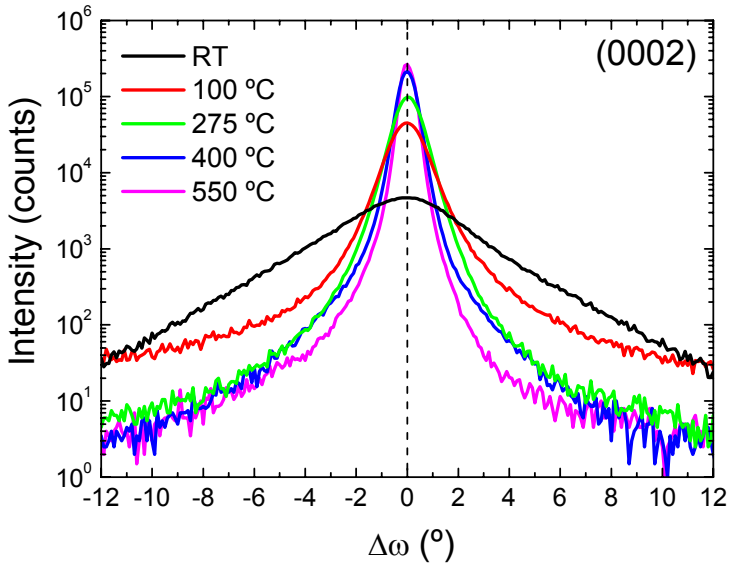

Figure 4.8 XRD ω-RCs in the (0002) plane. FWHM decreases with temperature indicating the better crystal quality. Data are courtesy of M. Vinnichenko.

For the systematic study of the temperature influence, a series of five ZnO samples was grown by PMS. The general experimental set-up of the system was already described in section 2.2.3. The samples were grown using a mixture of Ar ($8 \cdot 10^{-3}$ mbar) and O_2 ($1.4 \cdot 10^{-4}$-$3.4 \cdot 10^{-3}$ mbar) gas, up to a nominal thickness of 350-500 nm. Prior to the deposition, the surface of the substrate was treated with a RF O_2 plasma. The only modified parameter in this series was the substrate temperature (T), changed from RT to 550ºC. Higher temperatures were not applied because of limitations in the heater stage of the sample holder.

The first characterization of the crystal quality was carried out by means of XRD using a D8 diffractrometer (see section 2.4.2 and reference [9] for more details). Figure 4.8 shows ω-RCs along the (0002) plane for different temperatures. It is clear that the FWHM decreases with the growth temperature, and the peak shape evolves towards a Lorentzian function. The RCs were measured along four different in-plane substrate orientations and averaged to obtain a precise value. The FWHM at RT is as high as 4.157º, but it is rapidly falling to 1.181º at 100ºC, and reaches the minimum value at 550ºC (FWHM=0.366º) [9]. This trend confirms the increasing crystal quality with T. Further φ-scans in the $(10\bar{1}5)$ plane showed six strong peaks separated by 60º in all the samples, confirming the single-domain character of the layers [9].

In order to analyze the in-depth composition and crystal quality of ZnO layers, XRD results were complemented with RBS/C experiments at CMAM. The spectra were collected using a 3.035 MeV He^+ beam to increase the sensitivity to O thanks to the non-Rutherford cross-section (see previous section and chapter 2). Figure 4.9 shows the RBS/C spectra of two samples grown at 275 ºC and 550 ºC, together with the RBX simulations. Both samples were simulated with a stoichiometric ZnO layer with a very similar thickness. However, the sample grown at 550 ºC shows a non-abrupt interface with sapphire substrate, in comparison with the one at 275 ºC. This fact is evidenced by the slight tail in the Zn signal at large depths (around ~2000 keV). The RBX simulation shows that this effect corresponds to the Al-Zn interdiffusion at the interface, possibly induced by the high substrate temperature. This hypothesis is further confirmed by the measurements of samples grown with T>400 ºC, where the Al diffusion is still visible in the RBS spectra but it does not appear in the rest of the samples. Therefore, this process seems to be limited by the growth temperature, with a threshold between 300-400 ºC.

Regarding the crystal quality, the <0001> aligned spectra show a clear decrease in χ_{min} with temperature, being the lowest value obtained at 550 ºC (χ_{min}~19%). This trend is almost linear for T>100ºC, in perfect correspondence with the observed behavior of the FWHM in XRD scans. In addition, at T=550ºC (and 400 ºC) the dechanneling is increasing with depth, but it keeps almost constant for the sample grown at 275 ºC. This indicates a certain saturation of defects at low temperatures, which is consistent with the high minimum yield obtained (χ_{min}~69%). Figure 4.10 compares both parameters as a function of the temperature showing the clear correlation between them. Nevertheless,

despite the enhancement of the epitaxial growth, the results at 550 ºC are still far from the data obtained in bulk ZnO crystals (χ_{min}=2.8 % at this energy). Following the linear fitting of the data, the expected substrate temperature allowing a χ_{min}<4% (FWHM<0.25º) is ~650 ºC. As commented before, this temperature was not accessible due to technical restrictions of the system.

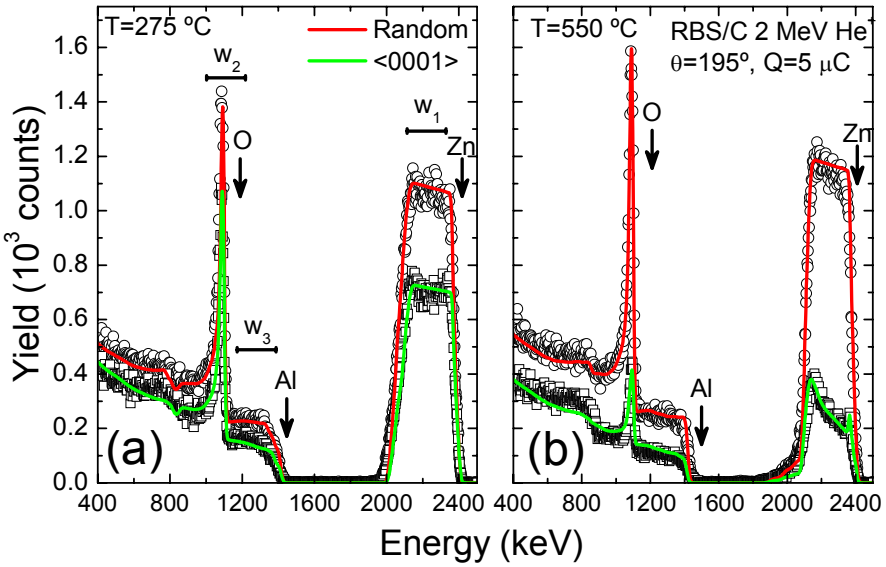

Figure 4.9 RBS spectra of two ZnO samples grown at (a) 275 ºC and (b) 550 ºC.

An important remark is the potential effect of Al diffusion on the crystal quality at high temperatures. In particular, samples grown at 550 ºC and 400 ºC show no channeling at the interface with sapphire (energies close to 2000 keV in Figure 4.9b), what reveals an amorphous or polycrystalline structure of the ZnO near the interface. Because the diffusion of Al at higher *T* can be significantly larger, this kind of mechanisms could influence the crystal quality during the growth of thin ZnO films for HSs.

Two energy windows were selected in the RBS/C spectra (see Figure 4.9), related with Zn (w_1) and O (w_2) signals. These windows were analyzed in angular scans along the <0001> axis. The O signal is overlapping with the Al one (from sapphire) in the RBS spectra, so its integration can be affected by the Al content. However, the O resonance makes the yield of O significantly higher than the Al one in w_2. Taking advantage of this fact, the O dip can be obtained by subtracting the Al background. This background is calculated in every point of the scan from w_3 (see Figure 4.9), placed before the O

surface signal and with the same width as w_2. The Al signal in w_3 is constant, so the variations due to the extrapolation in w_2 are supposed to be small. Both signals, from w_2 (O+Al) and w_3 (Al), are subtracted to determine the yield associated to O, which is normalized for the dip. Nevertheless, it has to be noted that, due to the narrow resonance, only the shallowest O signal can be analyzed.

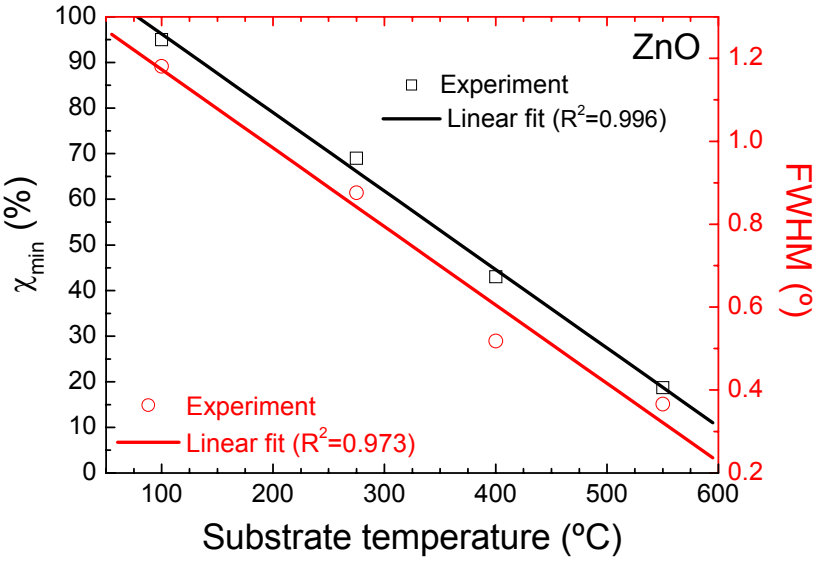

Figure 4.10 Comparison of χ_{min} and FWHM in ZnO layers grown at different temperatures. Errors lay inside the symbols.

Figure 4.11 shows the experimental <0001> dips of Zn and O in samples grown with different substrate temperatures. Note that the half-angle for O is larger than for Zn because of the lower mass (see chapter 3). A similar trend is observed in both sublattices, with a larger dip as *T* increases. The normalization of the O dip is complicated due to the poor statistics after the subtraction w_2-w_3, and the selection of the nominal random level (see the comment in section 3.3.3) can be affected by some uncertainty. Even so, the O dip at 550 ºC is significantly higher (χ_{min}~35 %) than the Zn one (χ_{min}~20%) at the same temperature, which might be interpreted as sublattices with a different degree of order in the wurtzite structure. This hypothesis is also suggested by the stable composition of the films observed in the random RBS spectra, ruling out the differences in the stoichiometry as a cause of the structural variations.

In order to further study the behavior of Zn and O sublattices with temperature, μ-Raman experiments were carried out at FZD. Raman spectroscopy is based on the

inelastic scattering of monochromatic light by phonons or vibrational modes of the target atoms [23]. In our experiments, a laser of λ=532 nm (5 mW) was used, being the measurements developed in a LabRam HR (*H-J-Y*) system. The backscattering geometry was combined with a long working distance of the objective (50x). The experimental magnitude under analysis is the light intensity as a function of the wavenumber shift between both probing and detected photons. The resolution in the Raman shift was 1.5 cm^{-1} and each spectrum was acquired for one hour. For the normalization, a sapphire (0001) substrate was used as reference.

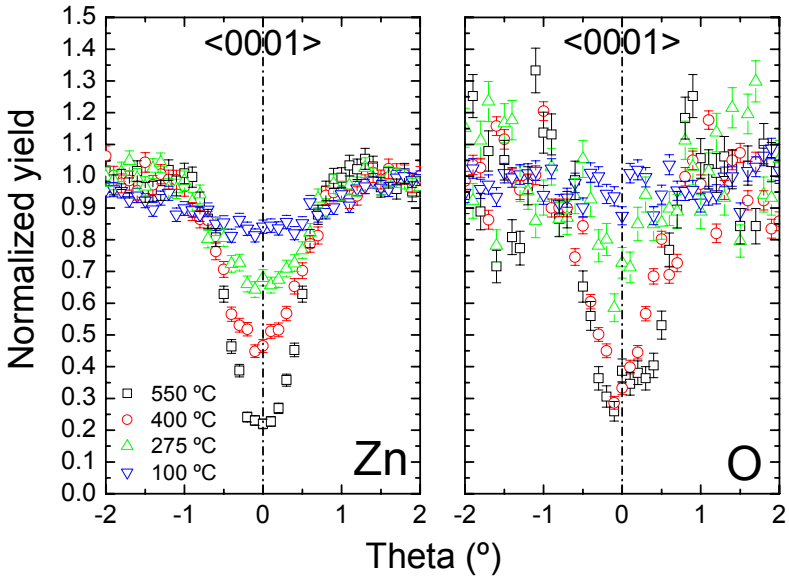

Figure 4.11 Angular scans for Zn (w_1) and O (w_2-w_3) elements in ZnO layers grown at different substrate temperatures.

Zn-O bonds show several vibrational modes in the Raman spectrum. Due to the wurtzite structure, the frequencies of both longitudinal optical (LO) and transverse optical (TO) phonons are split into two frequencies, parallel (A_1) and perpendicular (E_1) to the <0001> axis. Apart from these four optical modes, there are two important non-polar phonon modes (E_2) [24]. These E_2 modes are particularly interesting because they do not depend on the orientation, and they can be directly ascribed to Zn and O sublattices. In particular, the low frequency E_2 (~99 cm^{-1}) mode is associated to the vibration of heavy Zn atoms, while the E_2 (~438 cm^{-1}) mode involves only the O atoms [24].

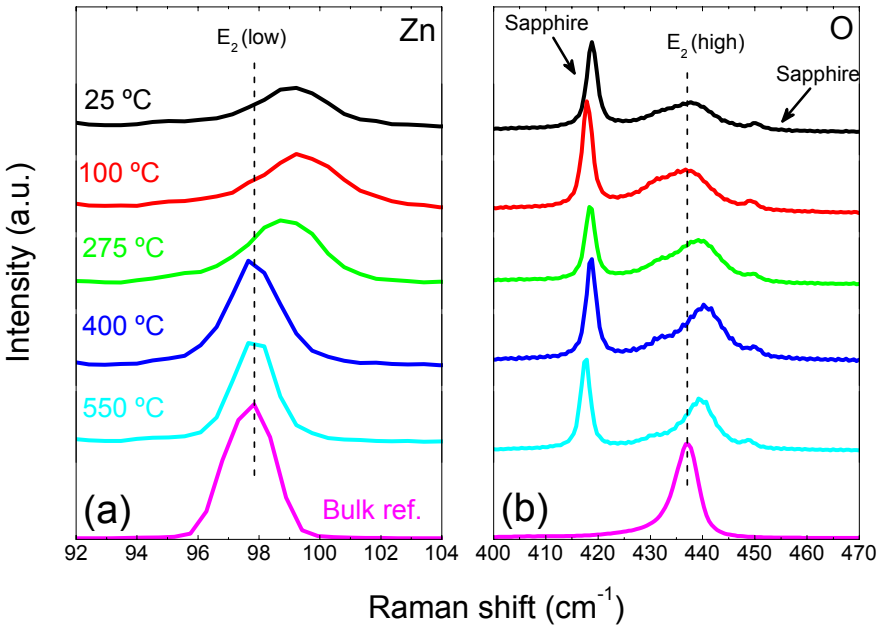

Figure 4.12 Raman E_2 peaks of ZnO as a function of the growth temperature. Data courtesy of M. Vinnichenko.

Several of these lines were observed in the Raman experiments, comprising E_2-low, E_2-high, A_1(TO), E_1(TO), and surface optical (SO) modes at 332 cm^{-1}, 547 cm^{-1}, and 587 cm^{-1}. Figure 4.12 shows the two E_2 lines as a function of the growth temperature. The spectrum from a ZnO bulk crystal is also included for reference. As expected, with the increase of T, the peak position progressively shifts towards the reference bulk crystal. However, the peak position evolution stops at ~400 °C, what indicates the end of a first phase of crystalline ordering. This fact is reinforced by the increase of the A_1 intensity (not shown here), which indicates the orientational ordering of the film in the <0001> direction. Nevertheless, although E_2-low position is the same as for ZnO reference, the E_2-high peak associated to O vibrations does not match exactly its expected position. Therefore, the Raman results confirm a different behavior of both Zn and O sublattices with temperature, in agreement with RBS/C. In addition, E_2-low suffers a downshift, whereas the E_2-high peak suffers an upshift. This feature has a qualitative analogue in the hydrostatic pressure dependence of ZnO [25], so it might be partially related with the increasing lattice stress of the film with the temperature. However, RBS/C measurements in the $<\bar{2}113>$ axis (not shown here) did not reveal the presence of strain at any depth.

Not only the peak position changes with *T*, but also the line widths become smaller. Actually, the Zn sublattice shows a better transition than O in this sense, because E_2-low line width is even lower than in the ZnO bulk crystal. On the contrary, the E_2-high line width is higher.

4.4. Conclusions

Along this chapter, the effect of the AlN and GaN NLs on the growth of GaN was investigated. Morphological (AFM) and structural (HR-XRD) analysis demonstrated the better growth of GaN layers on AlN. However, RBS/C experiments confirmed that the major part of the defects is generated in the first nm's of the NLs, being these defects considerably higher in the case of the GaN NL. For both AlN and GaN NLs, the final GaN base layer exhibited a good in-depth crystal quality, except for the near-interface region, where signs of strain were found in both RSMs and RBS/C angular scans. It can be concluded that AlN NLs mitigate in a better way the lattice-mismatch between sapphire and GaN by promoting the 2D growth at the early-stage of the deposition.

The influence of the substrate temperature was also evaluated in this chapter regarding the growth of ZnO layers on sapphire. The enhancement of the epitaxial growth was shown by XRD and RBS/C measurements. The layers showed a single-crystal domain and the stoichiometry of the compound was independent of the temperature. The Al-Zn interdiffusion was observed for temperatures ~400 ºC, affecting the crystal quality of the interface. Both Zn and O sublattices showed different crystal quality. The O resonance was used in RBS/C to determine the minimum yield related with this element, finding out significant differences compared to the Zn dip. This fact was further verified in Raman experiments, suggesting the better incorporation of the Zn atoms into the wurtzite metal sublattice.

4.5. References

[1] S. Fernández-Garrido, A. Redondo-Cubero, R. Gago, F. Bertram, J. Christen, E. Luna, A. Trampert, J. Pereiro, E. Muñoz and E. Calleja, J. Appl. Phys. **104**, 083510 (2008).

[2] D. A. Neumayer, and John G. Ekerdt, Chem. Mater. **8**, 9 (1996).

[3] H. Morkoç, *Nitride semiconductors and devices* (Springer, Berlin, 1999).

[4] H. Amano, N. Sawaki, I. Akasaki and Y. Toyoda, Appl .Phys. Lett. **48**, 353 (1986).

[5] K. Hiramatsu, S. Itoh, H. Amano, I. Akasaki, N. Kuwano, T. Shiraishi and K. Oki, J. Cryst. Growth **115**, 628 (1991).

[6] S. Nakamura, Jpn. J. Appl. Phys. **30**, L1705 (1991).

[7] E. Niikura, K. Murakawa, F. Hasegawa and H. Kawanishi, J. Cryst. Growth **298**, 345 (2007).

[8] H. Morkoç, and Ü. Özgür, *Zinc oxide: fundamentals, materials and device technology* (Wiley-VCH, Weinheim, 2009).

[9] M. Vinnichenko, N. Shevchenko, A. Rogozin, R. Grötzschel, A. Mücklich, A. Kolitsch, and W. Möller, J. Appl. Phys. **102**, 113505 (2007).

[10] I. Grzegory, B. Łucznik, M. Bockowski, S. Porowski, J. Cryst. Growth **300**, 17 (2007).

[11] S. M. Lee, M.A. Belkhir, X.Y. Zhu, Y.H. Lee, Y.G. Hwang and T. Frauenheim, Phys. Rev. B **61**, 116033 (2000).

[12] Y. Ohba, and R. Sato, J. Cryst. Growth **221**, 258 (2000).

[13] V. Tasco, A. Campa, I. Tarantini and A. Passaseo, F. González-Posada, A. Redondo-Cubero, K. Lorenz, N. Franco and E. Muñoz, J. Appl. Phys. (2009).

[14] J. R. Chierchia, T. Böttcher, H. Heinke, S. Einfeldt, S. Figge and D. Hommel, J. Appl. Phys. **93**, 8918 (2003).

[15] G. Bauer, and W. Richter, *Optical characterization of epitaxial semiconductor layers* (Springer, New York, 1996).

[16] B. Holländer, S. Mantl, M. Mayer, C. Kirchner, A. Pelzman, M. Kamp, S. Christiansen, M. Albrecht and H.P. Strunk, Nucl. Instr. Meth. **136–138**, 1248 (1998).

[17] S. Kitamura, K. Hiramatsu and N. Sawaki, Jpn. J. Appl. Phys. **34**, L1184 (1995).

[18] K. Jeganathan, M. Shimizu and H. Okumura, Appl .Phys. Lett. **86**, 191908 (2005).

[19] J. A. Leavitt, L.C. McIntyre Jr., M.D. Ashbaugh, J.G. Oder, Z. Lin and B. Dezfouly-Arjomandy, Nucl. Instr. and Meth. B **44**, 260 (1990).

[20] J. A. Leavitt, L.C. McIntyre, Jr., P. Stoss, J.G. Oder, M.D. Ashbaugh, B. Dezfouly-Arjomandy, Z.-M. Yang and Z. Lin, Nucl. Instr. and Meth. B **40/41**, 776 (1989).

[21] J. F. Ziegler, J.P. Biersack and U. Littmark *The stopping and range of ions in solids* (Pergamon Press, New York, 1985).

[22] Ü. Özgür, Ya. I. Alivov, C. Liu, A. Teke, M. A. Reshchikov, S. Doğan, V. Avrutin, S.-J. Cho, and H. Morkoç, J. Appl. Phys. **98**, 041301 (2005).

[23] C. B. Brundle, C. A. Evans, S. Wilson, *Encyclopedia of materials characterization* (Butterworth-Heinemann, Stoneham, 1992).

[24] P. Y. Emelie, J.D. Phillips, B. Buller and U.D. Venkateswaran, J. Electron. Mater. **35**, 525 (2006).

[25] F. J. Manjón, K. Syassen and R. Lauck, High Presure Res. **22**, 299 (2002).

5

Analysis of heterostructures out of lattice-matched conditions

This chapter shows the characterization of different ternary heterostructures out of lattice-matched conditions with relevance in the fabrication of electronic and optical devices. First, AlGaN/GaN systems are analyzed, paying especial attention to the detection of elements affecting the 2DEG in HEMTs, including some important impurities. Second, the miscibility problems associated to InGaN layers are studied in the whole compositional range. Finally, MgZnO layers are evaluated as a function of the composition, and for different substrate orientations. Afterwards, the modification of ZnO properties by ion implantation is evaluated.

We know very little, and yet it is astonishing that we know so much, and still more astonishing that so little knowledge can give us so much power. (Bertrand Russell)

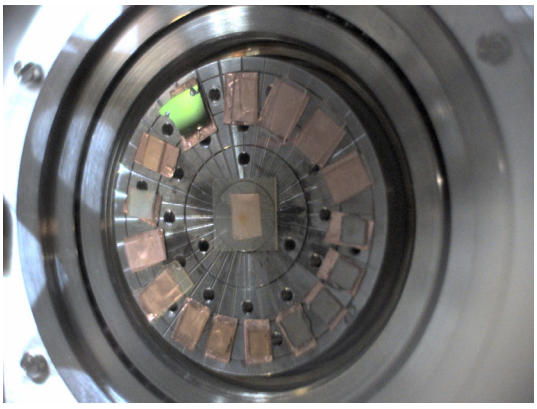

Samples and goniometer in a RBS experiment of this thesis.

5.1. Introduction

During the last two decades, the importance of ternary GaN-based and ZnO-based heterostructures (HSs) in the development of high-power electronics has been clearly manifested [1]. As explained in chapter 1, the use of AlGaN and InGaN layers is widely extended for the implementation of HEMTs and LEDs [2, 3], and similar MgZnO and CdZnO layers have been proposed to continue the progress of such devices [4]. All these ternaries, however, have the inconvenient of the lattice-mismatch with the base layers, which can induce several structural and compositional defects [5]. Indeed, the limitations in the use of light and heavy atoms for the replacement of Ga or Zn make narrower the theoretical limits for the bandgap engineering. This point is particularly critical in ZnO, since the stable binaries MgO and CdO are not hexagonal but cubic systems.

Next, IBA of relevant ternary HSs for electronic and optoelectronic devices is shown. AlGaN-based HSs have a compositional range tightly fixed by the requirements of the HEMTs [6]. However, the key point of such HEMTs is the 2D electron gas (2DEG) formed at the AlGaN/GaN interface [7], and the role of the compositional Al gradients in such boundary is very critical. Therefore, in this chapter the limitations and advantages of the techniques for the determination of the compositional profiles of Al are explored. Apart from these gradients, the presence of light impurities that can have a potential impact on the 2DEG will be explored too, especially the case of H. Concerning the InGaN-based HSs for optoelectronic devices, the major difficulties are focused on the miscibility of the binaries (InN and GaN) in the whole compositional range. This is a fundamental question restricting the development of high-quality epitaxial films, so it will be studied by means of RBS and XRD. Besides, the evolution of the strain state will be also investigated in both AlGaN and InGaN HSs.

Together with the well-established GaN-based compounds, most novel MgZnO HSs have been studied. These layers show several analogies with AlGaN, since the composition is used for bandgap engineering within a limited range (normally with less than 35 % of Mg) [8]. In this chapter, the relation between the composition and the bandgap will be studied for MgZnO layers grown on non-polar directions. Finally, the modification of these MgZnO films by N implantation will be carried out to check the viability of p-type doping by this approach. The inclusion of Mg can facilitate the p-

type character of the layers when doped, due to the carrier compensation by the deep levels introduced by Mg [9]. As mentioned in chapter 1, N-doping has been suggested to get p-ZnO [10], but the lack of reproducibility in such studies has generated doubts about this method [11], and this crucial unresolved debate is affecting the future applications of ZnO as WBS. The good control of the dose and the non-limited solubility of the implanted elements makes ion implantation a suitable method to study systematically the N doping [12]. Thus, in this chapter, the effect of N implantation in MgZnO HSs is evaluated, paying attention to the structural modification of the layers after the thermal annealing.

5.2. Ternary GaN-based heterostructures

Both AlGaN and InGaN systems have proved to be very useful in the development of electronic and optoelectronic devices [1]. However, the actual accessible compositional range for the ternaries is limited by several factors, such as the miscibility or the intrinsic strain, both of them influencing the epitaxy of the layers. In the following, these and other factors conditioning the good deposition of ternary layers are evaluated.

5.2.1. AlGaN layers for HEMTs

In the case of AlGaN/GaN HSs, the fundamental electrical properties of the HEMTs are directly dependent on the AlGaN barrier thickness (typically ~30 nm), and on the Al content (usually ~30%) [13]. For the active device structures, it is well known that higher Al concentrations of the AlGaN barrier layer lead to higher sheet carrier concentrations in the 2DEG due to larger polarization effects and larger conduction band discontinuities [6, 14]. In fact, variations of less than 5 % in the Al content can increase the electron mobility and the carrier density by a factor of 2, diminishing the sheet resistance in parallel [14, 15]. The increase of the thickness in the AlGaN barrier also contributes to enlarge the carrier density, despite this parameter saturates for thicknesses above 30 nm [6].

The impact of these variables may also be convoluted with the parallel development of strain within the layer [16], since the AlGaN layer starts growing pseudomorphic to the GaN substrate and then relaxes after reaching a critical thickness [15]. The critical thickness value decreases with the incorporation of Al in the AlGaN layer [17]. The

presence of strain in the AlGaN layer has relevant implications for the 2DEG properties through the polarization fields developed and the subsequent effects [18].

Therefore, it is important to establish an accurate method to determine the composition and thickness of the AlGaN layers in such HSs, especially with in-depth resolution, to detect the presence of Al gradients at the interface. Furthermore, since the strain state can affect the results and simulations obtained from XRD experiments, it is also convenient to warrant a strain independent measurement of the composition. IBA can be very useful in this particular point as it will be demonstrated in the following sections [19].

(a) Determination of the AlGaN composition in thick layers

A series of six $Al_xGa_{1-x}N$ samples were grown by MO-CVD (see chapter 2 for details) on GaN templates, in order to determine independently their compositions by three different techniques. The nominal thickness of the films was 150 nm. This value was selected because it allows a clear detection by both XRD and IBA methods (in terms of statistics and well-separated signals). The composition was varied with the growth conditions from 10 % to 30 % approximately, to evaluate the influence of the stoichiometry on the appearance of in-depth gradients.

First, HR-XRD measurements were taken in a 3D Bede Scientific Diffractometer using the $\omega/2\theta$ configuration around the symmetric (0002) and asymmetric $(10\bar{1}5)$ reflections, the latter under steep and shallow incidence. As mentioned in chapter 2, the symmetric and asymmetric reflections provide information about crystalline planes parallel and perpendicular to the sample surface, respectively. In addition, the width of the reflections scales with the number of dislocations present in the crystal [20]. The composition and the degree of relaxation (R) in the AlGaN layer affect the relative shifts of both symmetric and asymmetric reflections with respect to the reference GaN substrate. The values of these parameters can be extracted by fitting the experimental scans with a dynamical XRD model [21].

Figure 5.1 shows the HR-XRD scans from the (0002) and $(10\bar{1}5)$ reflections. It can be appreciated that the AlGaN reflection shifts to higher angles, in correlation with an increase of x (decrease in the lattice parameter). Both x and R were extracted from fitting the symmetric and asymmetric (under steep and shallow incidence) reflections

simultaneously. The samples were under strain (R<5%) except for the one with the highest Al content. In this case, the sample was partially relaxed (0%<R<20%). This change is not surprising, since the critical thickness for strain relaxation scales with the Al incorporation and falls in the range of ~100 nm for the Al contents used in this work [17].

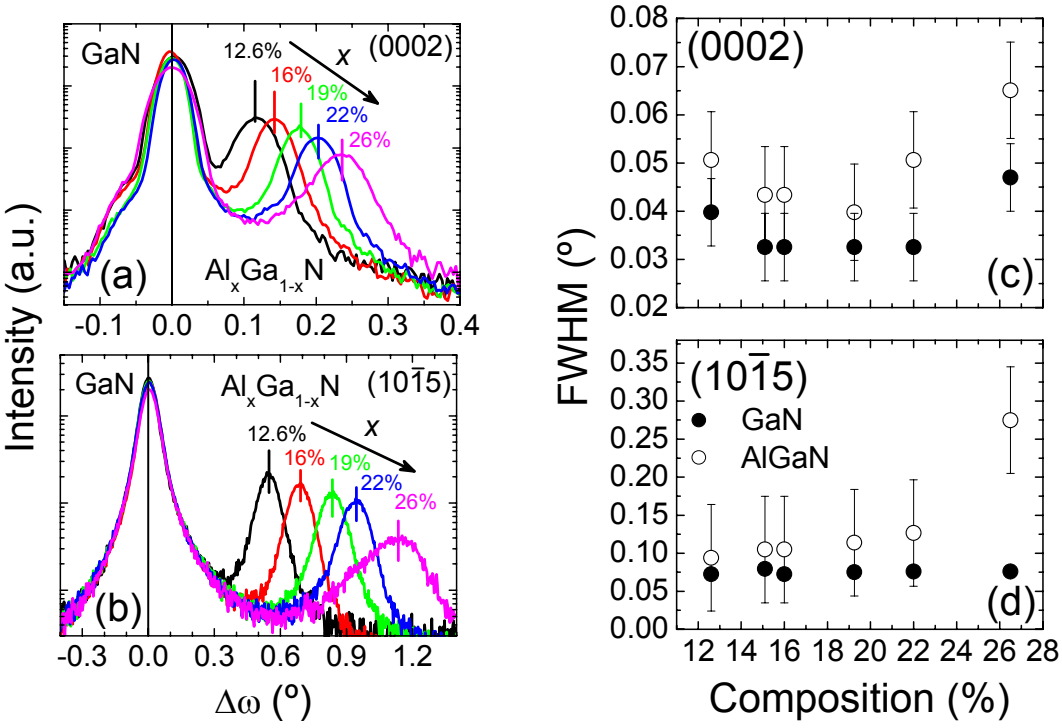

Figure 5.1 HR-XRD ω/2θ scans in the (a) symmetrical (0002) and (b) asymmetrical (10$\bar{1}$5) reflections for samples with different compositions (x). The peak position of the AlGaN reflection shifts to higher angles with the Al incorporation. The FWHM is also shown (c-d) for the two reflections.

The FWHM of the XRD reflections reveals the good crystalline and epitaxial quality of the layers (see section 2.4.2). The evolution of the FWHM upon Al incorporation in the AlGaN layer is displayed in Figure 5.1(c-d). The FWHM of the (0002) reflection remains nearly constant and starts to increase for x>20%. A sharp increase is also found in the FWHM of the (10$\bar{1}$5) reflection under shallow incidence, where the configuration is more sensitive to strain, for the largest Al content (x~26%). The previous trends indicate that the sample crystallinity slightly deteriorates upon Al incorporation above x~20 %, and that the strain within the layer is relevant for the highest compositions.

RBS experiments were performed on these HSs using 2 MeV He^+ ions. Backscattered ions were detected at 170º, with a total dose of 5 μC. Due to the high crystal quality of the layers and the difficult analysis of the Al signal, random spectra were collected by rotating the samples during the measurement, with the θ-χ scan discussed in chapter 2. The aligned <0001> spectra were acquired to quantify the minimum yield (see section 3.2.3).

Figure 5.2 shows the random and aligned RBS spectrum of two $Al_xGa_{1-x}N$ HSs with the lowest (x=12 %) and the highest (x~26 %) compositions. Due to the heavy mass of Ga, the RBS detection of this element presents a high cross-section. This high sensitivity for Ga and the signal overlap is detrimental in this case, since it imposes a reduced sensitivity to Al and N detection. The Ga signal presents a step in the surface region (higher energies) due to the Ga deficiency in the AlGaN layer. Hence, the increase in the Al incorporation in the films reflects in a parallel decrease in the Ga signal. In this case, the Al content can be determined by the deficiency in Ga and assuming a stoichiometric nitride, i.e. N content of ~50 at. %. This analysis implies an error of ~10% in the calculation of x value.

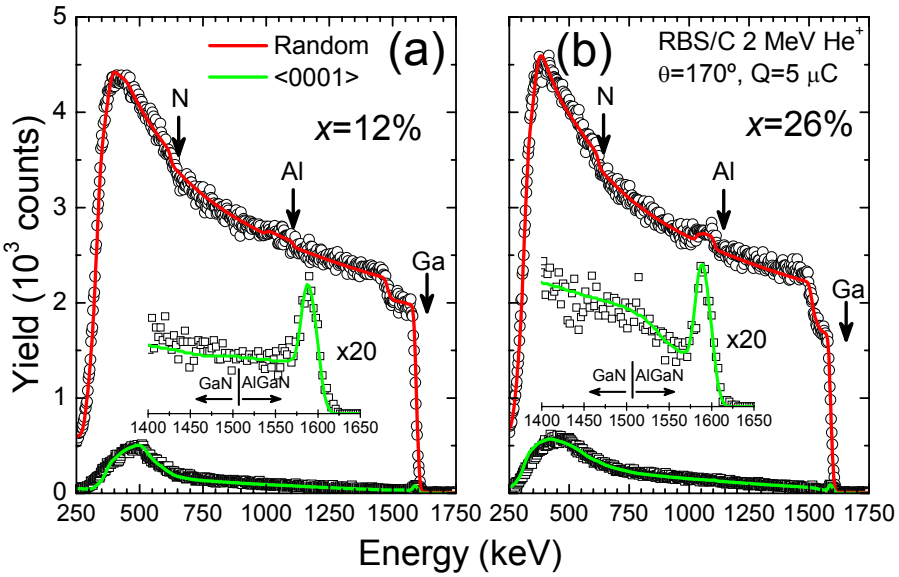

Figure 5.2 Random and <0001> aligned RBS spectra of two $Al_xGa_{1-x}N$/GaN HS with (a) x=11% and (b) x=26%. Solid lines are the RBX simulations. Insets show details of the aligned spectra.

The simulation of the random RBS spectra was developed with a simple two-layer model describing the AlGaN and the GaN films (see, for example, Figure 5.2a). The

fitting worked out successfully, except for the sample with x=26 %, where the AlGaN layer had to be divided into two sublayers with different composition for a proper simulation of the experimental data. In particular, for the sample shown in Figure 5.2b, an AlGaN layer with x=22 % (~30 nm) closer to the GaN interface, and an Al-richer layer (x=28 %) near the surface were deduced. This result indicates an in-depth gradient in the Al concentration, with an average composition closer to the value extracted from HR-XRD (x~26 %). The presence of these graded Al profiles have been related to the AlN limited solubility in the GaN matrix [22]. Eventual Al gradients should be taken into account when modeling the HEMT electrical properties, since they imply a lower Al concentration closer to the 2DEG region.

The RBS results can be used to improve the XRD analysis, especially in this mentioned inhomogeneous sample. This is shown in Figure 5.3, where XRD simulations considering a single layer model or an in-depth profile are displayed. In this latter case, the same layer model as derived from the RBS analysis has been assumed, together with a relaxation parameter R<0.05. It is clear that the correlation between the experimental and simulated data is strongly improved by considering the Al profile. Considering the error in the simulation, the effect of strain relaxation cannot be completely ruled out. Nevertheless, the simulations show that R is mainly affecting the peak position and only playing a minor role in the peak broadening. Consequently, the fitting of XRD data cannot be achieved based on the single assumption of film relaxation and the incorporation of different layers with varying Al contents is necessary.

The epitaxial growth of the ternary layer was assessed from aligned <0001> spectra (insets in Figure 5.2). RBS/C analysis of the $Al_{0.26}Ga_{0.74}N$/GaN HS reveals a χ_{min}=2.4 % (for the Ga signal close to the surface), but it can be as good as 1.7 % for samples with x<16%. These values confirm the excellent growth of the AlGaN compound even for thick films, which is also verified by XRD measurements. Indeed, obtained results for the AlGaN layer are comparable to commercial GaN templates and as good as the best values shown in the literature [23, 24]. However, a significant increase of dechanneling can be observed when x>12 %. In particular, the sample with x~26 % revealed a higher dechanneling in the AlGaN layer in comparison to the GaN buffer layer (note the slope change in the yield for the enlarged RBS/C spectrum in the inset of Figure 5.2). This fact may be related with the observed profile in the random spectra. Indeed, in

accordance to Vegard's law, these profiles indicate that a different lattice parameter is present for the grown AlGaN structure, explaining the rising of dechanneling. Besides, these observations about the dechanneling in samples with high Al content are consistent with the XRD trends displayed in Figure 5.1. Finally, some information regarding the GaN/Al_2O_3 interface can be obtained from the RBS Ga signal (250-450 keV). Here, a clear increase of dechanneling appears since the RBS/C yield reaches ~12 % of the random value. This fact has been already reported in other GaN based HS [24].

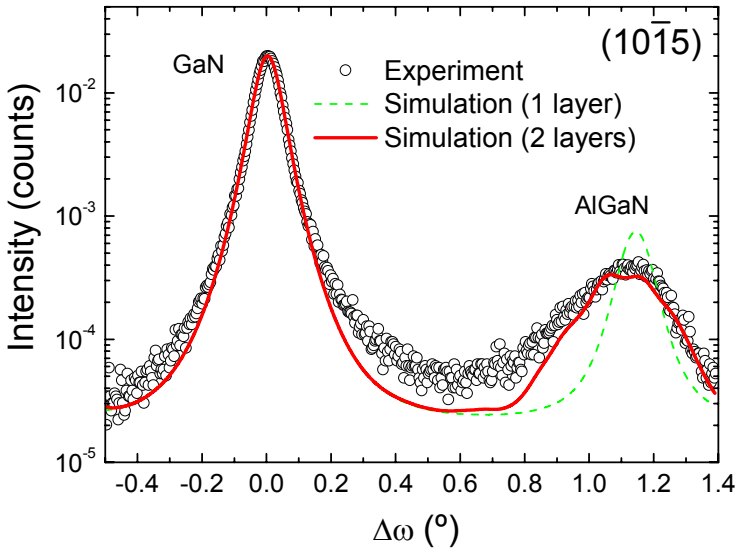

Figure 5.3 Simulations of the experimental XRD data for the $(10\bar{1}5)$ reflection considering a single AlGaN layer (x=26 %, green line) and the in-depth profile detected by RBS (red line).

In order to improve the sensitivity to light elements, such as Al and N, heavy ion ERD experiments were performed at FZD. ERD experiments were carried out using a Bragg ionization chamber (BIC) as discussed in detail in section 2.3.2. Figure 5.4 shows the ERD-BIC spectra of the already mentioned HSs with x=12 % (a) and x=26 % (c). As it is clearly observed, the signals from Al and N are well separated, overcoming the limitations of RBS. Since Ga is heavier than the Cl^{8+} projectiles, the probability of getting Ga recoils is rather low and, in addition, the Ga recoil line overlaps with the main contribution of scattered projectiles. Therefore, the Ga contribution can be obtained from the high-energy side of the scattered Cl^{8+} ions, corresponding to scattered projectiles from Ga(Cl,Cl)Ga atoms. The ERD-BIC spectra also show some slight oxygen contamination at the surface and a negligible amount of H in the AlGaN layers.

Due to the well-separated N, Al and Ga signals, concentration sensitivity is increased to less than 5 %. The analysis of the individual elements yields the compositional profile, shown in Figure 5.4, being the average value of the *x* parameter calculated by integration of the signals. As it is clear from Figure 5.4d, the sample with *x*=26 % also exhibits a depth profile close to the interface, in excellent agreement with RBS simulations. On the contrary, the sample with *x*=12 % does not show significant compositional gradients. Apart from this, the most important conclusion of these calculations is that the N content in the layer is constant and close to 50 %. Therefore, these ERD measurements justify the hypothesis used in the RBS simulations, where the N content was fixed to 50 % to attain the Al value. In addition, the achievement of stoichiometric AlGaN layers can also be expected from the good crystalline quality of the layers.

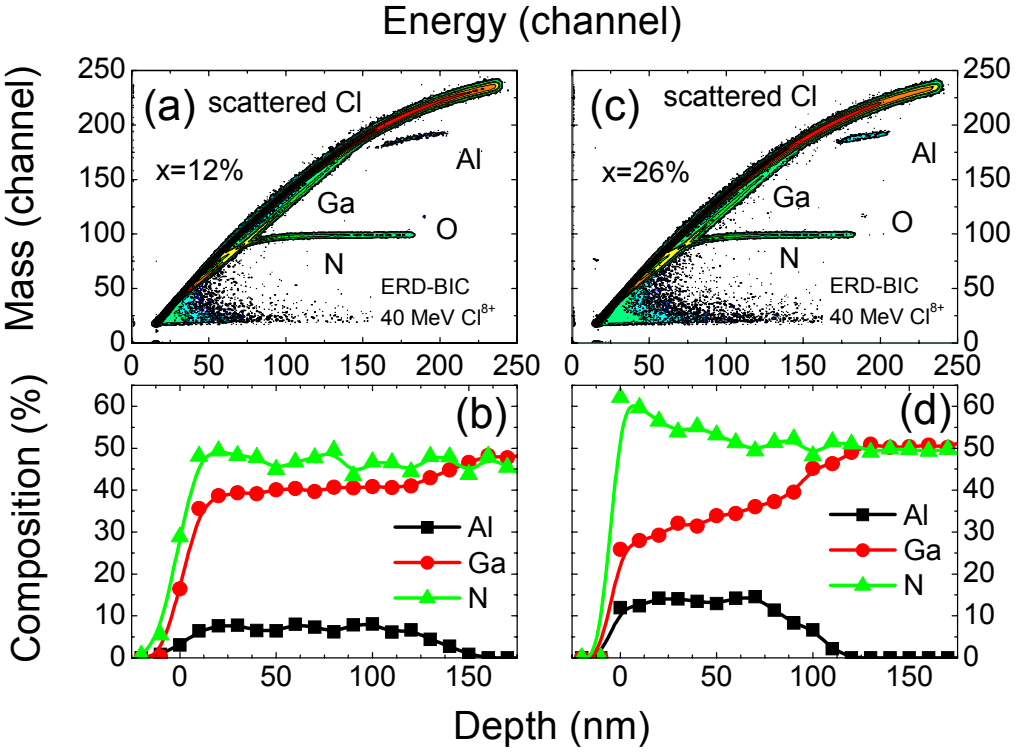

Figure 5.4 ERD-BIC spectra (a,c) of AlGaN/GaN HSs with *x*=12 % and *x*=26 %, respectively. Elemental depth profiles (b,d) obtained from the analysis of the spectra.

Figure 5.5 summarizes the results obtained from all the analytical methods employed. The main conclusion that can be extracted from them is the very good agreement between RBS and XRD analysis. Despite this fact, a slight overestimation of the Al

content by XRD is attained for small Al incorporation (x<18 %). Although in principle, x can be determined independently from R using the $(10\bar{1}5)$ reflection under steep incidence, which is less sensitive to strain, the simulation does not allow to distinguish between R=0 % and R<5 % states. Thus, the residual strain could still affect the estimation of x as derived from the XRD data, explaining the deviation from RBS results. It should be noted that XRD gives average values whereas RBS has shown the presence of in-depth resolved profiles, specially in the sample with the highest Al content (x=26 %). This fact points out some additional considerations that could not be directly extracted from the XRD data alone. Thus, the information given by IBA techniques regarding the presence of compositional profiles represents an important feedback in the characterization, and it should be taken into account when calculating the electrical properties of the 2DEG.

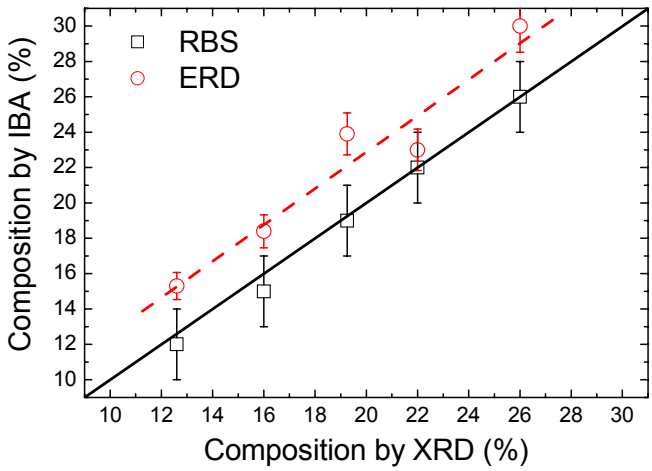

Figure 5.5 Comparison of the Al content determined by XRD and IBA. RBS agrees well with XRD. Mean values were taken for IBA when spectra showed depth concentration profiles.

Finally, as shown in Figure 5.5, ERD-BIC results reproduce the trend of the Al incorporation in the samples obtained from RBS. However, a systematic deviation from the ERD-BIC values with respect to RBS is observed, with an overestimation in the Al concentration. This fact could be explained by the uncertainties in the scattering cross section and deviations from the Rutherford formula regarding the collision events of Cl^{8+} ions with light elements. It should be mentioned that the Ga content is derived from the Cl^{8+} scattered ions, while the contribution of light elements is extracted from the recoil atoms (N and Al).

(b) Measurements of Al profiles in AlGaN thin layers grown on different base layers

The previous studies have demonstrated that IBA can improve the conventional XRD characterization of AlGaN/GaN HSs because of the sensitivity to compositional depth profiles. However, normal thicknesses for AlGaN layers in HEMTs are about 30 nm and hence, the resolution of RBS is clearly restricted (see section 2.3.1). Furthermore, due to the high background from the GaN buffer layer, the detection of compositional gradients is difficult. Here, the use of ERD-BIC to determine the composition in such HSs is applied.

To verify the resolution of this method, 12 $Al_xGa_{1-x}N$ samples were grown with a nominal thickness of 30 nm and a composition of x~30%. These values are comparable to those used in current HEMTs [14, 25]. The set of samples was divided in two, corresponding to the different growth methods and base layers. First group (6 samples) was grown by MO-CVD on a GaN base layer. The second group (6 samples) was grown by PA-MBE on a GaN:Al layer. Prior to the ERD experiment, an initial structural (HR-XRD) and electrical characterization of the HSs was carried out at ISOM. The carrier density and the threshold voltage (the maximum voltage at which the charge in the 2DEG disappears) of the 2DEG were obtained using a Hg probe (Hg-CV).

ERD-BIC experiments were developed, as described before, with a 40 MeV Cl^{8+} beam. Figure 5.6 shows the spectra for two samples with the same nominal composition but grown on different base layers. The sample belonging to the first set (Figure 5.6a) has a well-separated Al signal in the spectrum. However, for the sample belonging to the second group, the spectrum shows two Al regions. The first one is related with the AlGaN layer, and the second (long tail in Figure 5.6c) is shifted to lower energies, showing a low yield. The analysis of the compositional depth profiles (Figure 5.6d) proves that the additional Al signal is associated to residual Al along the GaN base layer. The presence of the Al in the GaN base layer was confirmed in all the samples of the second series, being their composition very similar (x~14 %).

Figure 5.6 confirms that the determination of Al depth profiles is feasible even for thin AlGaN layers by ERD-BIC. This is due to the higher sensitivity of this technique to light elements, solving the overlapping drawbacks of RBS and providing depth resolution to complement XRD measurements. This depth resolution can be very useful

in the detection of irregular gradients, and the relation of these gradients with the final electrical properties has to be taken into account when processing the HSs. Actually, the incorporation of such an extra amount of Al in the GaN buffer can become an important drawback for the development of HEMTs. The threshold voltage (V_{th}) and carrier density in the 2DEG are strongly dependent on the conduction-band discontinuity [13, 26], so a worse electric behavior of the samples with the GaN:Al base layer would be expected due to the lack of an abrupt interface. Indeed, our electrical measurements show a systematic increase of the threshold voltage (around -4 V) for the second series grown on GaN:Al when compared with samples grown on GaN (around -5.9 V). Carrier density is also slightly lower for samples with a AlGaN/GaN:Al interface, but the compositional differences between both series might be also affecting these results.

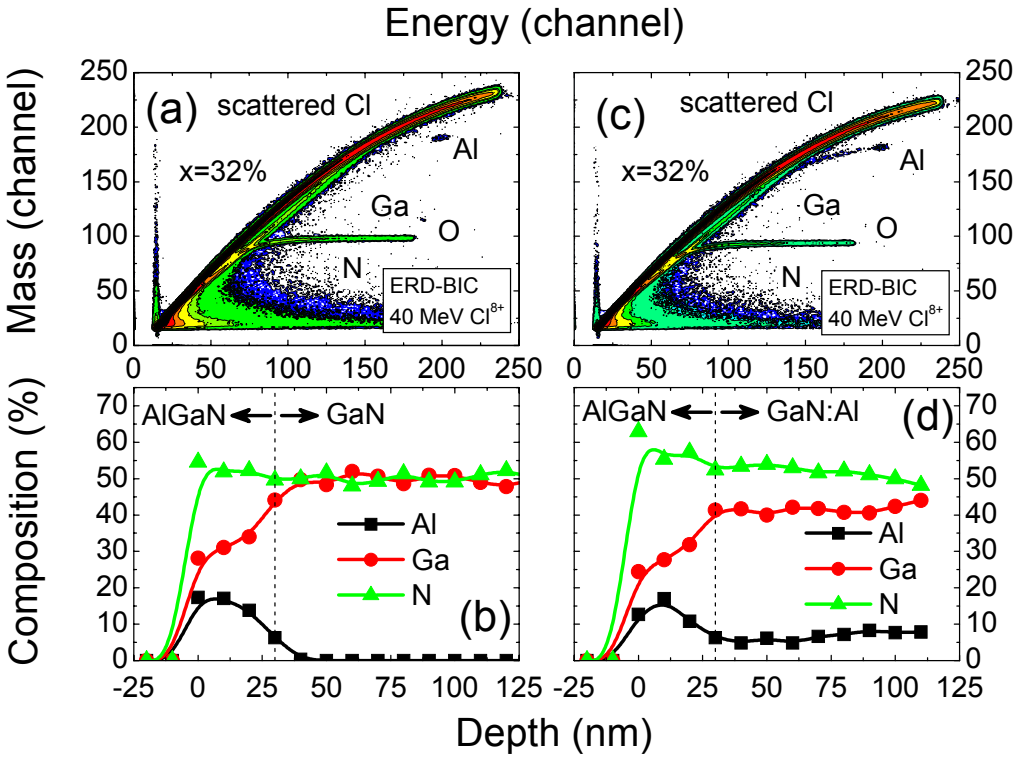

Figure 5.6 ERD-BIC spectra and the corresponding elemental depth profiles of samples grown on (a,b) GaN base layer and (c,d) GaN:Al base layer.

(c) Detection of H impurities by high-resolution methods

The lifetime and performance of AlGaN/GaN HSs is strongly affected by the presence of impurities, trapping centers, and defects [27]. In particular, H passivation of acceptors was a serious bottleneck to obtain p-type GaN [28]. Nevertheless, the impact

of H impurities in semiconductor physics is complex, since several effects can be induced simultaneously, such as dangling bonds termination, passivation or compensation of both shallow and deep defects, and the generation of extended defects [29]. Moreover, the presence of H can be used to reveal defects in the atomic structure by "decorating" them, i.e. H atoms become bonded to lattice defects [30].

GaN-based materials grown by MBE and MO-CVD can exhibit high H concentrations (~10^{20} cm^{-3}) due to the residual pressure during deposition or direct incorporation from the growth precursors [30]. Although other growth precursors have been studied as a route to achieve H-free GaN, most industrial manufacturing is done in a H contaminated environment, where atomic H can be unintentionally incorporated to III-nitrides during processing steps, for instance in HEMT and UV-LEDs [31].

Table 5.1 Main parameters and results for AlGaN/GaN HSs: composition (x), surface roughness (SR), dislocation density (DD), and H content at the surface (H_0) and at 110 nm depth (H_{110}). Mean values and standard deviation (in parenthesis) are shown.

Sample	Method	Precursor	x (%)	SR (nm)	DD (10^9 cm^{-2})	H_0 (%)	H_{110} (%)
A1	MO-CVD	NH_3	31(2)	0.9(2)	9(2)	0.9(1)	0.2(1)
A2	PA-MBE	NH_3	35(3)	1.7(7)	1.9(2)	0.83(7)	0.23(6)
A3	PA-MBE	N_2	29(7)	5(1)	5(2)	6(3)	0.31(5)
A4	PA-MBE	N_2	26(6)	0.6(2)	0.3(2)	2(1)	0.22(8)

So far, studies that explicitly address point defects and their interaction with H in AlGaN compounds are rare. H incorporation and diffusion in n-type, intrinsic and p-type GaN have been studied [32, 33], but no study in AlGaN/GaN HSs has been reported to the best of our knowledge. In addition, the majority of the studies found in the literature related to H incorporation use deuterium (D) to enhance the sensitivity detection by secondary ion mass spectrometry (SIMS) [31]. ERD analysis has been also used to verify the presence of D related to an AlGaN/GaN organic sensors [34].

Due to the high relevance of this issue, here on the presence of H in AlGaN/GaN HSs is investigated, as well as its effect on the 2DEG properties [35]. In this study, AlGaN/GaN HS were grown by MO-CVD and MBE methods. Four different groups of samples were analyzed, comprising a total number of 17 samples. The conditions for

each set of samples are listed in Table 5.1. In the case of MBE, both NH_3 (set A2) and N_2-plasma (sets A3 and A4) gas precursors were used. Samples were grown on sapphire (A1, A2) and Si(111) substrates (A3, A4). The thickness of the AlGaN layer was 20-25 nm in all cases, grown onto a GaN buffer with different nucleation layers. The samples grown with a NH_3-MBE have also a 2 nm GaN cap.

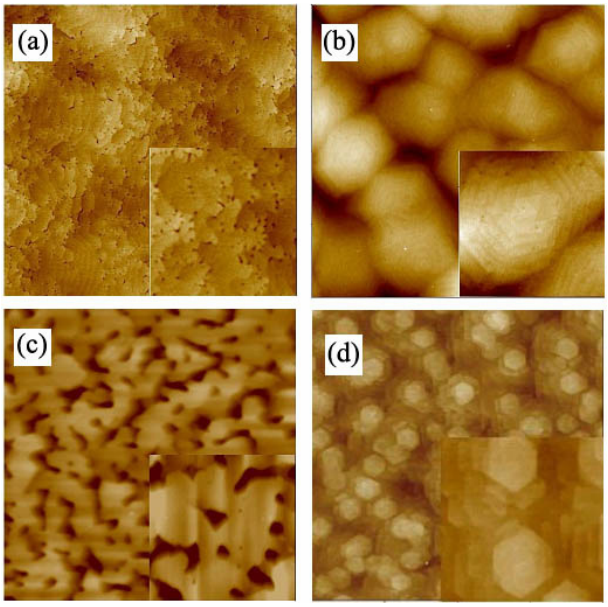

Figure 5.7 AFM 4x4 μm^2 images (inset image size is 1x1 μm^2) of the AlGaN HSs: (a) A1, (b) A2, (c) A3, (d) A4. The image/inset height scale limit is (a) 12.5/12.5 nm, (b) 20/12 nm, (c) 25/20 nm and (d) 8/8.5 nm. Adapted from [35].

The composition of the AlGaN barrier, the relaxation parameter and the rocking curve FWHM were obtained by HR-XRD, as mentioned in previous sections. Electrical properties were also assessed at ISOM. Sheet resistance (R_s) was measured using a Leighton system and mobility (μ) was determined by Van der Pau measurements in an Accent HL5500 Hall system. 2DEG density (n_s) was determined by a Hg-CV profiler. Surface roughness (SR) was extracted by AFM using a Nanoscope III (Veeco) system.

Figure 5.7 shows AFM images of four samples corresponding to A1-A4 groups. These pictures reveal the presence of morphological defects (pits and nano-cracks) and dislocations (edge and screw type). Dislocation density (DD) was measured in 1×1 and 2×2 μm^2 images. In the surface of A4 and A2 samples, clear differences between screw and edge dislocation were found, being the screw DD $0.3 \cdot 10^9$ and $0.18 \cdot 10^9$ cm^{-2}, respectively. Group A1 of samples have the highest DD ($9 \cdot 10^9$ cm^{-2}), exhibiting nanometric dislocations (1-10 nm) and enlarged shape occasionally. Surface DD

estimated for C samples is in the same range as in A1 and A2 samples, but defect sizes are higher. SR was analyzed in 0.5×0.5 – 4×4 μm^2 images. In A3 samples SR is clearly higher due to pits and cracks on the surface, with 50-150 nm lateral size and ~17 nm depth. Additionally, the electrical characteristics of selected samples show typical values of μ~770 cm^2/Vs, R_s ~520 Ω/sq. and n_s~$7 \cdot 10^{12}$ cm^{-2}. These values are in the usual range for standard AlGaN/GaN HEMT technology.

The H content was measured with high depth-resolution by means of NRA using the $^1H(^{15}N,\alpha\gamma)^{12}C$ reaction at FZD [36, 37]. The experimental system was described in detail in chapter 2. Depth profiling was obtained by sweeping the energy of the impinging ^{15}N ions above the resonance value (6.385 MeV), and recording the 4.43 MeV γ-rays produced [38]. Considering the stopping power for crystalline GaN obtained by SRIM code [39] and the energy width of the resonance (~8 keV), the depth resolution of this method is less than 4 nm.

Figure 5.8 shows the obtained high-resolution H profile up to ~110 nm into the AlGaN/GaN HS for the different samples. Neither the growth method nor the substrate seems to affect the H detected in the AlGaN/GaN HSs. This result indicates that no significant H incorporation is produced during the growth process. Moreover, in-depth H profiles decrease with depth, following an exponential behavior which can be described by interdiffusion mechanisms due to trapping effects [27]. Therefore, it can be concluded that H profiles are related to external sources after deposition.

The experimental H contents were determined at the near surface (H_0) and at 110 nm (H_{110}), the maximum analyzed depth (displayed in Table 5.1). The value of H_0 for MOCVD and NH_3-MBE samples is close to 1%, while higher values were found for N_2-plasma MBE growth. These values are similar to SIMS results published by Pearton *et al*. [40]. H content in the AlGaN/GaN interface is close to 0.5-0.4 %, (see Figure 5.8), but a different exponential decrement could be pointed out between NH_3 and N_2-plasma assisted growths. Finally, mean H_{110} detected was 0.24 ± 0.09 at. % for all the samples included in this study.

The behavior of H in n-type and p-type GaN is predicted to be different from the results in traditional semiconductors (Si and GaAs) and even between the two GaN types mentioned above [33]. The increment of H content in the depth profiles is usually

related to strained regions in GaN-based structures, such as interfaces and bulk and/or surface defects [41]. In this study, AlGaN/GaN wafers were grown pseudomorphically, where the AlGaN layer tends to be completely strained on the GaN layer, as verified by XRD. The presence of charge in the 2DEG could be also considered as another preferential site for H incorporation but, contrary to what it would be expected, Figure 5.8 shows no significant H increase at the AlGaN/GaN interface. This corroborates the low H incorporation during growth; a result verified by repetitive measurements of the H-NRA profile in the 25-50 nm region for samples A1 and A2. Therefore, H profile is neither sensitive to the AlGaN/GaN interface, nor to the 2DEG presence in the HS.

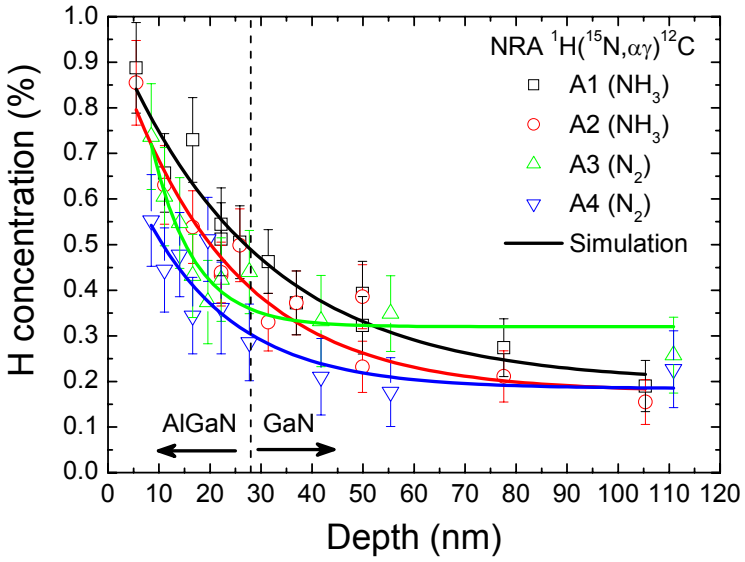

Figure 5.8 NRA of H profile for NH_3 (A1 and A2) and N_2-plasma (samples A3 and A4) growth precursors. Solid line is the simulation of the H profile. AlGaN/GaN separation in x-axis is figurative.

In order to analyze quantitatively the experimental H profiles, simulations considering different incorporation mechanisms were carried out. Levenberg-Marquardt algorithm was used to reduce residual parameters and to obtain a better accuracy [42]. Firstly, the sample was considered as a semi-infinite medium, keeping a constant H concentration at the surface. Secondly, the use of the Fick's equation for diffusion gives a solution corresponding to the well known complementary error-function, erfc(Z) [27]. However, the simulations did not fit accurately with the experimental data using this function. Consequently, trapping effects were incorporated into the model. When this is taken into account, the solution of the diffusion equation for the steady-state regime gives an

exponential decay for H composition, modulated by the capture radius of the trapping reaction [27]. This model fits better the obtained data, but the simulation accuracy is still poor. Due to the high H background detected, ex-situ post-growth H incorporation is postulated in order to find a good simulation of the experimental data. Thus, the trapping model was modified selecting an exponential behavior corrected by an independent term:

$$H(z) = H_{\infty} + H_s \cdot e^{-x/d} . \qquad (5.1)$$

Here, $H(z)$ is the H content at a depth z, H_s is the H content at the surface, H_∞ is the background level of H (corresponding to large depths and nominally close to zero) and d is the mean diffusion distance. Note that H_s is related with to the experimental value H_0 , by means of equation $H_s=H_0-H_\infty$, while H_∞ is an approximation close to H_{110}. For trapping models, the distance d corresponds to the depth at which the H concentration falls to one half of the maximum concentration in the profile [27]. Nevertheless, in the simulations this is only approximately true, since H_∞ is close, but not identical, to zero.

Figure 5.8 shows the simulation of the profiles (solid line) for the four different groups of samples, finding a good agreement with the experiment. Table 5.2 summarizes the parameters obtained from the proposed model (5.1). In order to compare directly these results with the experimental values, deduced H_0 is shown instead of H_s. Calculated values for H_0 and H_∞ are in good correlation with the first results given in Table 5.1.

Table 5.2 Calculated parameters from the fitting of the H profile.

Sample	H_0 (%)	H_∞ (%)	d (nm)
A1	1(2)	0.22(8)	29(6)
A2	0.93(7)	0.26(7)	24(4)
A3	4(3)	0.35(3)	7(3)
A4	0.8(2)	0.18(6)	18(9)

The extracted value for d is 29(6) and 24(4) nm for samples grown by MO-CVD and MBE, respectively. However, d is estimated to be 7(3) and 18(9) nm for samples A3

and A4, respectively. This significant decrease of d in A3 and A4 samples (grown by N_2-plasma MBE) is associated to the higher H content at the surface.

Regarding H_∞, similar concentration values were detected for all samples (see Table 5.2). However, the difference between A3 and A4 samples can be ascribed to the enhancement of H in-diffusion by the presence of the high defect density in the HSs. Taking into account that A3 and A4 samples were grown by the same technique (and with similar SR), this fact is supported by the distinct DD found between them by AFM (Table 5.1). In addition, XRD FWHM values of the GaN reflection are 900 arcsec for A3 samples, but only 300 arcsec for A4 samples.

The calculated values for H_0 from the simulations are very similar in series A1, A2 and A4, but significantly higher in samples A3. Figure 5.7 shows that the surface defects/dislocations in A3 samples have a bigger size and SR increases up to 5 nm. The SR is comparable to the thickness where H_0 is measured in the NRA. Therefore, these results suggest that SR, DD, and defect sizes are related somehow to H_0. Besides, Mimila-Arroyo *et al.* [43] have proposed a similar dependence, since they related the H content on the surface to plasma-induced defects. Moreover, assuming the conjecture of H diffusion pathways along threading dislocations [43], the size and density distribution of dislocations/defects may be affecting the H profile, which would explain the slight differences between H_{110} in the different types of samples (Table 5.1).

The measured values for H_0 and H_{110} (Table 5.1) are high enough to support the hypothesis made by G. Van de Walle and J. Neugebauer [44], who indicated that H atoms are probably part of the basic building blocks of the GaN and AlGaN atomic structures and cause changes in the surface reconstructions under realistic growth conditions and in post-growth processing.

Usually, a higher SR involves larger surface area exposed to the air. Besides, typical defect formation energies are lower at the surface than in the bulk, resulting in high defect concentrations at the surface [33]. Hence, it is possible that through external sources such as air exposure, sample surface cleaning (organics and acids), and/or further processing (by reactive ion etching or chemical vapor deposition methods), both H^+ and H^- are formed at the surface and diffuse inside the sample. This fact seems to be supported by the large differences obtained in samples A3 compared to A2 ones, and

the similar behavior of samples A1 and A2. No influence of the epitaxial growth method, plasma precursors and substrates was found.

Finally, AlGaN/GaN HEMT technology is struggling always with passivation, which is normally attained with silicon nitride (SiN) overlayers. CVD growth of such layers enables H to be incorporated in the passivant layer [45] and, then, to be in contact to the AlGaN surface. Therefore, a close look should be taken into the H inter-diffusion, after HEMT processing, assuming a ~25 nm mean diffusion distance mentioned above.

5.2.2. InGaN layers for optical devices

$In_xGa_{1-x}N$ is possibly the most important nitride compound for the development of UV LEDs and LDs [46, 47]. Nevertheless, the difference between InN and GaN optimal growth temperatures makes difficult to achieve InGaN layers with good structural quality across the whole compositional range, and problems such as In segregation [48, 49] or phase separation may appear [50, 51]. Due to the higher binding energy of GaN in comparison to that of InN, Ga atoms are preferentially incorporated into the crystal [52], so the growth conditions have to be carefully designed in order to obtain the desired In content. Therefore, despite InN and GaN growth diagrams are well known [53, 54], the growth regimes for InGaN are not clearly defined. Actually, there are very few studies reporting the growth of InGaN layers for intermediate compositions ($30\%<x<70\%$), since the miscibility of the binaries in such region is low. To understand the relation between the stoichiometry and the crystal quality in such InGaN layers, a detailed study of InGaN layers in the whole compositional range is shown here.

(a) Relation between composition and miscibility

A set of $In_xGa_{1-x}N$ samples was grown by PA-MBE on (0001) GaN templates. All the ternary layers were grown under metal-rich conditions (III/V>1), in order to keep them comparable. Every sample showed In droplets on its surface after the growth, which were removed with a HCl treatment. Considering the complex role of decomposition in the growth of InN [53, 55], both temperature and In/Ga flux ratio were modified simultaneously to accommodate the conditions to the desired composition. Table 5.3 summarizes the used growth parameters. Note that for samples with $x>50\%$, a constant temperature of 475 ºC was selected, since decomposition at higher temperatures would not allow the correct incorporation of In to the film. This is, in addition, a compromise

to keep a good crystal quality at high In contents. The In flux was fixed in samples B5-B7, to analyze independently the effect of the temperature at intermediate compositions.

Table 5.3 Growth parameters for PA-MBE InGaN layers and extracted RBS composition. The III/V ratio was slightly higher than 1 (metal rich).

Sample	$\Phi_{In}/(\Phi_{In}+\Phi_{Ga})$	T (ºC)	x (%)
B1 (R360)	**0.00**	**700(5)**	0(1)
B2 (R359)	**0.16**	**640(5)**	6(2)
B3 (R358)	**0.26**	**625(5)**	17(2)
B4 (R355)	**0.50**	**610(5)**	33(2)
B5 (R366)	0.58	**590(5)**	43(2)
B6 (R372)	**0.58**	**570(5)**	45(2)
B7 (R373)	0.58	**550(5)**	50(2)
B8 (R380)	**0.76**	**475(5)**	74(2)
B9 (R382)	**0.86**	**475(5)**	87(2)
B10 (R374)	**1.00**	**475(5)**	100(1)

RBS/C experiments were performed with a 2 MeV He^+ beam. However, considering the thickness of the films, at such energy In and Ga signals overlap in the spectra, so the analysis of the depth profiles can produce ambiguous results. In order to completely separate the In signal avoiding misinterpretations, further experiments were carried out with 4 MeV He^{2+}. Random and <0001> aligned spectra were collected in each sample, as usually.

Figure 5.9 shows four selected RBS spectra with different compositions, from x=17 % to x=74 %. The In signal is well separated due to its narrower extension coming from the lower stopping power of He^{2+} ions at 4 MeV. As an additional advantage, the sensitivity to N (not shown here for clarity purposes) in these conditions is higher than at 2 MeV because of the non-Rutherford cross section. The simulations of the experimental data show homogenous composition in the InGaN films, where a single layer model was assumed. Only sample E2 did not follow this behavior, exhibiting a pronounced gradient at the GaN interface (changing from x=4 % at the beginning of the growth to x=6 % at the surface). The nominal composition derived from the precursor

fluxes is normally not coinciding with the RBS one, because of the InN decomposition in the evaluated temperature range [52]. Therefore, the nominal values are overestimated, but this point will be analyzed in detail in the next section.

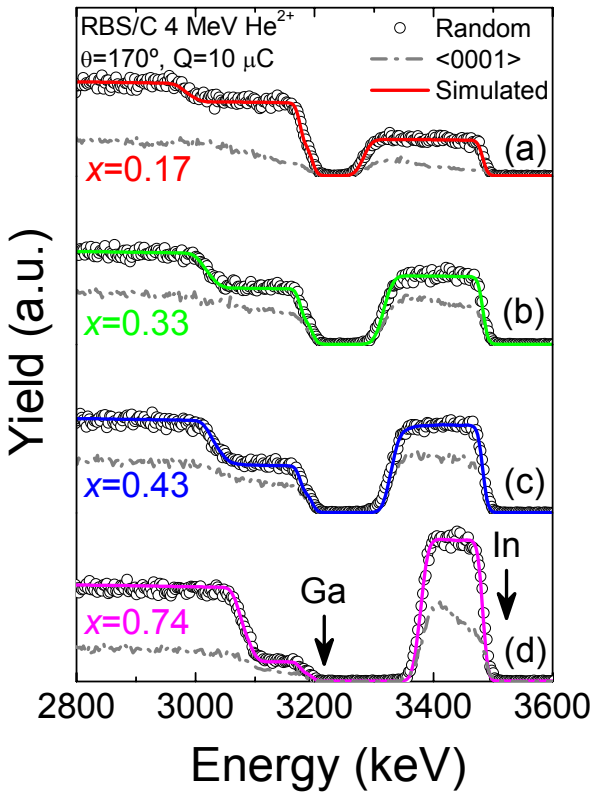

Figure 5.9 Random and <0001> aligned RBS spectra of InGaN HSs with different compositions. Simulation is also shown in the graph (solid line).

The <0001> aligned spectra are also shown in Figure 5.9. The minimum yield of the In signal gradually increases with the In content, reaching a maximum of ~25 % for $0.4<x<0.8$, and then decreases again. A similar behavior takes place from the Ga signal. This fact is a clear evidence of the loss of crystallinity in the layer with intermediate x, mainly ascribed to the low miscibility of both binary compounds (GaN and InN). For low and high values of x, χ_{min} is in the range from 2 % to 5 %. It is especially remarkable the low value χ_{min}=2.4 % obtained for InN, which is very good when compared to commercial GaN templates (χ_{min}=1.9 %).

In order to compare RBS/C results, (0002) RSMs were acquired by HR-XRD in a D8 diffractometer (see chapter 2). These RSMs are an alternative way to obtain the $\omega/2\theta$ scans, but with the additional advantage of completely separating the InGaN and GaN

signals (since the diffracted peaks are not overlapped in the RSM). This modus operandi, therefore, can enhance the resolution of conventional analysis using an open detector, which normally evidences a strong overlap of the GaN and InGaN peaks, especially for low *x*. FWHM was calculated from such *ω/2θ* scans (Figure 5.10), obtained by the integration of the RSMs.

A good correlation was found between χ_{min} and the FWHM (of XRD peaks), as shown in Figure 5.10. Therefore, it can be concluded that the best structural quality is obtained for layers with low or high *x* values, while layers close to *x*=50 % present a high degree of disorder. This result points out miscibility limitations when the presence of InN and GaN phases is similar in the compound.

(b) Growth diagram for PA-MBE InGaN layers

As mentioned before, the limitations in the growth of InGaN are not only due to the low miscibility of the binaries, but also to the key role of decomposition processes [52]. When the InN decomposition reaction takes place, N atoms form N_2, becoming non-reactive and In atoms segregate towards the surface. Therefore, decomposition acts like another III-element source, and when these In atoms reach the surface they can be desorbed or reincorporated [56].

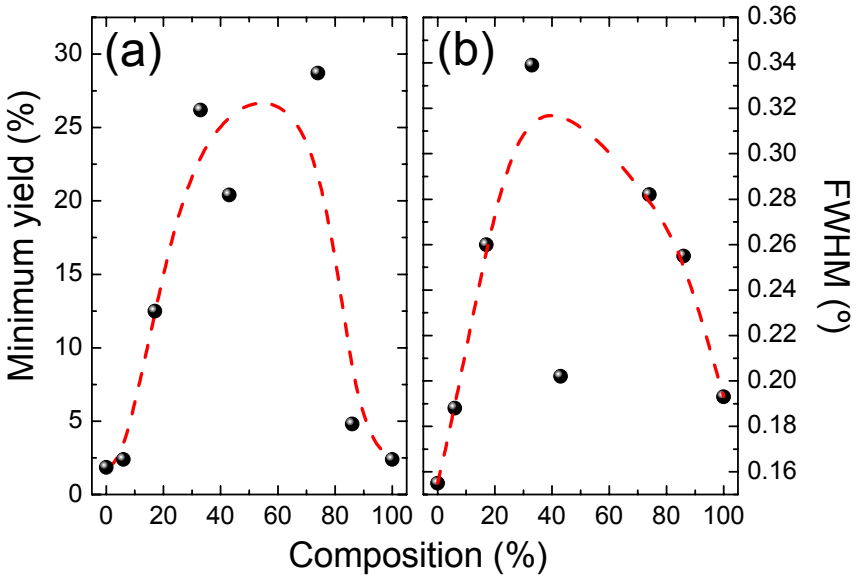

Figure 5.10 Comparison of minimum yield in RBS/C and FWHM from (0002) HR-XRD scans. Both parameters follow the same trend. Errors lay within the symbol size. The line is a guide for the eye.

Averbeck *et al*. [52] have described the decomposition mechanisms by means of an Arrhenius behavior, and therefore the effective (negative) flux of In is controlled by an activation energy (E_a):

$$\Phi_{In}^{dec}(T) = C \cdot x_{RBS} \cdot e^{-E_a/k_B T} . \tag{5.2}$$

Here, C is a constant factor, k_B is the Boltzmann constant, x_{RBS} is the actual composition (measured by RBS in our case), and T is the growth temperature. Of course, x_{RBS} does not correspond to the nominal x, so it can only be known after the deposition of the film. RBS measurements can be used, therefore, to determine the InN losses and the activation energy. The value of Φ_{In}^{dec} is estimated as the difference between the nominal flux and the incorporated one:

$$\Phi_{In}^{dec}(T) = \Phi_{In} - \Phi_{In}^{inc} .$$

For the calculation of the incorporated In flux, it should be taken into account that, for the used growth conditions, all the Ga reaching the surface is incorporated to the film. Thus, the composition of the InGaN film is given by the ratio:

$$x_{RBS} = \frac{\Phi_{In}^{inc}}{\Phi_{In}^{inc} + \Phi_{Ga}} \quad \Rightarrow \quad \Phi_{In}^{inc} = \frac{x_{RBS}}{1 - x_{RBS}} \Phi_{Ga} .$$

Finally, equation (5.2) can be transformed into:

$$\frac{\Phi_{In}^{dec}(T)}{x_{RBS}} = \frac{1}{x_{RBS}} \Phi_{In} - \frac{1}{1 - x_{RBS}} \Phi_{Ga} = C \cdot e^{-E_a/k_B T} , \tag{5.3}$$

where all the parameters in the first term can be known experimentally.

The Arrhenius fitting of equation (5.3) gives an activation energy of 2.0(2) eV for the InGaN series [57]. This value is in disagreement with the one obtained by Averbeck *et al*. [52] (3.5 eV) but compares well with the results of Gallinat *et al*. [53] (1.92 eV) for InN. Besides, the calculated activation energy is in good correspondence with the In-N binding energy (1.93 eV) [58]. As it will be shown in the next chapter, the value of 2 eV is also similar to that obtained for AlInN layers [55]. Consequently, current results suggest that the InN decomposition is independent on the In-containing nitride.

Using the deduced activation energy, a growth diagram for InGaN films can be developed. Figure 5.11 shows the deduced diagram for a given Φ_N-Φ_{Ga} value (3 nm/min). In this diagram the boundaries between the different growth regimes, namely, In-droplets, intermediate In-rich, and N-rich are represented. A fourth regime is shown (no In incorporation) where In incorporation is negligible due to thermal decomposition. The boundaries between the different regimes are derived from the conservation of In atoms at the growth front:

$$\Phi_{In}^{act} = \Phi_{In} + \Phi_{In}^{dec} - \Phi_{In}^{inc} - \Phi_{In}^{des}, \tag{5.4}$$

where Φ_{In}^{act} is the In accumulation rate (actual flux) and Φ_{In}^{des} is flux of desorbed In.

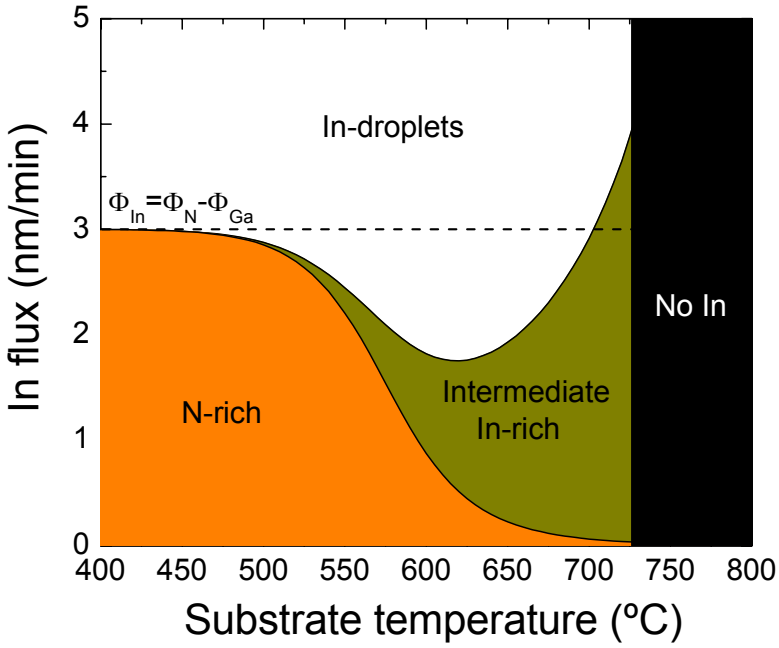

Figure 5.11 Growth diagram for PA-MBE InGaN layers for a fixed condition Φ_{In}=3 nm/min.

Three boundaries can be defined for (5.4). Below 550 ºC, the In desorption is a negligible process [53]. Then, the In incorporation is limited by N, being the border between the N-rich and the In-droplets regime given by:

$$\Phi_{In} + \Phi_{In}^{dec} = \Phi_{In}^{inc} = \Phi_N - \Phi_{Ga}.$$

Above 550 ºC, desorption becomes non negligible and the growth can be carried out under intermediate In-rich conditions with a dynamically stable In adlayer [55].

Therefore, the boundary between In-rich regimes (intermediate and droplets) is given by:

$$\Phi_{In} + \Phi_{In}^{dec} = \Phi_{In}^{inc} + \Phi_{In}^{des} = \Phi_N - \Phi_{Ga} + \Phi_{In}^{des},$$

where the activation energy for the In desorption is 2.49 eV [53].

Finally, at the no-In incorporation regime boundary, the In incorporation rate equals the InN losses caused by thermal decomposition. Inside this regime, the In incorporation tends to zero, although a small fraction of In always incorporates. Actually, above a certain temperature (~750 ºC), the boundary does not depend on the impinging In flux because the incorporation of In atoms is limited by the active N available.

(c) Relation between relaxation and temperature

The important role of the temperature to attain high quality InGaN layers, due to decomposition processes, has been shown in the previous section. The extra amount of In provided by the decomposition can affect, besides, to the stain state of the ternary layers. In order to evaluate this point, RSMs were acquired along the (0002) and the $(10\bar{1}5)$ reflections.

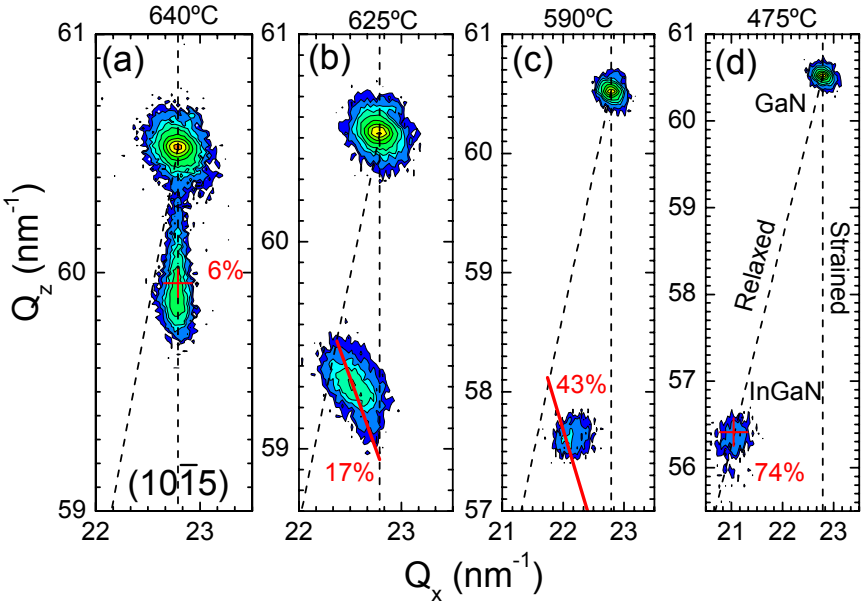

Figure 5.12 RSMs in the $(10\bar{1}5)$ reflection for samples with different composition. A transition from a strained to a relaxed state takes place. Lines correspond to lattice points with the same composition but different strain state.

Figure 5.12 shows the $(10\bar{1}5)$ RSMs evolution for different compositions. For very low compositions (x=6 %), the growth is pseudomorphic (a). As x increases (the temperature decreases) the layers experiment a partial relaxation (b,c). Then, for x>50 %, the InGaN appears almost completely relaxed (d). It is important to notice that sample B2 showed a clear gradient at the interface, which is the responsible for the elongated peak measured in the RSM (Figure 5.12a). On the contrary, in sample B3 (Figure 5.12b) the peak is tilted, corresponding to a line of constant composition (x=17 %), what indicates that the relaxation takes place preserving the In content. This kind of composition-independent relaxation can derive into phase separation, as it has been already reported by Pereira *et al.* [50]. However, in the current case, both (0002) and $(10\bar{1}5)$ RSMs show one single peak, so technically there is no phase separation in the InGaN film. As a remarkable point, sample B10 (InN) is not completely relaxed.

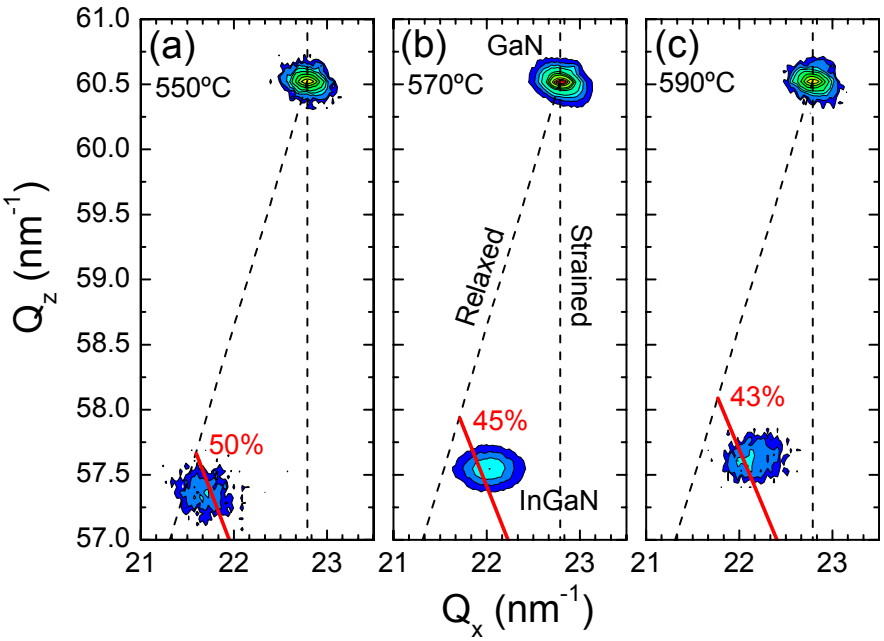

Figure 5.13 RSMs in the $(10\bar{1}5)$ reflection for samples with different temperatures. Relaxation is more pronounced at lower temperatures, when In content is higher.

These results indicate that relaxation is linked to high In contents, especially for x>50%. This fact is supported by the People-Bean model [59] for the calculation of the critical thickness. The application of this model to the $In_xGa_{1-x}N$ films shows a sharp decrease of the critical thickness from 10 nm (x=30 %) to only 1 nm for x=50 % [5]. Furthermore, the in-situ RHEED measurements showed a clear change from streaky

patterns (2D growth) at the beginning to spotty patterns (3D growth) after some nm's. Therefore, the physical mechanism inducing the relaxation of the films is associated to the fast In incorporation when decomposition is low.

As a final confirmation of this point, samples B5-B7 were studied, where only the temperature was varied. Figure 5.13 shows the $(10\bar{1}5)$ RSMs for these three samples. The In content in each sample is slightly affected by the temperature, as expected from the growth diagram of Figure 5.11. Therefore, sample B7 has x=50 % whereas B5 has only x=43 %. At the same time, a clear relaxation is taking place when the temperature diminishes. Since the In flux was not modified in this series, this fact can only be explained by the enhanced incorporation of In due to the minor decomposition at low temperatures, which provokes a fast relaxation of the film, as predicted by the People-Bean model.

In addition, the reduction of the strain state is not linear and can become very intense (Figure 5.14). In these samples, the strain state changed from -3.2 % (R=60%) to -0.5 % (R=95 %) in just 40 ºC. Therefore, considering that relaxation is an important phenomenon that generates phase separation via spinodal decomposition [60], this kind of processes has to be considered when fixing the conditions to grow high-quality InGaN layers.

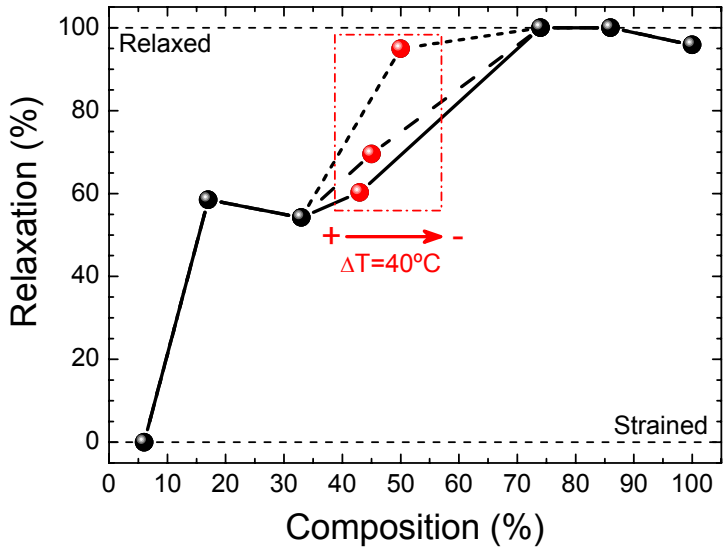

Figure 5.14 Relaxation parameter for InGaN samples with increasing composition. A progressive increase takes place but there is a critical dependence with the temperature.

5.3. Ternary ZnO-based heterostructures

Nowadays, an intense effort is being developed on ternary ZnO HSs [4]. In particular, the incorporation of Mg or Cd allows the modification of the bandgap in a controlled way within a limited range, because the wurtzite structure of ZnO is not preserved for high contents of these elements. Full-color ZnO-based LEDs have been already achieved using these MgZnO and CdZnO HSs [61].

MgZnO films have been also applied to enhance the p-type behavior of undoped [62] and doped [63] ZnO, which is one of the main challenges for the development of ZnO-based technology [64]. ZnO films with p-type characteristics have been accomplished usually by means of the incorporation of elements belonging to the V-group [65] such as N [10, 12], Sb [66, 67], P [68], etc. The high relevance of these issues, bandgap modification and p-type doping, motivates the following studies.

5.3.1. MgZnO layers for bandgap engineering

Two series of $Mg_xZn_{1-x}O$ samples were grown on sapphire by MO-CVD (see chapter 2 for details). The Mg content was modified by changing the Mg and Zn fluxes, but keeping a constant ratio VI/II=70. The growth temperature was 600 ºC and the deposition time 60 minutes. For each deposition, two kinds of substrates were selected to accomplish different orientations of the MgZnO film. On the one hand, a-plane MgZnO was grown on $(10\bar{1}2)$ sapphire. On the other hand, c-plane MgZnO was grown on $(11\bar{2}0)$ sapphire substrates. The deposition conditions were the same for both series, since the growth on both substrates was done simultaneously. The use of non-polar planes is proposed because of the adverse effect that intense electric fields can have in the lifetime and performance of WBS devices [69].

Despite the deposition time was the same for all the samples, due to the different growth rate the thickness changed from 350 nm to 790 nm. To ensure a complete separation of the Mg and Zn signals in this thickness range, getting at the same time a good sensitivity to O content, a beam energy of 3.035 MeV was selected in the RBS experiments. As discussed in chapters 2 and 4, the cross-section of O atoms in such conditions is 24 times higher than the Rutherford one, so it is easy to detect O-rich regions.

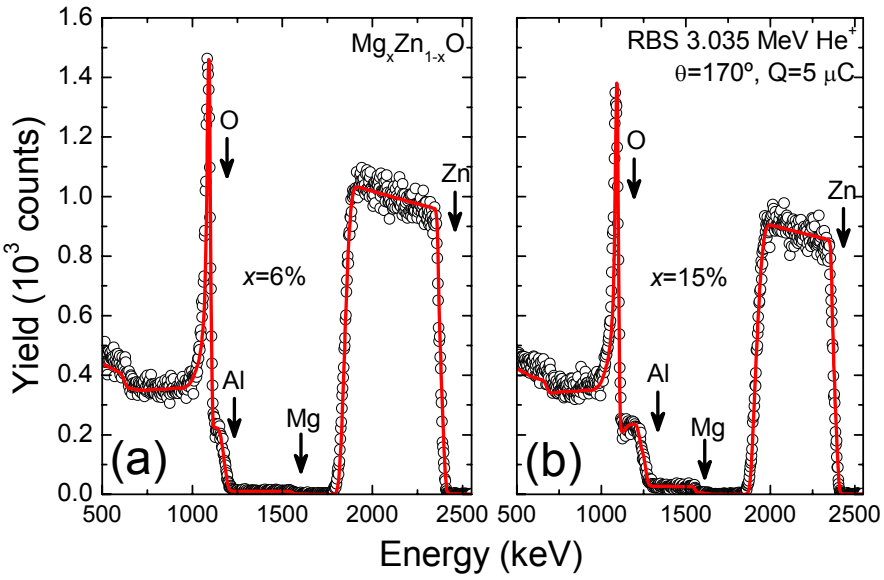

Figure 5.15 Random RBS spectra for two MgZnO layers with different compositions.

Figure 5.15 shows the experimental spectra of two samples with a different Mg content. The Mg signal is, in fact, well-separated from that of Zn, allowing an unambiguous compositional analysis. The O signal overlaps with that of Al from the sapphire substrate, but since the sensitivity to O is enhanced by the non-Rutherford cross-section (peak in the spectra) it can be clearly distinguished.

The simulations of the RBS data were done with the RBX software [70] as usual. The main result extracted from the fittings is the O-rich growth of the films. This means that the addition of Zn and Mg atoms is lower than the O one. This fact is not surprising because the VI/II ratio was 70 (O-rich conditions). Therefore, for the calculation of *x*, the Mg concentration was normalized to the total amount of Zn+Mg atoms.

The different orientation of the films seems to play no role in the actual composition of the films, because similar contents of Mg were found in both a- and c-planes. Indeed, the incorporation of the Mg is homogeneous, showing no in-depth gradients. However, the roughness at the sapphire interface seems to be higher for the second case (c-plane), and RBS spectra reveal a more pronounced Al-Zn interdiffusion.

Concerning RBS/C measurements, only the samples grown in the $<11\bar{2}0>$ direction showed a significant single crystalline behavior to allow channeling studies. This result, together with the increasing roughness of the MgZnO films grown in the <0001> direction, indicates a better growth of the a-plane MgZnO films. The angular scan along

the $<11\bar{2}0>$ axis is shown in Figure 5.16 for the three elements. Note that, thanks to the non-Rutherford cross-section, the O signal can be resolved even despite the overlapping with the Al background. This procedure, already discussed in chapter 4, consisting of the extraction of the normalized yield with two energy windows (one for O and one for Al) of the same width. The Al integrated signal is subtracted from the O signal and, in order to assume the constant background approximation, both windows are set as close as possible. From the angular dips, Mg and Zn signals follow the same trend, suggesting a good substitutional behavior of Mg atoms. Nevertheless, angular scans along further directions would be required to certify this conclusion via a triangulation procedure. Since the layers show a low crystalline quality (χ_{min}=65 % for Zn), these additional measurements along oblique axes were not feasible.

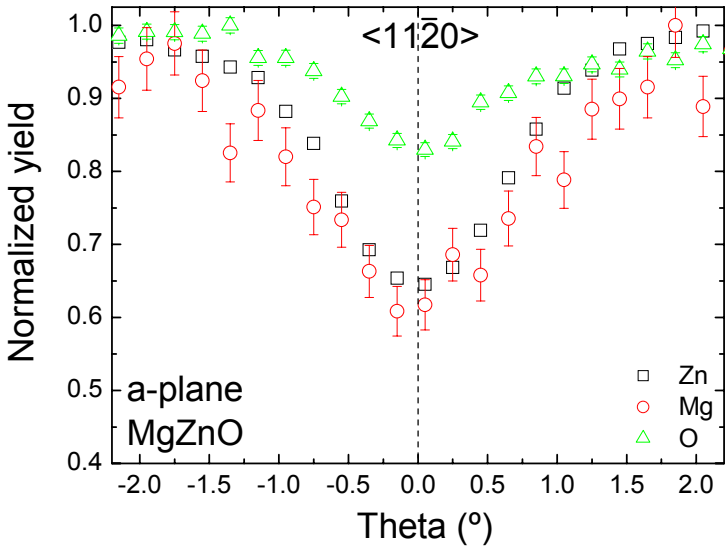

Figure 5.16 Angular scan along the $<11\bar{2}0>$ axis of a MgZnO film. Despite the low quality, Mg and Zn atoms show the same behavior.

The composition extracted from RBS measurements was compared with the bandgap energy of the films. The gap was determined using the absorption coefficient (see Figure 5.17a), which was extracted from the transmittance measurements of the films. As shown in Figure 5.17b, the bandgap energy increases with the Mg content, following an almost linear behavior (calculations with further series show a quadratic term of -0.08). The performance of Schottky diodes based on these MgZnO HSs has been studied by Hierro *et al.* [9], showing the carrier compensation by two deep levels associated to the presence of Mg.

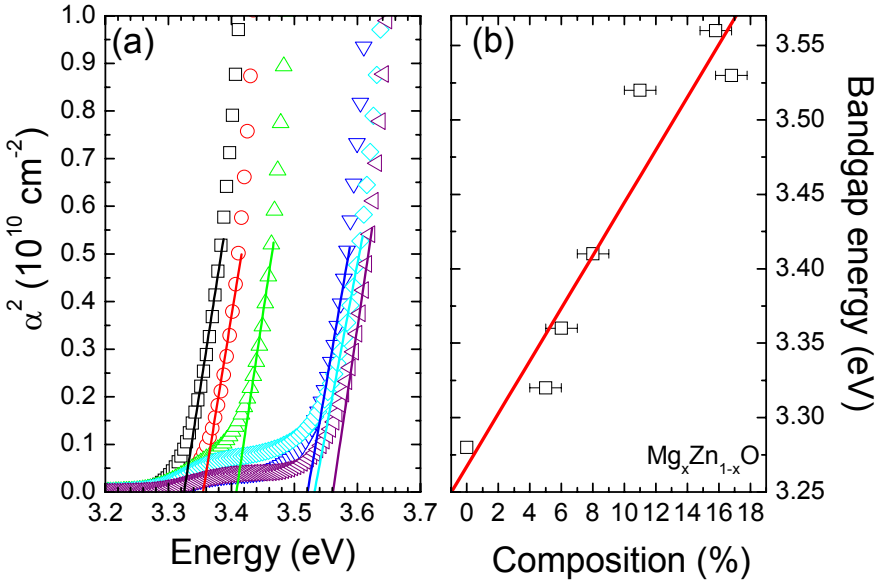

Figure 5.17 (a) Determination of the bandgap using the absorption coefficient of MgZnO films (data are courtesy of A. Nakamura) (b) Bandgap energy as a function of the composition.

5.3.2. N doping of MgZnO layers by ion implantation

Currently, the p-type doping of ZnO has become a great mystery, generating a lot of skepticism. The normal approach for p-doping of ZnO is the inclusion of elements belonging to the group-V (N, P, As, Sb…). Due to the similar atomic radii, N has been normally preferred [64]. N incorporation can be carried out not only during the growth of the films, but also by ion implantation. Of course, the implantation has the important drawback of crystal damage, which has to be reconstructed by subsequent thermal annealing. However, this technique is not limited by the solubility, so it is suitable for basic structural and systematic studies.

Considering that the carrier compensation of MgZnO films can enhance the p-type behavior [9], N implantation was carried out in a new series of these films. Again, a-plane and c-plane orientations were used for the MgZnO layers. The nominal thickness was 750 nm, despite reference ZnO samples were thinner (250 nm) to allow a better separation of the elements in the RBS spectra. The growth temperature was 700 ºC, what allowed a significant increase of the crystal quality of the layers with respect to the previous set (grown at 600 ºC). Actually, the values found in ZnO were χ_{min}=19.1% for <0001> axis and χ_{min}=36.9% for $<11\bar{2}0>$. It is worth mentioning that the χ_{min} in the <0001> axis is comparable to that found in PMS layers grown at 550 ºC (see chapter 4).

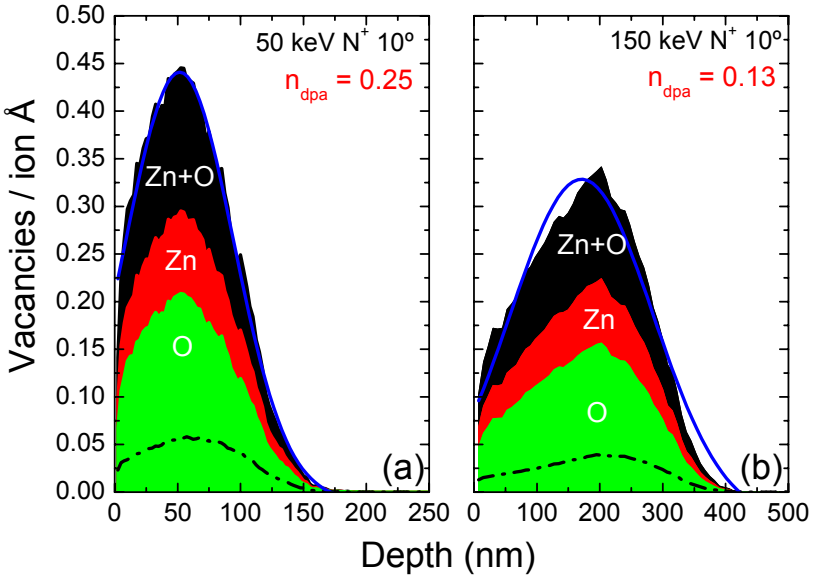

Figure 5.18 SRIM simulations of the generated vacancies during the N implantation at (a) 50 keV and (b) 150 keV. The number of displacement per atom is also displayed.

Prior to the implantation, the energy range was selected by means of SRIM simulations [39]. Considering the different thicknesses of the reference ZnO samples and the MgZnO layers, two energies were selected: 50 keV and 150 keV. These values are a good compromise to cover a large region, warranting the absence of N atoms at the interface. Figure 5.18 shows the expected range and generated vacancies after the implantation. Assuming both Zn and O vacancies, the number of displacements per atom (n_{dpa}) was calculated for a dose of 10^{15} cm^{-2}. The mean values obtained were 0.25 (50 keV) and 0.13 (150 keV), respectively. Since n_{dpa} is significantly lower than 1, the crystal damage of the layers is supposed to be low [71].

The implantation was carried out using the *Danfysik* system (210 kV high flux ion implanter, Model 1090) at ITN (Figure 5.19a). The samples were tilted 10º to avoid channeling effects. After the implantation, different annealing treatments were carried out. For the reference samples, the annealing was developed in a tube furnace (*Thermolab*). Since the SRIM simulations predicted a low value of n_{dpa}, a short time (10 minutes, in air, 1000 mbar) was selected for the annealing. The optimization was done in a 50 keV N implanted sample, using consecutive annealings at 500 ºC, 700 ºC, and 900 ºC. The samples were annealed using a proximity cap layer of ZnO to avoid the O losses. Between each treatment, the RBS random and <0001> aligned spectra were

acquired. Preliminary measurements at 1100 ºC demonstrated the strong Al-Zn interdiffusion in those conditions, so this limit was not attained.

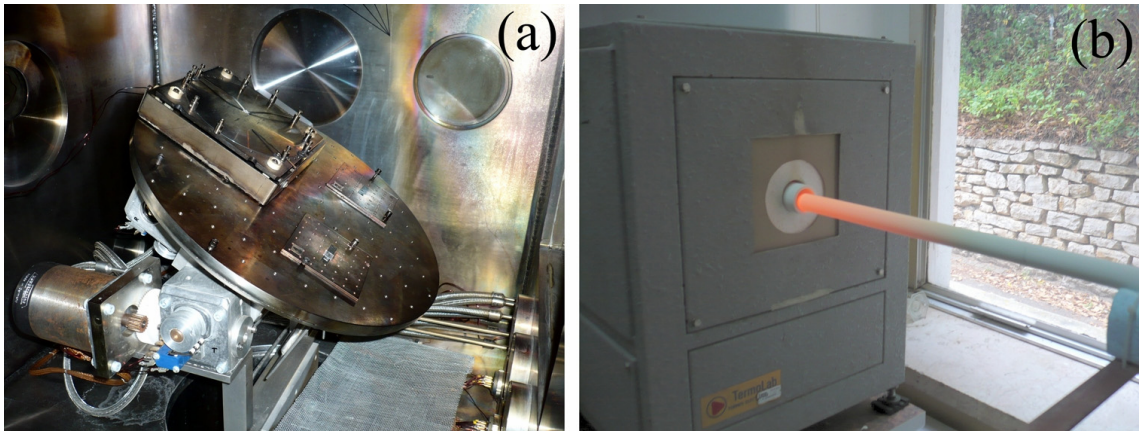

Figure 5.19 (a) Implantation chamber. (b) Furnace tube for thermal annealing.

Figure 5.20 shows the results of the RBS/C experiments for every step of the annealing. It can be seen from the figure that the damage fraction decreases with temperature being the best quality obtained at 900 ºC. Actually, χ_{min} drops from 23.4 % (as implanted) to 11 % (900 ºC), which is even better than the value for virgin samples. Therefore, the quality of the layers can be considered completely recovered at 900 ºC.

With this previous knowledge, the N implantation of four $Mg_xZn_{1-x}O$ samples was developed at 150 keV for different compositions (from x=0 % to x=16 %). Considering that the maximum damage level at this energy is lower than at 50 keV by a factor of ~2 (Figure 5.18), the expected optimum temperature for the annealing should be close to the obtained value in the reference samples (900 ºC). In addition, due to the good crystal reconstruction of the reference samples annealed at this temperature during 10 minutes, a shorter time was selected for the annealing of the MgZnO samples. In particular, a rapid thermal annealing (RTA) of the samples was carried out in an IR lamp (*Mila-3000*). The procedure consisted on a fast (20 s) heating of the sample up to 900 ºC, followed by a steady 2 minutes annealing, and finished with a 15 minutes cooling. As in the previous case, the samples were covered with a ZnO cap to avoid O losses. However, the RTA was also carried out under a N_2 (1000 mbar) atmosphere, so this effect is minimized by these conditions.

Figure 5.21a shows the RBS spectra of a MgZnO sample before and after the implantation (and RTA treatment). The main effect of the RTA is the Al-Zn interdiffusion at the interface with sapphire. This fact is evidenced by the gradients of

the Al (~1300 keV) and Zn signals (~2100 keV), and verified by further RBX simulations. This behavior was not present in the as-implanted sample, i.e., without the RTA, so it is a consequence of the thermal treatment. However, as discussed in chapter 4, this kind of profiles is also common during the growth, even at low temperatures (400 ºC). No significant variations were found in the Mg signal for any composition, what suggests that MgZnO structure is kept after the RTA (no segregation takes place).

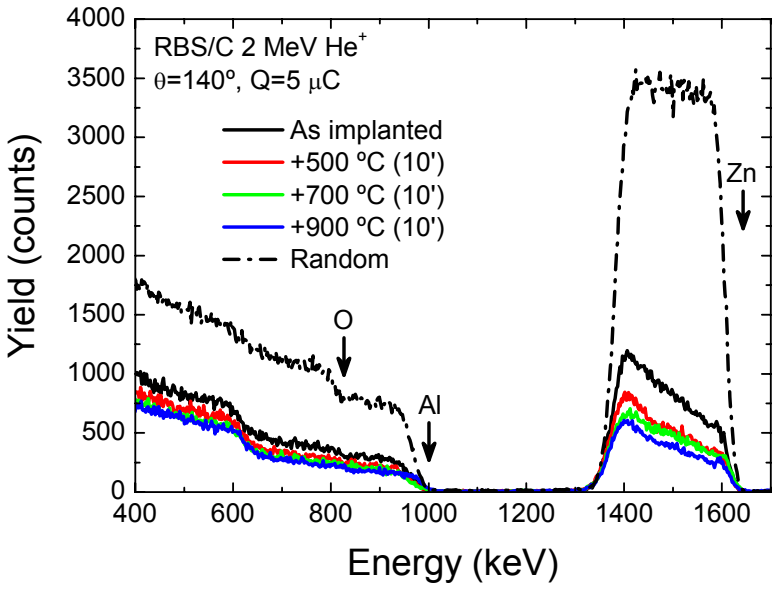

Figure 5.20 RBS/C spectra of a ZnO:N sample after different temperature annealings.

In order to determine the effect of the implantation and the RTA on the defects of the MgZnO layers, the photoluminescence (PL) of the samples was measured. In a PL experiment the sample is excited with a monochromatic laser, detecting the emitted radiation as a function of the wavelength [72]. The samples were cooled down to 8 K in a cryostat and the incident light was originated in a He-Cd laser (λ=325 nm, 5 mW). The emitted light was detected in backscattering geometry with a photomultiplier after passing through a monochromator. More details of the system can be found in reference [73].

Figure 5.21b shows the PL spectra for the as-grown samples. With the increasing composition, the peak shifts to higher energies and becomes broader. The blue-shift (from 3.36 eV to 3.59 eV) is a direct evidence of the bandgap modification with the Mg content, while the broadening of the band edge emission is usually ascribed to alloying. As expected, for as-implanted samples no PL signal was detected due to the generated

defects. However, as shown in Figure 5.21c, after the RTA at 900 ºC, the PL intensity is perfectly recovered (and improved in some cases). Besides, the PL peak in samples with high Mg concentrations is narrower after the RTA treatment. The current results show the correct recovery of the crystal quality in MgZnO:N layers. During the writing of this thesis, the processing of MgZnO:N samples is being prepared to determine the final electrical properties of the material, and further RBS/C experiments will be carried out.

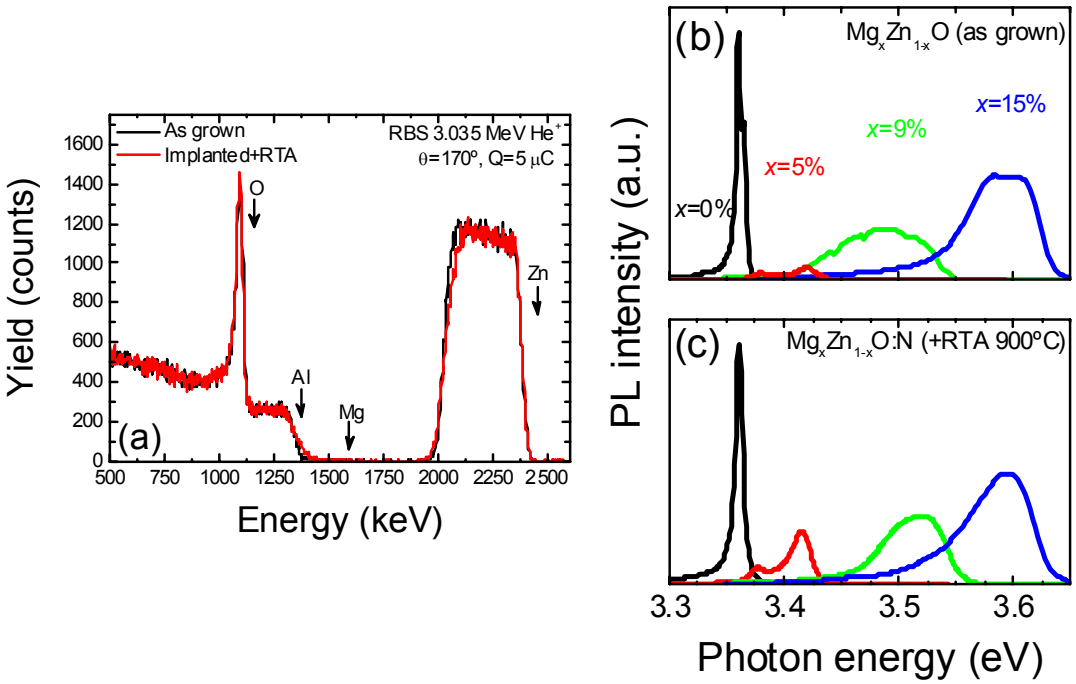

Figure 5.21 (a) Random RBS spectra of as grown and implanted $Mg_xZn_{1-x}O$ sample with x=5%. (b,c) PL spectra of as grown and implanted MgZnO samples. The spectra have the same scales and were normalized with the same reference.

5.4. Conclusions

In this chapter, the characterization of several WBG HSs out of lattice-matched conditions were studied by means of different ion beam techniques (RBS, ERD, NRA) in combination with HR-XRD. AlGaN-based HSs were analyzed as a function of the composition, paying special attention to the detection of Al profiles at the GaN interface. It was proved that IBA can enhance the XRD detection of Al gradients, explaining some of the features observed in the rocking curves. These compositional gradients were observed at high Al contents, and associated to strain relaxation. A good correlation was found between the IBA and the XRD results. The good depth resolution of ERD-BIC for the determination of this kind of profiles in thin layers was

demonstrated on samples with different interfaces. The significant presence of H impurities at the AlGaN/GaN interface was checked with a NRA. The study, performed on samples grown by very different methods, proved the existence of H independently on the growth technique. A diffusive model explains the depth-resolved profiles obtained for H, pointing out the environmental origin of the impurities. No preferential incorporation was found between AlGaN and GaN layers, and a non-negligible amount of H was detected close to the 2DEG region.

Regarding PA-MBE InGaN/GaN HSs, the effect of the miscibility on the crystal quality and composition was investigated. A clear deterioration of the crystal quality was obtained for intermediate compositions, accompanied by a relaxation of the lattice parameters. The RBS results were used to develop a growth diagram for InGaN layers, based on the previous determination of the activation energy for InN decomposition. Three different regions were established.

The composition of MgZnO layers was analyzed by RBS in two different orientations and for different fluxes. The O-rich growth was confirmed by the measurements, and the linear increasing of the gap was correlated with the Mg concentration. Angular scans showed a good crystalline behavior only for a-plane MgZnO films, with a similar trend of Mg and Zn atoms. Finally, N implantation of MgZnO layers was carried out aiming at p-type doping. It was proved that the crystal damage can be recovered with a thermal annealing at 900 ºC, and with a PL emission even higher than the original one. The treatments at this temperature do not affect in a great way the migration of the elements of the layers, except for a slight Al-Zn interdiffusion.

5.5. References

[1] K. Takahashi, A. Yoshikawa and A. Sandhu, *Wide bandgap semiconductors* (Springer, Berlin, 2007).

[2] H. Morkoç, *Nitride semiconductors and devices* (Springer, Berlin, 1999).

[3] E. F. Schubert, *Light-emitting diodes* (Cambridge University Press, Cambridge, 2006).

[4] Ü. Özgür, Ya. I. Alivov, C. Liu, A. Teke, M. A. Reshchikov, S. Doğan, V. Avrutin, S.-J. Cho, and H. Morkoç, J. Appl. Phys. **98**, 041301 (2005).

[5] S. Pereira, M.R. Correia, E. Pereira, K.P. O'Donnell, E.Alves, N. Franco and A.D.Sequeira Appl .Phys. Lett. **81**, 1207 (2002).

[6] A. Jiménez, *Crecimiento y fabricación de transistores HEMT de AlGaN/GaN por epitaxia de haces moleculares*, (Universidad Politécnica de Madrid, Madrid, 2003)

[7] R. F. Davis, S. Einfeldt, E.A. Preble, A.M. Roskowski, Z.J. Reitmeier and P.Q. Miraglia, Acta Mater. **51**, 5961 (2003).

[8] K. Wang, Z. Ding, S. Yao, Nucl. Instr. and Meth. B **259**, 966 (2007).

[9] A. Hierro, G. Tabares, J. M. Ulloa, E. Muñoz, A. Nakamura, T. Hayashi, and J. Temmyo, Appl .Phys. Lett. **94**, 232101 (2009).

[10] C. W. Zou, X. D. Yan, J. Han, R. Q. Chen, W. Gao and J. Metson, Appl .Phys. Lett. **94**, 171903 (2009).

[11] J. L. Lyons, A. Janotti and C. G. Van de Walle, Appl .Phys. Lett. **95**, 252105 (2009).

[12] H.-T. Wang, B. S. Kang, Jau-Jiun Chen, T. Anderson, S. Jang, F. Ren, H. S. Kim, Y. J. Li, D. P. Norton, and S. J. Pearton, Appl. Phys. Lett. **88**, 102107 (2006).

[13] A. Sozza, *Reliability of AlGaN/GaN HEMTs for RF and microwave applications*, (Università degli studi di Padova, Padova, 2005)

[14] O. Ambacher, J. Smart, J. R. Shealy, N. G. Weimann, K. Chu, M. Murphy, W. J. Schaff, L. F. Eastman, R. Dimitrov, L. Wittmer, M. Stutzmann, W. Rieger and J. Hilsenbeck J. Appl. Phys. **85**, 3222 (1999).

[15] M. Fieger, M. Eickelkamp, L. Rahimzadeh Koshroo, Y. Dikme, A. Noculak, H. Kalisch, M. Heuken, R.H. Jansen, A. Vescan, J. Cryst. Growth **298**, 843 (2007).

[16] Y. Wang, L. Ma, Z. Yu and L. Tian, Superlattices Microstruct. **36**, 869 (2004).

[17] S. R. Lee, D.d. Koleske, K.C. Cross, J.A. Floro, K.E. Waldrip, A.T. Wise and S. Mahajan, Appl. Phys. Lett. **85** 6164 (2004).

[18] B. Shen, T. Someya and Y. Arakawa, Appl. Phys. Lett. **76**, 2746 (2000).

[19] A. Redondo-Cubero, R. Gago, F. González-Posada, U. Kreissig, M.-A. di Forte Poisson, A.F. Braña and E. Muñoz, Thin Solid Films **516**, 8447 (2008).

[20] S. D. Hersee, J.C. Ramer and K.J. Malloy, MRS Bull. **22**, 45 (1997).

[21] O. Brandt, P. Waltereit and K.H. Ploog, J. Phys. D: Appl. Phys. **35**, 577 (2002).

[22] S. Krukowski, Diam. Relat. Mater. **6**, 1515 (1997).

[23] J. C. Zhang, M.F. Wu, J.F. Wang, J.P. Liu, Y.T. Wang, J. Chen, R.Q. Jin and H. Yang, J. Cryst. Growth **270**, 289 (2004).

[24] M. F. Wu, A. Vantomme, S. Hogg, G. Langouche, W. Van der Stricht, K. Jacobs and I. Moerman, Nucl. Instr. Meth. B **174**, 181 (2001).

[25] M. Miyoshi, T. Egawa, and H. Ishikawa, Solid-state Electron. **50**, 1515 (2006).

[26] J. L. Sanchez-Rojas, J. A. Garrido and E. Muñoz Phys. Rev. B **61**, 2773 (2000).

[27] S. J. Pearton, J. W. Corbett and T. S. Shi, Appl. Phys. A **43**, 153 (1987).

[28] T. Naono, H. Fujioka, J. Okabayashi, M. Oshima and H. Miki, Appl .Phys. Lett. **88**, 152114 (2006).

[29] J. Neugebauer, and C.G. Van de Walle, Phys. Rev. Lett. **75**, 4452 (1995).

[30] J. Chevallier, and B. Pajot, Solid State Phenomena **85-86**, 203 (2002).

[31] S. J. Pearton, C.R. Abernathy, C.B. Vartuli, J.W. Lee, J.D. MacKenzie, R.G. Wilson, R.J. Shul, F. Ren and J.M. Zavada J. Vac. Sci. Technol. A **14**, 831 (1995).

[32] S. M. Myers, A.F. Wright, G.A. Petersen, W.R. Wampler, C.H. Seager, M.H. Crawford and J. Han, J. Appl. Phys. **89**, 3195 (2001).

[33] C. G. Van de Walle, and J. Neugebauer, J. Appl. Phys. **95**, 3851 (2004).

[34] A. T. Winzer, R. Goldhahn, G. Gobsch, A. Dadgar, A. Krost, O. Weidemann, M. Stutzmann and M. Eickhoff, Appl .Phys. Lett. **88**, 024101 (2006).

[35] F. González-Posada Flores, A. Redondo-Cubero, R. Gago, A. Bengoechea, A. Jiménez, D. Grambole, A.F. Braña and E. Muñoz, J. Phys. D: Appl. Phys. **42**, 055406 (2009).

[36] J. F. Ziegler, C.P. Wu, P. Williams, C.W. White, B. Terreault, B.M.U. Scherzer, R.L. Schulte, E.J. Schneid, C.W. Magee, E. Ligeon, J.L. 'Ecuyer, W.A. Lanford, F.J. Kuehne, E.A. Kamykowski, W.O. Hofer, A. Guivarc'h, C.H. Filleux, V.R. Deline, C.A. Evans Jr., B.L. Cohen, G.J. Clark, W.K. Chu, C. Brassard, R.S. Blewer, R. Behrisch, B.R. Appleton and D.D. Allred, Nucl. Instr. Meth. **149**, 19 (1978).

[37] W. A. Landford, Nucl. Instr. Meth. **149**, 1 (1978).

[38] W. Rudolph, D. Grambole, R. Grotzschel, C. Heiser, F. Herrmann, P. Knothe and C. Neelmeijer 1988 Nucl. Instr. Meth. B **33** 503 (1988).

[39] J. F. Ziegler, J.P. Biersack and U. Littmark *The stopping and range of ions in solids* (Pergamon Press, New York, 1985).

[40] S. J. Pearton, H. Cho, F. Ren, J.I. Chyi , J. Han and R.G. Wilson MRS Internet J. Nitride Semicond. Res. **5S1 F99** (2000).

[41] S. J. Pearton, C.R. Abernathy, C.B. Vartuli, J.D. Mackenzie, R.J. Shul, R.G. Wilson, and J.M. Z, Electron. Lett. **31**, 836 (1995).

[42] D. W. Marquardt, J. Soc. Indust. Appl. Math. **11**, 431 (1963).

[43] J. Mimila-Arroyo, M. Barbé, F. Jomard, J. Chevallier, M.A. di Forte-Poisson, S.L. Delage and C. Dua Appl .Phys. Lett. **90**, 072107 (2007).

[44] C. G. Van de Walle, and J. Neugebauer, Phys. Rev. Lett. **88**, 066103 (2002).

[45] A. Redondo-Cubero, R. Gago, M. F. Romero, A. Jiménez, F. González-Posada, A.F. Braña and E. Muñoz, Phys. Status Solidi c **5**, 518 (2007).

[46] S. Nakamura, Science **281**, 956 (1998).

[47] S. Nakamura, M. Senoh, and T. Mukai, Appl .Phys. Lett. **62**, 2390 (1993).

[48] J. Miguel-Sánchez, *Nitride and dilute nitride: growth, physics and devices* (Transworld Research Network, Kerala, 2007).

[49] A. Dussaigne, B. Damilano, N. Grandjean and J. Massies, J. Cryst. Growth **251**, 471 (2003).

[50] S. Pereira, M.R. Correia, E. Pereira, K.P. O'Donnell, E.Alves, A.D.Sequeira and N. Franco, Appl. Phys. Lett. **79**, 1432 (2001).

[51] T. Takayama, M. Yuri, K. Itoh, T. Baba y J. S. Harris, J. Appl. Phys. **88**, 1104 (2000).

[52] R. Averbeck, and H. Riechert, Phys. Stat. Sol. (a) **176**, 301 (1999).

[53] C. S. Gallinat, G. Koblmüller, J.S. Brown and J.S. Speck, J. Appl. Phys. **102**, 064907 (2007).

[54] G. Koblmüller, S. Fernandez-Garrido, E. Calleja and J. S. Speck Appl. Phys. Lett. **91**, 161904 (2007).

[55] S. Fernández-Garrido, Ž. Gačević and E. Calleja, Appl .Phys. Lett. **93**, 191907 (2008).

[56] S. Fernandez-Garrido, G. Koblmüller, E. Calleja and J.S. Speck J. Appl. Phys. **104**, 033541 (2008).

[57] J. Pereiro, A. Redondo-Cubero, S. Fernández-Garrido, J. Grandal, R. Gago, K. Lorenz, M.A. Sánchez, N. Franco, E. Alves, E. Calleja and E. Muñoz, J. Appl. Phys. **(submitted)** (2010).

[58] J. H. Edgar, *Group-III nitrides* (INSPEC, London, 1994).

[59] R. People, and J.C. Bean, Appl .Phys. Lett. **47**, 322 (1985).

[60] S. Y. Karpov, MRS Internet J. Nitride Semicond. Res. **3**, 16 (1998).

[61] A. Nakamura, T. Ohashi, K. Yamamoto, J. Ishihara, T. Aoki, J. Temmyo and H. Gotoh, Appl. Phys. Lett. **90**, 093512 (2007).

[62] Y. F. Li, B. Yao, Y. M. Lu, Z. P. Wei, Y. Q. Gai, C. J. Zheng, Z. Z. Zhang, B. H. Li, D. Z. Shen, X. W. Fan, and Z. K. Tang, Appl. Phys. Lett. **91** 232115 (2007).

[63] M. X. Qiu, Z. Z. Ye, H. P. He, Y. Z. Zhang, X. Q. Gu, L. P. Zhu and B. H. Zhao, Appl .Phys. Lett. **90**, 182116 (2007).

[64] S. J. Pearton, D.P. Norton, K. Ip, Y.W. Heo, T. Steiner, Prog. in Mat. Sci. **50**, 293 (2005).

[65] D. C. Look, and B. Claflin, Phys. Stat. Sol. (b) **241**, 624 (2004).

[66] L. J. Mandalapu, Z. Yang, S. Chu, and J. L. Liu, Appl. Phys. Lett. **92**, 122101 (2008).

[67] J. Z. Zhao, H.W. Liang, J.C. Sun, J.M. Bian, Q.J. Feng, L.Z. Hu, H.Q. Zhang, X.P. Liang, Y.M. Luo and G.T. Du, J. Phys. D: Appl. Phys. **41**, 195110 (2008).

[68] Y. W. Heo, Y. W. Kwon, Y. Li, S. J. Pearton and D. P. Norton, Appl .Phys. Lett. **84**, 3474 (2004).

[69] T. Deguchi, K. Sekiguchi, A. Nakamura, T. Soga, R. Matsuo, S. Chichibu and S. Nakamura, Jpn. J. Appl. Phys. **38**, L914 (1999).

[70] E. Kótai, Nucl. Instrum. Meth. B **85**, 588 (1994).

[71] K. Lorenz, E. Alves, E. Wendler, O. Bilani, W. Wesch and M. Hayes, Appl. Phys. Lett. **87**, 191904 (2005).

[72] C. B. Brundle, C. A. Evans, S. Wilson, *Encyclopedia of materials characterization* (Butterworth-Heinemann, Stoneham, 1992).

[73] S. Fernández-Garrido, *Crecimiento de nitruros del grupo III por epitaxia de haces moleculares para la fabricación de diodos electroluminiscentes en el rango visible-ultravioleta*, (Universidad Politécnica de Madrid, Madrid, 2009)

6

Analysis of heterostructures close to lattice-matched conditions

This chapter shows the characterization of lattice-matched HSs by RBS/C and HR-XRD methods, paying attention to the determination of the crystal quality and the strain state. The importance of the anomalous channeling scans in the determination of the strain is evaluated in several samples through the experiments, establishing the limits for the application of RBS/C by Monte Carlo simulations. Main parameters influencing the angular scans are discussed.

It was as if you fired a 15-inch naval shell at a piece of tissue paper and the shell came right back and hit you. (Ernest Rutherford)

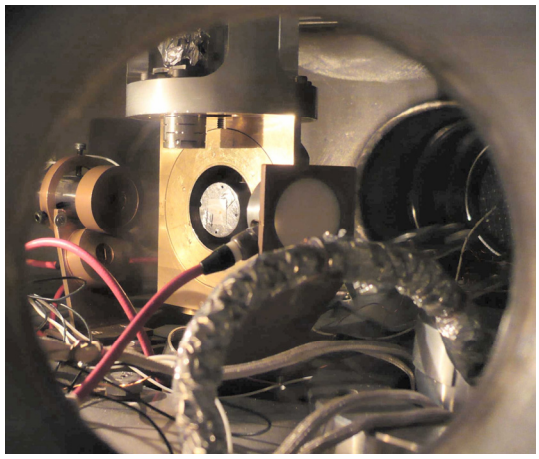

RBS/C experiment of a lattice-matched HS at ITN.

6.1. Introduction

Lattice-matched (LM) heterostructures (HSs) have attracted a lot of interest in the last years due to the multiple applications of these systems [1]. First references related to the growth of AlInN layers appeared in 1981 [2], while the feasibility of growing AlGaInN films was delayed until 1992 [3, 4]. Since then, the application of LM AlInN HSs have been demonstrated in field-effect-transistors [5], Bragg mirrors [6] and HEMTs [7, 8], whereas AlGaInN HSs have been applied for UV-LEDs [9-11] due to the enhanced exciton localization in In-containing compounds. The nominal LM composition to GaN for $Al_{1-x}In_xN$ films is x=18.2 %, what means a fixed bandgap of ~4.4 eV. For the quaternaries, it is possible to control independently the bandgap and the lattice parameters, which is one of their main advantages.

The need of LM HSs is imposed by the fundamental role of the elastic strain in semiconductor materials, not only affecting the crystal quality, but also some electronic properties such as the effective mass, the bandgap and the carrier density [12, 13]. The strain is indeed an important feature for the development of high-power electronic and optoelectronic devices based on III-N compounds due to the large values of the piezoelectric coefficients [14, 15]. In addition, the conventional growth of GaN is normally made on sapphire substrates where, due to the lattice mismatch between both materials (~16 %), the crystal quality decreases significantly by the presence of dislocations and strain [16]. Therefore, there is a considerable attention towards strain-free HSs with low dislocation densities, which seems feasible by the increasing availability of free standing GaN substrates.

Al(Ga)InN systems can be used to achieve LM conditions, but their growth has become a technological challenge because of the inherent differences between the binaries (especially for AlN and InN) associated with lattice parameters, bonding energies and growth temperatures [17]. Thus, some remaining problems can still restrict the capabilities of these HSs. In particular, phase separation [1, 18-21], In segregation [22, 23], relaxation processes [24] and deviations from Vegard's law [25-28] have been already identified experimentally and theoretically in these HSs. Phase separation is, furthermore, one of the proved mechanisms related with the enhanced luminescence in AlGaInN epilayers [29, 30].

Apart from these drawbacks, it must be considered that the most frequent method for determining the strain state of crystalline thin films is XRD. However, this technique does not provide in-depth information in the conventional geometries and, in some cases, the interpretation of the scans is difficult due to the overlapping of reflection peaks. This inconvenience is actually taking place for Al(Ga)InN layers grown close to the LM conditions. On the one side, the compositional analysis of ternaries carried out by XRD is highly dependent on the exact knowledge of the lattice parameters and elastic constants of binary nitrides. On the other side, the XRD compositional analysis of quaternary nitrides is not possible due to the large number of fitting parameters. Therefore, the need of complementary techniques for the determination of composition, strain and crystal quality in these situations is clear (see chapter 1 and 2 for a detailed discussion).

RBS/C in random and aligned geometries is another approach for assessing compositional and structural properties in these crystalline materials (chapter 3). Besides, RBS is especially suitable for the compositional analysis of AlInN ternaries for two reasons. Firstly, the In signal is always separated from Ga one (normally coming from the GaN buffer), which gives a high sensitivity to the In concentration. Secondly, the Al signal, overlapped with the Ga background due to the lighter mass, is well-resolved in LM HSs because of the high content of this element (~82 %). Consequently, RBS analysis can be easily performed on this kind of HSs, avoiding the normal limitations for AlGaN or InGaN layers. Of course, ion channeling can be also used to check the crystal quality and strain with depth resolution, which is an additional advantage.

In this chapter, combined RBS/C and HR-XRD studies on both ternary and quaternary HSs close to LM conditions are discussed. The limitations on the growth of these HSs by PA-MBE are explored, but also the restrictions of the mentioned techniques for the determination of composition and strain state. Finally, the influence of fundamental parameters (thickness, strain state, beam energy) on the accurate measurement of strain by ion channeling is evaluated. Experimental results were simulated by Monte Carlo (MC) methods (FLUX), providing a solid background to interpret the experimental data (see chapter 3) and the accurate determination of the strain in these HSs.

6.2. Characterization of AlInN films grown by PA-MBE

The growth of III-N ternary layers without Ga incorporation is commonly affected by several difficulties during their growth due to the large differences between AlN and InN binaries (detailed in chapter 1). Structural and compositional variations may occur, however, as a function of diverse parameters: the thickness [24], the growth rate [17], the III/V ratio, the temperature [17], the morphology, etc. Currently, phase separation in AlInN has been reported in several works, normally linked to relaxation processes during the growth [24, 25]. Nevertheless, the experimental evidences of phase separation in the whole compositional range are not coinciding with theoretical predictions [31] as it has been pointed out by Hums *et al.* [18]. Moreover, the results derived from this thesis have revealed that, in some cases, phase separation can take place even for completely relaxed films verifying LM conditions [21]. Therefore, the primary mechanisms controlling the growth of these LM HSs are not understood so far.

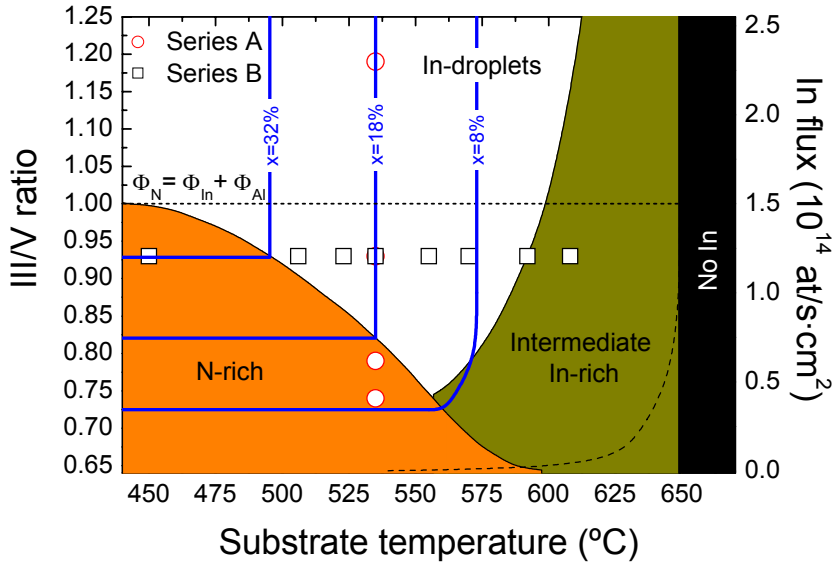

Figure 6.1 Growth diagram summarizing the four different regimes of PA-MBE AlInN films: N-rich, In-droplets, intermediate In-rich and no In. The two sets of analyzed samples are shown. Curves for x=32%, x=18% and x=8% compositions are also represented. Adapted from [17] (courtesy of S. Fernández-Garrido).

Recently, Fernández-Garrido *et al.* [17] established four growth regions for PA-MBE AlInN films, depending on the III/V ratio and the substrate temperature. Using two series of samples, they demonstrated the influence of decomposition and desorption

processes on the growth mode, analogously to what was shown in the previous chapter for InGaN. Figure 6.1 represents the growth diagram of AlInN together with the two sets of samples used for the study in reference [17], one with constant temperature (series A) and one with constant III/V ratio (series B). Varying these parameters different growth regimes can be reached, from N-rich to In-droplets, intermediate In-rich and no In [17].

It is important to note that the nominal III/V ratio does not determine completely the growth regime, since the temperature controls the effective incorporation of In to the ternary [17, 32]. Thus, to avoid misunderstandings, the In-rich regime is called In-droplets regime. The existence of In-droplets is based on experimental facts (SEM images) and not on theoretical calculations, so proceeding this way the distinction between N-rich and In-droplets regime is objective.

The use of one or another growth regime (N-rich, In-droplets or intermediate In-rich) may induce the appearance of compositional depth gradients and relaxation, limiting the quality of the LM AlInN films. In order to clarify the influence of the growth parameters on these aspects, RBS/C and HR-XRD experiments were carried out on the two sets of AlInN samples used in reference [17]. Both of them were grown in the PA-MBE system described in chapter 2, under constant N (Φ_N =4.2·10^{14}) and Al fluxes (Φ_{Al}=2.7·10^{14} at/s·cm^2). The additional details on the growth conditions are summarized in Table 6.1.

6.2.1. Composition and crystal quality

(a) Effect of the III/V ratio: the role of In flux

The set A of samples was composed of four AlInN films grown at 535 ºC, but varying the In flux from Φ_{In}=4·10^{13} to Φ_{In}=2.3·10^{14} at/s·cm^2. Thus, the III/V ratio was changed from 0.74 (N-rich) to 1.19 (In rich). The expected or nominal composition (x) can be calculated by the ratio $x=\Phi_{In}/(\Phi_{In}+\Phi_{Al})$ and, consequently, as the In flux increases the composition of the film should increase too. For this series the calculated x values vary from x=12% (A4) to x=46% (A1). Note that sample A1 has a nominal III/V>1 (In-rich) while samples A2-A4 has a nominal III/V<1 (N-rich).

After the growth, the presence of In-droplets on the surface was checked by SEM [17]. Samples A1 and A2 showed this kind of droplets on the surface, with a size of 1-2 μm. Therefore, despite sample A2 was nominally N-rich, it has to be considered also in the In-droplets regime (see Figure 6.1). The droplets were removed by a surface treatment in HCl before RBS experiments, and the surface roughness after this process was lower than 1 nm in all the samples.

Table 6.1 Growth conditions and main RBS results for PA-MBE $Al_{1-x}In_xN$ samples. For all the samples $\Phi_N = 4.2(1)\cdot10^{14}$ at/s·cm^2 and $\Phi_{Al} = 2.7(1)\cdot10^{14}$ at/s·cm^2.

Sample	T (ºC)	III/V	x_{RBS} (%)	d_{RBS} (nm)	χ_{min} (%)
A1 (R463)	535(5)	**1.19(4)**	18(1)	55(5)	23.3(4)
A2 (R464)	535(5)	**0.93(4)**	18(1)	58(5)	18.8(4)
A3 (R476)	535(5)	**0.79(4)**	15(1)	59(5)	8.5(2)
A4 (R477)	535(5)	**0.74(4)**	10(1)	56(5)	14.3(4)
B1 (R487)	**608(5)**	0.93(4)	2(1)	37(5)	29(2)
B2 (R486)	**586(5)**	0.93(4)	7(1)	51(5)	9.5(4)
B3 (R482)	**555(5)**	0.93(4)	11(1)	54(5)	20.3(5)
B4/A2 (R464)	**535(5)**	0.93(4)	18(1)	58(5)	18.8(4)
B5 (R478)	**523(5)**	0.93(4)	24(1)	70(5)	16.3(3)
B6 (R477)	**506(5)**	0.93(4)	29(1)	70(5)	23.0(3)
B7 (R485)	**450(5)**	0.93(4)	32(1)	74(5)	54(1)

RBS/C experiments were performed with a 2 MeV He^+ beam to determine the evolution of the composition and the crystal quality (using the <0001> axis) with the III/V ratio. Backscattered ions were detected at a scattering angle of 195º, acquiring a total dose of 5 μC. The experimental spectra of sample A2 (also belonging to the series B) are shown in Figure 6.2 together with the RBX simulation. As usually, the N signal is overlapped with the background from the GaN template and, consequently, a stoichiometric nitride was assumed in the simulations. Although the Al/In ratio can be always determined from the data using the areas of the signals, the assumption of the hypothesis of a stoichiometric nitride has to be considered for the calculation of the uncertainty in the concentrations of Al and In (see chapter 2 on this subject). Moreover, the low cross-

section of Al and the Ga background in the spectrum, the GaN stopping force (not measured but used to determine the charge), and the presence of non-detectable light elements can also affect the accuracy of the simulations.

A more detailed view of random and <0001> aligned spectra is shown in Figure 6.3 only for the In signal. The four samples are represented as a function of the III/V ratio, being the main results summarized in Table 6.1. Regarding the random spectra, the first point to consider is the fact that the composition of the layers is overestimated by the relation $\Phi_{In}/(\Phi_{In}+\Phi_{Al})$, as it is shown in Figure 6.4a. In particular, a large difference appears for samples inside the In-droplets regime (A1 and A2), whereas a good agreement was found for samples at low In fluxes. Furthermore, samples A1 and A2 have the same composition, even though the ratio between the In fluxes of both films is ~2. Then, some kind of saturation is taking place during the growth when reaching the In-rich regime, what suggests the influence of non-linear mechanisms on the In incorporation.

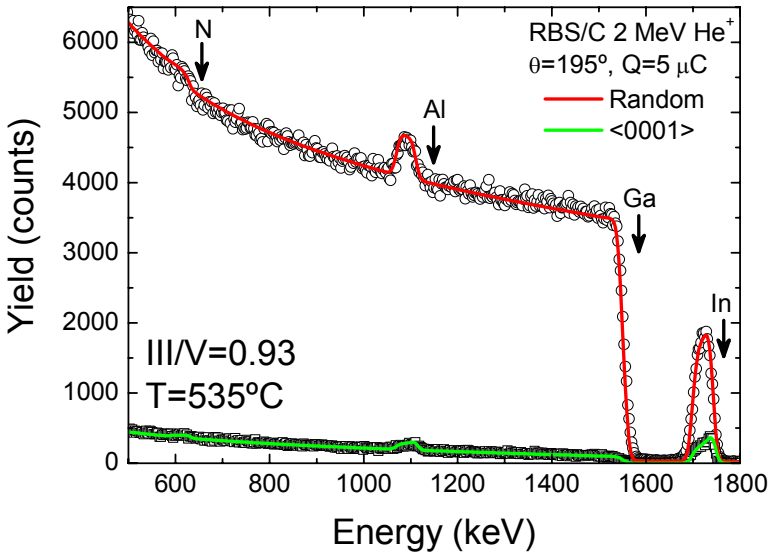

Figure 6.2 Random and <0001> aligned RBS spectra of sample A2=B4 (III/V=0.93, T=535ºC). The composition of the film is 2.6 lower than the predicted one.

These results can be understood on the basis of the growth diagram of Figure 6.1. At the growth temperature (535 ºC) of this series, the formation of the ternary AlInN is limited by the creation of In-N bonds, since the Al sticking coefficient is 1 [33]. However, the formation of the InN depends, not only on the amount of In atoms reaching the surface

(Φ_{In}), *but* also on the InN decomposition rate (starting for T>500 ºC) [22]. Consequently, due to the InN decomposition, there is an effective additional supply of In at the growth front, usually producing metallic In droplets, and desorption of N_2 molecules. This fact modifies the actual growth regime of the samples, since additional N is needed for stoichiometric films.

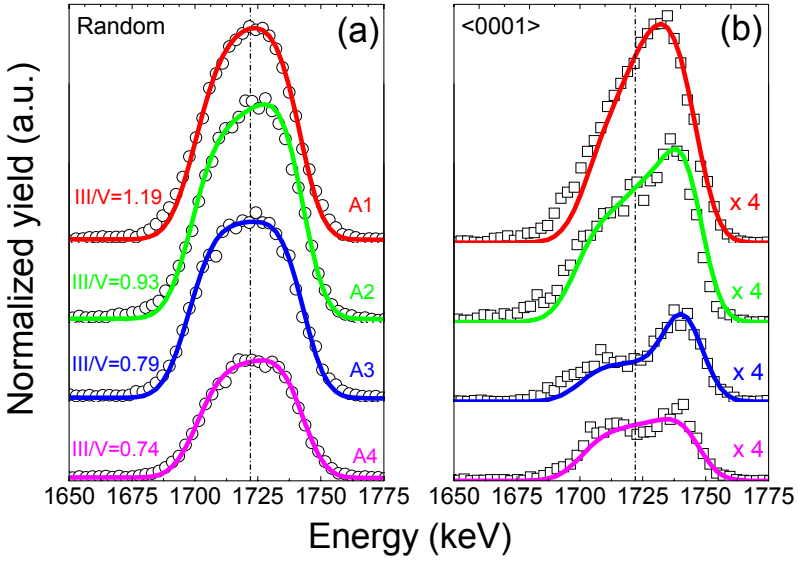

Figure 6.3 Random (a) and <0001> aligned (b) RBS spectra for all the samples of series A. Only In signal is shown for clarity purposes. Composition is preserved in samples grown with In-droplets (III/V>0.9), but a clear decrease takes place for samples grown in the N-rich regime (III/V<0.9). Samples with droplets also show lower crystal quality in the <0001> spectra.

Taking these considerations into account, the nominal N-rich conditions can result in an In-rich behavior. This is exactly the case of sample A2 (III/V=0.93), where In-droplets were found. Thus, the saturation of the composition shown by RBS in samples A1 and A2 reflects that decomposition processes are taking place during the growth. Therefore, the excess of In coming from the InN decomposition in these samples was used for the local formation of droplets but not for the nitridation. The growth of the AlInN film is limited then by the N flux, and due to the insufficient amount of N, the actual composition is lower than the nominal one. As a result of the constant value of the N flux, the saturation of the composition is reached as soon as the In-droplets regime is attained, explaining the features obtained in Figure 6.3.

In contrast to samples A1-A2, the composition of samples A3 and A4 is in good agreement with the nominal value within the experimental errors. This result is an

evidence of the effective N-rich growth in these samples. Actually, for low III/V ratios (<0.9) the N flux is high enough to compensate the N losses from the decomposition, so the actual trend in *x* is expected to follow the theoretical behavior. The segregation of In towards the surface can be easily recombined with the N atoms in these conditions, and no droplets were visible on the surface of these samples.

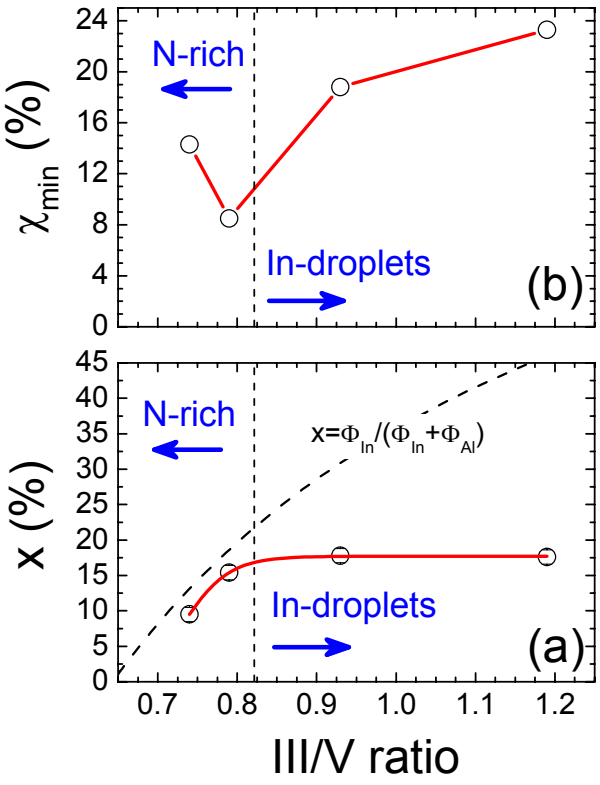

Figure 6.4 Composition (a) and minimum yield (b) as a function of the III/V ratio in series A. Both parameters are flux dependent due to the different growth regimes reached.

It is important to note that the calculated RBS thickness of the samples remain practically constant (see Table 6.1) independently on the growth regime. This fact might seem contradictory considering that the total In flux used along this series increases. Nevertheless, in the N-rich regime the expected variations in the growth rate are low enough to not perceive this effect within the experimental error. Neither are significant variations observed in the In-droplets regime, despite it is reasonable to expect a change due to droplets formation in the growth front of the layer. However, RBS data rule out this circumstance, pointing out that droplets move forward with the growth front, not affecting the total thickness. This conclusion is in agreement with the lack of metallic In signal in the XRD measurements, and also with additional RBS data of AlGaInN

samples discussed later on. The size of the droplets observed by SEM seems to increase with thickness, but during the writing of this thesis, more analyses are being performed to further analyze this point.

The RBS/C spectra along the <0001> axis were used to analyze the crystal quality and the possible effect of the In droplets on it. As can be observed in Figure 6.3b, the lack of microscopic In-droplets inside the film does not mean that crystal quality is preserved. Quite the opposite, the presence of these In-droplets in the growth front (samples A1 and A2) is clearly contributing to the formation of defects; increasing the minimum yield up to 23 % (Figure 6.4b and Table 6.1). This point is especially important, because samples A1 and A2 have the composition required for LM condition with GaN. Therefore, the achievement of high-quality LM AlInN layers is also influenced by the choice of the proper growth regime. Actually, sample A3, grown in the N-rich regime, shows the lower χ_{min} of series A.

The observed behavior of χ_{min} is ascribed to the different mobility of adatoms in the surface during the growth [32, 33]. When III/V ratio is much lower than 1 (N-rich), the mobility is low, making difficult the atomic rearrangements in the lattice positions. For III/V ratios higher than 1 (In-droplets), the droplets induce defects. Therefore, since sample A3 is the closest one to the equilibrium border between the N-rich and the In-droplets regime, the good balance between both phenomena explains the better crystal quality of the film.

This fact could be also related with the obtained RBS depth-profiles. For low III/V ratios (A3-A4), the compositional profile is almost homogenous (Figure 6.3a) demonstrating that, under these conditions, the incorporation of In to the film takes place almost instantaneously. On the contrary, samples A1 and A2 (high III/V ratios) show slight gradients from the GaN interface to the surface, what can be interpreted by the transition from the N-rich regime to the In-droplets regime at the beginning of the growth (note that surface roughness is the same for all the samples, so these gradients cannot be ascribed to this parameter).

(b) Effect of the substrate temperature

Despite the proved essential role of III/V ratio on the composition, the substrate temperature is another parameter affecting decomposition and desorption processes

[17]. These physical phenomena, as discussed in the previous chapter, follow an Arrhenius behavior and, therefore, increase rapidly with the temperature. In order to evaluate these effects, series B (7 samples) was selected. This series was grown at a constant III/V=0.93 (In flux of $1.2 \cdot 10^{14}$ at/s·cm^2), but varying the substrate temperature from 450 ºC to 608 ºC.

Since III/V<1 in this series, the growth was carried out at nominal N-rich conditions. Nevertheless, samples B3-B6 showed droplets on the surface revealing the effective In-rich growth. These droplets were removed before RBS experiments, which were carried out equally to those for the previous series A.

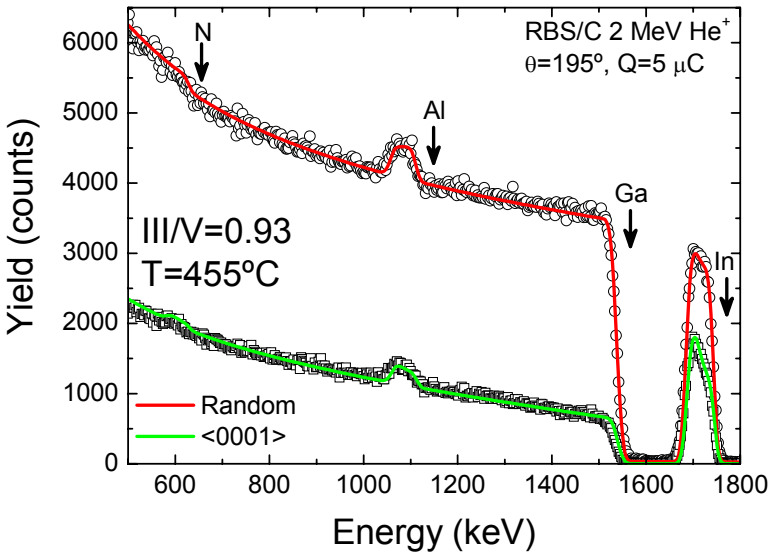

Figure 6.5 Random and <0001> aligned RBS spectra of sample B7 (III/V=0.93, T=450ºC). Composition of the film is in agreement with the nominal value due to the growth under N-rich conditions.

Varying the temperature, different growth regimes of the AlInN layers are obtained. Therefore, to facilitate the discussion about the effect of the temperature on the composition and crystal quality, it is convenient to separate the results in the three regimes of the diagram (Figure 6.1).

N-rich regime (T<500ºC)

The only sample grown with N-rich conditions was B7. Figure 6.5 shows random and <0001> aligned spectra of this sample. In this case the measured RBS composition fits perfectly with the nominal *x* of 31(3) % (see Table 6.1). This fact is explained because,

at very low temperatures (T<500ºC), desorption and decomposition can be neglected, and all the In atoms reaching the surface are incorporated to the ternary film. The formation of metallic In-droplets was not detected because the high enough amount of N available makes possible the recombination of the decomposed InN, avoiding the InN losses, i.e.:

$$\Phi_N \geq \Phi_{In} + \Phi_{Al}. \quad (6.1)$$

The minimum yield of sample B7 is the highest one, reaching 54 %. This bad crystal quality is due to the very low mobility of In adatoms, what prevents their incorporation in lattice-sites. Consequently, although the stoichiometry is maintained in this regime, these conditions are clearly not adequate for growing high-quality AlInN films.

In-droplets regime (500ºC<T<570ºC)

Figure 6.6a shows the RBS spectra of samples B3-B6 for the In signal. As the temperature increases in these samples, the In content clearly decreases, being always below the nominal value. This decrease is not linear, as it will be shown later on (Figure 6.10). Indeed, the calculated thickness by RBS (Table 6.1) is also reduced, so the growth rate is affected by the temperature.

The origin of this behavior is the temperature dependence of the decomposition rate. As shown in the previous series A, for T>500 ºC the decomposition mechanisms are enhanced, which induces the formation of metallic In-droplets. Since the additional In can be reincorporated to the crystal only partially, the formation of the In-droplets provokes an effective reduction of the stoichiometry in the growth front. Under steady state conditions, the thermal decomposition is expected to follow an Arrhenius behavior given by equation (6.2) [32], explaining the non-linear trend of x obtained from RBS. Thus, during the growth in the In-droplets regime, equation (6.1) does not apply, and the equilibrium at the growth front is reached when:

$$\Phi_N = \Phi_{In} + \Phi_{In}^{dec}(T) + \Phi_{Al}. \quad (6.2)$$

Actually, taking advantage of these RBS results, the activation energy of this process can be determined, as in the InGaN case. For that, $\Phi_{In}^{dec}(T)$ is calculated as the difference between the nominal flux and the incorporated one (see chapter 5), assuming

a sticking coefficient of 1 for Al [33]. The corresponding Arrhenius fit gives an activation energy of 2.0(2) eV [17], in good agreement with the In-N bond energy (1.93 eV) [34], the activation energy for thermal decomposition of the In-face InN (1.92 eV) [32], and the results in InGaN compounds (chapter 5). This result points out the universal behavior of the InN decomposition, independently on the selected matrix.

The minimum yield in this regime can be considered essentially constant (~20 %). However, sample B6 shows a flat <0001> aligned spectrum (Figure 6.6b) in contrast to the profiles detected for the other samples. This point might indicate the different velocity of the defect production in the first stages of the growth. This effect could be related to the variable growth rate, the different mobility of the adatoms with the temperature, or the synergy between both phenomena. Actually, sample B6 was grown at the lowest temperature, so both parameters could be the responsible for the extra amount of defects found at the interface.

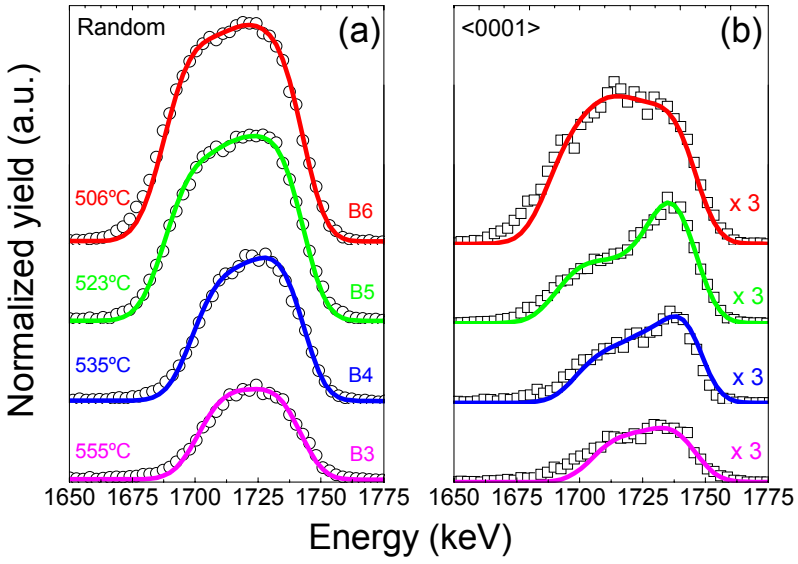

Figure 6.6 Random (a) and <0001> aligned (b) RBS spectra for all the samples grown in the In-droplets regime (B3-B6). As temperature increases the composition diminishes and the aligned spectra show a gradient towards the surface.

Intermediate In-rich regime (585 ºC<T<620 ºC)

Two samples (B1-B2) were grown at very high temperatures (T>560 ºC) but with the absence of In-droplets. The formation of droplets is prevented because, at such high temperatures, In desorption becomes dominant [32], playing an important role in the

growth conditions. Actually, desorption and decomposition can be considered competitive processes. Decomposition results in an effective positive flux of In at the surface, wheras the InN desorption has the opposite effect, behaving as a negative In flux. Thus, equation (6.2) has to be reformulated to take this into account:

$$\Phi_N = \Phi_{In} + \Phi_{In}^{dec}(T) - \Phi_{In}^{des}(T) + \Phi_{Al}\,. \qquad (6.3)$$

As in the decomposition processes, desorption follows an Arrhenius behavior but with a different activation energy (2.5 eV) [32]. Desorption opens a new regime for the growth, named intermediate In-rich, within which a balance between $\Phi_{In}^{dec}(T)$ and $\Phi_{In}^{des}(T)$ can be reached.

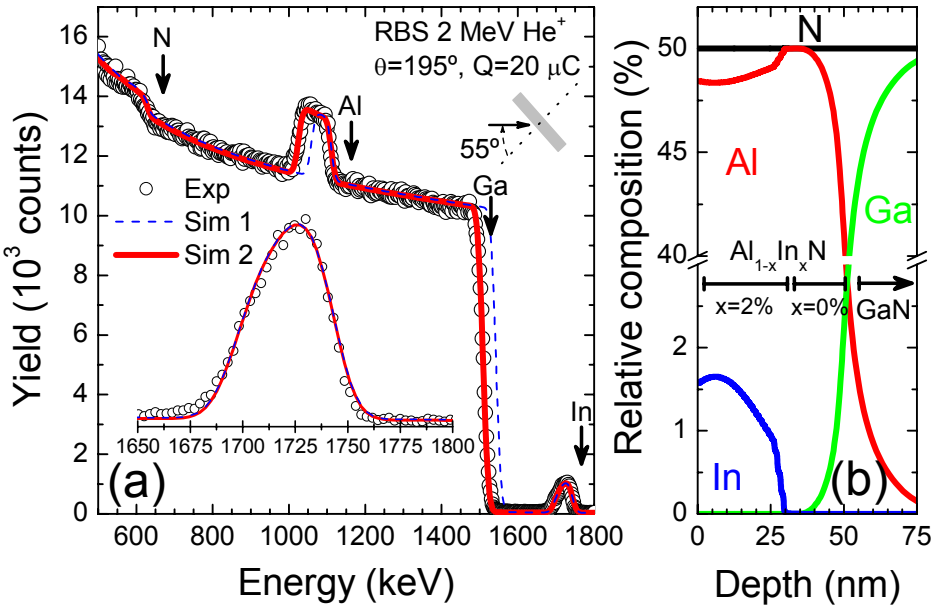

Figure 6.7 (a) RBS spectra and simulation of sample B1, grown at 608 ºC. The data cannot be fitted with simulation 1 (dashed blue line) consisting on an AlInN ternary with a compositional gradient towards the surface. Simulation 2 (red solid line) was carried out including an AlN layer prior to the AlInN and then the spectrum is well-fitted. (b) Relative composition from simulation 2 demonstrates the inhomogeneous growth of the film.

The In content derived from RBS in the two samples grown in the intermediate In-rich regime also decreases with temperature (Figure 6.10). This decrease is faster than in the In-droplets regime because now more In flux would be required in order to compensate the In desorption. However, desorption can only be partially compensated by

decomposition in a dynamical equilibrium. The importance of such a dynamical equilibrium for the uniform growth of AlInN films is very high, and this fact could be verified in samples B1 and B2, so they deserve a special attention.

Note that sample B1 was grown inside the intermediate In-rich regime, that is, with a dominant influence of the desorption factor on the decomposition. Due to the low In content and thickness of this sample, an additional experiment was developed to exactly determine the depth profile in this particular case. RBS measurements were carried out tilting 55º the incidence angle and with a high dose (20 μC). Figure 6.7a shows the random spectrum with the corresponding fitting. The first noticeable feature is the asymmetry of the In signal, revealing that the AlInN layer cannot be fitted with a single layer of homogeneous composition. Consequently, an asymmetric Gaussian gradient with a mean value of x=2.3 % was used to model the In incorporation in the film. The second point to highlight is that In and Al signals do not correspond to the same depth region. To verify this, a simulation with a single AlInN layer (with the mentioned Gaussian gradient, ~30 nm) was performed: simulation 1 in Figure 6.7a. The resulting simulation fits the In signal, but clearly not the experimental Al signal, neither the Ga one from the substrate. Then, a new simulation was performed, including a single AlN layer near the interface between GaN and AlInN (simulation 2 in Figure 6.7a). Thus, the experimental spectrum was fitted perfectly, being the resulting depth profile shown in Figure 6.7b.

RBS results were further confirmed by RSMs carried out on sample B1, shown in Figure 6.8. The $(10\bar{1}5)$ reflection of the AlInN film shows a partially relaxed layer but, as it is clear from the figure, the peak does not fit with a relaxation process for an AlInN film with a constant x=2.3 %. On the contrary, the $Al_{1-x}In_xN$ peak lies within the region delimited by x=0 % and x=2.3 % (see figure). Thus, the elongated reflection in the RSM can be ascribed to the compositional gradient observed by RBS. In addition, the relaxation associated to the compositional gradient can also explain the deterioration of the crystal quality observed by RBS/C in this sample (χ_{min}=29 %).

The conclusion from this comparative study is that the growth conditions were self-altered during the growth. At the beginning, the temperature at the surface was high enough to desorb all the In atoms reaching it, so the formation of the AlInN film was not possible. As a consequence, only AlN was deposited. However, after ~20 nm of

AlN growth, the surface conditions changed and the In atoms started to be incorporated to the ternary AlInN film. More and more In was added to the layer as the growth continued.

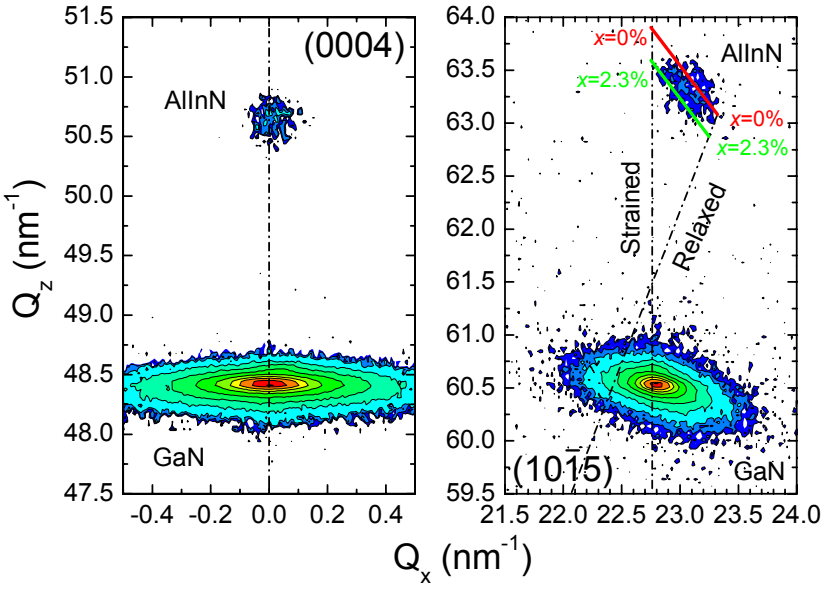

Figure 6.8 RSMs of sample B1, grown at 608 ºC. The $(10\bar{1}5)$ reflection of the AlInN film lies between the lines for x=2.3 % (green line) and x=0 % (red line), evidencing the presence of a compositional gradient, in agreement with RBS results.

The alteration detected in the growth of sample B1 can be associated to a transition towards the dynamic equilibrium of equation (6.3), since activation energies for InN desorption (2.49 eV) and decomposition (2.0 eV) are different. Then, at the beginning of the growth, the desorption of InN is dominant, but as time increases, the local formation of In due to the decomposition can provide enough In excess to compensate it. This kind of In segregation is already known in the growth of InGaAs layers, and responds to a simple mathematical model proposed by Muraki *et al.* [35]. In that model, for a certain initial composition x_0, it is assumed that a fraction R of In atoms on the topmost layer segregate to the next monolayer. The other portion, 1-R, is really incorporated to the film. Therefore, the In composition in each monolayer changes. This model is in good agreement with the experimental depth profile shown here, so its extension to the group of III-nitrides is being considered. However, some improvements

could be necessary since Muraki *et al.* presume a constant probability *R*, independent of the impinging In flux, which can lead to physically unrealistic situations.

In contrast to sample B1, sample B2 was designed to grow verifying the condition for stoichiometry given by (6.3), i.e., almost in the border between the In-droplets and the intermediate In-rich regime. Then, the growth was carried out keeping a balance between decomposition and desorption. Figure 6.9 shows the random and <0001> aligned spectra in this sample. A slightly In poor interface (x~6 %) was found in the RBS analysis, but no evidence of AlN formation was found so the thickness of the ternary film corresponds to the nominal one. Therefore, in this sample it can be concluded that the dynamical equilibrium was reached almost instantaneously. RSMs of sample B2 shows a slight relaxation of the AlInN layer, but it does not correspond to the compositional gradient (see next section).

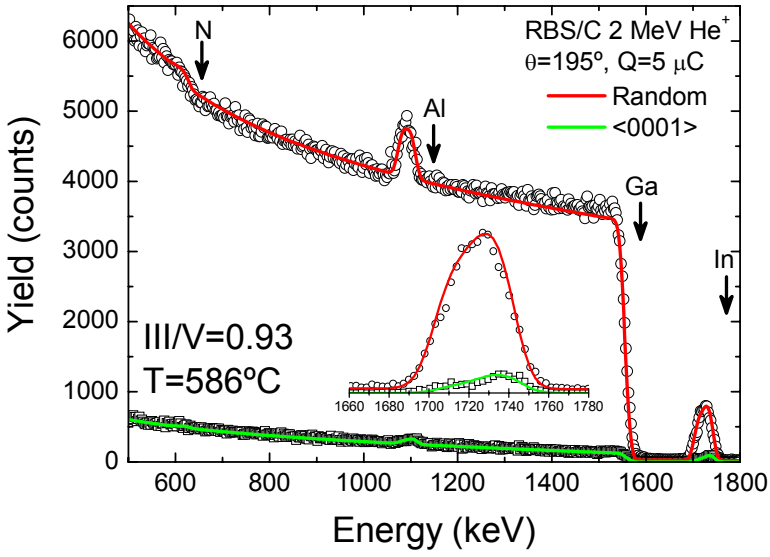

Figure 6.9 Random and <0001> aligned RBS spectra of sample B2 (III/V=0.93, T=586 ºC).

Concerning the crystal quality, within the intermediate In-rich regime the lowest values of χ_{min} are expected, because for such regime the presence of a surfactant In adlayer enhances the mobility of the adatoms. This behavior has been demonstrated in the growth of quaternary films [22, 23]. Sample B2 shows, in fact, the lowest χ_{min} in this series (9.5 %), confirming the good growth of the AlInN close to the In-droplets border. However, sample B1 has a χ_{min}=29 %. The explanation for this high value is, as discussed before, the unstable growth of this sample due to the lack of a dynamical equilibrium between decomposition and desorption. The subsequent compositional

profiles together with the relaxation of the film induce the deterioration of the crystal quality.

It is important to emphasize that the existence of the observed gradients during the growth are critical for the development of high-quality HSs based on multilayers of very few nm's, such as MQW, HEMTs or DBRs. Hence, the discovery of these phenomena could impose a fixed condition for the optimal growth of AlInN HSs.

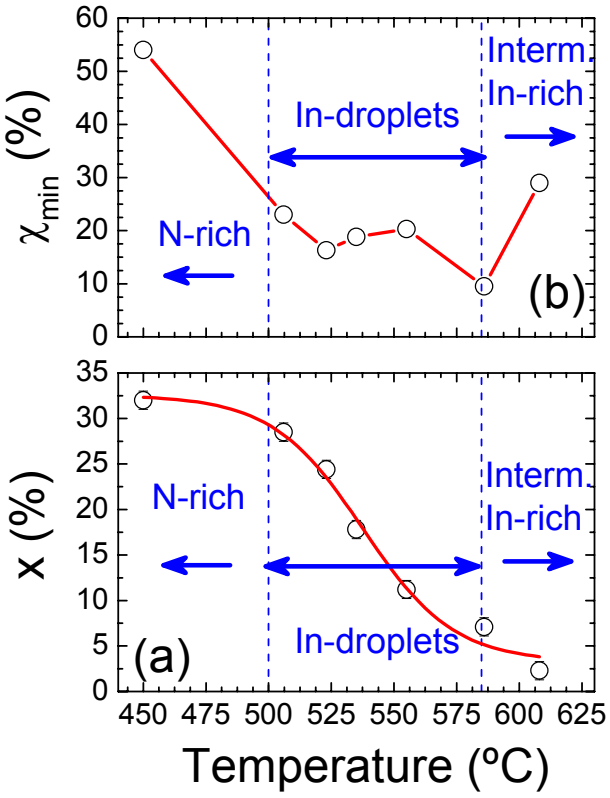

Figure 6.10 Main RBS results for series B. Both composition and thickness decrease with the temperature. Crystal quality is clearly lower at low temperatures, but almost constant for the In-droplets regime.

As a summary of the analyzed samples, Figure 6.10 shows the main results obtained in series B, considering the three different regimes accomplished. The composition corresponds to the nominal value only for the N-rich regime. Then, *x* follows a non-linear decreasing in good agreement with the mentioned Arrhenius behavior of InN decomposition. When temperature is very high (intermediate In-rich), desorption also affects the growth conditions and the composition trends to zero. This reduction in *x* is

accompanied by a decrease of the thickness, what indicates the effect of the temperature on the growth rate.

Nevertheless, the minimum yield does not follow exactly the same behavior as the composition. For very low temperatures (450 ºC), χ_{min} is high (~50 %) because of the low mobility of adatoms. It decreases to χ_{min} ~20% for intermediate temperatures (500 ºC<*T*<570 ºC), where it remains stable due to the presence of In-droplets. Then, for *T*=585 ºC, the crystalline quality reaches its best value (χ_{min}=9.5 %) when the equilibrium between decomposition and desorption is good. At *T*=608 ºC it suddenly increases again to 29 % as a consequence of the compositional profiles and relaxation processes in the film.

6.2.2. Lattice parameters and strain state

As a continuation of the RBS/C study, HR-XRD measurements were performed on both A and B series. Lattice parameters and strain state of the films were obtained from RSMs, normally performed in the $(10\bar{1}5)$ reflection. Figure 6.11 shows the resulting RSMs for selected samples. On the one hand, the evolution in series A, indicated in (a-c) graphics, confirms the pseudomorphic growth of all of them, independently of the III/V ratio. The red crosses in the maps display the expected peak position for a fully strained AlInN layer with the RBS composition. A good agreement with the experimental data was found within RBS errors for these samples.

On the other hand, series B is indicated in (d-f) graphics, covering the In-droplets and the intermediate In-rich regime. Sample B7 did not produce any signal in the RSMs, possibly due to the bad crystal quality of the film at such low temperatures (450 ºC). Thus, the sample with the lowest temperature is B6 (Figure 6.11d). Although in this case the AlInN peak is not completely separated due to the proximity of the GaN reflection, the sample B6 clearly shows a slight relaxation. This also happens for the highest temperatures (Figure 6.11f), but not for intermediate values (Figure 6.11e).

The main results obtained from RSMs are summarized in Table 6.2. To further analyze the influence of the growth regime on the strain state of the films, the lattice parameters of both series of samples are plotted in Figure 6.12. Regarding series A, the *c* parameter linearly increases with *x*, while the *a* parameter remains constant. This means that, at

this temperature, the III/V ratio does not influence the pseudomorphic growth of the AlInN layer, even when passing from the N-rich regime to the In-droplets one.

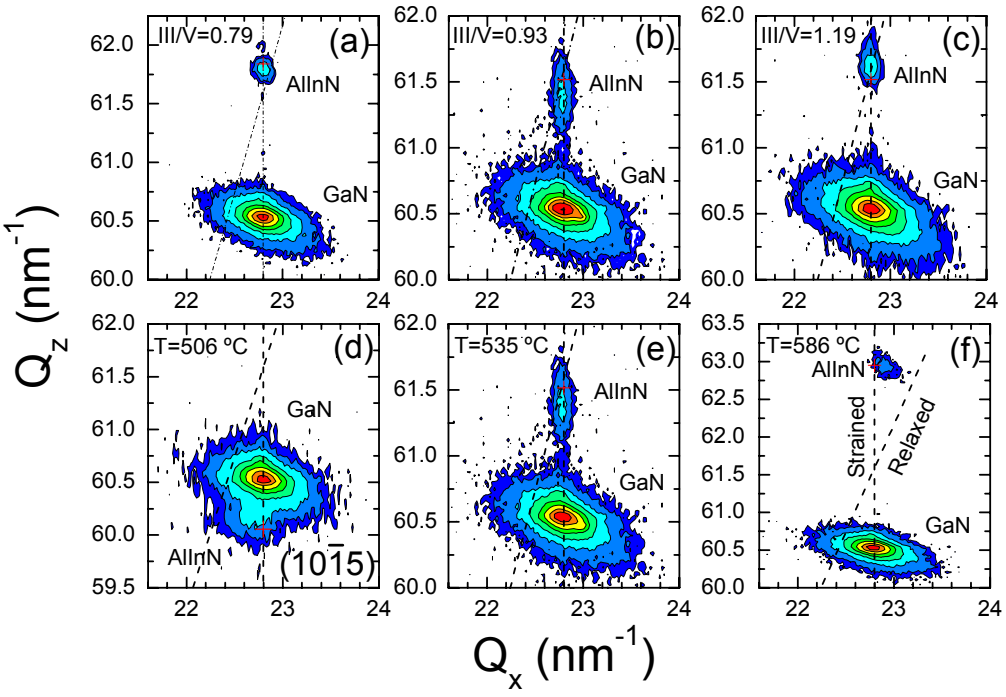

Figure 6.11 RSMs in the $(10\bar{1}5)$ reflection for series A (a-c) and series B (d-f). (a) A3, (b) A2, (c) A1, (d) B6, (e) B4 and (f) B2. The red crosses indicate the expected position for strained AlInN films with the RBS measured composition.

Nevertheless, series B shows different features due to the variation of the temperature. A good pseudomorphic growth was observed for samples B3-B5, grown within the In-droplets region. For these conditions (520-555 ºC), a constant *a* parameter was measured, with a *c* parameter increasing linearly with the In composition. When temperature decreases to 506 ºC (B6) this behavior is not preserved, and both *a* and *c* parameters change. This fact can be explained by the relaxation observed in this layer (Figure 6.11d), probably related to the low substrate temperature and the higher strain due to the composition (far from LM condition). Finally, samples B1-B2, grown in the intermediate In-rich region, show also a linear increase of both parameters with composition. As discussed previously, both samples are partially relaxed, but due to different reasons. Relaxation in sample B1 follows a compositional gradient due to the lack of stable conditions during the growth. Sample B2, however, shows a relaxation process with an approximately constant composition.

Table 6.2 Main structural results from HR-XRD.

Sample	a (nm)	c (nm)	ε_T (%)	$\Delta\theta_{XRD}$ (º)	x_{XRD} (%)
A1	0.3181(1)	0.5098(1)	**0.1(3)**	0.38(2)	16.4(5)
A2	0.3182(1)	0.5120(1)	**-0.2(3)**	0.31(2)	18.5(5)
A3	0.3181(1)	0.5084(1)	**0.3(3)**	0.45(2)	15.2(5)
A4	0.3181(1)	0.5028(1)	**1.3(3)**	0.73(2)	10.0(5)
B1	0.3145(1)	0.4964(1)	**1.4(3)**	0.76(2)	1.1(5)
B2	0.3165(1)	0.4992(1)	**1.5(3)**	0.79(2)	5.3(5)
B3	0.3182(1)	0.5040(1)	**1.2(3)**	0.68(2)	11.1(5)
B4/A2	0.3182(1)	0.5120(1)	**-0.2(3)**	0.31(2)	18.5(5)
B5	0.3181(2)	0.5162(2)	**-1.2(3)**	0.05(3)	22.0(5)
B6	0.3195(2)	0.5220(2)	**-1.8(3)**	-0.11(3)	28.1(6)
B7	-	-	**-**	-	-

RBS/C angular scans along $<\bar{2}113>$ axis were performed to compare with the XRD derived tetragonal strain. Figure 6.13 shows three of these scans for different compositions and tetragonal strains. In and Ga signals were studied independently, integrating different energy windows in the RBS spectra (due to the low thickness of the layers only one window was used for In). The kink angle ($\Delta\theta$) was calculated between the AlInN film and the GaN as explained in chapter 2. The value θ=0º corresponds to the position where the minimum yield from the AlInN layer was found. The tetragonal distortion was determined using experimental $\Delta\theta$ values.

Of course, since a and c parameters of the films and the substrate are known (from the RSMs), the expected $\Delta\theta$ between the layers can be calculated (Table 6.2). However, the RBS/C values of $\Delta\theta$ show significant discrepancies with respect to the HR-XRD derived ones. For example, Figure 6.13 shows $\Delta\theta$=-0.01º for sample B6, while HR-XRD predicts -0.11º (Table 6.2). A less pronounced deviation is obtained for sample B4, with a experimental $\Delta\theta$=0.40º and an expected value of 0.31º. These differences are associated to the irregular features of the angular scans in Figure 6.13, such as double-

dips (b) and no-shift between dips (c). Consequently, gaussian or multigaussian fittings are needed for the analysis of the dips, making difficult the accurate determination of the strain state. Such anomalous channeling behaviors have been detected in several semiconductor HSs [36-38], including GaN [27], and they have been linked to the steering of ions at the interface of the HSs [27, 39] when the kink angle is close to the critical angle for channeling. However, the study of this kind of effects involves MC simulations and deserves an especial attention, so it will be studied in detail in section 6.4.

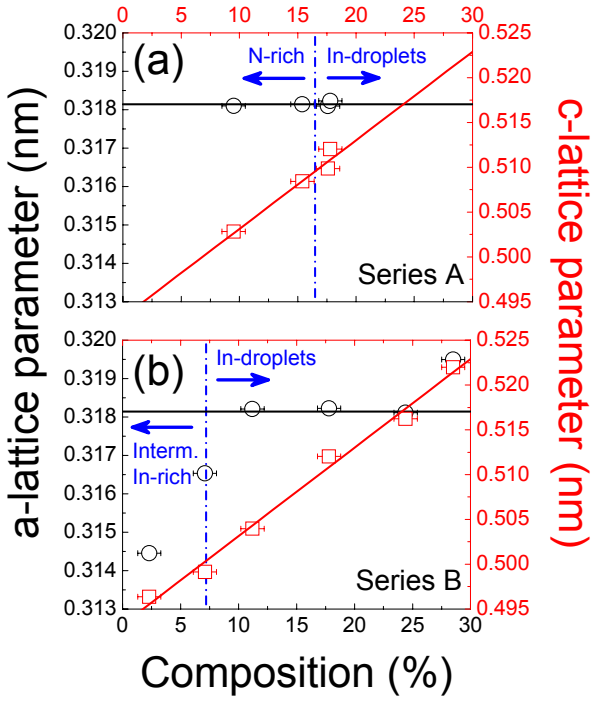

Figure 6.12 Lattice parameters obtained from $(10\bar{1}5)$ RSMs for (a) series A and (b) series B. The increment in *c* is well-fitted by a linear function, but *a* shows different behaviors depending on the growth regime.

Figure 6.14 summarizes the tetragonal distortion for the studied series of samples from both RBS/C and HR-XRD methods. A good correlation between both techniques was found, apart from the anomalous behaviors previously cited. Moreover, composition and strain follow a good linear behavior for intermediate compositions (10%<*x*<25%). In this region, the AlInN layers were pseudomorphic, so the change in composition does not modify the *a* parameter. When composition is far from the LM condition (*x*~18 %), the in-plain strain increases until it saturates. Samples B1 (Figure 6.8), B2 and B6

(Figure 6.12) are partially relaxed and show this saturation of the parallel strain. For them, the change in the composition does not modify the parallel strain, which is ~1 % for both tensile (B1, B2) and compressive states (B6). One possible reason for that is the existence of a critical stress for the layers, but results from series A and B have demonstrated that the interplay between III/V ratio and temperature can create non-equilibrium local conditions modifying the growth dynamics. This fact is clear in sample B1, where the evolution of the ternary layer is determined by the competition between decomposition and desorption. Thus, compositional variations have to be considered not always as a cause, but also as a consequence of these microscopic phenomena. B2 and B6 were grown close to equilibrium conditions (one under intermediate In-rich and the other under to N-rich), so the link between relaxation processes and composition could be more complex than it appears by Vegard's law [40] if such kind of phenomena are considered.

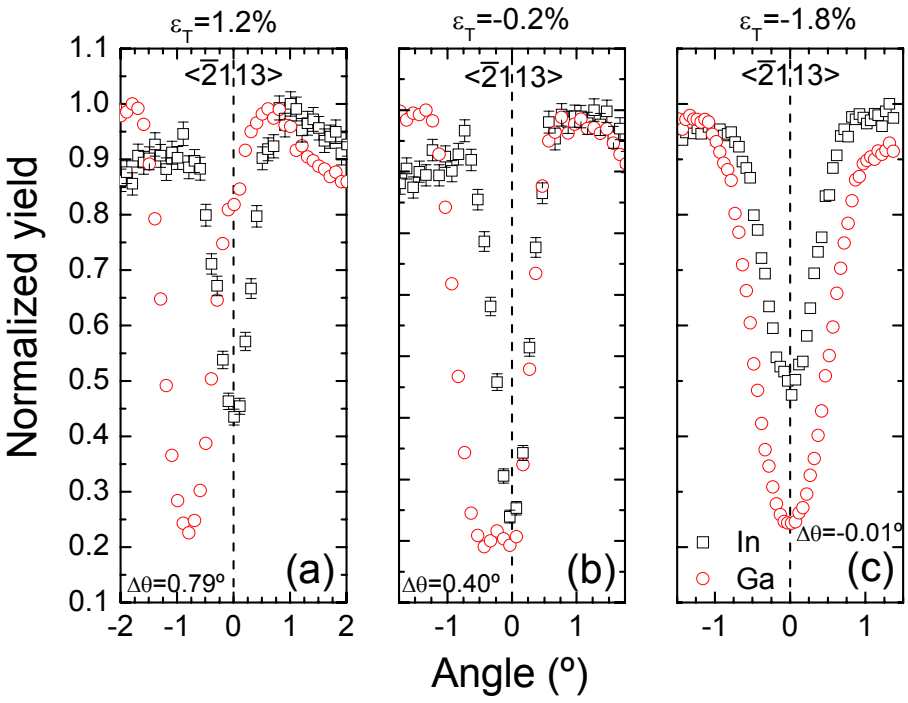

Figure 6.13 Angular scans along $< \bar{2}113 >$ axis for (a) B3 (x=11%, ε_T=1.2%), (b) B4 (x=18%, ε_T=-0.2%) and (c) B6 (x=29%, ε_T= -1.8%). Predicted kink angles are (a) 0.68º, (b) 0.31º and (c) -0.11º. These values do not correspond exactly to experimental ones. Angular scans for Ga show anomalous behaviors with additional dips at θ=0º.

Concerning the verification of Vegard's law, one important test provided by these XRD measurements is the comparison of the compositional values with RBS results. Several works have indicated deviations or corrections to Vegard's law in AlInN films grown by different methods [25, 26]. These deviations have been also proposed from a theoretical point of view [28, 41]. Using the lattice parameters obtained from RSMs, the composition of the films can be determined. In order to separate the effect of strain and composition, the calculation has to be carried out assuming a biaxial strain. Then, Poisson's equation is solved using Newton's method (see chapter 2).

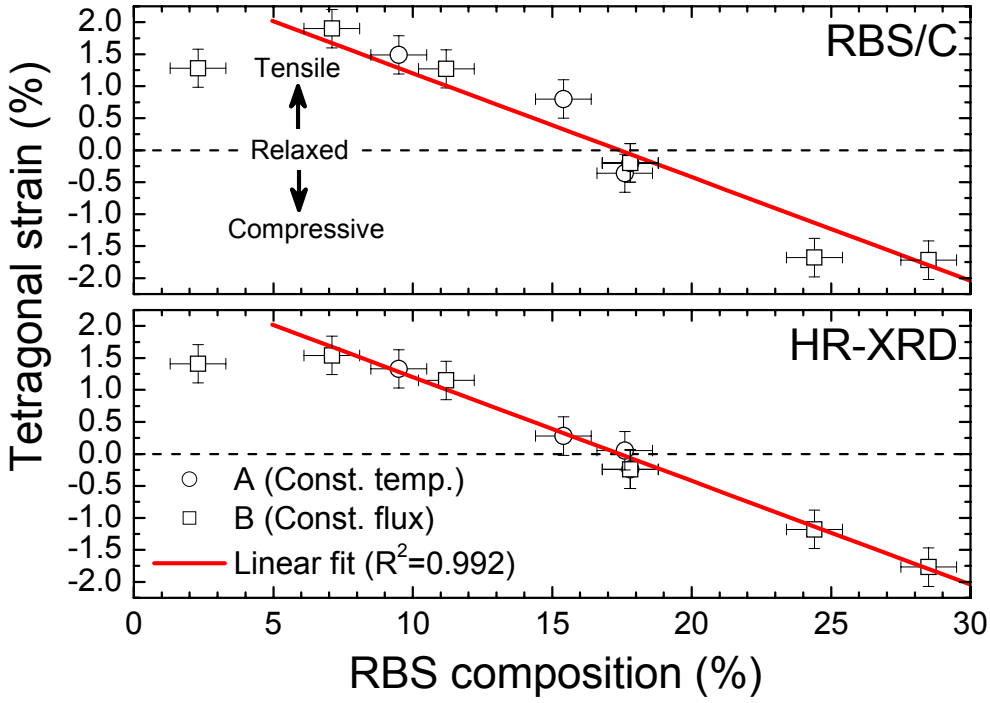

Figure 6.14 Tetragonal strain as a function of the RBS composition for both AlInN series. XRD and RBS/C results are compared. Samples follow a linear behavior except for the case of B1, grown with a compositional gradient in the intermediate In-rich regime.

A good agreement between RBS and XRD results was found within experimental errors. The linear fitting of the data (Figure 6.15) provided a slope of 1.00(5), with a determination coefficient of R^2=0.985. Consequently, in the studied range, Vegard's law is found to be generally satisfied.

At this point, it is important to mention that errors in the composition are, normally, difficult to estimate in XRD. If only the uncertainty in the lattice parameters is

considered, the error for XRD estimation is low. However, the main causes contributing to the uncertainty in this calculation are linked to the large number of required parameters, i.e, C_{13}, C_{33}, a_0 and c_0 for both AlN and InN binaries. These parameters are not always well-established (especially for InN), so the propagation of their uncertainties when using Vegard's law through Poisson's equation can be significant. Moreover, the requirement of using a numeric method to calculate x, makes cumbersome to take all these considerations into account. As it was mentioned in chapter 1, to minimize these errors, lattice parameters and elastic constants from Table 1.1 were assumed. During the calculation of uncertainties in Table 6.2, and to ensure a generous estimation, the contribution of these parameters was considered as important as the one due to the XRD measurement. This latter was calculated using Newton's method for the extreme values of a and c in each case.

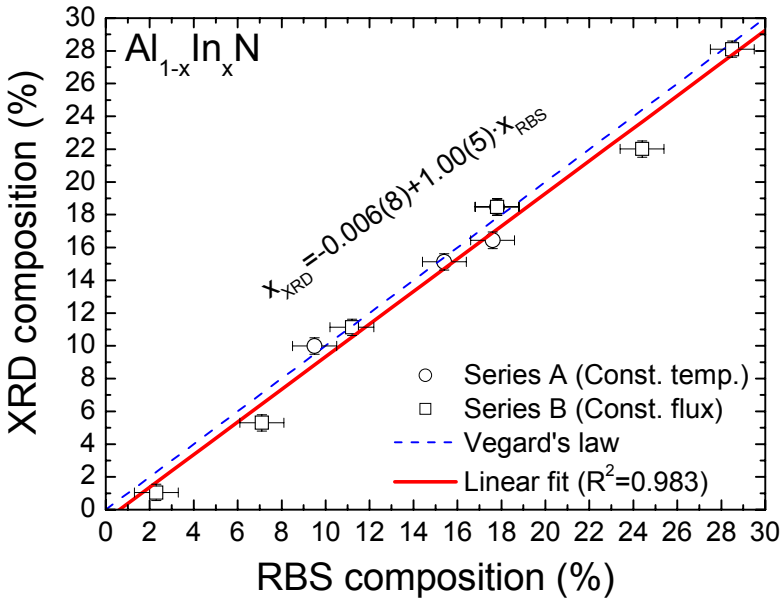

Figure 6.15 Comparison of AlInN composition obtained by RBS and XRD for both studied series of samples. The linear fit is in good agreement with calculations using Vegard's law and elasticity theory for the evaluated range.

Finally, it has to be noticed that, even considering the accurate values given by XRD, the existence of depth profiles can make these estimations inexact. As a confirmation of this aspect, it can be pointed out the clear underestimation of x from XRD for sample B1 (x_{RBS} = 2 %), which had a compositional gradient during the growth (Figure 6.7). Sample B2 (x_{RBS} = 7 %) also differs from a linear fit by about 20 %. This sample, as B1,

was grown in the intermediate In-rich regime and it shows relaxation in the RSM too. Although in this case the relaxation was not directly linked to compositional changes in the film (within RBS errors), these processes can restrict the applicability of Vegard's law as indicated by Darakchieva *et al.* [25]. In the present set of samples, deviations from Vegard's law were always below 10 % of relative error, except for B1 and B2. Since these two samples were the only ones grown under intermediate In-rich conditions, it suggests that equilibrium processes between desorption and decomposition could be the origin of relaxation mechanisms in the samples studied here.

On the basis of the analysis performed on A and B series, the comprehensive growth diagram of PA-MBE AlInN films (Figure 6.1) can be better understood. For series A, it was shown that the variation of the III/V ratio has an important impact on the composition and quality of the AlInN films due to the decomposition of InN. Gradients in random and aligned geometries were related with the presence of droplets during the growth. On the other hand, the in-plane lattice parameter is preserved for these series, proving the pseudomorphic growth in both N-rich and In-droplets regime.

In series B, a more complex transition is possible when temperature rises and desorption is considered. This allows an intermediate In-rich regime, despite, as it was verified in sample B1, the limit between one and another region is not well-defined due to the lack of a steady state at the beginning of the growth. The strain state of this series increases linearly with the temperature, but the *a* parameter is not always preserved and some relaxation mechanisms were observed for very high and very low temperatures.

6.3. Characterization of AlGaInN films grown by PA-MBE

The growth of LM quaternary HSs has, a priori, several advantages over the AlInN ones. On the one hand, the inclusion of Ga into the system mitigates the typical phase separation processes of AlInN layers. On the other hand, with the quaternary layers, the bandgap and the lattice parameters can be modified separately. However, there is also an important drawback in the characterization of quaternary HSs: XRD measurements cannot be used for determining the composition because of the large number of fitting parameters. Therefore, the relevance of RBS compositional analysis for these HSs is very high [22, 33, 42]. For this reason, a complete study of three series of AlGaInN

samples close to LM conditions was carried out, as an extension of the initial study on AlInN films. Again, the PA-MBE system was used due to the high accurate control of the growth parameters that it allows.

6.3.1. Composition and crystal quality

(a) Effect of the III/V ratio: the role of Al flux

The first two sets of samples (series C and D) were grown at a fixed temperature of 610 ºC and with constant N, In and (Al+Ga) fluxes. In each series, the Al/Ga proportion was varied exclusively, keeping a constant (Al+Ga) flux. Specific details of the samples are listed in Table 6.3. For all the samples, Φ_N =5.8·10^{14} at/s·cm^2. Series C was grown with a nominal In composition of ~25 %, while series D had ~20 % of In. In such conditions, the nominal III/V ratio was 0.91 and 0.90 for series C and D, respectively. The nominal thickness of the samples was ~250 nm.

The selection of these growth conditions was done considering that the best crystal quality is obtained for the intermediate In-rich growth [33] due to the presence of an adlayer during the deposition. Assuming the growth diagram from Figure 6.1, no-droplets were expected in the current situation. This point was confirmed by the absence of droplets after the growth by SEM. However, the main difference with the AlInN flux series is that, in the current case, the growth regime is not affected by the III/V ratio, which is constant inside each series.

In principle, since the total metal flux is not modified by this procedure, the active N is always constant, and then no variations in the In composition should appear. Nevertheless, the interrelation between Al and In fluxes have been recently pointed out by Monroy *et al.* [22], and even for constant III/V ratios the effective In composition could vary with the Al/Ga ratio. Using these series, it will be verified if Al atoms are indeed playing such a catalytic role. Two additional series (not shown in Table 6.3) were grown at higher III/V ratios (0.92 and 0.93) to check the reproducibility of the results.

With the previous studies on the growth of AlInN layers, it was demonstrated that the III/V ratio is an important parameter that controls the composition of the films. Despite this, Monroy *et al.* have shown that III/V ratio is not the *only* parameter controlling the

composition at a fixed temperature. Here, the role of the Al flux in the incorporation of In atoms is evaluated using RBS/C with 2 MeV He^+ ions.

Table 6.3 Growth conditions and RBS results for PA-MBE $Al_yGa_{1-x-y}In_xN$ samples. For all the samples, $\Phi_N = 5.8(1)\cdot10^{14}$ at/s·cm^2.

Sample	Φ_{In} (at/s·cm^2)	T (ºC)	Al/Ga	x_{RBS} (%)	y_{RBS} (%)	d_{RBS} (nm)	χ_{min} (%)
C1 (R172)	$1.1(1)\cdot10^{14}$	610(5)	**0.05(3)**	8.0(5)	2(3)	252(8)	2.9(1)
C2 (R184)	$1.1(1)\cdot10^{14}$	610(5)	**0.11(3)**	4.8(5)	10(3)	242(8)	2.4(1)
C3 (R185)	$1.1(1)\cdot10^{14}$	610(5)	**0.18(3)**	2.8(5)	19(3)	242(8)	2.1(1)
C4 (R186)	$1.1(1)\cdot10^{14}$	610(5)	**0.26(4)**	2.0(5)	28(3)	226(8)	2.2(1)
D1 (R181)	$1.3(1)\cdot10^{14}$	610(5)	**0.05(3)**	8.3(5)	2(2)	245(8)	-
D2 (R192)	$1.3(1)\cdot10^{14}$	610(5)	**0.12(3)**	6.5(5)	13(2)	229(8)	-
D3 (R189)	$1.3(1)\cdot10^{14}$	610(5)	**0.19(3)**	6.7(5)	20(2)	238(8)	-
D4 (R188)	$1.3(1)\cdot10^{14}$	610(5)	**0.28(3)**	5.4(5)	28(2)	232(8)	-
E1 (R214)	$1.1(1)\cdot10^{14}$	**565(5)**	0.11(3)	14.8(5)	8(3)	380(9)	24.4(5)
E2 (R213)	$1.1(1)\cdot10^{14}$	**595(5)**	0.11(3)	7.3(5)	11(3)	359(9)	2.7(2)
E3 (R210)	$1.1(1)\cdot10^{14}$	**615(5)**	0.11(3)	4.5(5)	10(3)	339(9)	2.8(2)
E4 (R211)	$1.1(1)\cdot10^{14}$	**625(5)**	0.11(3)	0.8(5)	9(3)	324(9)	2.6(5)
E5 (R212)	$1.1(1)\cdot10^{14}$	**637(5)**	0.11(3)	0.2(5)	12(3)	323(9)	-
E6 (R224)	$1.1(1)\cdot10^{14}$	**660(5)**	0.11(3)	0.1(7)	12(4)	326(9)	-

The actual composition of the films was obtained by means of RBX simulations of random RBS spectra. Due to the high crystal quality of the samples, the random spectra was obtained (see chapter 2) adding several spectra recorded in a (θ,χ)-scan. The <0001> aligned spectra were also acquired to determine the crystalline quality with depth resolution.

Figure 6.16 shows the random and <0001> aligned RBS spectra for sample C4, and the random spectra for the other AlGaInN samples comprising series C (inset). Note that, due the low amount of Al in contrast to the AlInN films, the sensitivity of RBS is limited for this element (and for N too). Consequently, the composition was derived assuming a stoichiometric nitride, being the Al content calculated in terms of In and Ga deficiency. The data were fitted satisfactorily assuming a homogeneous In concentration along the growth direction, i.e., with one single quaternary layer. However, as in AlInN, the In content does not correspond to the nominal one. This fact is, again, due to the substrate temperature used; which enhances the decomposition and reduces the effective In incorporation rate.

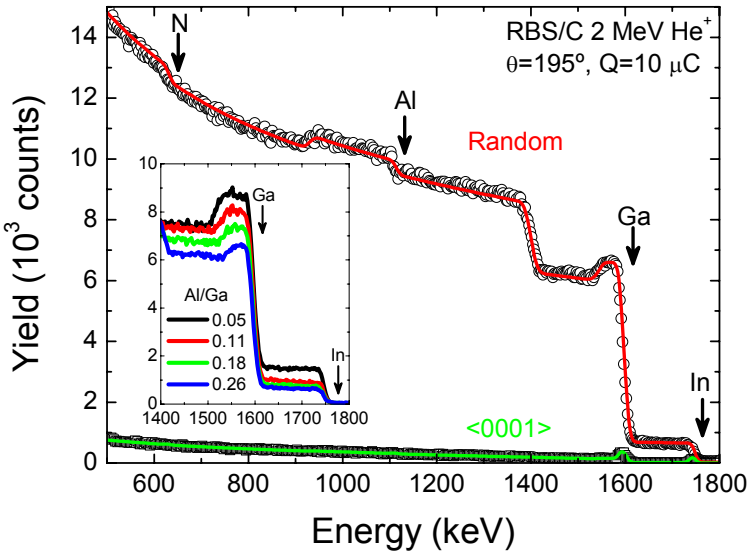

Figure 6.16 Random and <0001> aligned RBS spectra for sample C4. The inset shows a detail of the experimental data for the four samples comprising series C. As the Al/Ga ratio increases, the In content diminishes despite the constant flux.

The RBS results evidence the influence of the Al flux on the total amount of In incorporated into the film. A progressive decrease of In content is visible with the rising Al/Ga ratio for series C, but also for series D. This fact cannot be understood on the single basis of the growth diagram. On the contrary, the most accepted explanation for this phenomenon is the additional enhancement of the InN segregation at a microscopic level due to the high binding energy of Al-N (2.88 eV) compared to In-N (1.98 eV) and Ga-N (2.20 eV) [22, 23]. Elastic strain has been sometimes considered as a

supplementary driving force for the InN segregation [33]. However, in such case inhomogeneous In incorporation along the growth direction due to the progressive relaxation of the film would be expected. There is no evidence of such inhomogeneous compositional profile in the RBS spectra for any sample of series C and D, and further analysis by HR-XRD will show that all the samples were grown pseudomorphic to GaN. Therefore, the effect of the elastic strain in the studied samples is ruled out.

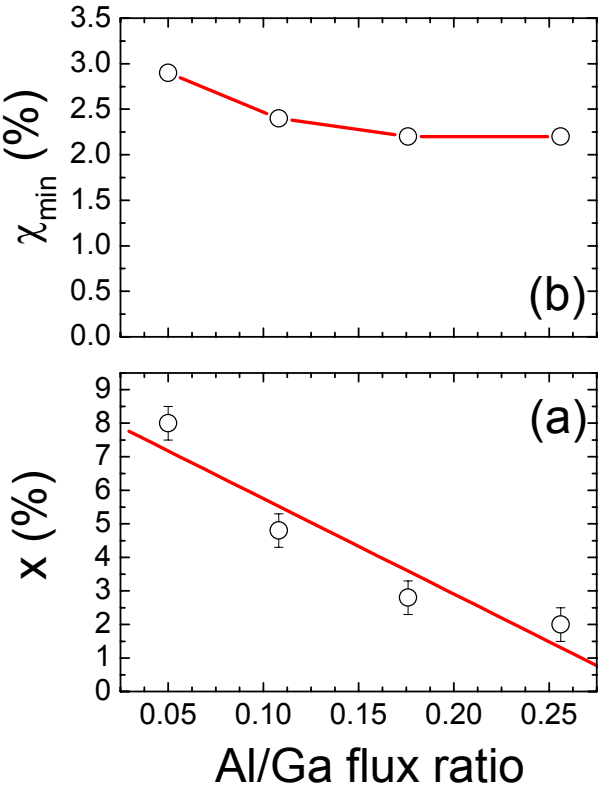

Figure 6.17 Main RBS results for series C. (a) A clear influence of the Al/Ga ratio on the In content is visible. (b) Minimum yield remains essentially constant.

Figure 6.17 summarizes the main RBS results listed in Table 6.3. The In composition shows a linear behaviour with the Al/Ga ratio, what was also observed in series D and two additional series (Figure 6.18). Thus, the link between Al and In flux is demonstrated, not only for series C, but for different III/V ratios between 0.90 and 0.92. The progressive decrease in the In content is accompanied by a slight drop in the thickness, indicating that the Al/Ga ratio also affects the growth rate [23].

The minimum yield (for In) remained essentially constant along the series, showing the very low mean value of χ_{min}=2.4(1) %. This excellent crystalline quality was also

checked with the FWHM of rocking curves around the 0002 Bragg reflection in HR-XRD measurements. The FWHM values lie between 280 arcsec and 365 arsec, with no correlation with the alloy composition [23]. These results confirm the good crystal growth of the quaternary layers, as expected in the selected intermediate In-rich regime.

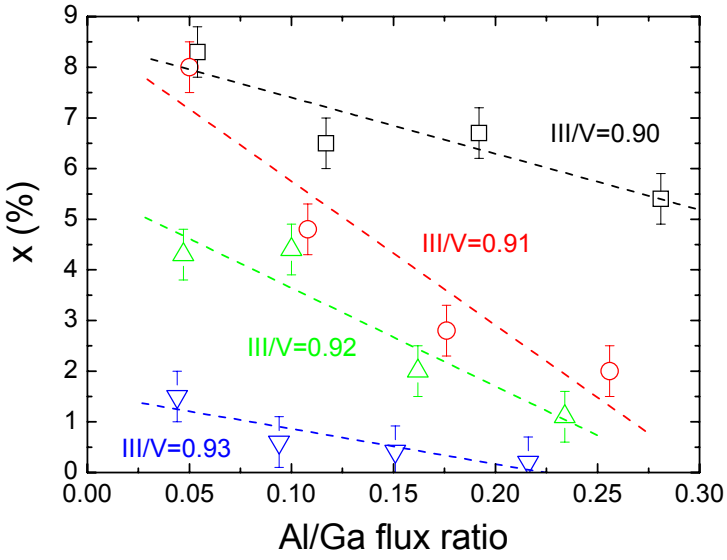

Figure 6.18 Effect of the Al/Ga ratio on the In incorporation for different III/V ratios.

(b) Effect of the substrate temperature

The second set of samples (series E) was grown at fixed flux conditions, but changing the substrate temperature from 565 ºC to 660 ºC. The In flux was the same as in series C, with III/V=0.90. A constant Al/Ga ratio of 0.11 was selected. Here, as in the case of AlInN, a reduction of In is expected for high temperatures due to the influence of desorption mechanisms. Again, no droplets were visible on the surface of the samples after the growth. Nominal thickness for samples in series E was ~350 nm.

Figure 6.19 shows RBS spectra for sample E1 and E2, grown with a difference of only 30 ºC in the substrate temperature. Noticeably, In content rapidly decreases with temperature. This reduction is accompanied by a drastic change in χ_{min} from 24.4 % to 2.7 %. This circumstance is related with the very narrow window for growing on the intermediate In-rich border. Thus, sample E1 is slightly In-rich considering the growth diagram from Figure 6.1, while E2 is clearly inside the intermediate In-rich regime. These data point out the importance of a good control and calibration of the temperature

in the growth system, since the crystal quality can be strongly affected by small variations. The χ_{min} remains almost constant (~2.7 %) for all the temperatures above 595ºC.

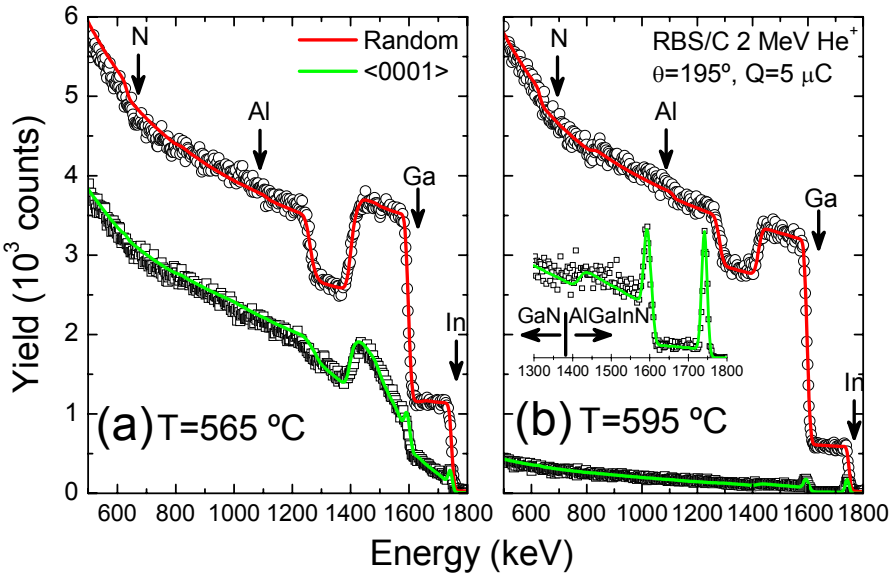

Figure 6.19 Random and <0001> aligned RBS spectra for samples (a) E1 and (b) E2. Despite there is only 30ºC between them, the In content decreases and a drastic reduction of minimum yield is observed too.

Figure 6.20 summarizes the main results from RBS data in set E (see also Table 6.3). A clear influence of the substrate temperature is observed on the composition and thickness of the quaternary films. In fact, the observed behavior follows an Arrhenius dependence as in the AlInN series, because here the desorption and decomposition processes restrict the growth rate too. For temperatures above 615 ºC the In incorporation is very low, being almost negligible (less than 0.15%) for T>635 ºC.

Samples grown with T>615 ºC revealed an In surface peak in the random RBS spectra. These peaks were simulated with a very thin In layer of ~$6 \cdot 10^{14}$ at/cm^2. The presence of these peaks, together with the observed streaky RHEED pattern during the growth [23], suggest that the reduction of the In incorporation is not due to the lack of In at the growth front, i.e., it is not completely desorbed. Consequently, the InN decomposition is still a relevant factor for the growth, which may be conditioned by the Al flux. The decrease of thickness with the temperature indicates the reduction of the growth rate, also explained by desorption and decomposition mechanisms.

As a final remark, the optical behavior of the AlGaInN samples was characterized by photoluminescence (PL) at room temperature [43]. In all cases, a single peak associated to the AlGaInN layer was found [44], which shows a clear blue-shift as the Al/Ga ratio (series D) or the temperature (series E) are increased. This shift indicates the larger bandgap of the material due to the lower In incorporation. In both cases, there is also a huge enhancement of the integrated PL intensity for low In contents, confirming that the grown AlGaInN layers are very good candidates for UV-LEDs. The observed enhancement is usually interpreted as a steady reduction in the density of non-radiative recombination centers [23, 45, 46] and the In exciton localization as a consequence of microscopic compositional fluctuations.

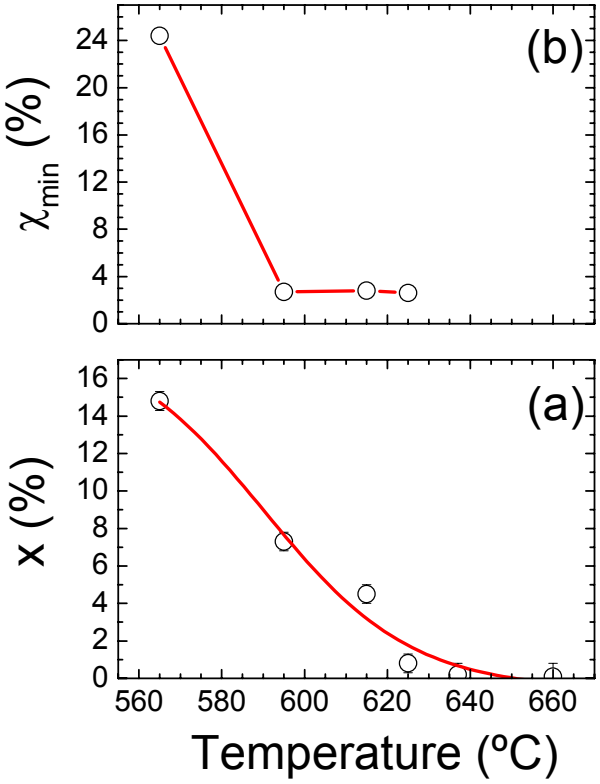

Figure 6.20 Main results from RBS analysis for series E. Temperature affects both In composition in analogy with the results for AlInN films.

6.3.2. *Lattice parameters and strain state*

In order to complete the structural characterization of the AlGaInN layers, the evolution of the strain state of the films was investigated. Series D was selected as a prototype for studying the effect of the Al/Ga ratio on the lattice parameters. HR-XRD measurements

were performed on series D, recording the (0004) and $(10\bar{1}5)$ RSMs, being the results summarized in Table 6.4. The (0004) reflections (not shown here) for the films and the GaN lied on the same horizontal line, revealing that there are no macroscopic tilts between the crystal planes of both layers. The $(10\bar{1}5)$ RSMs are shown in Figure 6.21. All the samples exhibit a pseudomorphic growth with the GaN layer, being D3 the closest one to the LM condition. A progressive decrease in the strain takes place as the Al/Ga ratio is increased. This rising follows a linear trend as shown in Figure 6.22. The expected Al/Ga ratio for a completely relaxed quaternary layer is 0.33.

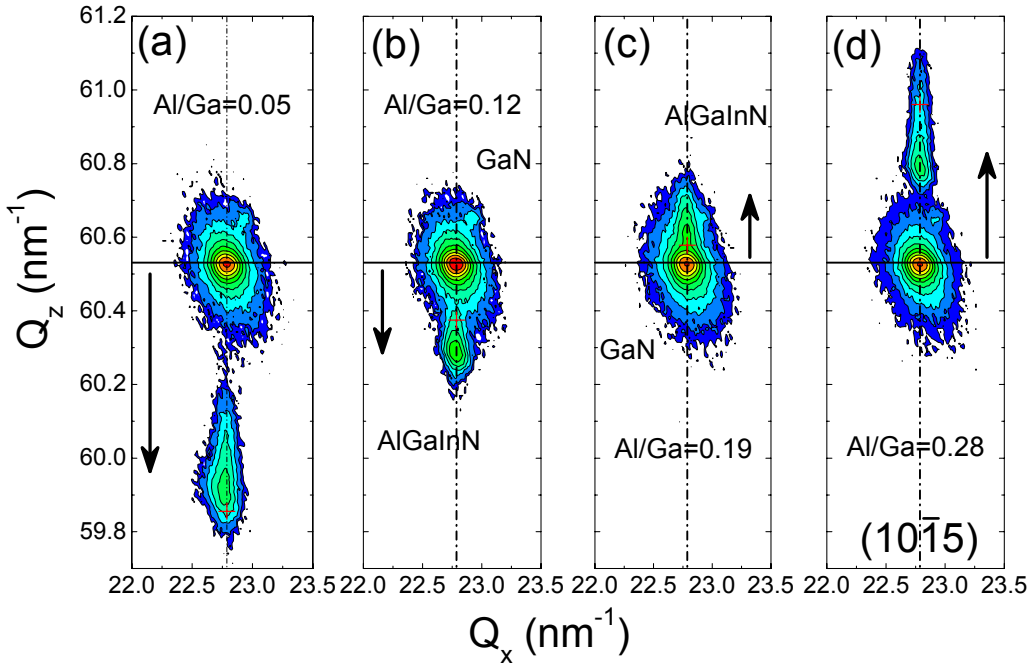

Figure 6.21 RSMs for AlGaInN samples in the $(10\bar{1}5)$ reflection: (a) D1, (b) D2, (c) D3, (d) D4. Pseudomorphic growth is evidenced in all of them. Red crosses represent the expected position for fully strained films assuming the RBS composition.

RBS/C angular scans along the $<\bar{2}113>$ axis were also recorded to compare with the XRD derived tetragonal strain. Samples D1 and D4 were selected for this study since they correspond to the highest and the lowest tetragonal distortion values. Figure 6.23 shows both scans for the In and Ga signals related with the quaternary layer and the GaN substrate, respectively. In the case of AlGaInN, the Ga signal of the quaternary layer can be also analyzed, because it is also well-separated in the spectra. However, in our experiments no significant changes were found between Ga and In signals from the

quaternary layer. This fact corroborates the good lattice location of both elements in the wurzite structure.

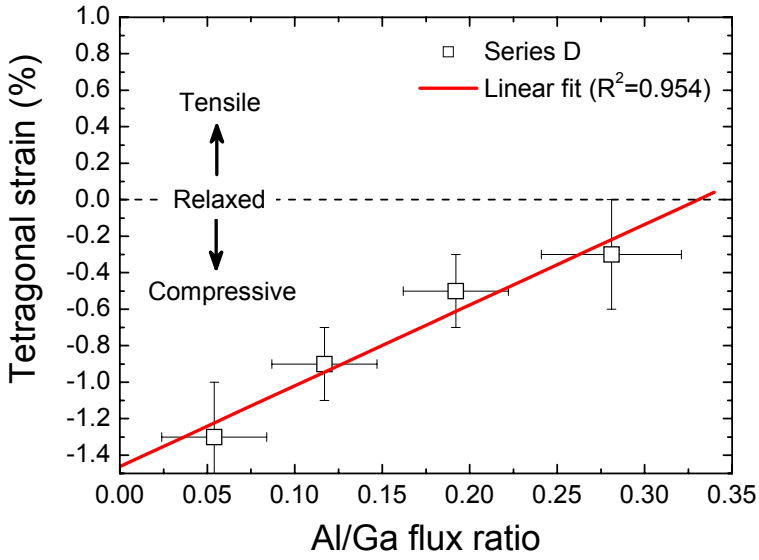

Figure 6.22 HR-XRD results for the strain state of series D. A linear behavior was found with the increasing Al/Ga flux ratio, being all the samples under compressive strain.

Table 6.4 Main results from HR-XRD measurements in series D.

Sample	*a* (nm)	*c* (nm)	ε_T (%)	$\Delta\theta_{XRD}$ (º)
D1	0.3186(2)	0.5244(2)	-1.3(3)	-0.24(4)
D2	0.3185(1)	0.5211(1)	-0.9(2)	-0.16(2)
D3	0.3185(1)	0.5183(1)	-0.5(2)	-0.02(2)
D4	0.3185(2)	0.5168(2)	-0.3(3)	0.05(4)

For both studied samples, Figure 6.23 shows no angular shift between the dips from the film and the substrate. However, XRD calculations in Table 6.4 show an expected $\Delta\theta$ of -0.24(4)º and 0.05(4)º, respectively. Although this latter value for sample D4 could be too low to be detected in the scan, this would not be the case in the D1 sample. Actually, the angular scan in D1 was performed in steps of 0.05º to avoid this kind of uncertainties. Consequently, as in the case of the AlInN layers, this is a new confirmation of the limitation of RBS/C in the determination of the strain state due to the anomalous channeling effects (see section 6.4). Due to the lower theoretical $\Delta\theta$ of

our quaternary films, as compared to AlInN ones, the angular scans show the most extreme situation, where no shift at all is visible.

Preliminary measurements on series E showed a similar conduct, with no-shift between the GaN and the quaternary layer. Therefore, no further RBS/C measurements were done. On the contrary, in order to investigate in detail the origin of the physical phenomena affecting the angular scans, an analysis via MC simulations was performed, which is discussed in the following section.

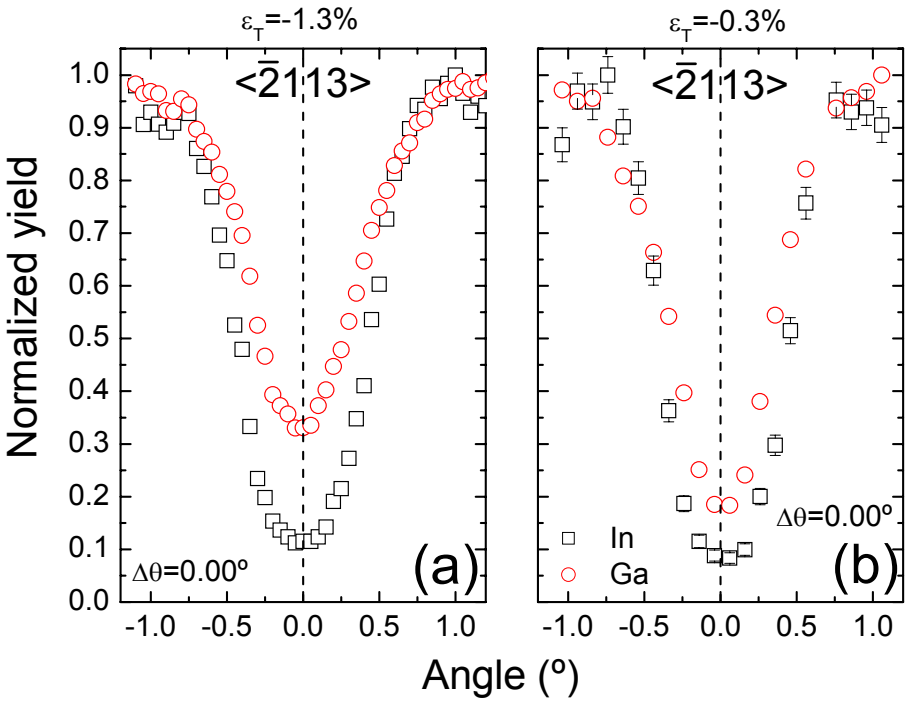

Figure 6.23 Angular scans along the $< \bar{2}113 >$ axis for (a) D1 (x=8.3%, ε_T=-1.3%), (b) D4 (x=5.4%, ε_T=-0.2%). Predicted kink angles are (a) -0.24º, (b) 0.05º. However, no angular shift is visible from the experimental dips due to the anomalous channeling.

6.4. Accurate determination of strain state in Al(Ga)InN heterostructures by ion channeling

The studies developed on both ternary and quaternary HSs have revealed that RBS/C can have important limitations to determine the strain state of these LM films for particular beam/target configurations. To explain, predict, and overcome these restrictions, simulations of the angular scans through MC methods have been performed

[47, 48]. The description and foundations of these simulations were explained in detail in chapter 3. As a general rule, it has been observed that the sensitivity to strain state is higher when the kink angle is larger than the critical angle for channeling (ψ_1=0.695º at 2 MeV), in agreement with references [27, 36]. In order to get a deeper understanding of such effects, the relevance of the steering effects at the interface of the HSs and the possible influence of other experimental parameters such as the thickness, the strain state, or the probing energy has been evaluated.

6.4.1. Steering effects in ion channeling measurements

As mentioned in chapter 2, the conventional way of measuring strain by RBS/C is the determination of the kink angle ($\Delta\theta$). As shown in previous sections, this procedure is not accurate in certain LM HSs, giving double-dips or no-shift situations, especially when the strain state of the film corresponds to a low kink angle ($\Delta\theta<\psi_1$). The accepted explanation for this behavior is the influence of the steering effects (deviation of the projectiles due to electrostatic interactions with the target atoms) at the interface of the HS [27]. When these effects are significant, most ions entering the GaN substrate are able to modify their trajectory without suffering significant large angle scattering events, producing the anomalous scans mentioned before. Thus, in order to understand and predict the experimental observations, this new scenario has been investigated with the FLUX program [48].

For better understanding of the steering effects, the most unfavorable case of all the samples analyzed in this work was chosen. In particular, sample D1 (Figure 6.23a) was selected because no shift was detected in the corresponding angular scan, making impossible the determination of the strain state by RBS/C.

For the MC simulations of this sample, a two-layer model was employed: a first layer with the quaternary $Al_{0.02}Ga_{0.90}In_{0.08}N$ (250 nm, see Table 6.3) and the second with the GaN substrate. The strain state of the AlGaInN was incorporated by means of a rotation matrix between both layers as described in chapter 3, using the nominal kink angle ($\Delta\theta$=-0.24º) as an input. A total number of 10000 ions was used to guarantee low statistical error [49], with the simulated angular scan performed in the $<\bar{2}113>$ axis along the $(10\bar{1}0)$ plane. Vibration amplitudes u_2 of the participant atoms (see chapter 3) were 0.008 nm (Al), 0.011 nm (Ga), 0.013 nm (In) and 0.009 nm (N).

Figure 6.24 compares the simulation with the experimental data. In (from the quaternary layer) and Ga (from the substrate) signals were analyzed. A good agreement between experiment and simulation was found, showing $\Delta\theta$=0º in both cases. The slight misfit of the simulation with respect to the experimental data can be explained by restrictions in the FLUX code, which does not take into account lattice defects. These defects, however, have been observed in the RBS/C spectra, since the AlGaInN dechanneling rate was 3.6 times higher than that for the GaN substrate. Therefore, MC results confirm that the RBS/C is not sensitive to $\Delta\theta$ in such HS.

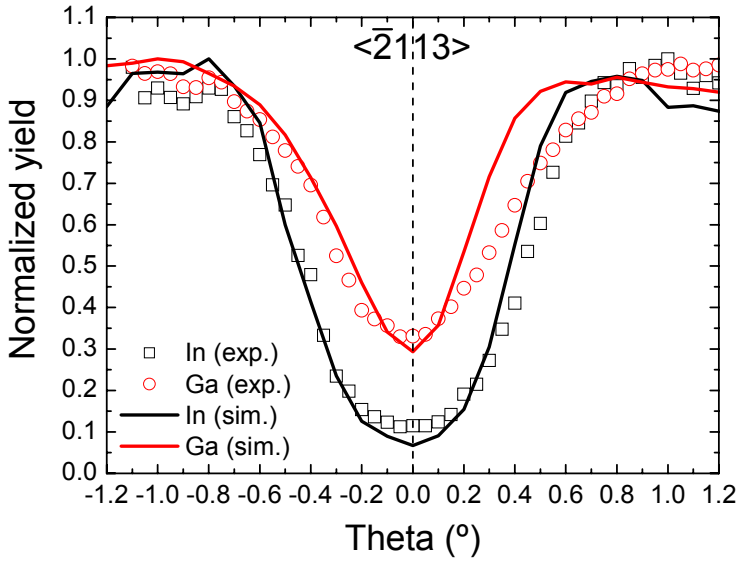

Figure 6.24 Experimental and MC simulated angular scans along the $<\bar{2}113>$ axis for sample D1 (x=8.3%, ε_I=-1.3%) The simulation is in good agreement with the RBS/C data, revealing a $\Delta\theta$=0º.

In analogy with Davidson *et al.* [50], this situation has been related to the large thickness of the quaternary layer compared to the mean free path ($\lambda_\perp$) of He^+ ions inside the $<\bar{2}113>$ channel. This parameter can be calculated from relation (3.10) [51]. In the present situation, this gives $\lambda_\perp$=55.2 nm (taking $\psi_1=\psi$), which is 4.5 times lower than the thickness of the layer. In such conditions He^+ ions can reach the interface without the typical oscillatory behavior that takes place at the beginning of the process of channeling, enhancing the presumed steering towards the substrate.

The previous assumption is confirmed by further simulations, where the same quaternary composition as D1 was used, but with different film thickness (from 10 nm to 250 nm). Figure 6.25 shows the results of the simulations for the Ga signal (from the

GaN layer) of the HS. In the graph, θ=0º corresponds to the position of the minimum for the surface film.

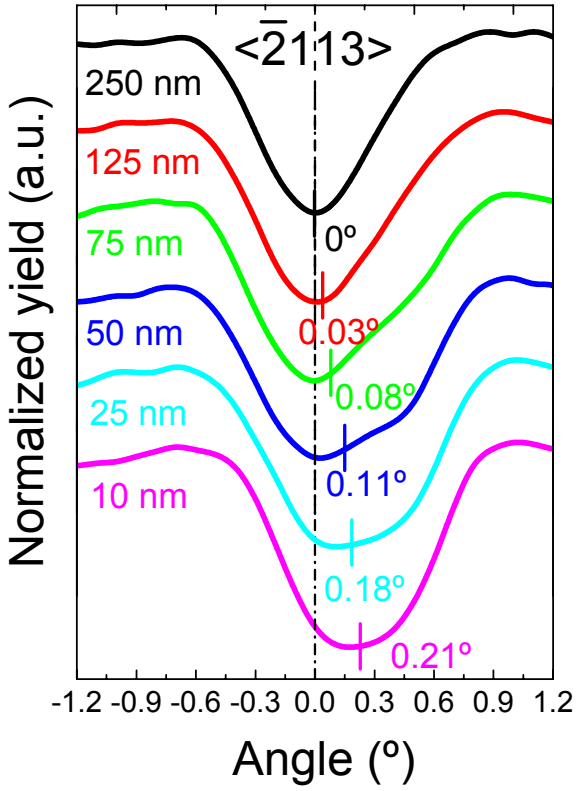

Figure 6.25 MC simulated angular scans along the $<\bar{2}113>$ axis for a sample with the same composition and strain state as D1 ($\Delta\theta$=-0.24º) but with different thicknesses. The dip corresponds to the Ga signal from the GaN layer. The angular shift coincides with the input kink angle only for low thicknesses.

In addition, the close encounter probability for He ions was extracted from the simulation at three different incident angles (0º, -0.6º and +0.6º). To evaluate the influence of such parameter on the steering effects, the results for three different thicknesses are shown in Figure 6.26. For thin quaternary layers ($<½\lambda_{\perp}$) the change of the close encounter probability in the interface is dependent on the sign of the incidence angle (Figure 6.26). For such thickness, RBS/C is sensitive to $\Delta\theta$ and the shift of the simulated scans is in good agreement with the input value of -0.24º. For thicknesses of $\sim\lambda_{\perp}$, a strong asymmetry is still visible in the dip, indicating that flux oscillations are not completely removed. This fact is clear from Figure 6.26, where the first flux peak appears at ~50 nm, in excellent agreement with the analytical calculation of $\lambda_{\perp}$. A double minimum configuration then appears in the angular scan. For thick layers ($>2\lambda_{\perp}$),

the close encounter probability becomes independent of the sign of the incidence angle leading to symmetric channeling dips. This is accompanied by the decay of ion oscillations (normally appearing in the second period [50]), visible in Figure 6.26. Thus, for large thickness values, the $\Delta\theta$ stays undetectable by RBS/C and no shift is visible in the dip, in agreement with the current experimental data.

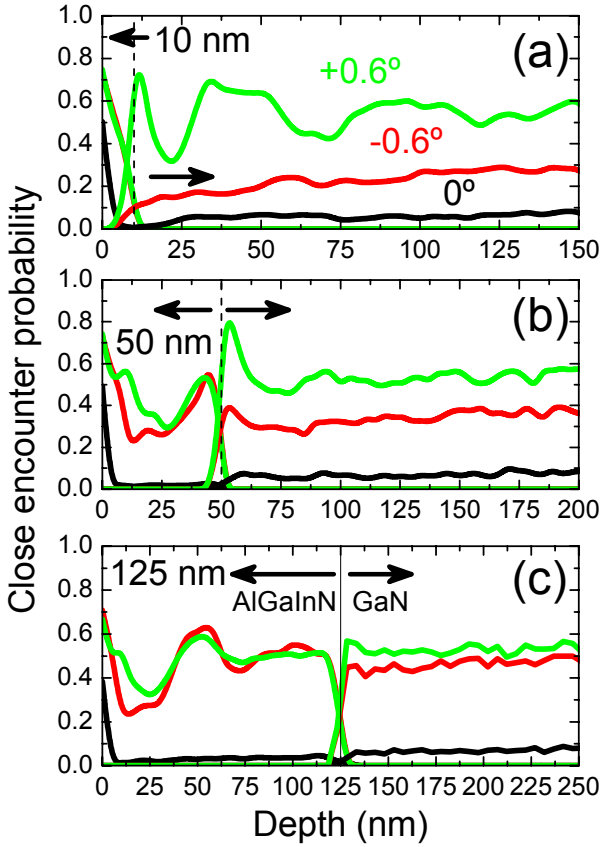

Figure 6.26 MC simulations of close encounter probability for different AlGaInN thicknesses: (a) 10 nm, (b) 50 nm, (c) 125 nm. Three incidence angles were used at θ=0º (aligned with the $<\bar{2}113>$ axis of the AlGaInN layer) and θ=-0.6º and θ=+0.6º. The probability in the GaN layer is symmetric for high thicknesses but not for low ones.

As a final demonstration of the thickness dependence of the steering effects, Figure 6.27 shows MC simulations of 100 ion tracks in the same $Al_{0.02}Ga_{0.90}In_{0.08}N$/GaN HS. In correspondence with Figure 6.26, 10 nm, 50 nm and 125 nm thicknesses were considered. For quaternary layers with 10 nm, the deflected ions at the interface are only a small fraction of the total flux. However, for 50 nm and 125, the incident beam reaching the GaN layer clearly separates into two branches. Apart from the trajectories following the initial direction at 0º, the other branch (marked with a red arrow) is

located exactly at an inclination of -0.24º. Therefore, it corresponds to the ions steered into the GaN layer. This branch is more intense as the thickness is increased, and it is responsible for the observed symmetry of the close encounter probability.

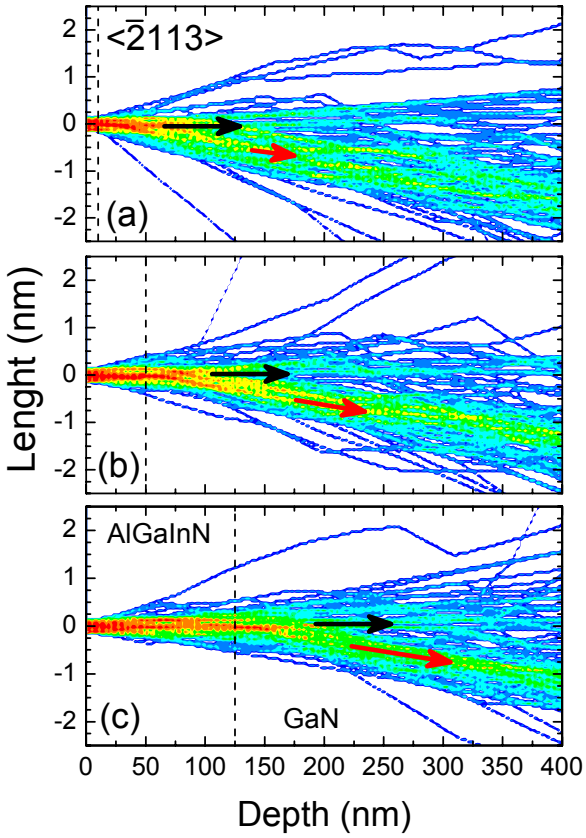

Figure 6.27 MC simulations of 100 ion tracks in an $Al_{0.02}Ga_{0.90}In_{0.08}N$/GaN HS with different thicknesses: (a) 10 nm, (b) 50 nm, (c) 125 nm. Input kink angle (red arrow) is -0.24º as for sample D1. Steering effects at the interface become more important with the increasing thickness.

Consequently, the MC simulations of RBS/C experimental data obtained from sample D1 have proved that RBS/C is not sensitive to the kink angle because of the important role of steering effects in this sample (and also in others). This kind of hyperchanneling phenomena has been also identified by Appleton *et al.* [52] and, like in this case, they have been related with the thickness of the layers [53]. Besides, recent MC simulations by Breese *et al.* [54] indicate the strong relation between the spatial and the angular coordinates of ion trajectories for low critical angles, which establish a new link with the thickness. Some theoretical and experimental works point out statistical equilibrium as the essential mechanism controlling the channeling phenomena [50, 55, 56]. This particular question seems to be supported by the MC simulations of this thesis on the

close encounter probability, since the importance of a non-oscillatory stable state for the enhanced steering of the ions has been corroborated.

6.4.2. Influence of the thickness on the steering effects

Considering the key role of the thickness on the steering effects and the final determination of the strain state in the studied HSs, specific RBS/C data were evaluated to prove this fact experimentally. Due to the easier growth and structure of the ternary films, three $Al_{1-x}In_xN$ samples with similar compositions (x~14%) but different thicknesses were grown by MO-CVD at 840 ºC, with 35 nm, 122 nm and 210 nm, respectively. The characterization of the films was carried out by RBS/C and HR-XRD methods at ITN, being the main results summarized in Table 6.5. The expected kink angle was calculated using the lattice parameters obtained in the RSMs around the $(10\bar{1}5)$ reflection. All of the samples exhibited a pseudomorphic growth and hence, the values of $\Delta\theta$ were very similar.

Table 6.5 Main measured parameters for MO-VPE $Al_{1-x}In_xN$ samples.

Sample	x_{RBS} (%)	d (nm)	a (nm)	c (nm)	ε_T (%)	$\Delta\theta$ (%)
F1	0.136(5)	35(8)	0.3185(1)	0.5101(1)	0.1(2)	0.44(2)
F2	0.132(5)	122(8)	0.3185(1)	0.5064(1)	0.8(2)	0.62(2)
F3	0.143(5)	210(8)	0.3185(1)	0.5088(1)	0.3(2)	0.51(2)

MC simulations were developed assuming a pseudomorphic $Al_{0.86}In_{0.14}N$/GaN structure and changing the thickness according to Table 6.5. The experimental angular scans were fitted with the calculated kink angle. Figure 6.28 shows both experimental and simulated dips, confirming the good agreement between them. Since the kink angles of the three AlInN samples are close to the critical angle for channeling, MC calculations can still be used to correct the anomalous scans. Apart from this fact, the increasing relevance of the steering effects with the thickness should be noticed. This feature is clear if the intensity of the component at θ=0º is considered. For 35 nm thickness (F1), this component is about 50 % of the main dip, located at 0.63º (nominally 0.44º). For 122 nm thickness (F2), the intensity at θ=0º is still ~50% but, since this sample has a higher nominal kink angle (0.62º). This means that the steering effect is more

pronounced in F2 than in sample F1. Finally, for 210 nm (F3), the component at θ=0º is about 100% of the main one (at 0.73º), resulting in a mixed dip with two minima.

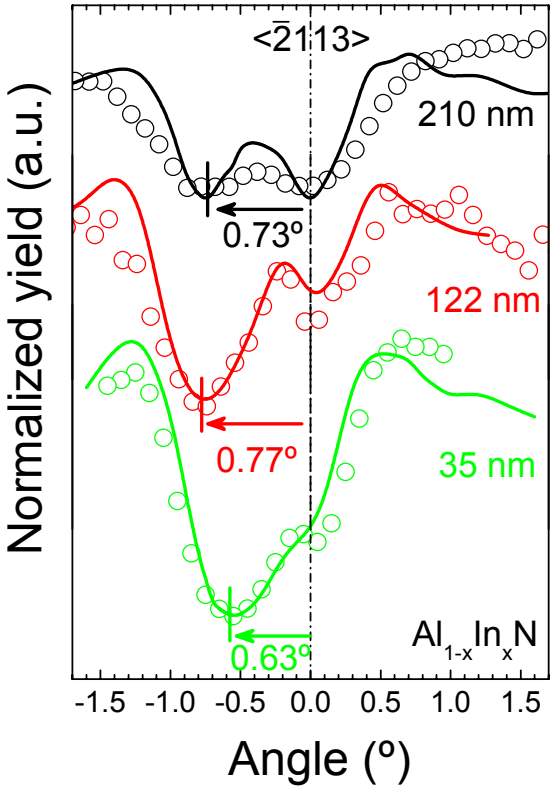

Figure 6.28 Experimental (circles) and MC simulated (solid lines) angular scans along the $< \bar{2}113 >$ axis for AlInN samples with different thicknesses but the same composition.

It is important to note that standard thicknesses of HSs for HEMTs or DBRs are lower than 100 nm, so the steering effects in these circumstances can play a minor role. However, if MC simulations are not considered for the analysis, the relative error (RE) in the determination of the angular shift can be significant, even for thin samples. As a confirmation of this point, bigaussian fittings of our experimental data were done assuming a fixed component at θ=0º. The RE then increases from 24 % at 35 nm up to 100 % at 210 nm. Consequently, the need of MC methods for the analysis of the strain state in such LM HSs is obvious, especially in the case when HR-XRD measurements have to be complemented by RBS/C.

6.4.3. Influence of the strain state on the steering effects

Although the thickness of the layer is a critical parameter for the steering of ions, there is a limit for the maximum strain that allows this behavior. Indeed, the RBS/C studies

shown here have demonstrated that the strain state of the film is also a critical factor for the appearance of the steering effects (see, for example, Figure 6.13). When the strain state is such that *a/c* ratio of the Al(Ga)InN film is very close to that of GaN (~0.61497), the kink angle is low and the steering effects are more pronounced. It is important to note that, low strain values do not mean, exactly, low kink angles. This is so because the kink angle is calculated with respect to the GaN layer, while the strain state is always derived with respect to a theoretically relaxed Al(Ga)InN layer assuming Vegard's law (see chapter 1). Consequently, although both physical parameters are strongly associated, it is important to separate them during the discussion.

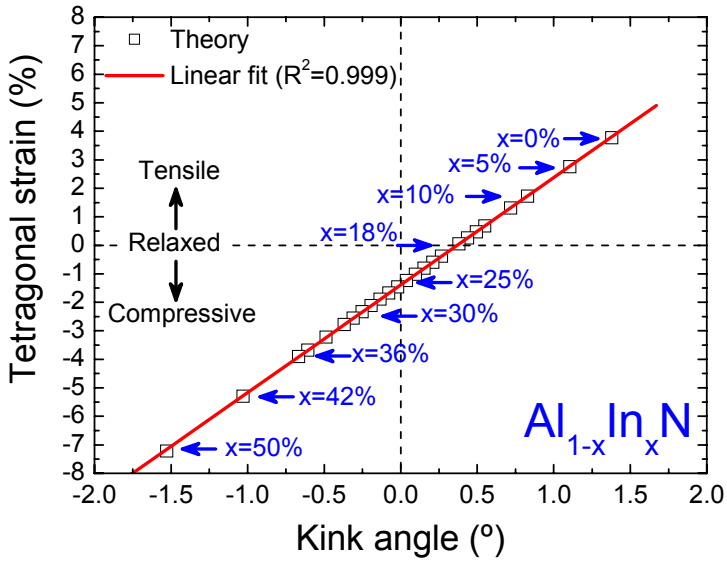

Figure 6.29 Theoretical values of tetragonal strain and kink angle for pseudomorphic AlInN films. The relation is almost linear for low values of the strain state.

Figure 6.29 illustrates this point for the case of pseudomorphic $Al_{1-x}In_xN$ films. The correspondence between tetragonal strain and kink angle for this kind of pseudomorphic growth is almost linear. However, the tetragonal strain is zero for x=18%, while $\Delta\theta$=0.38º (compare this value with that from sample B4 in Figure 6.13b). On the contrary, the kink angle is zero for x=25%, with a strain state of -1.46% (see sample B6 in Figure 6.13c). Therefore, steering effects will be more intense in the second situation than in the first one, as it is clear in the experimental scans from Figure 6.13. Since the kink angle is always used as the input in the MC simulations, in the following this parameter is taken as the reference for the discussion of the steering effects.

Ab initio MC simulations were developed to study the effect of the strain state on the anomalous channeling in pseudomorphic AlInN layers. A layer of 125 nm was used, since this value is large enough to induce the appearance of steering effects and it is also less time-consuming in the simulations. The *a* parameter of the lattice was fixed as 0.3189 nm (relaxed value of GaN). Then, the composition was varied and the expected *c* lattice parameter for fully strained AlInN layer was calculated taking the *a* parameter into account and using Poisson's equation for elastic deformation (see chapter 1). The tetragonal distortion was set as an input via the kink angle.

For each simulation, the angular shift was calculated by a Gaussian fitting of the simulated channeling dip and compared with the expected $\Delta\theta$ used as input in the simulations, obtaining the relative error. Figure 6.30 shows the results of RE for the pseudomorphic AlInN layers with different $\Delta\theta$ (corresponding to different compositions). Three regions can be clearly distinguished in the graph, depending on the intensity of the steering effects. For $|\Delta\theta| > 1.5^{\circ}$, the deflection of the ions at the GaN interface is rather difficult, being the steering effects negligible and the RE below 5 %. In this region the experimental angular scan can be used directly to obtain the strain state of the layer. However, for lower values ($1.5^{\circ} > |\Delta\theta| > 0.5^{\circ}$) the presence of steering effects becomes more important, and double dips are visible in the scan. In this range, a large fraction of the ions is still able to bend their trajectory at the interface and then the observed angular shift does not match the theoretical $\Delta\theta$. Indeed, RE is higher than 5 % and grows with decreasing $\Delta\theta$. This behavior can be fitted by an exponential function (solid line in the graph). The correct $\Delta\theta$ can be determined from experimental scans only when MC simulations are used to fit the experimental data. For values of $|\Delta\theta| < 0.5^{\circ}$, the steering effects are intense enough to make the shift undetectable in the scan and just a slight asymmetry is observable in the dip. Hence, $\Delta\theta$ cannot be directly measured or fitted by MC calculations.

In order to demonstrate experimentally the transition between these three stages, MC results were compared with the angular scans of selected samples from series A and B. Six samples (B2, B3, A3, A2, B5, B6) were used considering their different composition and strain state. New MC simulations were carried out but choosing a thickness of 60 nm, which is a good compromise for the different RBS results obtained in series A and series B (see Table 6.1). The input kink angle was obtained from HR-

XRD results in Table 6.2 and, then, the partial relaxation that some samples exhibited (B2 and B6) was also considered. Of course, with the increasing value of x in the AlInN layer, the in-plane strain state can be modified from tensile to compressive (Figure 6.29). The chosen samples have a tetragonal distortion varying from ε_T =1.5% (B2, x=7%) to ε_T =-1.8% (B6, x=29%), as shown in Figure 6.14, which is the most interesting region to check the steering effects.

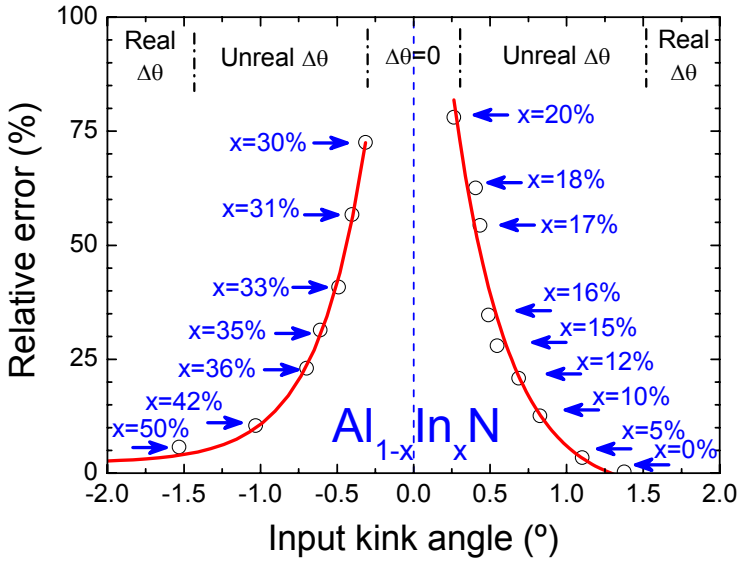

Figure 6.30 Relative error in the determination of the kink angle MC data (circles) and exponential fit (solid line) for different $Al_{1-x}In_xN$ layer on GaN. Three regions are clearly distinguished, corresponding to different intensities of the steering effects.

The comparison between the experimental and the MC simulated angular scans is shown in Figure 6.31, finding a very good agreement between them. As expected, for high tensile strain states (ε_T>1 %, x<15 %), the dip is well-separated from the component associated to bent ions (θ=0º) and the RBS/C experimental kink angle is very close to the nominal one. However, as the LM condition (ε_T~0 %, x~18 %) is reached, the strain becomes so low that the two components of the dip coming from directly and indirectly channeled particles are mixed, resulting in asymmetric dips. Here, MC simulations are essential to correct the experimental kink angle from RBS/C scans (see Figure 6.31). If x is further increased, a compressive strain state is obtained. Two samples were grown in these conditions (ε_T<1 %, x>18 %), but both show no angular shift in the scans. Note that for x~25 %, this behavior is expected because the a/c ratio is the same as for GaN (Figure 6.29). Nevertheless, assuming a pseudomorphic

growth for x=29 %, the MC simulations predict an asymmetry in the scan which is not visible in sample B6. This asymmetry is not present because this sample is partially relaxed as shown in Figure 6.11. Therefore, the film has an *a/c* ratio close to that of GaN, and taking the relaxation into account in the simulation, the experimental scan is well reproduced.

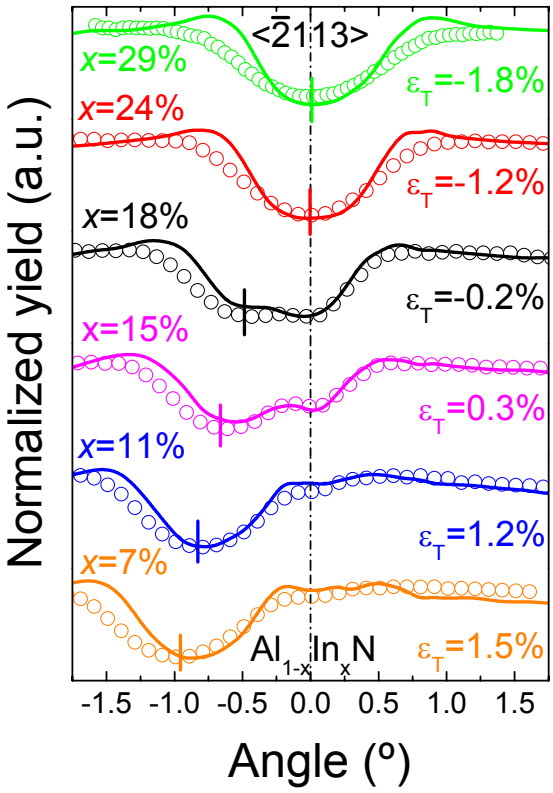

Figure 6.31 Experimental (circles) and MC simulated (solid lines) angular scans along the $< \bar{2}113 >$ axis for AlInN samples. The different compositions create strain states with tensile or compressive character, affecting the intensity of the steering effects. In the simulations a pseudomorphic growth was always assumed.

With help of the MC simulations, three different regions have been identified where elastic strain affects the accuracy of RBS/C measurements. The relative error in the conventional estimation of the kink angle is then conditioned by the actual strain state of each particular sample. In the case of LM AlInN films (x~18 %), the presence of steering effects has been clearly confirmed from both experimental and simulated scans, but the exact determination of the tetragonal distortion can be achieved by the MC fittings. However, for compositions close to x~25 %, the simulations cannot correct the effect of the ion steering.

The extension of these regions for the other ternaries (AlGaN and InGaN) was also calculated [39]. Nevertheless, in these systems it is not possible to reach LM conditions, being the relevance of the steering effects not so significant as in the case of AlInN films.

6.4.4. Influence of the probing energy on the steering effects

As shown in the previous studies, the limitations of the RBS/C in the determination of the strain state of the HSs can be explained and corrected by MC simulations. Even so, depending on the thickness and the strain state, there are critical cases with $\Delta\theta$=0º which cannot be resolved with the MC approach because different situations can fit the same experimental results. In such cases, the method does not warrant that the solution is unique, and only a bottom limit for the strain state can be obtained. The question posed then is: how can RBS/C be used to find out the actual strain state in these circumstances?

In order to answer this question, a novel way to measure the strain state of LM HSs by means of the breakdown of the steering effects is proposed [57]. It is important to note that, in all the preceding simulations, the beam energy was kept at 2 MeV, which is the conventional one for this kind of analysis. Despite this energy has several advantages (high cross section of the elements, good depth resolution), we have to take into account that the underlying physics of the steering effects is mainly determined by one single parameter: the critical angle (ψ_1=0.695º at 2 MeV). Strain states corresponding to kink angles below this ψ_1 are normally affected by anomalous channeling. However, Lindhard's formula (3.5) relates the critical angle and the ion energy and, therefore, opens an alternative to break these anomalous conditions. With He ions, the maximum achievable energy in 5 MV accelerators is 15 MeV, so the reduction of ψ_1 could be a factor of 2 or more. This reduction implies a fundamental advantage for the determination of the strain state in our LM HSs so, in the following, it will be analyzed for two specific samples.

As an additional comment, it should be noted that the energy is not the unique parameter than can be tuned experimentally. Following Lindhard's equation, one could also change the incident ion from He to H, what means an additional reduction of a factor of 2 in ψ_1. Therfore, the combination of both effects (a change in the energy and

in the ion mass) would be very powerful in samples very close to LM conditions and it will be considered in future experiments.

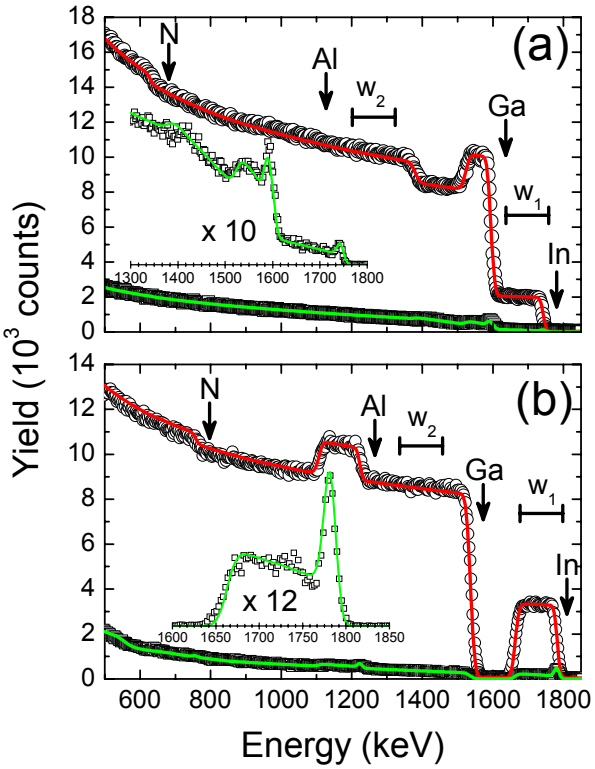

Figure 6.32 Random and <0001> aligned spectra (circles and squares) and simulation (solid line) from RBS/C experiments at 2 MeV. Inset shows the aligned spectrum in detail. Windows of the film (w_1) and the substrate (w_2) signals for the angular scans are also shown.

For the proposed study, D1 and F2 samples were selected because they show both compressive and tensile strain states and, at the same time, different thicknesses. Prior to the experiments, MC simulations with increasing beam energy were performed. The simulations demonstrated the progressive elimination of the steering effects in the angular scans and predicted an exact measurement of the kink angle at 15 MeV (for D1) and 8 MeV (for F2).

Therefore, *ad-hoc* designed experiment was done with a 1 mm^2 ^4He beam and different probing energies from 2 MeV up to 10 MeV, using the 5 MV accelerator at CMAM. Angular scans along the $<\bar{2}113>$ axis were recorded in both samples at each energy. Steps of 0.05º (1 μC per point) and 0.1º (0.1 μC per point) were selected for D1 and F2, respectively. Figure 6.32 shows random and <0001> aligned spectra of both HSs from RBS/C experiments. Aligned spectra along the <0001> direction (insets in Figure 6.32)

reveal a minimum yield of χ_{min}=4 % for both HSs. This parameter confirms the high crystalline quality of the samples, although it is double of those values typical for GaN substrates, and an appreciable dechanneling is visible in the spectra.

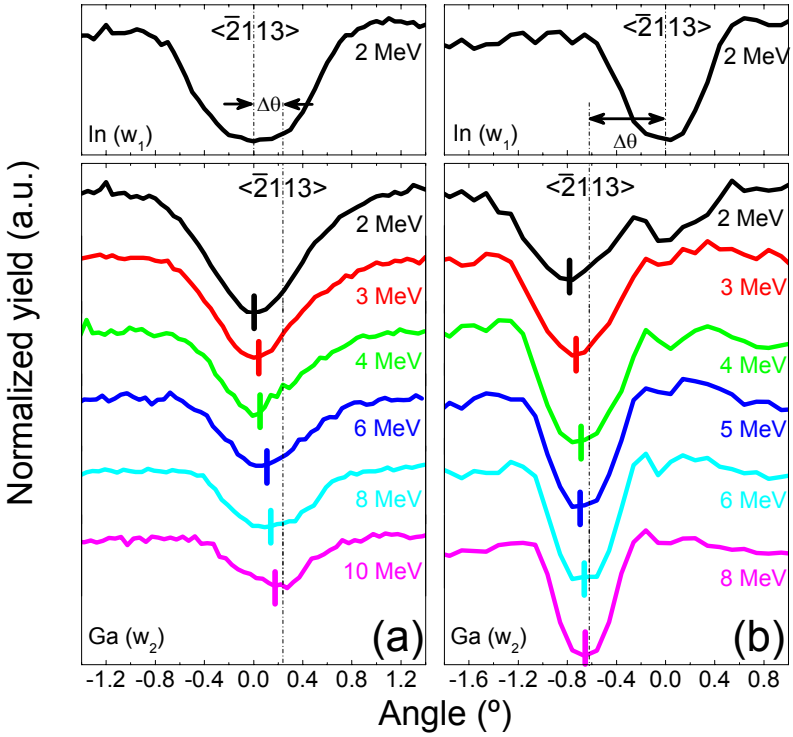

Figure 6.33 Experimental angular scans across the $<\bar{2}113>$ axis for different energies in strained AlGaInN/GaN (a) and AlInN/GaN (b) HSs. As a reference, the angular scan from the active layer (w_1) at 2 MeV is shown (top graphics). The shift from the substrate (w_2) does not match the real kink angle due to steering effects, which gradually diminishes with energy.

For the analysis of the angular scans of the layer and the substrate in Figure 6.32, the energy regions corresponding to the In (w_1) and Ga (w_2) signals were considered. Figure 6.33 shows the experimental $<\bar{2}113>$ scans of the substrate (w_2) for different beam energies. As a reference, the angular scan at 2 MeV is also shown for the layer signal (w_1), being 0º the position where the minimum yield of this first layer is achieved. This position remains constant with the beam energy since ion channeling in the first layer is not disturbed by steering effects. As mentioned before, the angular shifts between the dips at low energies (2 MeV) do not correspond to the real $\Delta\theta$ marked in Figure 6.33. However, this anomalous behavior gradually disappears by increasing the energy, and $\Delta\theta$ converges to the nominal value. This fact is forced by the decrease of ψ_1 by a factor of 2 or more for the studied energy range. Thus, at low beam

energies an appreciable part of the channeled ions can be deflected at the interface and remains channeled in the GaN layer, whereas at high energies ions suffer a significant number of direct scattering events causing dechanneling of the beam. Therefore, features corresponding to the steering effects, such as the additional minimum at 0º in Figure 6.33(b) (where the beam is aligned with the film), are progressively removed. The ternary sample reaches the expected value of 0.62º at 8 MeV. However, the scan in the quaternary HS shows an asymmetric dip even at 10 MeV, being the two components (0º for the substrate and 0.24º for the layer) not well resolved yet. Further measurements above 10 MeV to eliminate this artifact were not performed because of the radioactive activation of the sample during the experiment.

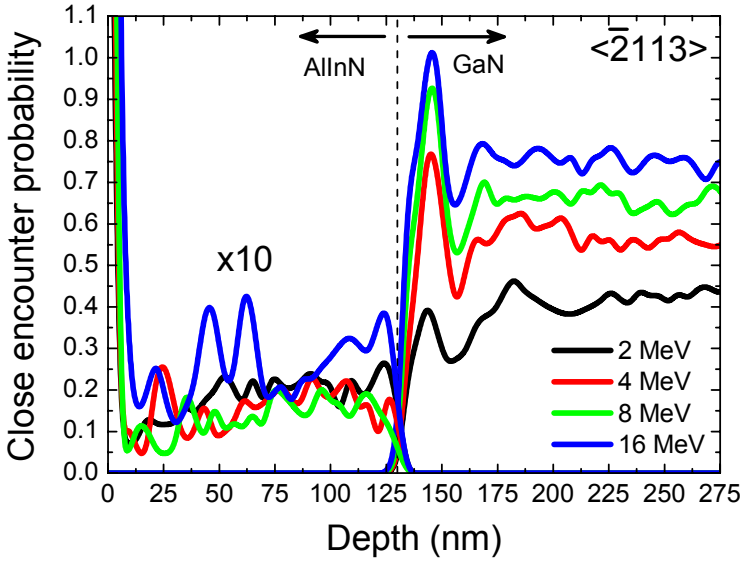

Figure 6.34 Energy dependence of the close encounter probability for an AlInN/GaN HS.

The weakening of the ion steering at the GaN interface for higher beam energies is well explained in the MC simulations by the increase in the close encounter probability (Figure 6.34). Indeed, the simulations predict a sharp increase of the probability from ~0.025 before the interface to 0.44 (0.63, 0.68) at 2 (4, 8) MeV after the interface for an incident angle of 0º (i.e., beam aligned with the axis of the first layer). These values can be even higher at 16 MeV, which is very close to the maximum energy accessible in the CMAM accelerator. The changes of the close encounter probability reflect variations of the flux distribution of the ions, which depend on the time that the ion remains channeled in the layer [50, 53, 54]. Since this time is also controlled by the particle energy, the change in the probability can be directly correlated with it.

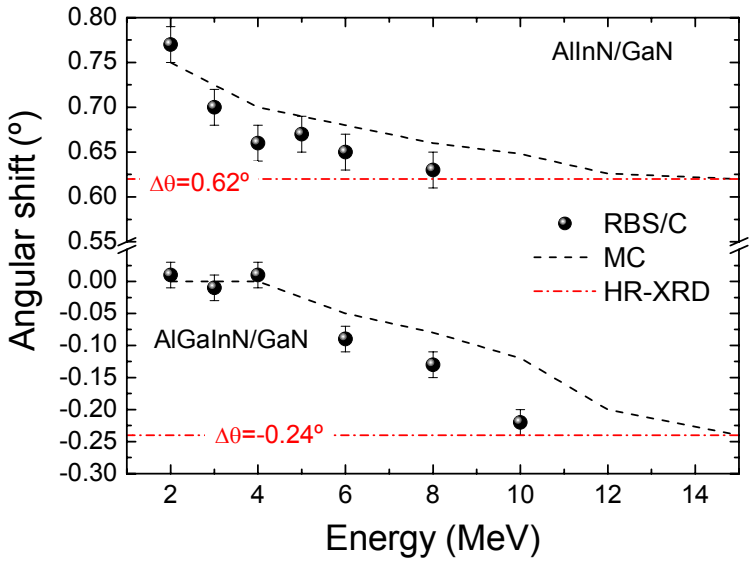

Figure 6.35 Experimental angular shifts and MC predictions for the HSs analyzed as a function of the probing energy.

Figure 6.35 shows the theoretical results for the angular shift obtained from MC simulations in comparison to the experimental results. Both experimental and simulated shifts were determined by Gaussian fittings of the dips. The trend of the experimental angular shift is well reproduced by MC simulations, although a slight underestimation is visible for both samples. This means that the experimental angular shift converges faster than expected to $\Delta\theta$. This fact can be explained by the defects in the first layer of the HSs, which enhance dechanneling and alleviate the impact of steering effects. A limitation to this approach for very small kink angles is given by the accuracy of the RBS/C technique to determine $\Delta\theta$ (~0.05º) and the maximum energy of typical tandem accelerators (15-18 MeV for He^{++}).

6.5. Conclusions

In this chapter, the useful combination of RBS/C and HR-XRD techniques for the characterization of ternary and quaternary LM HSs was discussed. RBS analysis was performed on AlInN films grown by PA-MBE within three different growth regimes previously identified. It was demonstrated that the nominal III/V ratio is normally underestimated because of the extra In contribution coming from decomposition. The substrate temperature also affects the actual In incorporation because of the concurrence

of decomposition and desorption mechanisms. The atypical compositional profile found in the intermediate In-rich regime proved that the transition to dynamical equilibrium is required for the growth of the ternary film, which imposes fixed conditions for the development of high-quality AlInN-based devices. The AlInN layers showed a pseudomorphic growth for the In-rich regime, with slight deviations at high and low temperatures. Strain state calculated from HR-XRD and RBS/C follow the same linear trend (from compressive to tensile), despite singular angular scans were detected in the RBS/C influencing the accuracy of this method. Vegard's law was generally satisfied in the AlInN films for the studied compositional range.

Concerning the analysis of the quaternary layers, it was shown that the Al flux is a limiting factor in the In incorporation even for fixed III/V ratios. This fact was related with the higher binding energy of the Al-N bond. A drastic reduction of In was found by increasing the substrate temperature because of the desorption and decomposition mechanisms. High crystal quality of these quaternary samples was verified, finding out a pseudomorphic growth under compressive strain. RBS/C angular scans showed anomalous dips with a null angular shift between the layer and the substrate.

MC simulations developed on several LM systems with different strain states demonstrated that the anomalous features found in the RBS/C experiments are due to the presence of steering effects, normally enhanced by large thickness and low strain state. The influence of these parameters was studied in detail using specific AlInN samples. The MC simulations can explain and correct (in some cases) the observed dips to provide an accurate determination of the strain state by RBS/C. In the situations where this is not possible, a new method was proposed and validated experimentally to eliminate the steering effects tuning the beam energy. Experiments at high energies demonstrated that the breakdown of the anomalous channeling phenomena can be achieved by this procedure, overcoming the initial limitations of RBS/C.

6.6. References

[1] R. Butté, J-F. Carlin, E. Feltin, M. Gonschorek, S. Nicolay, G. Christmann, D. Simeonov, A. Castiglia, J. Dorsaz, H.J. Buehlmann, S. Christopoulos, G. Baldassarri Höger von Högersthal, A.J.D. Grundy, M. Mosca, C. Pinquier, M. A. Py, F. Demangeot, J. Frandon, P.G. Lagoudakis, J.J. Baumberg and N. Grandjean, J. Phys. D: Appl. Phys. **40**, 6328 (2007).

[2] K. Starosta, Phys. Status Solidi a **68**, K55 (1981).

[3] F. G. McIntosh, K.S. Boutros, J.C. Roberts, S.M. Bedair, E.L. Piner and N.A. El-Masry, Appl .Phys. Lett. **68**, 40 (1996).

[4] T. Matsuoka, N. Yoshimoto, T. Sasaki and A. Katsui, J. Electron. Mater. **21**, 157 (1992).

[5] A. Dadgar, F. Schulze, J. Bläsing, A. Diez, A. Krost, M. Neuburger, E. Kohn, I. Daumiller and M. Kunze, Appl .Phys. Lett. **85**, 5400 (2004).

[6] J.-F. Carlin, and M. Ilegems, Appl .Phys. Lett. **83**, 663 (2003).

[7] M. Gonschorek, J.-F. Carlin, E. Feltin, M. A. Py and N. Grandjean, Appl .Phys. Lett. **89**, 062106 (2006).

[8] J. Xie, X. Ni, M. Wu, J.H. Leach, Ü. Özgür and H. Morkoç, Appl .Phys. Lett. **91**, 132116 (2007).

[9] T. Wang, Y. H. Liu, Y. B. Lee, J. P. Ao, J. Bai and S. Sakai, Appl .Phys. Lett. **81**, 2508 (2002).

[10] H. Hirayama, J. Appl. Phys. **97**, 091101 (2005).

[11] S. Nagarajan, Y.S. Lee, M. Senthil Kumar, O.H. Cha, C.-H. Hong and E.-K. Suh, J. Phys. D: Appl. Phys. **41**, 012001 (2008).

[12] D. J. Dunstan, J. Mater. Sci.-Mater. Electron. **8**, 337 (1997).

[13] Y. Sun, S.E. Thompson and T. Nishida, J. Appl. Phys. **101**, 104503 (2007).

[14] F. Bernardini, V. Fiorentini and D. Vanderbilt, Phys. Rev. B **56** R10024 (1997).

[15] M. Suzuki, and T. Uenoyama, J. Cryst. Growth **189**, 625 (1998).

[16] L. Liu, and J.H. Edgar, Mater. Sci. Eng. R **37**, 61 (2002).

[17] S. Fernández-Garrido, Ž. Gačević and E. Calleja, Appl .Phys. Lett. **93**, 191907 (2008).

[18] C. Hums, J. Bläsing, A. Dadgar, A. Diez, T. Hempel, J. Christen, A. Krost, K. Lorenz and E. Alves, Appl .Phys. Lett. **90**, 022105 (2007).

[19] M. Marques, L. K. Teles, L. M. R. Scolfaro, L. G. Ferreira and J. R. Leite, Phys. Rev. B **70**, 073202 (2004).

[20] T. Matsuoka, Appl .Phys. Lett. **71**, 105 (1997).

[21] A. Redondo-Cubero, K. Lorenz, R. Gago, N. Franco, M.-A. di Forte Poisson, E. Alves and E. Muñoz, J. Phys. D: Appl. Phys. **43**, 055406 (2010).

[22] E. Monroy, D. Gogneau, D. Jalabert, E. Bellet-Amalric, Y. Hori, F. Enjalbert, L. S. Dang and B. Daudin, Appl .Phys. Lett. **82**, 2242 (2003).

[23] S. Fernández-Garrido, A. Redondo-Cubero, R. Gago, F. Bertram, J. Christen, E. Luna, A. Trampert, J. Pereiro, E. Muñoz and E. Calleja, J. Appl. Phys. **104**, 083510 (2008).

[24] K. Lorenz, N. Franco, E. Alves, S. Pereira, I.M. Watson, R.W. Martin, K.P. O'Donnell, J. Cryst. Growth **310**, 4058 (2008).

[25] V. Darakchieva, M. Beckers,M.-Y. Xie, L. Hultman, B. Monemar, J.-F. Carlin, E. Feltin, M. Gonschorek and N. Grandjean, J. Appl. Phys. **103**, 103513 (2008).

[26] T. Seppänen, L. Hultman, J. Birch, M. Beckers and U. Kreissig, J. Appl. Phys. **101**, 043519 (2007).

[27] K. Lorenz, N. Franco, E. Alves, I.M. Watson, R.W. Martin and K.P. O'Donnell, Phys. Rev. Lett. **97**, 85501 (2006).

[28] B.-T. Liou, S.-H. Yen and Y.-K. Kuo, Appl. Phys. A **81**, 651 (2005).

[29] C. H. Chen, Y.F. Chen, Z.H. Lan, L.C. Chen, K.H. Chen, H.X. Jiang and J.Y. Lin, Appl. Phys. Lett. **84**, 1480 (2004).

[30] H. Hirayama, A. Kinoshita, T. Yamabi, Y. Enomoto, A. Hirata, T. Araki, Y. Nanishi and Y. Aoyagi, Appl .Phys. Lett. **80**, 207 (2002).

[31] M. Ferhat, and F. Bechstedt, Phys. Rev. B **65**, 075213 (2002).

[32] C. S. Gallinat, G. Koblmüller, J.S. Brown and J.S. Speck, J. Appl. Phys. **102**, 064907 (2007).

[33] E. Monroy, N. Gogneau, F. Enjalbert, F. Fossard, D. Jalabert, E. Bellet-Amalric, L. S. Dang and B. Daudin, J. Appl. Phys. **94**, 3121 (2003).

[34] J. H. Edgar, *Group-III nitrides* (INSPEC, London, 1994).

[35] K. Muraki, S. Fukatsu, Y. Shiraki and R. Ito, Appl .Phys. Lett. **61**, 557 (1992).

[36] C. Wu, S. Yin, J. Zhang, G. Xiao, J. Liu and P. Zhu, J. Appl. Phys. **68**, 2100 (1990).

[37] G. M. Cohen, D. Ritter, V. Richter and R. Kalish, Appl. Phys. Lett. **74**, 43 (1999).

[38] T. Matsushita, W. Sakai, K. Nakajima, M. Suzuki, K.Kimura, A. Agarwal, H.-J. Gossmann, M. Ameen and H. Harimac, Nucl. Instr. Meth. B **249**, 432 (2006).

[39] A. Redondo-Cubero, K. Lorenz, N. Franco, S. Fernández-Garrido, R. Gago, P.J.M. Smulders, E. Muñoz, E. Calleja and E. Alves, J. Phys. D: Appl. Phys. **42**, 065420 (2009).

[40] L. Vegard, Z. Phys. **5**, 17 (1921).

[41] V. Darakchieva, M.-Y. Xie, F. Tasnádi, I.A. Abrikosov, L. Hultman, B. Monemar, J. Kamimura and K. Kishino, Appl .Phys. Lett. **93** (2008).

[42] S. Zhou, M.F. Wu, S.D. Yao, J.P. Liu and H. Yang, Superlattices Microstruct. **39**, 429 (2006).

[43] S. Fernández-Garrido, J. Pereiro, F. González-Posada, E. Muñoz, E. Calleja, A. Redondo-Cubero and R. Gago, J. Appl. Phys. **103**, 046104 (2009).

[44] S. Fernández-Garrido, *Crecimiento de nitruros del grupo III por epitaxia de haces moleculares para la fabricación de diodos electroluminiscentes en el rango visible-ultravioleta*, (Universidad Politécnica de Madrid, Madrid, 2009)

[45] S. Nakamura, Science **281**, 956 (1998).

[46] S. F. Chichibu, A. Uedono, T. Onuma, B. A. Haskell, A. Chakraborty, T. Koyama, P. T. Fini, S. Keller, S. P. Denbaars, J. S. Speck, U. K. Mishra, S. Nakamura, S. Yamaguchi, S. Kamiyama, H. Amano, I. Akasaki, J. Han, and T. Sota, Nat. Mater. **5**, 810 (2006).

[47] J. H. Barrett, Phys. Rev. B **3**, 1527 (1971).

[48] P. J. M. Smulders, and D.O. Boerma, Nucl. Instr. Meth. B **29**, 471 (1987).

[49] J. F. Ziegler, J.P. Biersack and U. Littmark *The stopping and range of ions in solids* (Pergamon Press, New York, 1985).

[50] B. A. Davidson, L.C. Feldman, J. Bevk and J.P. Mannaerts, Appl. Phys. Lett. **50**, 135 (1987).

[51] J. Lindhard, Mat. Phys. Medd. K. Dan. Vidensk. Selsk. **34**, 1 (1965).

[52] B. R. Appleton, C.D. Moak, T.S. Noggle, J.H. Barrett, Phys. Rev. Lett., 1307 (1972).

[53] J. S. Rosner, Gibson, W.M., J.A. Golovchenko, A.N. Goland and H.E. Wegner, Phys. Rev. B **18**, 1066 (1978).

[54] M. B. H. Breese, D.G. de Kerckhove, P.J.M. Smulders and D.N. Jamieson, Nucl. Instr. Meth. B **159**, 248 (1999).

[55] J. H. Barrett, Phys. Rev. Lett. **31**, 1542 (1973).

[56] R. W. Fearick, Nucl. Instr. Meth. B **164-165**, 88 (2000).

[57] A. Redondo-Cubero, K. Lorenz, R. Gago, N. Franco, S. Fernández-Garrido, P. J. M. Smulders, E. Muñoz, E. Calleja, I. M. Watson and E. Alves, Appl .Phys. Lett. **95**, 051921 (2009).

7

Conclusions and future work

This chapter summarizes the most important results and conclusions achieved in this thesis. In addition, some possible future lines that could be interesting as a continuation of this work are pointed out.

I don't care about demonstrations; I only want to know the truth. (P.A.M. Dirac)

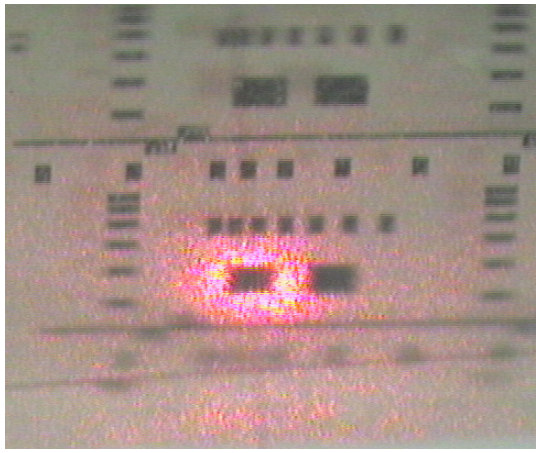

TLMs measured during this thesis in the microbeam line at CMAM.

7.1. Conclusions

Several objectives were established for the achievement of this thesis, mainly conducted by the roadmap of the KORRIGAN project and other national projects and collaborations. Within this diversified framework, this thesis has tackled different processing issues of WBS HSs, as studied by IBA techniques and other complementary techniques. In the preceding chapters, the most relevant results have been compiled, that deepen the understanding of the growth phenomena of such materials and that certainly contribute to the optimization of their preparation processes. In the following, the major contributions are summarized.

7.1.1. Contributions to the optimization of base layers

The benefits of the AlN and the GaN nucleation layers (NLs) on the subsequent growth of GaN base layers were compared, showing the enhancement of the 2D growth mode and the reduction of defects in the former case. It was shown that a relatively high density of defects is produced in the first nm's of the NLs. However, the structural defects are confined to this near-interface region and both AlN and GaN NLs allow the growth of GaN base layers with a good in-depth crystal quality. In addition, the presence of strain was detected at the first stages of the growth of the base layers for both kinds of NLs.

The enhancement of the epitaxial growth of ZnO on sapphire by PMS at moderate substrate temperatures (550 ºC) was found by XRD and RBS/C measurements. In such case, the ZnO layers showed a single-crystal domain. The Zn and O signals showed different behaviors with the temperature in RBS/C and Raman spectra, suggesting the better structural ordering of the Zn sublattice. For temperatures equal or above 400 ºC, Al-Zn interdiffusion was observed at the film-substrate interface, which affects the crystal quality in this region.

7.1.2. Contributions to the optimization of heterostructures out of lattice-matched conditions

The detection of Al profiles in AlGaN/GaN HSs with different Al contents was successfully characterized by IBA. Compositional gradients were observed at high Al contents and were associated to the effect of strain relaxation. A good correlation was

found between the IBA and the XRD results, where the compositional profiles could explain the features observed in diffraction rocking curves. The good depth resolution and high sensitivity to Al of ERD-BIC, was determinant for the measurement of the compositional profiles and the characterization of HSs designed for HEMTs with different layer configurations. The significant presence of H impurities at the AlGaN/GaN interface was checked by means of NRA. The study, performed on samples grown by very different methods, evidenced the incorporation of low but non negligible amount of H. The H concentration is independent on the growth technique, and a significant amount of H was detected close to the 2DEG region, which may be relevant for the final device performance. A diffusive model was used to explain the depth-resolved profiles obtained for H, pointing out the post-deposition incorporation of the H impurities.

The effect of the miscibility on the crystal quality and composition of InGaN/GaN HSs grown by PA-MBE was investigated. A clear decrease in the crystal quality was observed for intermediate compositions, accompanied by a relaxation of the lattice parameters. The RBS analysis was used to establish a growth diagram for InGaN, based on the determination of the activation energy for InN decomposition. In this way, three different growth regions were established.

The composition of MgZnO layers grown on two different non-polar orientations of the substrate and for different precursor fluxes was analyzed by RBS. The O-rich growth regime was confirmed by the RBS measurements, and the linear increase in the bandgap was correlated with the Mg concentration. RBS/C angular scans showed a low single crystalline character of the samples, with a similar trend of Mg and Zn signals. Finally, N implantation of MgZnO layers was carried out. After implantation, it was found that the crystal damage can be recovered with a thermal annealing at 900 ºC. PL emission of implanted (and annealed) samples was even higher than that of the non irradiated samples, confirming the crystal reconstruction evidenced by RBS/C. The treatments at this temperature do not affect in a great way the migration of the elements from the layers, except for a slight Al-Zn interdiffusion at the film-substrate interface.

7.1.3. Contributions to the optimization of heterostructures close to lattice-matched conditions

The useful combination of RBS/C and HR-XRD techniques for the characterization of ternary and quaternary LM HSs has been shown. RBS analysis on the AlInN films grown by PA-MBE within three different growth regimes was carried out. It was demonstrated that nominal III/V ratio is normally underestimated because of the extra In contribution coming from InN thermal decomposition. The substrate temperature also reduces the actual In incorporation because of the concurrence of decomposition and desorption mechanisms. Typical compositional profiles in the intermediate In-rich regime showed that the transition to dynamical equilibrium is required for the growth of ternary film with a high crystal quality. This condition should be incorporated for future development of high-performance AlInN-based devices. The AlInN layers showed a pseudomorphic growth for the In-rich regime, with slight deviations at high and low temperatures. Strain state calculated from HR-XRD and RBS/C followed the same linear trend (from compressive to tensile), although anomalous channeling effects were detected in RBS/C scans, apparently (see below) affecting the strain sensibility of this method. Vegard's law was generally satisfied in the AlInN films within the studied compositional range.

Concerning the analysis of the quaternary layers, it was shown that the Al flux is a limiting factor for the In incorporation, even for fixed III/V ratios. This fact was related with the higher binding energy of the Al-N bond with respect to In-N. A drastic reduction of the In content was found by increasing the substrate temperature, due to thermal induced desorption and decomposition mechanisms. High crystal quality of these quaternary samples was verified, finding out a pseudomorphic growth under compressive strain. RBS/C angular scans showed again anomalous dips with an unexpected null angular shift between the signals from the layer and the substrate.

MC simulations developed on very different LM systems demonstrated that the anomalous features mentioned above in the RBS/C experiments are due to the presence of steering effects of the projectiles at the HS interface. The simulations show that such effects are normally enhanced by the larger thickness and the lower strain state of the active layer. The influence of these parameters was confirmed experimentally using selected AlInN samples. In this way, MC simulations can explain and correct (in certain

cases) the observed dips to provide an accurate determination of the strain state by RBS/C. In the situations where this approach is not possible, an alternative method is proposed to eliminate the steering effects by tuning the beam energy. Experiments at high energies demonstrated the breakdown of the anomalous channeling phenomena, proving the suitability of this procedure to overcome the apparent limitations of RBS/C.

7.2. Future work

The results obtained in this thesis have shed some light in the growth of WBS HSs, but also open new issues and questions for the continuation of the work. Additionally, due to the limited time imposed for the production of this thesis, some interesting studies could not be addressed or were developed to a lower state than the ones presented in this manuscript. Other ongoing works are currently under analysis and will be completed in the near future. In this section, some of the possible continuations of this work are gathered and suggested.

7.2.1. Future work on base layers

The growth of GaN and ZnO base layers on sapphire has reached a reasonable quality at the present moment, but further improvements are still possible. The following tasks are suggested in this line:

- The analysis of the growth of GaN on ZnO buffer layers, and vice versa. The combination of both binaries is becoming more and more common, and it has shown benefits on the strain state and the crystal quality of the base layers.

- The analysis of impurities, such as H or C, in ZnO base layers. These impurities could play an important role as traps for carriers, affecting the electrical properties of the layers, and preventing or making unstable the p-type doping.

- The study of the lattice positions of dopants in ZnO. It would be particularly interesting to carry out NRA for N detection under channeling conditions. This would allow the determination of the exact location of N atoms in the wurtzite lattice and yield valuable information in the activation of N dopants, to effectively modify the band structure. For other V-elements as Sb or As, the RBS/C analysis would be a good approach due to the well-resolved signals in the spectra.

7.2.2. Future work on heterostructures

Although this thesis has shown the analysis of a large variety of WBS HSs, there are still some unexplored systems of great interest. Therefore, several tasks are proposed for the future. However, prior to the analysis, a complete optimization of the programs controlling the acquisition and analysis by RBS/C at CMAM should be carried out. The codes developed in this thesis have solved some initial limitations presented at the beginning of this thesis, establishing valuables methods to obtain random and aligned spectra. However, they cannot be considered as definitive. Indeed, the strong analogies between RBS/C and XRD experiments suggest the use of similar computer programs for controlling the motion of the goniometer, the acquisition in real-time, and the fitting of the peaks for the alignment; everything under a friendly-user graphical display. Thus, the first proposal is the improvement of the current codes for RBS/C analysis, especially concerning real-time measurements.

Once the experimental system is optimized, new tasks can be explored. This includes:

- The study of the mechanisms affecting the phase separation in ternary and quaternary HSs. This is a general but very critical feature, which is still not well-understood. It can play a significant role in the deterioration of the layers, so further efforts should be focused on this item. More concretely, it is unclear if there is always a causal link between composition and strain relaxation.

- The systematic study of the incorporation of H and other light impurities in the 2DEG of AlGaN/GaN HEMTs, and their correlation with the electrical performance of the transistors.

- The analysis of the compositional limits in MgZnO and CdZnO layers with respect to the miscibility of cubic phases in the wurtzite lattice. The determination of the lattice sites of Mg and Cd by MC simulations of the angular scans.

- The study of the relation between the growth mode (N-rich, In-droplets, intermediate In-rich) and the compositional gradients in AlInN layers. In addition, the understanding of the physical phenomena inducing the formation of In-droplets during the growth could give important information about the origin of structural defects.

- The analysis of superlattices and MQW structures in LM conditions and, in particular, the evolution of the strain state with the thickness and number of bilayers.

7.2.3. Related works on HEMTs

Although this thesis was focused on the optimization of the base and active layers of the devices, this is only the first part of a large series of steps in the device fabrication processes. There are two significant parts of the device that can strongly affect the performance and reliability of the devices, such as the ohmic contacts and the passivant layers. These items were studied to a lesser extent during this thesis and a systematic study for the optimization of these procedures was not finished completely.

In particular, RBS analysis of ohmic contacts should be very useful in the determination of the migration species during the RTA, as evidenced by some preliminary tests done at CMAM. In these measurements, the layered structure of the contact was verified by means of in-depth compositional analysis. Further, it was found by RBS that samples after the RTA process present a diffusion profile of the elements of the contact (Au, Ti, Al, Ni…), which can affect the sheet resistance of the contact. This parameter is very important for the device performance. Consequently, the continuation of the study on ohmic contacts is strongly suggested. However, other analytical tools apart from RBS should be considered since, in this technique, the overlapping signals from the present elements make the analysis very complicated. In the particular case of IBA techniques, ERD-TOF or ERD-BIC systems can be an effective alternative.

The study of passivant layers is also another important point to be developed in the future. These layers are normally deposited by CVD, and mainly consist of SiN. Nevertheless, the results obtained during this thesis have evidenced very high concentrations of H within these layers. Considering the proposed in-diffusion model of H in AlGaN (see chapter 5) and the high working temperatures of the devices, the reduction of H in the passivant layers could become a significant advantage. Hence, further optimization of the passivant layers is proposed.

Of course, the major goal that can be suggested for the future is the measurement of a complete integrated device by IBA. This kind of experiment would require a micro-beam in vacuum conditions to study, for example, different parts of a transistor with sub-micron lateral resolution. Currently, there are several laboratories with the

capability to generate such beams, which would allow the analysis of the reliability of the devices in their final fabrication state. Actually, during this thesis, TLM contacts with feature sizes of some microns were measured in the external microbeam station at CMAM, demonstrating the feasibility of this approach. Such studies could also yield valuable information about deterioration of the device after operation, and even in-situ measurements during real-time operation could be envisaged.

Appendix I

List of abbreviations

2DEG:	Two dimensional electron gas
AES:	Auger electron spectroscopy
AFM:	Atomic force microscopy
BIC:	Bragg ionization chamber
CCD:	Charge-coupled device
CFOM:	Combined figure of merit
DBR:	Distributed Bragg reflector
DD:	Dislocation density
DPA:	Displacement per atom
EDXS:	Energy dispersive X-ray spectroscopy
EELS:	Electron energy loss spectroscopy
ERD:	Elastic recoil detection
FWHM:	Full width at half maximum
GI-XRD:	Grazing incidence XRD
HEMT:	High electron mobility transistor
Hg-CV:	Mercury probe for capacitance-voltage measurements
HR-XRD:	High resolution X-ray diffraction
HS:	Heterostructure
IBA:	Ion beam analysis
III-N:	Group of III-nitrides (AlN, GaN, InN)
IR:	Infra-red
LD:	Laser diode
LED:	Light emission diode
LM:	Lattice matched
LO:	Longitudinal optical
MBE:	Molecular beam epitaxy
MC:	Monte Carlo
ML:	Mono-layer
MO-CVD:	Metal-organic chemical vapor deposition
MQW:	Multi-quantum well
NL:	Nucleation layer
NRA:	Nuclear reaction analysis
PA-MBE:	Plasma assisted molecular beam epitaxy
PID:	Proportional-integral-derivative
PL:	Photoluminescence
PMS:	Pulsed magnetron sputtering
QMS:	Quadrupole mass spectrometer
QW:	Quantum well
RBS/C:	RBS in channeling mode
RBS:	Rutherford backscattering spectrometry

RC:	Rocking curve
RE:	Relative error
RF:	Radio frequency
RHEED:	Reflection high energy electron diffraction
RSM:	Reciprocal space map
RT:	Room temperature
RTA:	Rapid thermal annealing
SE:	Spectroscopic ellipsometry
SEM:	Scanning electron microscopy
SIMS:	Secondary ion mass spectrometry
SO:	Surface optical
SR:	Surface roughness
TEM:	Transmission electron microscopy
TLM:	Transmission line model
TO:	Transverse optical
TOF:	Time of flight
UHV:	Ultra high vacuum
UV:	Ultra-violet
WBS:	Wide bandgap semiconductor
XPS:	X-ray photoelectron spectroscopy
XRD:	X-ray diffraction
XRR:	X-ray reflectrometry
ZBL:	Ziegler-Biersack-Littmark

Appendix II

Source code for RBS acquisition

The program *AngScan* was developed for the acquisition of angular scans in the Standard beamline at CMAM in 2008. This program is based on previous versions by Dr. Ángel Muñoz-Martín, but includes some improvements such as the movement in the φ axis and the direct control of the step. Figure A2.1 shows the aspect of the main window of *AngScan*. In the first part of the window, the file options (sample name, folder, path) can be introduced. In the second, the scan parameters are selected (range, steps, dose, number of points). The program allows linear scans in φ, θ, and χ, but also the combination of the θ-χ for the acquisition of random spectra.

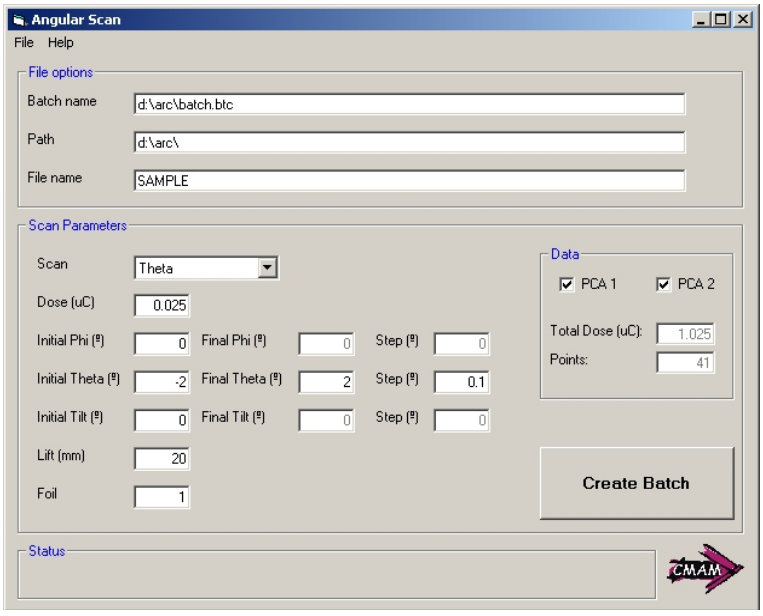

Figure A2.1. Main window of the AngScan program.

Next, the source code of the program in Visual Basic is shown (the character ";" was used as a line separator).

```
Option Explicit


Private Sub FileExit_Click()        ' MENU FILE OPCION EXIT
   'Beep
End;      End Sub

Private Sub mnuHelp_Click()      ' MENU HELP
Dim msj
msj = MsgBox("    A.R.C.    2008", vbOKOnly)
If msj = vbOK Then Exit Sub
End;      End Sub

Private Sub Combo_Click()         'SCAN TYPE
   Select Case Combo.ListIndex
   Case 0  'PHI
      pointnum(0).Text = 0
      txtphi(1).Enabled = True;       txtphi(2).Enabled = True
      txttheta(1).Enabled = False;    txttheta(2).Enabled = False
      txttilt(1).Enabled = False;     txttilt(2).Enabled = False
      txttheta(1).Text = 0;           txttheta(2).Text = 0
      txttilt(1).Text = 0;            txttilt(2).Text = 0
      pointnum(0).Enabled = False
   Case 1  'THETA
      pointnum(0).Text = 0
      txtphi(1).Enabled = False;      txtphi(2).Enabled = False
      txttheta(1).Enabled = True;     txttheta(2).Enabled = True
      txttilt(1).Enabled = False;     txttilt(2).Enabled = False
      txtphi(1).Text = 0;             txtphi(2).Text = 0
      txttilt(1).Text = 0;            txttilt(2).Text = 0
      pointnum(0).Enabled = False
   Case 2  'TILT
      pointnum(0).Text = 0
      txtphi(1).Enabled = False;      txtphi(2).Enabled = False
      txttheta(1).Enabled = False;    txttheta(2).Enabled = False
      txttilt(1).Enabled = True;      txttilt(2).Enabled = True
      txtphi(1).Text = 0;             txtphi(2).Text = 0
      txttheta(1).Text = 0;           txttheta(2).Text = 0
      pointnum(0).Enabled = False
   Case 3  'THETA-TILT
      pointnum(0).Text = 0
      txtphi(1).Enabled = False;      txtphi(2).Enabled = False
      txttheta(1).Enabled = True;     txttheta(2).Enabled = False
      txttilt(1).Enabled = True;      txttilt(2).Enabled = False
      txtphi(2).Text = 0;             txttheta(2).Text = 0
      txttilt(2).Text = 0
      pointnum(0).Enabled = True
   End Select
End Sub

Private Sub Create_Click() '************************************************************
Dim n, i As Long; Dim q As Double; Dim sel As Byte; Dim itext As String
Dim th0, tl0 As Double; Dim th, tl As Double; Dim r, rth, rtl As Double

Select Case Combo.ListIndex
Case 0  'PHI
   On Error Resume Next;    n = Abs(Val(txtphi(1).Text) - Val(txtphi(0).Text)) / (Val(txtphi(2).Text))
Case 1  'THETA
   On Error Resume Next;   n = Abs(Val(txttheta(1).Text) - Val(txttheta(0).Text)) / (Val(txttheta(2).Text))
Case 2  'TILT
```

```
   On Error Resume Next;    n = Abs(Val(txttilt(1).Text) - Val(txttilt(0).Text)) / (Val(txttilt(2).Text))
Case 3  'THETA-TILT
   On Error Resume Next
   n = Abs(Val(pointnum(0).Text))
   th0 = (Val(txttheta(1).Text) + Val(txttheta(0).Text)) / 2
   tl0 = (Val(txttilt(1).Text) + Val(txttilt(0).Text)) / 2
   rth = Abs(Val(txttheta(0).Text) - th0)
   rtl = Abs(Val(txttilt(0).Text) - tl0)
End Select

Select Case Combo.ListIndex
Case 0, 1, 2                                                ' LINEAR SCAN
   For i = 1 To n + 1;          itext = CStr(i)
      On Error Resume Next
      Open txtbatchname.Text For Append As 1                'Open batch.btc
      SMS.Caption = "Writing " + itext;        SMS.Refresh

      Print #1, "(" + itext + ")";       Print #1, "Operator=Ghost"
      Print #1, "Dose=" + txtdose.Text
      Print #1, "Phi=" + Str$(Val(txtphi(0).Text + (i - 1) * Abs(txtphi(2).Text)))
      Print #1, "Theta=" + Str$(Val(txttheta(0).Text + (i - 1) * Abs(txttheta(2).Text)))
      Print #1, "Tilt=" + Str$(Val(txttilt(0).Text + (i - 1) * Abs(txttilt(2).Text)))
      Print #1, "Lift=" + txtlift.Text
      Print #1, "Translate="
      Print #1, "Foils=" + txtfoils.Text
      If chkpca1.Value = 1 Then;        Print #1, "Acquire1=yes"
      ElseIf chkpca1.Value = 0 Then;  Print #1, "Acquire1=no";       End If
      Print #1, "Name1=" + txtfilename.Text + "_F_" + CStr(Format(Val(i), "00"))
      Print #1, "Description1="
      Print #1, "Filename1=" + txtfilename.Text + "_F_" + CStr(Format(Val(i), "00"))
      Print #1, "Path1=" + txtpath.Text
      If chkpca2.Value = 1 Then;          Print #1, "Acquire2=yes"
      ElseIf chkpca2.Value = 0 Then;    Print #1, "Acquire2=no";       End If
      Print #1, "Name2=" + txtfilename.Text + "_M_" + CStr(Format(Val(i), "00"))
      Print #1, "Description2="
      Print #1, "Filename2=" + txtfilename.Text + "_M_" + CStr(Format(Val(i), "00"))
      Print #1, "Path2=" + txtpath.Text
      Close #1                                  'Close batch.btc
   Next
   SMS.Caption = "DONE !"

Case 3                                                      'CIRCULAR SCAN
   For i = 1 To n
      itext = CStr(i)
      th = rth * Cos(2 * 3.14159265358 * (i - 1) / n) + th0
      tl = rtl * Sin(2 * 3.14159265358 * (i - 1) / n) + tl0

      On Error Resume Next;        Open txtbatchname.Text For Append As 1
      SMS.Caption = "Writing " + itext;        SMS.Refresh
      Print #1, "(" + itext + ")";       Print #1, "Operator=Ghost"
      Print #1, "Dose=" + txtdose.Text
      Print #1, "Phi=" + Str$(Val(txtphi(0).Text))
      Print #1, "Theta=" + Str$(Val(th))
      Print #1, "Tilt=" + Str$(Val(tl))
      Print #1, "Lift=" + txtlift.Text
      Print #1, "Translate="
      Print #1, "Foils=" + txtfoils.Text
      If chkpca1.Value = 1 Then;        Print #1, "Acquire1=yes"
      ElseIf chkpca1.Value = 0 Then;          Print #1, "Acquire1=no";       End If
      Print #1, "Name1=" + txtfilename.Text + "_F_" + CStr(Format(Val(i), "00"))
```

```
      Print #1, "Description1="
      Print #1, "Filename1=" + txtfilename.Text + "_F_" + CStr(Format(Val(i), "00"))
      Print #1, "Path1=" + txtpath.Text
      If chkpca2.Value = 1 Then;          Print #1, "Acquire2=yes"
      ElseIf chkpca2.Value = 0 Then;          Print #1, "Acquire2=no";       End If
      Print #1, "Name2=" + txtfilename.Text + "_M_" + CStr(Format(Val(i), "00"))
      Print #1, "Description2="
      Print #1, "Filename2=" + txtfilename.Text + "_M_" + CStr(Format(Val(i), "00"))
      Print #1, "Path2=" + txtpath.Text
      Close #1
   Next
   SMS.Caption = "DONE !"
End Select
End Sub

Private Sub pointnum_Change(Index As Integer)
Dim n As Long; Dim q As Double
n = Abs(Val(pointnum(0).Text))
Select Case Combo.ListIndex
   Case 0, 1, 2;       q = (n + 1) * Abs(Val(txtdose.Text))
   Case 3;       q = n * Abs(Val(txtdose.Text))
End Select
TotalDose(1).Text = CStr(q)
End Sub

Private Sub txtdose_Change()                    ' DOSE
Dim n As Long ;Dim q As Double
On Error Resume Next
Select Case Combo.ListIndex
   Case 0;       n = Abs(Val(txtphi(1).Text) - Val(txtphi(0).Text)) / Abs(Val(txtphi(2).Text))
   Case 1;       n = Abs(Val(txttheta(1).Text) - Val(txttheta(0).Text)) / Abs(Val(txttheta(2).Text))
   Case 2;       n = Abs(Val(txttilt(1).Text) - Val(txttilt(0).Text)) / Abs(Val(txttilt(2).Text))
   Case 3;       n = Val(pointnum(0).Text)
End Select
q = (n + 1) * Abs(Val(txtdose.Text)); TotalDose(1).Text = CStr(q)
End Sub

Private Sub txtphi_Change(Index As Integer)      ' PHI
Dim n As Long; Dim q As Double; Dim modulo As Long
Debug.Print txtphi(0).Text; Debug.Print txtphi(1).Text; Debug.Print txtphi(2).Text
If Combo.ListIndex = 0 Then;    On Error Resume Next
   n = Abs(Val(txtphi(1).Text) - Val(txtphi(0).Text)) / Abs(Val(txtphi(2).Text))
   q = (n + 1) * Val(txtdose.Text)
   pointnum(0).Text = Str$(n + 1);    TotalDose(1).Text = CStr(q)
End If
End Sub

Private Sub txttheta_Change(Index As Integer)    ' THETA
Dim n As Long Dim q As Double

If Combo.ListIndex = 1 Then;    On Error Resume Next
   n = Abs(Val(txttheta(1).Text) - Val(txttheta(0).Text)) / Abs(Val(txttheta(2).Text))
   q = (n + 1) * Val(txtdose.Text)
   pointnum(0).Text = Str$(n + 1);    TotalDose(1).Text = CStr(q)
End If
If Combo.ListIndex = 3 Then;    On Error Resume Next
   n = Val(pointnum(0).Text)
   q = (n + 1) * Val(txtdose.Text);    TotalDose(1).Text = CStr(q)
End If
End Sub
```

```
Private Sub txttilt_Change(Index As Integer)        ' TILT
Dim n As Long; Dim q As Double
If Combo.ListIndex = 2 Then;   On Error Resume Next
   n = Abs(Val(txttilt(1).Text) - Val(txttilt(0).Text)) / Abs(Val(txttilt(2).Text))
   q = (n + 1) * Abs(Val(txtdose.Text))
   pointnum(0).Text = Str$(n + 1);   TotalDose(1).Text = CStr(q)
End If
End Sub
```

Appendix III

Source code for RBS/C analysis

The program *Dipito* was developed for the analysis of angular scans in the Standard beamline at CMAM in 2008. *Dipito* is based on a previous version by Dr. Ángel Muñoz-Martín, but introduces the φ angle in the analysis and the visualization of the data in real-time. Figure A3.1 shows the aspect of the main window of *Dipito*. In the first part of the window, the file options (sample name, folder, path) can be introduced. In the second, the energy windows for the integration are selected. A total of three windows can be defined for both fixed and movable detectors. At the right side the real-time calculation is shown.

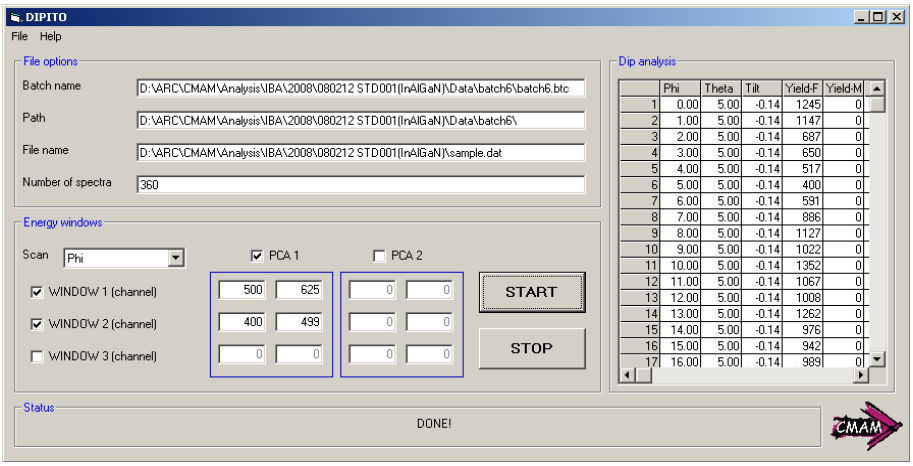

Figure A3.1 Main window of Dipito program.

Next, the source code of the program in Visual Basic is shown (the character ";" was used as a line separator).

```
Private Declare Function GetPrivateProfileString Lib "kernel32" Alias "GetPrivateProfileStringA" (ByVal lpApplicationName As String, ByVal lpKeyName As Any, ByVal lpDefault As String, ByVal lpReturnedString As String, ByVal nSize As Long, ByVal lpFileName As String) As Long
Private Declare Function WritePrivateProfileString Lib "kernel32" Alias "WritePrivateProfileStringA" (ByVal lpApplicationName As String, ByVal lpKeyName As Any, ByVal lpString As Any, ByVal lpFileName As String) As Long

Public Phi, Theta, Tilt, FIN; Public win0f, win1f, win2f; Public win0m, win1m, win2m

Private Sub mnuFileExit_Click()' MENU FILE OPCION EXIT
   'Beep;    End
End Sub

Private Sub mnuHelp_Click()     ' MENU HELP
Dim msj
msj = MsgBox("A.R.C.  2008", vbOKOnly); If msj = vbOK Then Exit Sub; End
End Sub

Function GetFromINI(sSection As String, sKey As String, sDefault As String, sIniFile As String)
   Dim sBuffer As String, lRet As Long
   ' Fill String with 255 spaces
   sBuffer = String$(255, 0)
   ' Call DLL
   lRet = GetPrivateProfileString(sSection, sKey, "", sBuffer, Len(sBuffer), sIniFile)
   If lRet = 0 Then
      ' DLL failed, save default
      If sDefault <> "" Then AddToINI sSection, sKey, sDefault, sIniFile
      GetFromINI = sDefault
   Else
      ' DLL successful
      ' return string
      GetFromINI = Left(sBuffer, InStr(sBuffer, Chr(0)) - 1)
   End If
End Function

' Returns True if successful. If section does not exist it creates it.
Function AddToINI(sSection As String, sKey As String, sValue As String, sIniFile As String) As Boolean
   Dim lRet As Long
   ' Call DLL
   lRet = WritePrivateProfileString(sSection, sKey, sValue, sIniFile)
   AddToINI = (lRet)
End Function

Private Sub CO()                              'INITIAL CONDITIONS
   FIN = False;    Panel.Clear;    Panel.Cols = 7
   Panel.Rows = Val(DIP.NumSpc.Text) + 1
   Panel.ColWidth(0) = 600;    Panel.ColWidth(1) = 600;    Panel.ColWidth(2) = 600
   Panel.ColWidth(3) = 600;    Panel.ColWidth(4) = 600;    Panel.ColWidth(5) = 600
   Panel.ColWidth(6) = 800;    Panel.Row = 0;    Panel.Col = 1
   Panel.Text = "Phi";          Panel.Col = 2
   Panel.Text = "Theta";        Panel.Col = 3
   Panel.Text = "Tilt";         Panel.Col = 4
   Panel.Text = "Yield-F";    Panel.Col = 5
   Panel.Text = "Yield-M"
   win0f = win1f = win2f = 0
   win0m = win1m = win2m = 0
End Sub
```

```
Public Sub FindDip(NombreFichero)      '*********************************************
Dim DipData() As Double; Dim i As Integer
Dim Filename As String, lpAppName As String, lpKeyName As String * 200
Dim lpDefault As String, temp As String * 200, X As Long

Open DIP.txtfilename.Text For Output As #2
Call CO
ReDim DipData(Val(DIP.NumSpc.Text), 10)
Filename = NombreFichero

For i = 1 To Val(DIP.NumSpc.Text)
   lpAppName = Str(i)

   lpKeyName = "phi";    lpDefault = "0"
   X = GetPrivateProfileString(lpAppName, lpKeyName, lpDefault, temp, Len(temp), Filename)
   Phi = Left(temp, InStr(temp, Chr(0)) - 1)

  lpKeyName = "theta";    lpDefault = "0"
   X = GetPrivateProfileString(lpAppName, lpKeyName, lpDefault, temp, Len(temp), Filename)
   Theta = Left(temp, InStr(temp, Chr(0)) - 1)

   lpKeyName = "Tilt";    lpDefault = "0"
   X = GetPrivateProfileString(lpAppName, lpKeyName, lpDefault, temp, Len(temp), Filename)
   Tilt = Left(temp, InStr(temp, Chr(0)) - 1)

   Path1 = DIP.txtpath.Text

   If DIP.chkpca1.Value = 1 Then
      lpKeyName = "Filename1";       lpDefault = "0"
      X = GetPrivateProfileString(lpAppName, lpKeyName, lpDefault, temp, Len(temp), Filename)
      Filename1 = Left(temp, InStr(temp, Chr(0)) - 1)
      file1 = Path1 + Filename1 + ".spc"
      If FIN = True Then;           DIP.SMS.Caption = " STOPPED! ";           Exit For
         Close 2
      End If
      ReadSpectrumF (file1)
    End If

   If DIP.chkpca2.Value = 1 Then
      lpKeyName = "Filename2";       lpDefault = "0"
      X = GetPrivateProfileString(lpAppName, lpKeyName, lpDefault, temp, Len(temp), Filename)
      Filename2 = Left(temp, InStr(temp, Chr(0)) - 1)
      file2 = Path1 + Filename2 + ".spc"            ' Nombre del espectro i del detector fijo a analizar
      If FIN = True Then;           DIP.SMS.Caption = " STOPPED! ";           Exit For
         Close 2
      End If
      ReadSpectrumM (file2)
   End If

   DIP.SMS.Caption = " Analyzing spectrum " + Str$(i)
   DipData(i, 0) = Phi;    DipData(i, 1) = Theta;    DipData(i, 2) = Tilt
   DipData(i, 3) = win0f;    DipData(i, 4) = win1f;    DipData(i, 5) = win2f
   DipData(i, 6) = win0m;    DipData(i, 7) = win1m;    DipData(i, 8) = win2m
   Datos = Str$(DipData(i, 0)) + Chr(9) + Str$(DipData(i, 1)) + Chr(9) + Str$(DipData(i, 2)) + Chr(9) +
Str$(DipData(i, 3)) + Chr(9) + Str$(DipData(i, 4))

   Call PONER_DATOS(DipData(), i)
   Print #2, Phi, Theta, Tilt, win0f, win1f, win2f, win0m, win1m, win2m
Next i
Close 2
```

```
If FIN = False Then;    DIP.SMS.Caption = " DONE! ";    Beep; End If
End Sub

Private Sub PONER_DATOS(Matriz() As Double, indice As Integer)
   Panel.Row = indice;    Panel.Col = 0
   Panel.Text = indice;    Panel.Row = indice
   Panel.Col = 1;    Panel.Text = Format(Matriz(indice, 0), "###0.00")
   Panel.Col = 2;    Panel.Text = Format(Matriz(indice, 1), "###0.00")
   Panel.Col = 3;    Panel.Text = Format(Matriz(indice, 2), "###0.00")
   Panel.Col = 4;    Panel.Text = Matriz(indice, 3)
   Panel.Col = 5;    Panel.Text = Matriz(indice, 6)
End Sub

Public Sub ReadSpectrumF(spectrum)
Open spectrum For Binary As 1
Dim integf(3) As Double
posicion = 0;       channel = 0;        sumchnl = 0
i = 0;              j = 0

Do While posicion < LOF(1)

   DoEvents
   Linea = Input(1, #1);   posicion = Loc(1)
   If Loc(1) = 512 Then;   For i = 0 To 3;       integf(i) = 0;    Next i
   For i = 512 To LOF(1)
      channel = channel + 1;       inform = Input(3, #1)
      sumchnl = 0;                 posicion = Loc(1)
      For j = 1 To 3
         valor = (Mid(inform, j, 1))
         res = Asc(valor)
         cdb = (256 ^ (j - 1)) * res
         sumchnl = sumchnl + cdb
      Next j

      If DIP.w(0).Enabled Then                                  ' WINDOW1
         If channel > (Val(DIP.ch0(0).Text) - 1) And channel < (Val(DIP.ch0(1).Text) + 1) Then
            integf(0) = integf(0) + sumchnl;            win0f = integf(0);          End If
      End If
      If DIP.w(1).Enabled Then                                   ' WINDOW 2
         If channel > (Val(DIP.ch1(0).Text) - 1) And channel < (Val(DIP.ch1(1).Text) + 1) Then
            integf(1) = integf(1) + sumchnl;            win1f = integf(1);          End If
      End If
      If DIP.w(2).Enabled Then                                   ' WINDOW 3
         If channel > (Val(DIP.ch2(0).Text) - 1) And channel < (Val(DIP.ch2(1).Text) + 1) Then
            integf(2) = integf(2) + sumchnl;            win2f = integf(2);          End If
      End If
      If posicion = LOF(1) Then;          Exit Do;       End If
   Next i
   End If
   If FIN = True Then;       Exit Do;       Close 2;    End If
Loop;    Close 1
End Sub
Public Sub ReadSpectrumM(spectrum)

Open spectrum For Binary As 1; Dim integm(3) As Double
posicion = 0;       channel = 0;        sumchnl = 0
i = 0;              j = 0

Do While posicion < LOF(1)
```

```
   DoEvents
   Linea = Input(1, #1)
   posicion = Loc(1)
   If Loc(1) = 512 Then

   For i = 0 To 3;       integm(i) = 0;    Next i
   For i = 512 To LOF(1)   ' Step 3
      channel = channel + 1;       inform = Input(3, #1)
      sumchnl = 0;                 posicion = Loc(1)
      For j = 1 To 3
         valor = (Mid(inform, j, 1))
         res = Asc(valor)
         cdb = (256 ^ (j - 1)) * res
         sumchnl = sumchnl + cdb
      Next j

      If DIP.w(0).Enabled Then                          ' WINDOW 1
         If channel > (Val(DIP.ch0(2).Text) - 1) And channel < (Val(DIP.ch0(3).Text) + 1) Then
            integm(0) = integm(0) + sumchnl;            win0m = integm(0);          End If
      End If
      If DIP.w(1).Enabled Then                           'WINDOW 2
         If channel > (Val(DIP.ch1(2).Text) - 1) And channel < (Val(DIP.ch1(3).Text) + 1) Then
            integm(1) = integm(1) + sumchnl;            win1m = integm(1);          End If
      End If
      If DIP.w(2).Enabled Then                          ' WINDOW 3
         If channel > (Val(DIP.ch2(2).Text) - 1) And channel < (Val(DIP.ch2(3).Text) + 1) Then
            integm(2) = integm(2) + sumchnl;            win2m = integm(2);          End If
      End If
      If posicion = LOF(1) Then;          Exit Do;          Close 2;       End If
   Next i
   End If
   If FIN = True Then;       Exit Do;    End If
Loop;    Close 1
End Sub

Private Sub BOTON2_Click();       FIN = True;     End Sub
Private Sub Form_Load();          FIN = False;    End Sub
Private Sub BOTON1_Click();       FindDip (txtbatchname.Text);    End Sub

Private Sub chkpca1_Click()
If chkpca1.Value = 0 Then
   If w(0).Value = 1 Then;       ch0(0).Enabled = False;       ch0(1).Enabled = False;    End If
   If w(1).Value = 1 Then;       ch1(0).Enabled = False;       ch1(1).Enabled = False;    End If
   If w(2).Value = 1 Then;       ch2(0).Enabled = False;       ch2(1).Enabled = False;    End If
Else
 If w(0).Value = 1 Then;       ch0(0).Enabled = True;       ch0(1).Enabled = True;    End If
   If w(1).Value = 1 Then;      ch1(0).Enabled = True;       ch1(1).Enabled = True;    End If
   If w(2).Value = 1 Then;      ch2(0).Enabled = True;       ch2(1).Enabled = True;    End If
End If
End Sub

Private Sub chkpca2_Click()
If chkpca2.Value = 0 Then
   If w(0).Value = 1 Then;       ch0(2).Enabled = False;       ch0(3).Enabled = False;    End If
   If w(1).Value = 1 Then;       ch1(2).Enabled = False;       ch1(3).Enabled = False;    End If
   If w(2).Value = 1 Then;       ch2(2).Enabled = False;       ch2(3).Enabled = False;    End If
Else
 If w(0).Value = 1 Then;       ch0(2).Enabled = True;       ch0(3).Enabled = True;    End If
   If w(1).Value = 1 Then;     ch1(2).Enabled = True;       ch1(3).Enabled = True;    End If
   If w(2).Value = 1 Then;     ch2(2).Enabled = True;       ch2(3).Enabled = True;    End If
```

```
End If
End Sub

Private Sub w_Click(Index As Integer)
If w(0).Value = 0 Then
   ch0(0).Enabled = False;    ch0(1).Enabled = False;    ch0(2).Enabled = False;    ch0(3).Enabled = False
Else
   If chkpca1.Value = 1 Then;       ch0(0).Enabled = True;       ch0(1).Enabled = True;    End If
   If chkpca2.Value = 1 Then;       ch0(2).Enabled = True;       ch0(3).Enabled = True;    End If
End If
If w(1).Value = 0 Then
   ch1(0).Enabled = False;    ch1(1).Enabled = False;    ch1(2).Enabled = False;    ch1(3).Enabled = False
Else
   If chkpca1.Value = 1 Then;       ch1(0).Enabled = True;       ch1(1).Enabled = True;    End If
   If chkpca2.Value = 1 Then;       ch1(2).Enabled = True;       ch1(3).Enabled = True;    End If
End If
If w(2).Value = 0 Then
   ch2(0).Enabled = False;    ch2(1).Enabled = False;    ch2(2).Enabled = False;    ch2(3).Enabled = False
Else
   If chkpca1.Value = 1 Then;       ch2(0).Enabled = True;       ch2(1).Enabled = True;    End If
   If chkpca2.Value = 1 Then;       ch2(2).Enabled = True;       ch2(3).Enabled = True;    End If
End If
End Sub
```

Appendix IV

Abstract (translation) / Resumen

Esta tesis versa sobre la aplicación del análisis con haces de iones (IBA) al estudio de diversas heteroestructuras semiconductoras con un gran ancho de banda electrónica (gap). Los estudios llevados a cabo a lo largo de la presente tesis están motivados por la necesidad de mejorar el crecimiento epitaxial de las capas base y activas en los transistores de alta movilidad electrónica (HEMT) y en otros dispositivos optoelectrónicos de alta potencia. Al mismo tiempo, esta memoria evalúa las ventajas y límites de las técnicas de haces de iones en la caracterización estructural y composicional de tales heteroestructuras, como alternativa y complemento a otros métodos como la difracción de rayos X. A continuación se especifican los principales aspectos considerados en este trabajo.

Respecto al crecimiento de capas base sobre zafiro, se investigó el efecto de las capas de nucleación y de la temperatura de crecimiento para el GaN y el ZnO, respectivamente. Los resultados obtenidos en la investigación se usaron para determinar las condiciones óptimas de crecimiento de las capas de GaN y ZnO, especialmente en lo relativo a la calidad cristalina y a la incorporación adecuada de los distintos elementos en la red wurzita.

Considerado como un punto importante en el desarrollo de transistores de alta movilidad, se estudió la presencia de gradientes de Al en las intercaras AlGaN/GaN por medio de distintas técnicas de haces de iones. Tales perfiles composicionales de Al fueron examinados junto con la relajación inducida de la tensión. La aplicación de las técnicas IBA en láminas delgadas de AlGaN fue también utilizada para diferenciar el efecto de diferentes capas base. En relación con este estudio, se desarrollaron análisis de alta resolución en profundidad para determinar el contenido de hidrógeno en muestras preparadas por distintos métodos de crecimiento. Se exploró, además, el papel relevante de los mecanismos de difusión para la introducción de hidrógeno en la región del gas bidimensional de electrones.

Esta memoria también trata el difícil crecimiento de capas ternarias de InGaN de alta calidad, asociado a la baja miscibilidad del In en la matriz de GaN. Este fenómeno fue investigado en una serie de muestras crecidas a distinta temperatura y cubriendo todo el rango composicional. El deterioro de la calidad cristalina de las láminas de InGaN para contenidos intermedios se verificó y evaluó como función de la progresiva relajación de los parámetros de red. El efecto crítico de la temperatura en este sentido se manifestó en los experimentos, y los resultados obtenidos se emplearon para establecer un diagrama de crecimiento de InGaN sobre la base de la composición efectiva de las láminas.

La ingeniería del ancho de la banda electrónica en capas de MgZnO se investigó en relación con el contenido de Mg para determinar la dependencia de las propiedades eléctricas con la estequiometría. Sobre estas capas se realizó un dopaje con N por medio de implantación iónica a baja energía. La optimización del tratamiento térmico posterior a la implantación se llevó a cabo por medio de estudios de fotoluminiscencia adicionales.

Finalmente, los estudios mostrados en esta tesis en compuestos de AlInN y AlGaInN con acuerdo de red revelaron la sinergia entre la razón III/V y la temperatura de crecimiento en el crecimiento epitaxial de las láminas, afectando a la calidad cristalina y a la composición final. El estado de tensión de las capas se analizó por canalización iónica y por difracción de rayos X, evidenciando la presencia de comportamientos de canalización anómalos. Las simulaciones de Monte Carlo explicaron estos fenómenos, vinculados a los efectos de reconducción de los iones en la intercara. Las simulaciones se usaron, a su vez, para establecer el papel de la distorsión tetragonal, el espesor, y la energía del haz sobre estos efectos. La ruptura de los sucesos de canalización anómala se demostró teórica y experimentalmente en heteroestructuras específicas en acuerdo de red, permitiendo la determinación de la tensión con una alta precisión.

Appendix V

Conclusions and future work (translation) / Conclusiones y trabajo futuro

Conclusiones

Para la consecución de esta tesis se establecieron diversos objetivos, pricipalmente siguiendo la hoja de ruta del proyecto KORRIGAN, junto con otros proyectos nacionales y colaboraciones. Dentro de ese marco diversificado, esta tesis ha abordado diferentes temas relativos al procesado de WBS HSs, estudiados por técnicas IBA y otras complementarias. En los capítulos precedentes se han compilado los resultados más relevantes, proporcionando una comprensión más profunda de los fenómenos de crecimiento de tales materials, y que ciertamente contribuyen a la optimización de los procesos de preparación. A continuación se resumen las contribuciones más importantes.

Contribuciones a la optimización de capas base

Los beneficios de las capas de nucleación (NLs) de AlN y GaN sobre el crecimiento de capas base de GaN fue comparado, encontrándose una clara mejoría del crecimiento bidimensional y una reducción de los defectos en el primer caso. Se demostró que la relativamente alta densidad de defectos se produce fundamentalmente en los primeros nanómetros de la capa de nucleación. Sin embargo, los defectos estructurales están confinados en esa región próxima a la intercara, de manera que la calidad cristalina del resto de la capa es alta en ambos casos (con NLs de AlN o de GaN). Además, la presencia de tensión en los primeros estadios del crecimiento fue verificada en los dos tipos de capas base.

Se comprobó por medio de RBS/C y XRD que el crecimiento epitaxial de ZnO sobre zafiro por PMS mejora a moderadas temperaturas del sustrato (550 ºC). En tales

circunstancias, las capas de ZnO muestran un único dominio cristalino. La señales de Zn y de O mostraron distintos comportamientos con la temperatura, tanto en RBS/C como en los espectros Raman, sugiriendo el mejor ordenamiento de la subred del Zn. Para temperaturas por encima de 400 ºC, se observó la interdifusión Al-Zn en la intercara lámina-sustrato, lo que afecta a la calidad cristalina en esa región.

Contribuciones a la optimización de heteroestructuras en desacuerdo de red

La caracterización por medio de técnicas IBA de los perfiles composicionales de Al en HSs de AlGaN/GaN con diferente estequiometría fue realizada con éxito. Se observaron gradientes composicionales para contenidos altos de Al, y se asociaron con efectos de relajación de la tensión en las capas. Se encontró, además, una clara correlación entre los resultados obtenidos por IBA y por XRD. Los perfiles de composición obtenidos permitieron explicar las los barridos angulares efectuados por XRD. La buena resolución en profundidad, y la alta sensibilidad al Al de ERD-BIC fueron factores determinantes para la medida de perfiles composicionales y la caracterización de HSs diseñadas para HEMTs con distintas estructuras. La presencia significativa de H en la intercara AlGaN/GaN se comprobó por medio de NRA. El estudio, llevado a cabo en muestras crecidas por distintos métodos, evidenció la incorporación de H en pequeñas, pero no despreciables, cantidades. La concentración de H es independiente de la técnica de crecimiento empleada, y se halló una cantidad significativa en la región próxima al 2DEG, lo que puede ser relevante en el funcionamiento final del transistor. Un modelo difusivo permitió explicar los perfiles resueltos en profundidad obtenidos para el H, señalando un origen ambiental posterior al depósito de las capas.

Se investigó el efecto de la miscibilidad en la calidad cristalina y la composición para HSs InGaN/GaN crecidas por PA-MBE, observando una clara disminución de la calidad para composiciones intermedias, acompañada por una relajación de los parámetros de red. Los análisis de RBS se usaron para establecer un diagrama de crecimiento para el InGaN, sobre la base de la determinación de la energía de activación para la descomposición del InN. De esta forma, se delimitaron tres regiones de crecimiento diferentes.

La composición de capas de MgZnO crecidas sobre sustratos con orientación no polar y para distintos flujos del gas precursor se analizó por RBS. Se comprobó el carácter rico en O de las muestras, y el aumento lineal del ancho entre bandas fue relacionado con el contenido de Mg. Los barridos angulares mostraron una baja calidad cristalina de las muestras, con una tendencia similar de las señales de Mg y Zn. Finalmente, la dopaje con N de las capas se realizó por medio de implantación iónica a baja energía. Tras la implantación, se encontró que el daño producido podía recuperarse gracias a un tratamiento térmico a 900 ºC. Las medidas de PL de las muestras implantadas (y calentadas) mostraron una emisión superior a la de las muestras no irradiadas, confirmando la buena reconstrucción descubierta por RBS/C. Los tratamientos a esta temperatura no afectan a la migración de los elementos de las capas, excepto por una ligera interdifusión Al-Zn en la intercara entre lámina y sustrato.

Contribuciones a la optimización de heteroestructuras en acuerdo de red

Se demostró la útil combinación de las técnicas de RBS/C y HR-XRD para la caracterización de capas ternarias y cuaternarias en acuerdo de red. Los análisis de RBS de las laminas de AlInN crecidas por PA-MBE dentro de tres regímenes diferentes se llevó acabo, demostrando que el valor nominal de la razón III/V está normalmente infraestimado debido a la contribución adicional de In proveniente de la descomposición térmica del InN. La temperatura de crecimiento también reduce la incorporación de In debido a la concurrencia de los mecanismos de descomposición y la desorción. Los perfiles composicionales encontrados para el régimen intermedio rico en In muestra que la transición hacia un equilibrio dinámico es necesaria para el crecimiento de la capa ternaria con una alta calidad cristalina. Esta condición debe considerarse para el desarrollo y la funcionalidad de dispositivos basados en AlInN. Las capas de AlInN mostraron, además, un crecimiento pseudomófico para el régimen rico en In, con ligeras desviaciones a altas y bajas temperaturas. El estado de tensión fue calculado por HR-XRD y RBS/C, siguiendo la misma tendencia lineal (de compresivo a tensil), aunque se detectaron efectos anómalos de canalización en los barridos angulares que, aparentemente (ver más adelante), afectan a la sensibilidad a la tensión del método. La ley de Vegard se satisface, por lo general, en las capas de AlInN para el rango composicional estudiado.

Respecto al análisis de capas cuaternarias, se demostró que el flujo de Al es un factor limitante en la incorporación efectiva del In, incluso para proporciones fijas III/V. Este hecho se relacionó con la mayor energía de enlace en el binario Al-N con respecto al In-N. Se encontró una drástica reducción de In con el aumento de la temperatura debido a la desorción y descomposición inducida térmicamente. Se verificó la alta calidad de estas láminas cuaternarias, crecidas pseudomorficamente bajo tensión compresiva. Los barridos angulares de RBS/C mostraron, de nuevo, efectos anómalos con un inesperado desplazamiento nulo entre las señales de la capa y el sustrato.

Las simulaciones de MC desarrolladas en sistemas en acuerdo de red probaron que las características anómalas de la canalización mencionadas anteriormente se deben a efectos de reconducción de los iones en la intercara de la HS. Las simulaciones muestran también que tales efectos se ven normalmente acrecentados por los espesores elevados y las bajas tensiones de las capas activas. La influencia de estos parámetros se confirmó experimentalmente en muestras seleccionadas de AlInN. De esta manera, los métodos MC pueden explicar y corregir (en ciertos casos) las curvas angulares observadas, para proporcionar una determinación precisa del estado de tensión por RBS/C. En las situaciones donde esta aproximación no es posible, se propuso un método alternativo para eliminar los efectos de reconducción por medio de la energía del haz. Los experimentos a alta energía probaron que la ruptura de los fenómenos de canalización anómalos es posible, permitiendo superar las aparentes limitaciones del RBS/C.

Trabajo futuro

Los resultados obtenidos en esta tesis han arrojado luz sobre el crecimiento de HSs de WBS, pero también han abierto nuevos campos y cuestiones para la continuación del trabajo. Además, debido al limitado tiempo para la producción de esta tesis, algunos estudios interesantes no pudieron ser abordados, o fueron desarrollados en un grado inferior al del resto de estudios contenidos en esta memoria. Otros trabajos están siendo analizados en la actualidad y se completarán en un futuro cercano. En esta sección se sugieren algunas posibles continuaciones de este trabajo.

Trabajo futuro en capas base

El crecimiento de capas base de GaN y ZnO sobre zafiro ha alcanzado una calidad razonable en el momento actual, pero todavía son posibles mejoras adicionales. En particular, se sugieren las siguientes tareas en esta línea:

- El análisis del crecimiento de capas de GaN sobre ZnO, y viceversa. La combinación de ambos binarios se está volviendo cada vez más común, y ha mostrado tener grandes beneficios sobre el grado de tensión y cristalinidad de las capas base.

- El análisis de impurezas tales como H o C en capas base de ZnO. Estas impurezas podrían jugar un papel importante como trampas para los portadores, afectando a las propiedades eléctricas de las capas y condicionando las posibilidades del dopaje tipo p.

- El estudio de las posiciones de red ocupadas por los dopantes en ZnO. Sería particularmente interesante llevar a cabo experimentos de NRA para estudiar la localización del N en condiciones de canalización iónica. Esto permitiría la determinación exacta de la posición del N en la red wurzita y proporcionaría una información muy valiosa sobre la activación del N como dopante, para modificar de manera efectiva la estructura de bandas. Para otros elementos de grupo V, como Sb o As, el RBS/C sería un buen método debido a la buena separación de las señales en el espectro.

Trabajo futuro en heteroestructuras

Aunque esta tesis ha mostrado el análisis de una gran variedad de HSs de WBS, quedan algunos sistemas de gran interés todavía inexplorados. Por consiguiente, se proponen algunas tareas para el futuro en este sentido. No obstante, con antelación a los análisis, deberían llevarse a cabo varias mejoras en los programas de control y adquisición de RBS/C en el CMAM. Los códigos desarrollados en esta tesis han resuelto algunas de las limitaciones iniciales presentes al principio de este trabajo, estableciendo métodos valiosos para obtener espectros alineados y aleatorios. Sin embargo, las fuertes analogías entre los experimentos de RBS/C y XRD sugieren el uso de programas de ordenador similares para el control del movimiento del goniómetro, la adquisición en

tiempo real, y el ajuste de los picos para el alineamiento, todo ello dentro de un entorno gráfico sencillo. Así, la primera propuesta es la mejora de los códigos actuales de análisis por RBS/C, especialmente relativos a las medidas en tiempo real.

Una vez los sistemas experimentales estén optimizados, nuevas tares pueden ser exploradas, incluyendo:

- El estudio de los mecanismos que afectan a la separación de fases en HSs ternarios y cuaternarios. Éste es un punto muy crítico y bastante extendido que todavía no está bien entendido. Además, la separación de fases juega un papel significativo en el deterioro de las capas, así que deberían focalizarse más esfuerzos en este tema. Más concretamente, no está claro si hay siempre una relación causal entre la composición y la relajación de la tensión.

- El estudio sistemático de la incorporación de H y otras impurezas ligeras en el 2DEG de los transistores de AlGaN/GaN, y su correlación con el funcionamiento eléctrico de los dispositivos.

- El análisis de los límites de composición en capas de MgZnO y CdZnO con respecto a la miscibilidad de las fases cúbicas en la red wurzita. La determinación de las posiciones de red del Mg y el Cd por medio de simulaciones MC de los barridos angulares.

- El estudio de la relación entre el régimen de crecimiento (rico en N, con gotas de In, o intermedio rico en In) y los gradientes composicionales en capas de AlInN. Además, la comprensión de los fenómenos físicos que inducen la formación de gotas de In durante el crecimiento podría dar información importante sobre el orígen de los defectos estructurales.

- El análisis de superredes y estructuras de MQW en acuerdo de red y, en particular, la evolución del estado de tensión con el espesor y el número de bicapas.

Trabajos relacionados con HEMTs

A pesar de que esta tesis se ha centrado en la optimización de las capas base y activas de los dispositivos, ésta es sólo una parte de la gran serie de procesos de fabricación. En particular, el depósito de capas pasivantes y la formación de contactos óhmicos puede

afectar en gran manera el funcionamiento y la fiabilidad de los dispositivos. Estos dos temas fueron estudiados en menor extensión durante esta tesis pero no se finalizó complemente ningún estudio sistemático.

El análisis por RBS de los contactos óhmicos podría ayudar a la determinación de la migración de especies durante los tratamiento térmicos, como se ha evidenciado de hecho en las pruebas preliminares realizados en el CMAM. En estas medidas, la estructura de multicapa del contacto se verifico con análisis composicionales en profundidad, encontrando a su vez que el proceso de RTA induce una difusión inhomogénea de los elementos del contacto (Au, Ti, Al, Ni…). Esto puede afecta a la resistencia superficial, un parámetro importante para el funcionamiento del dispositivo. Consecuentemente, se sugiere fuertemente la continuación del estudio de los contactos óhmicos. No obstante, se deberían considerar otras herramientas analíticas diferentes al RBS, ya que el solape de señales en RBS hace el análisis muy complicado. En el caso particular de las técnicas IBA, los sistemas de ERD-TOF o ERD-BIC pueden ser alternativas eficaces en este sentido.

El estudio de capas pasivantes es otro punto importante para los desarrollos futuros en transistores. Estas capas se depositan normalmente por CVD, y consiste principalmente en SiN. Los resultados obtenidos durante esta tesis han evidenciado concentraciones muy altas de H en estas capas. Teniendo en cuenta el modelo de difusión de H propuesto en AlGaN (capítulo 5) y las altas temperaturas de trabajo de los dispositivos, la reducción del H en estas capas pasivantes podría ser un logro destacable. Por tanto, se propone una optimización adicional de estas capas.

Por supuesto, el mayor objetivo que puede ser sugerido para el futuro es la medida de un dispositivo completamente integrado por IBA. Esta clase de experimento requeriría el uso de un microhaz en condiciones de vacío para el estudio, por ejemplo, de distintas partes de un transistor con resolución lateral submicrométrica. En la actualidad, hay varios laboratorios con la capacidad para generar ese tipo de haces, que permitirían analizar la fiabilidad de los dispositivos en su estado final de fabricación .De hecho, durante esta tesis, se midieron contactos TLM con tamaños micrométricos en la línea de microhaz externo del CMAM, demostrando la viabilidad de este procedimiento. Tales estudios, podrían además dar información muy valiosa sobre el deterioro de los

dispositivos después de su funcionamiento, e incluso, sobre la operación en tiempo real del transistor con medidas in-situ.

Publications and contributions

List of publications related with this thesis

1. S. Fernández-Garrido, E. Calleja, A. Redondo-Cubero, R. Gago, J. Pereiro, F. González-Posada and E. Muñoz, *Properties and growth by plasma assisted molecular beam epitaxy of quaternary III-nitrides*, 289-313, NITRIDE AND DILUTE NITRIDE: GROWTH, PHYSICS, AND DEVICES (ISBN 978-81-7895-250-5), Special Review Books (Phys. Sci.), Transworld Research Network, Kerala (India), 2007.

2. A. Redondo-Cubero, R. Gago, M. F. Romero, A. Jiménez, F. González-Posada, A.F. Braña and E. Muñoz, *Study of SiN_x:H_y passivant layers for AlGaN/GaN high electron mobility transistors*, Phys. Stat. Sol. (c) 5, 518-521, 2008.

3. S. Fernández-Garrido, J. Pereiro, F. González-Posada, E. Muñoz, E. Calleja, A. Redondo-Cubero and R. Gago, *Photoluminescence enhancement in quaternary III-nitrides alloys grown by molecular-beam epitaxy with increasing Al content*, J. Appl. Phys. 103, 046104 (3 p.), 2008.

4. A. Redondo-Cubero, R. Gago, F. González-Posada, U. Kreissig, M.-A. di Forte Poisson, A.F. Braña and E. Muñoz, *Aluminium incorporation in AlGaN/GaN heterostructures: a comparative study by ion beam analysis and X-ray diffraction*, Thin Solid Films 516, 8447-8452, 2008.

5. S. Fernández-Garrido, A. Redondo-Cubero, R. Gago, F. Bertram, J. Christen, E. Luna, A. Trampert, J. Pereiro, E. Muñoz and E. Calleja, *Effect of the growth temperature and AlN mole fraction on In incorporation and properties of quaternary III-nitride layers grown by molecular beam epitaxy*, J. Appl. Phys 104, 083510 (7 p.), 2008.

6. F. González-Posada Flores, A. Redondo-Cubero, R. Gago, A. Bengoechea, A. Jiménez, D. Grambole, A.F. Braña and E. Muñoz, *High-resolution hydrogen profiling in AlGaN/GaN heterostructures grown by different epitaxial methods*, J. Phys. D: Appl. Phys. 42, 055406 (5 p.), 2009.

7. A. Redondo-Cubero, K. Lorenz, N. Franco, S. Fernández-Garrido, R. Gago, P.J.M. Smulders, E. Muñoz, E. Calleja and E. Alves, *Influence of steering effects on strain detection in AlGaInN/GaN heterostructures by ion channelling*, J. Phys. D: Appl. Phys. 42, 065420 (8 p.), 2009.

8. V. Tasco, A. Campa, I. Tarantini, A. Passaseo, F. González-Posada, A. Redondo-Cubero, K. Lorenz, N. Franco and E. Muñoz, *Investigation of different mechanisms of GaN growth induced on AlN and GaN nucleation layer*, J. Appl. Phys 105, 063510 (5 p.), 2009.

9. A. Redondo-Cubero, K. Lorenz, R. Gago, N. Franco, S. Fernández-Garrido, P.J.M. Smulders, E. Muñoz, E. Calleja, I. M. Watson and E. Alves, *Breakdown of anomalous channeling with ion energy for accurate strain determination in GaN-based heterostructures*, Appl. Phys. Lett. 95, 051921 (3 p.), 2009.

10. A. Redondo-Cubero, K. Lorenz, R. Gago, N. Franco, M.-A. di Forte Poisson, E. Alves and E. Muñoz, *Depth-resolved analysis of spontaneous phase separation in the growth of lattice-matched AlInN*, J. Phys. D: Appl. Phys. 43, 055406 (5 p.), 2010.

11. J. Pereiro, A. Redondo-Cubero, S. Fernández-Garrido, J. Grandal, R. Gago, K. Lorenz, M.A. Sánchez-García, N. Franco, E. Alves, E. Calleja and E. Muñoz, *On the control of alloy composition and structural quality of $In_xGa_{1-x}N$ layers ($0<x<1$) grown by plasma-assisted molecular beam epitaxy*, J. Appl. Phys. (submitted).

12. J. Pereiro, A. Redondo-Cubero, S. Fernandez-Garrido, C. Rivera, A. Navarro, E. Muñoz, E. Calleja and R. Gago, *Mg doping of InGaN layers grown by PA-MBE for the fabrication of Schottky barrier photodiodes*, J. Phys. D: Appl. Phys. (submitted).

Contributions to Congresses related with this thesis

1. M.F. Romero, A. Jiménez, J. Miguel-Sánchez, F. González-Posada, A. Redondo-Cubero, A. F. Braña and E. Muñoz, *Impact of N_2 plasma pre-treatment on AlGaN/GaN HEMT device performance*, 15th European Workshop on Heterostructure Technology HeTech 2006, Manchester (United Kingdom), 02.10.2006, ORAL.

2. S. Fernández-Garrido, E. Calleja, F. González-Posada, A. Braña, E. Muñoz, A. Redondo-Cubero, R. Gago, A. Muñoz-Martín, A. Trampert and K. H. Ploog, *Strong carrier localization enhancement in InAlGaN layers grown by MBE*, International Workshop on Nitride Semiconductors (IWN 2006), Kyoto (Japan), 22.10.2006, ORAL.

3. K. Bejtka, R.W. Martin, S. Fernández-Garrido, E. Calleja, A. Redondo-Cubero and F. González-Posada, *Composition and luminescence of AlInGaN layers grown by PA-MBE*, United Kingdom Nitride Consortium 2007, Cambridge (United Kingdom), 04.01.2007, ORAL.

4. A. Redondo-Cubero, R. Gago, F. González-Posada, S. Fernández-Garrido, J. Pereiro, A. Muñoz-Martín, A.F. Braña, U. Kreissig, and E. Muñoz, *Ion beam analysis of ternary and quaternary $Al_xIn_yGa_{1-x-y}N$ heterostructures for high-power electronic devices*, European Materials Research Society 2007 (Symposium F), Strasbourg (France), 30.05.2007, ORAL.

5. A. Redondo-Cubero, M. F. Romero, R. Gago, A. Muñoz-Martín, A.F. Braña, A. Jiménez and E. Muñoz, *Study of a-SiN:H passivant layers for GaN-based high electron mobility transistors*, European Materials Research Society 2007 (Symposium F), Strasbourg (France), 31.05.2007, POSTER.

6. A. Redondo-Cubero, R. Gago, F. González-Posada, U. Kreissig and E. Muñoz, *Elastic recoil detection of Al in AlGaN/GaN heterostructures*, Engineering and characterisation of nanostructures by photon, ion beam and nuclear methods, Smolenice (Slovakia), 04.05.2008, POSTER.

7. A. Redondo-Cubero, K. Lorenz, N. Franco, S. Fernández-Garrido, R. Gago, E. Muñoz and E. Alves, *Influence of steering effects on ion channeling determination of strain in GaN-based heterostructures*, Charged and neutral particles channeling phenomena (Channeling 2008), Erice (Italy), 28.10.2008, ORAL.

8. A. Redondo-Cubero, M. Vinnichenko, M. Krause and R. Gago, Structural investigations of ZnO thin films grown by reactive pulsed magnetron sputtering at different substrate temperatures, Charged and neutral particles channeling phenomena (Channeling 2008), Erice (Italy), 28.10.2008, POSTER.

9. S. Fernández-Garrido, Ž. Gačević, E. Calleja, A. Redondo-Cubero, R. Gago and E. Muñoz, *A comprehensive diagram to grow InAlN alloys by plasma-assisted molecular beam epitax*y, 15th European Molecular Beam Epitaxy Workshop (EuroMBE 2009), Zakopane (Poland), 09.03.2009, ORAL.

10. A. Redondo-Cubero, J. Pereiro, J. Grandal, K. Lorenz, N. Franco, R. Gago, E. Muñoz, M. A. Sánchez-García, E. Calleja and E. Alves, *Structural study of the epitaxial growth in InGaN/GaN heterostructures by ion beam analysis*, 33rd Workshop on Compound Semiconductor Devices and Integrated Circuits (WOCSDICE 2009), Málaga (Spain), 18.05.2009, ORAL.

11. A. Redondo-Cubero, R. Gago, K. Lorenz, N. Franco, E. Muñoz, M.-A. di Forte Poisson and E. Alves, *Depth-resolved analysis of phase separation in AlInN by ion channeling*, 19th International meeting on Ion Beam Analysis (IBA 2009), Cambridge (United Kingdom), 07.09.2009, POSTER.

12. A. Redondo-Cubero, K. Lorenz, N. Franco, S. Fernández-Garrido, R. Gago, P.J.M. Smulders, E. Muñoz, E. Calleja, I.W. Watson and E. Alves, *Accurate measurement of strain in semiconductor heterostructures by high-energy ion channeling: the influence of steering effects*, 19th International meeting on Ion Beam Analysis (IBA 2009), Cambridge (United Kingdom), 10.09.2009, ORAL.

13. E. Muñoz, C. Rivera, F. González-Posada, A. Redondo-Cubero, M.F. Romero, R. Cuerdo, F. Calle, R. Gago, A. Jiménez and C. Palacio, *Materials and strain issues in AlGaN/GaN HEMT degradation*, 2009 International Conference on Solid State Devices and Materials (SSDM 2009), Miyagi (Japan), 07.10.2009, INVITED.

Other publications

1. R.J. Martín-Palma, A. Redondo-Cubero, R. Gago, J.V. Ryan and C.G. Pantano, *Rutherford backscattering spectrometry characterization of nanoporous chalcogenide thin films grown at oblique angle*s, J. Anal. At. Spectrom. 23, 981-984, 2008.

2. J.A. Sánchez-García, L. Vázquez, R. Gago, A. Redondo-Cubero, J.M. Albella and Zs. Czigány, *Tuning surface morphology in self-organized ion beam nanopatterning of Si(001) via metal incorporation: from holes to dots*, Nanotechnology 19, 355306 (9 p.), 2008.

3. J.A. Sánchez-García, R. Gago, R. Caillard, A. Redondo-Cubero, J.A. Martín-Gago, F.J. Palomares, M. Fernández and L. Vázquez, *The production of nanohole/nanodot patterns on Si(001) by ion beam sputtering with simultaneous metal incorporation*, J. Phys.: Condens. Matter 21, 224009 (13 p.), 2009.

4. R. Gago, A. Redondo-Cubero, J.L. Endrino, I. Jiménez and N. Shevchenko, *Aluminium incorporation in nanocrystalline $Ti_{1-x}Al_xN$ films studied by X-ray absorption near edge structure*, J. Appl. Phys. 105, 113521 (6 p.), 2009.

5. V. Carcelén, A. Redondo-Cubero, E. Gutiérrez-Puebla, J.A. Rodríguez-Velamazán, M.A. Monge, E. Diéguez and D. Martín y Marero, *Study of structural modification of CdZnTe bulk crystals induced by Bismuth doping*, Chem. Phys. Lett. 485, 207-210, 2010.

6. R. Gago, M. Vinnichenko, A. Redondo-Cubero and L. Vázquez, *Structural and morphological correlation in TiO_2 films grown by reactive pulsed magnetron sputtering at room temperature and different O_2 partial pressures*, Plasma Process. Polym. (submitted).

7. M. Díaz, L. Martínez, E. Román, A. Redondo-Cubero, M.A. Muñoz-Márquez, G. van der Laan, N. D. Telling, P. Bailey, T.C.Q. Noakes, Y. Huttel, *Compositional and structural medium energy ion scattering study of the temperature mediated diffusion determination at the Co/V interface in Co/V/MgO(100)*, J. Anal. At. Spectrom. (submitted).

Other contributions to Congresses

1. R. Gago, L. Vázquez, J.A. Sánchez-García, O. Plantevin, T.H. Metzger, J. Muñoz-García, R. Cuerno, M. Castro, J.M. Albella, A. Redondo-Cubero and A. Climent-Font, *Nanodot patterning of Si surfaces by ion beam sputtering*, Trends in NanoTechnology TNT 2006, Grenoble (France), 08.09.2006, POSTER.

2. A. Redondo-Cubero, J.A. Sánchez-García, R. Gago, L. Vázquez, J. Muñoz-García, M. Castro and R. Cuerno, *Surface nanodot patterning of amorphous silicon films by low-energy ion beam sputtering*, Nanopatterning via ions, photon beam and epitaxy, Sestri Levante (Italy), 23.09.2007, POSTER.

3. V. Carcelén, D. Martín y Marero, A. Redondo-Cubero, E. Diégez, *Ion channelling study in single crystals of CdZnTe*, V Reunión del Grupo Especializado de Física del Estado Sólido, Santiago de Compostela (Spain), 06.02.2008, POSTER.

4. R. Gago, A. Redondo-Cubero, M. Vinnichenko, I. Jiménez, Zs. Czigány and L. Vázquez, *Correlation between morphology and bonding structure in titanium oxide films produced by reactive pulsed magnetron sputtering*, European Materials Research Society 2009 (Symposium H), Strasbourg (France), 11.06.2009, POSTER.

5. R. Gago, J.A. Sánchez-Gracía, A. Redondo-Cubero and L. Vázquez, *Tuning the morphology of silicon surface nanopatterns induced by low-energy ion beam sputtering with simultaneous metal incorporation*, Nanoscale Modification of Surfaces and Thin Films Workshop 2009, Rathen (Germany), 31.08.2009, INVITED.

6. L. Vázquez, R. Gago, J.A. Sánchez-García, J. Muñoz-García, R. Cuerno, A. Redondo-Cubero, M.M. García-Hernández and M. Castro, *Hole, dot and cellular nanopatterns induced on Silicon surfaces by ion bombardment*, Materials Research Society 2009 (Symposium KK), Boston (U.S.A.), 01.12.2009, INVITED.